



**Process optimisation for Fe-based nanocrystalline soft-
magnetic alloys produced with laser additive
manufacturing**

Merve Gizem Özden

Under the supervision of Nicola A. Morley

*A thesis submitted in partial fulfilment of the requirements for
the degree of Doctor of Philosophy*

Department of Material Science and Engineering

Faculty of Engineering

The University of Sheffield

UK

December 2023

Abstract

Fe-based amorphous and nano-crystalline alloys have emerged as promising substitutes for silicon steel in power electronics and electrical machines due to their lower coercivity (H_c) and significantly reduced core loss. Nevertheless, these amorphous/nano-crystalline materials still exhibit a lower saturation flux density (B_s) compared to silicon steel. Enhancing the power density and efficiency of advanced electronic devices relies on the development of Fe-based nanocrystalline alloys with high B_s and low core loss. However, the production of application-sized parts from Fe-based nanocrystalline alloys with high B_s faces challenges due to their low glass-forming ability. This limits the manufacturability of such alloys, making nanocrystallization a difficult process. Utilising high cooling rates during laser powder bed fusion (LPBF) process presents a favourable opportunity for fabricating Fe-based amorphous/nanocrystalline alloys with intricate geometries. This work demonstrated an extensive process optimization for Fe-based nanocrystalline alloys to produce parts with high bulk density and soft-magnetic behaviour.

The optimization of process parameters in the LPBF technique has been examined by considering the volumetric energy input (E), which encompasses key build parameters such as laser power (P), scan speed (v), layer thickness (t), and hatch spacing (h). This investigation focused on understanding the impact of these major process parameters on the physical and magnetic properties of Fe-based amorphous/nanocrystalline composites ((Fe_{87.38}Si_{6.85}B_{2.54}Cr_{2.46}C_{0.77}, mass %)) fabricated through LPBF. Various combinations of process parameters involving P and v were applied while considering t and h .

The magnetic properties exhibit notable variations attributed to the amorphous phase content and the presence of nanocrystalline phases within the microstructure, and their size is greatly influenced by the process parameters. The microstructure undergoes transformation during the laser scanning process, resulting in the formation of molten pools (MP) and heat-affected zones (HAZ) due to the significant thermal gradient between laser tracks. The molten pools primarily consisted of α -Fe(Si) nanograins, while the heat-affected zones typically contained clusters of nanocrystalline Fe₂B and Fe₃Si. The size and quantity of these nanocrystallites played a crucial role in determining the magnetic properties. For this reason, the detailed microstructural analysis was performed to comprehend the change in the soft-magnetic behaviour, depending on the process parameters.

Acknowledgements

Completing this PhD thesis has been a challenging, yet rewarding journey that would not have been possible without the support, guidance, and encouragement of many individuals. I would like to express my sincerest gratitude to all those who have contributed to my success.

Firstly, I would like to thank my supervisor, *Nicola A. MORLEY*, for her constant support, guidance, and encouragement throughout my PhD journey. Her expertise, insights, and feedback were invaluable in shaping the direction and outcomes of this research. I am also grateful for her dedication to my personal and professional growth, and for the opportunities she has provided me to present my work at conferences and publish papers.

I would also like to express my heartfelt gratitude to my family, especially my parents *Arife ÖZDEN* and *Şaban ÖZDEN*, for their unwavering support, love, and encouragement throughout my life. Their sacrifices and commitment to my education have been instrumental in helping me achieve my academic goals. I would also like to thank my sisters *Gamze Nur GÜLER* and *Zeynep Sude ÖZDEN* and my aunt *Birsen AKBAŞLI* for their constant encouragement and motivation. I extend my heartfelt gratitude to my niece, *Tuana GÜLER*, for always brightening up my visits to Turkey and constantly motivating me to complete my PhD as soon as possible, so that I can spend more time with her.

To my friends, *Hüda Nur DURAK*, *Meryem ÜSTÜN-YAVUZ* and *Kübra GENÇ*, thank you for your unwavering support and for being there for me through the ups and downs of this journey. Your encouragement, laughter, and kindness have helped me maintain a positive outlook and persevere through the challenges.

I would like to express my gratitude to my colleagues and the members of the Functional Magnetic Material (FMM) team for their valuable discussions, feedback, and assistance throughout this research. Their collaboration has enriched my research experience and contributed to the successful outcomes of this thesis.

I am also grateful to the staff and faculty at the *University of Sheffield*, *Sorby Electron Microscopy* and *Royce Discovery Centre* who have provided me with the necessary resources and facilities to conduct this research.

Lastly, I would like to acknowledge the financial support provided by the *Republic of Turkey Ministry of National Education*, which has enabled me to pursue my academic goals.

To all those who have supported me throughout this journey, I am deeply grateful. Your contributions have played a significant role in shaping the outcomes of this thesis and my personal and professional growth. Thank you.

Declaration

I, the author, confirm that the Thesis is my own work. I am aware of the University's Guidance on the Use of Unfair Means. This work has not been previously presented for an award at this, or any other, university.

Signed:

Merve Gizem ÖZDEN

List of Symbols and Acronyms

B_s – Saturation flux density

H_c – Coercivity

$wt.\%$ - Weight percentage

M_s – Saturation magnetization

E – Volumetric energy input/energy density

P – Laser power

v – Laser scan speed

h – Hatch spacing

t - Layer thickness

m – Magnetic moment

I – Current

A – Area or Exchange stiffness

B – Magnetic induction / Magnetic flux density

H – Magnetic field

ϕ - Magnetic flux within the medium

M – Magnetization

V – Volume

μ_0 – Permeability of free space

X – Susceptibility

μ - Permeability

M_r – Remanence magnetization

T_c – Curie temperature

H_d – Demagnetizing field

E_{ms} – Magnetostatic energy

N_d – Magnetization factor

E_{mc} – Magneto-crystalline energy

K_{mc} , K_1 and K_2 - Cubic anisotropy constants

α_1, α_2 and α_3 - Direction cosines in three-dimensional space of the magnetization vector

K_{u0}, K_{u1} and K_{u2} - Uniaxial anisotropy constants

E_{ex} - Exchange energy

S_i and S_j - Spins of two adjacent electrons

J_{ex} - Exchange constant

φ_{ij} - Angle between \vec{S}_i and \vec{S}_j

E_z - Zeeman energy

L_{ex} - Exchange length

K_{loc} - Local magnetic anisotropy

l - Length scale of random anisotropy change

K_{am} - Anisotropy constant of inter-granular amorphous matrix

$\langle K \rangle$ - Exchange-averaged anisotropy

K_i - Magneto-crystalline anisotropy constant

D - Grain size

λ_s - Saturation magnetostriction

at. % - Atomic percentage

J_s - Saturation polarisation

ΔH_{cry} - Crystallisation enthalpy

μ_e - Effective permeability

μ_{max} - Maximum permeability

T_g - Glass transition temperature

HBNAs - High B_s nano-crystalline alloys

TTT - Time-temperature-transformation

LAM - Laser additive manufacturing

BMG - Bulk metallic glass

DED - Direct energy deposition

LPBF – Laser powder bed fusion

3D – Three-dimensional

SI - Système international (The International System of Units)

cgs - Centimetre gram second (Common Grading Scale)

ALM – Additive layer manufacturing

SLM – Selective laser melting

LENS – Laser-engineered net shaping

FMM – Functional magnetic material

GFA – Glass forming ability

PM – Powder metallurgy

AM – Additive manufacturing

DC – Direct current

SLS – Selective laser sintering

EBM – Electron beam melting

EBSD – Electron backscatter diffraction

APFA – Amorphous phase forming ability

TRS – Transverse rupture strength

XRD – X-Ray powder diffraction

LSF – Laser solid forming

DLF – Directed light fabrication

DMD – Direct metal deposition

EBAM – Electron-beam additive manufacturing

WAAW – Wire and arc additive manufacturing

DSC – Differential scanning calorimetry

LED – Laser energy density

MP – Melt pool

HAZ – Heat affected zone

HR-SEM – High-resolution field emission scanning electron microscope

TEM – Transmission electron microscope

FIB – Focused ion beam

EDS - Energy Dispersive X-ray spectroscopy

MANCs – Metal amorphous nanocomposites

SQUID - Superconducting quantum interference device

Table of Contents

Abstract.....	ii
Acknowledgements.....	iii
Declaration.....	iv
List of Symbols and Acronyms.....	v
Chapter 1 – Introduction.....	1
1.1 Thesis Outline.....	5
References.....	7
Chapter 2 – Theoretical Background.....	12
2.1 Fundamentals of Magnetism.....	12
2.2 Magnetization and Magnetic Materials.....	14
2.2.1 Magnetic Induction and Magnetization.....	14
2.2.2 Flux Density.....	15
2.2.3 Susceptibility and Permeability.....	16
2.2.4 The Ferromagnetic Hysteresis Loops.....	18
2.2.5 Curie Temperature.....	20
2.2.6 Various Forms of Energy within Magnetic Materials.....	21
2.2.7 Random Anisotropy Model.....	26
2.2.8 Effect of oxygen content on the soft-magnetic performance of amorphous-nanocrystalline materials.....	29
2.3 Additive Manufacturing of Soft Magnetic Materials.....	31
2.3.1 Fe-Si alloys.....	32
2.3.2 Fe-Ni alloys.....	34
2.3.3 Fe-Co alloys.....	35
2.3.4 Soft-Magnetic Composites (SMCs).....	36
2.3.5 Soft Ferrites.....	38
2.4 Additive Manufacturing of Amorphous Alloys.....	38
2.5 Future Trends and Challenges.....	42
References.....	45
Chapter 3 – Literature Review Paper.....	67
Abstract.....	67
3.1 Introduction.....	68
3.2 Amorphous Fe-based Magnetic Alloys.....	69
3.3 Additive Manufacturing of Amorphous Fe-based Magnetic Alloys.....	75
3.3.1 Powder-Bed Fusion.....	75
3.3.2 Direct Energy Deposition.....	88
3.4 Conclusions.....	96

References.....	96
Chapter 4 – Research Paper I.....	107
Abstract.....	107
4.1 Introduction.....	108
4.2 Material and Methods.....	111
4.2.1 Powder Characterization.....	111
4.2.2 Laser Powder Bed Fusion (LPBF) process.....	113
4.2.3 Characterization of printed samples.....	113
4.3 Results and Discussion.....	114
4.3.1 Design of Experiment.....	130
4.4 Conclusion.....	132
Acknowledgement.....	132
CRediT author statement.....	133
References.....	133
Chapter 5 – Research Paper II.....	138
Abstract.....	138
5.1 Introduction.....	139
5.2 Experimental Procedure.....	142
5.2.1 Material.....	142
5.2.2 Methods.....	142
5.3 Results and Discussion.....	143
5.4 Conclusion.....	154
Acknowledgement.....	155
References.....	155
Chapter 6 – Research Paper III.....	161
Abstract.....	161
6.1 Introduction.....	162
6.2 Experimental Procedure.....	165
6.2.1 Material.....	165
6.2.2 Methods.....	165
6.3 Results and Discussion.....	167
6.4 Conclusion.....	175
Acknowledgement.....	176
CRediT author statement.....	176
References.....	177
Chapter 7 – Conclusions and Future Work.....	183
7.1 Conclusions.....	183

7.2 Future Work.....	185
References.....	187

1. Introduction

Electrical machines and power electronics are crucial components in various industries and daily activities. However, the widely utilized soft-magnetic material, silicon steel, possess limitations such as inferior magnetic softness and higher core loss. Hence, researchers are working to find alternatives to silicon steel. Fe-based amorphous and nano-crystalline alloys have emerged as promising replacements for silicon steel in power electronics and electrical machines due to their lower coercivity (H_c) and significantly lower core loss [1]. Nonetheless, their saturation flux density (B_s) is still lower than that of silicon steel. Consequently, increasing the B_s of these amorphous/nano-crystalline materials has become a major research focus in recent years [1-3].

Amorphous alloys, also known as metallic glasses, are a type of metal-based material that exhibits short-range ordered structure on an atomic scale [4-8]. Unlike conventional crystalline alloys, amorphous alloys lack grains and grain boundaries in their microstructure, resulting in a more uniform composition. These alloys are manufactured using the rapid solidification technique, which involves heating materials from a solid to a liquid state [9-12], then quenching them to form the amorphous solid. Nanocrystalline soft magnetic alloys can be produced through two primary methods: direct grain refinement and amorphous crystallization. Direct grain refinement involves melting crystals and rapidly solidifying them at such a cooling rate to prevent their growth, resulting in small nanocrystalline particles. On the other hand, the amorphous crystallization method uses external control factors such as heating, light, radiation, current, magnetic fields, etc. to induce the nucleation and growth of small nanocrystalline particles in an amorphous matrix from the parent amorphous alloy precursor. Fe-based nanocrystalline soft magnetic materials are typically fabricated through the amorphous crystallization method, where nano-sized α -Fe grains are formed in the amorphous matrix following the crystallization of an amorphous quenched ribbon [4, 13-15]. Resulting from their low core loss, high electrical resistivity, high mechanical strength, fracture toughness, high saturation magnetization, high permeability, short production process, and environmental friendliness, these materials are well-suited for fabricating switching power supplies, pulse transformer, differential mode inductance and reactor cores, transformers, magnetic amplifiers and peak suppressors [16].

To create a nanoscale nano-crystalline microstructure, several reported alloys have high concentrations of non-magnetic elements [6, 17-19]. This reduces substantially

the magnetization and increases raw material costs [20]. In Fe-based nano-crystalline materials, for the direct grain refinement, mostly Cu, Nb along with the elements like Ag, Ni, Pt, Zr, Mo and Hf are added to facilitate hetero-nucleation, refine the nano-crystallite size, and stabilize the amorphous phase [6, 20, 21]. The presence of Cu in Finemet alloys results in the formation of Cu-rich clusters due to its positive mixing-enthalpy and immiscibility with Fe [21]. These clusters promote the precipitation of α -Fe grains by lowering the activation energy [18, 22]. Meanwhile, the Nb, with its big atom size and slow diffusion rate, enhances the glass forming ability (GFA) of the ribbon precursors and refines the grain structure, preventing the formation of hard magnetic phases [18, 20, 21, 23]. Nevertheless, these heavy metal elements often cause lower B_s in the Finemet and Nanoperm alloys [20, 21]. Although the Nanomet alloys possess higher B_s , their difficult to control nucleation-growth processes have hindered their industrialization [17, 24, 25]. Thus, there is a trade-off between magnetic properties and manufacturability, which continue to be a significant challenge according to the nucleation and grain growth mechanism of the glassy phase [21].

To overcome this challenge, a potential solution is to develop new alloys with a lower content of metalloids and a high concentration of Fe similar to industrial silicon steel (which contains Fe content higher than 95%) [26]. However, this unconventional approach requires addressing several issues, including the precursor production under industrial conditions, the refinement of nano-crystallites and the precipitations of the single α -Fe phase over a broad temperature range [20, 21, 27]. It is crucial to develop high B_s nano-crystalline alloys (HBNAs) that do not include traditional nucleation promoting and diffusion hindering elements, to enable novel compositional design approaches and fabrication mechanisms [28].

The remarkable technological significance of Fe-based amorphous/nanocrystalline alloys in terms of their soft magnetic properties is predominantly hindered by the existing technical challenges associated with the absence of viable industrial methods for producing large-sized and complex-shaped metallic components. At present, these alloys find their primary application in low-power applications where they vie with permalloys in the manufacturing of specialized small devices, primarily for sensing and switching. Additionally, they serve as transformers in certain high-power applications [1].

Devices are constructed using thin ribbons or wires of glassy alloys, typically measuring about 50 μ m in thickness. These are obtained through rapid cooling techniques, such as melt-spinning or immersing a stream of molten alloy into a water bath. To improve their soft magnetic characteristics, these ribbons undergo a post-heat

treatment to partially crystallize them into nanocrystalline mixtures [29]. The microstructure of the partially nanocrystallized matrix is hard to control precisely and largely depends on heterogeneous nucleation processes. A more significant drawback lies in the manufacture of components with these materials, which involves stacking, winding, or cutting exceedingly thin and fragile laminations or wires, making it a challenging and costly process.

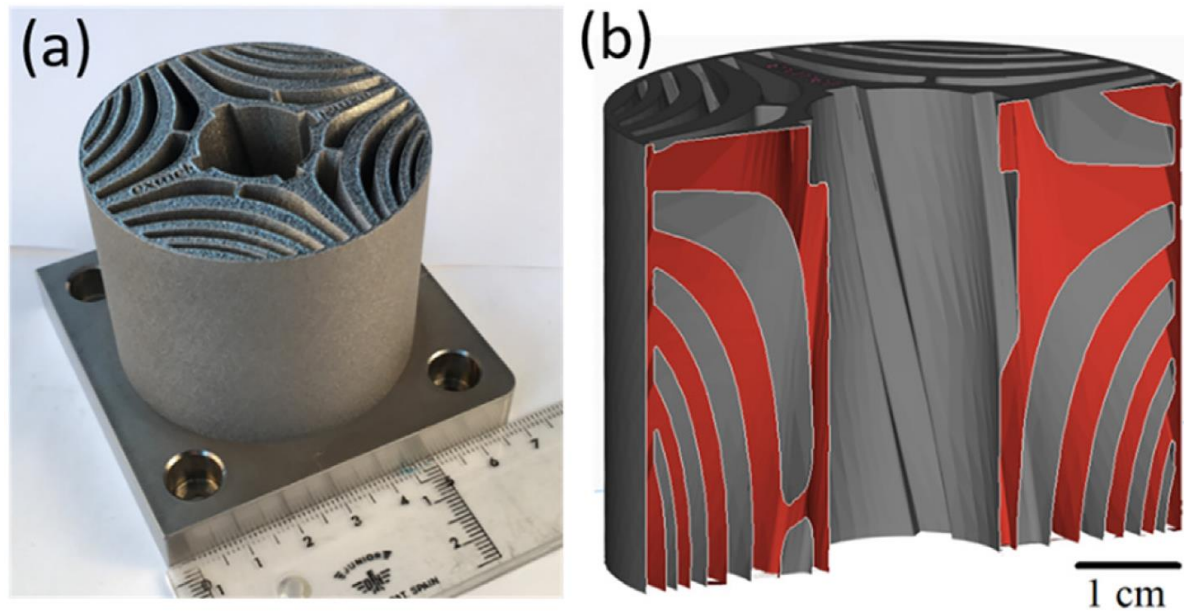


Figure 1.1: (a) The photograph of the LBPB-processed electric motor-rotor, still attached to the building platform and (b) the image showing the intricate internal configuration of the rotor when viewed in a vertical cross-sectional plane, aligned with the building direction [30].

This study represents a significant advancement, as it involved the process optimization of laser additive manufacturing (LAM) to allow the creation of a large soft magnetic material rotor with a complex 3D inner design that cannot be achieved through conventional methods like casting or injection moulding. The innovative internal design approach considered in the work of Thorsson et al. [30] paves the way for a departure from current laminated structures, which are designed to manage and minimize eddy currents, towards more integrated, monolithic structures. The optimization of laser powder bed fusion (LPBF) process was required so that the electric motor rotor with the intricate inner design can be produced having excellent soft-magnetic behaviour. For this purpose, a commercial amorphous powder composed of Fe, Si, Cr, B and C elements (similar to HBNA (FeSiBPC)), known for its accessibility and sustainability, was utilized as it excludes elements like Co and rare earth elements such as Nd. The conventional techniques to fabricate them have size limitations, thermal stability issues and, needs post-processing (annealing to control microstructure), increasing production time, energy, and cost. While powder

consolidation and thermal pressure-sintering can overcome the dimensional limitations, LAM remains an appealing option due to the following reasons:

1. LAM allows for the fabrication of complex shapes, including lattice structures, that would otherwise be much more difficult or impossible to make using conventional techniques.
2. The use of complicated moulds and tools, which is required by traditional techniques, can be avoided with LAM. This is particularly significant for low volume manufactured parts to decrease initial costs.
3. LAM enables the creation of compositionally and functionally graded materials. Varying the LAM process parameters can result in bulk metallic glass (BMG) nanocomposites with a gradient in microstructure and thus properties, even for the same BMG composition. Conventional processes do not offer the capability to fabricate compositionally graded materials in the same and easier way as LAM [10].

The most commonly utilized LAM techniques are typically classified into two categories: direct energy deposition (DED) and laser powder bed fusion (LPBF). The DED technique involves the feeding of powders (or wire) into a laser or electron beam that melts them, enabling the printing of desired parts in layer-by-layer fashion. On the other hand, the LPBF technique spreads a thin layer of powder particles (20-100 μ m) onto a platform, and the laser or electron beam melts the powder layer. The process is repeated with a new powder layer until the desired 3D part is built. LPBF technique provides superior dimensional accuracy, is more cost-effective and is particularly suitable for manufacturing intricate components. Additional information regarding the engineering aspects of LAM processes can be obtained from these highly informative review articles [31-35].

The utilization of LPBF technique for BMGs has been more prevalent [10, 12]. Yet, a small proportion of recent research has been dedicated to optimizing the LPBF process for Fe-based BMGs to reduce the defects such as cracking and porosity [36], developing improved scanning strategies [37, 38] and investigating the level of amorphization [39], mechanical [40, 41] and magnetic properties of Fe-based BMGs [30, 42, 43]. Nevertheless, those studies did not address nano-crystallinity in Fe-based amorphous alloys processed with LPBF and its effect on their magnetic properties. This work presents an extensive experimental study on the LPBF process optimization in the aim to obtain Fe-based amorphous/nanocrystalline 3D bulk parts having high bulk density and soft-magnetic behaviour, i.e., high saturation magnetization (M_s) and

low coercivity (H_c). This is so that low volume manufactured components with intricate design can be produced with LPBF technique in order to increase the efficiency of the parts by adding the complexity to their design, as well as reducing production time, cost, and energy. Hence, the main aim of this PhD project is to fabricate parts with high bulk density ($> 99\%$), high M_s ($> 200 \text{ Am}^2/\text{kg}$) and low H_c ($< 100 \text{ A/m}$) by optimizing the LPBF process, which will be accomplished by the following objectives;

- i. To identify the major laser process parameters affecting the final properties.
- ii. To investigate the effect of different combination of the process parameters on the final properties.
- iii. To examine the effect of the individual process parameters on final properties.
- iv. To comprehend the microstructural change with different process parameters.
- v. To understand how microstructural change affect the magnetic properties.
- vi. To define the controlling laser process parameters for each final property.
- vii. To develop new scanning strategies to obtain superior material properties.

1.1. Thesis Outline

The following is the structure of this thesis, which consists of seven chapters:

Chapter 2 provides an introduction to the basics of magnetism and magnetic materials, as well as an overview of the various magnetic energies (magnetostatic, magnetocrystalline anisotropy, exchange, and Zeeman energies) that explains the occurrence of the magnetic domain structures. Additionally, the random anisotropy model is discussed, along with its dependence on grain (crystallite) size to comprehend the magnetic behaviour of nanocrystalline materials.

Chapter 3 presents an extensive review of the previous research on the laser additive manufacturing of Fe-based amorphous/nanocrystalline soft-magnetic alloys. It includes studies conducted on the properties of Fe-based amorphous/nanocrystalline materials produced with laser powder bed fusion and directed energy deposition.

This chapter was published as a review paper in the "*Magnetochemistry*" journal. Its detail is as follows:

Laser Additive Manufacturing of Fe-based magnetic amorphous alloys

Merve G. Ozden, Nicola A. Morley *Magnetochemistry* 2021, 7(2), 20.

<https://doi.org/10.3390/magnetochemistry7020020>

Chapter 4 covers the optimization of laser process parameters in the laser powder bed fusion (LPBF) technique for Fe-based amorphous/nanocrystalline soft-magnetic alloys using the volumetric energy input (E), which includes the major build parameters; laser power (P), scan speed (v), layer thickness (t) and hatch spacing (h). It investigates how the major process parameters influence the physical and magnetic properties of LPBF-processed Fe-based amorphous/nanocrystalline composites.

This chapter of the thesis was published in the “*Journal of Alloys and Compounds*” as a research paper. The details are as follows;

Optimizing Laser Additive Manufacturing Process for Fe-based Nanocrystalline Soft-Magnetic Materials

Merve G. Ozden, Nicola A. Morley *Journal of Alloys and Compounds* 2023, 960, 170644.

<https://doi.org/10.1016/j.jallcom.2023.170644>

Chapter 5 addresses the issue of controlling the microstructure during the LPBF process to comprehend how microstructural development influences magnetic properties of Fe-based alloys as well as how bulk density changes with different process parameters. To do this, all major process parameters were considered: laser power (P), laser scan speed (v), hatch spacing (h) and layer thickness (t). Researchers have generally investigated the effects of laser power and laser scan speed on the properties of Fe-based amorphous/nanocrystalline soft-magnetic composite materials. This work provides a comprehensive experimental study to optimize the LPBF process for the differing process parameters (P , v , h and t).

This chapter of the thesis was published in the “*Advanced Engineering Materials*” as a research paper. The details are as follows;

Soft-Magnetic Behaviour of Fe-Based Nanocrystalline Alloys Produced Using Laser Powder Bed Fusion

Merve G. Ozden, Felicity SHB Freeman, Nicola A. Morley *Advanced Engineering Materials* 2023, 25(19), 2300597.

<https://doi.org/10.1002/adem.202300597>

Chapter 6 introduces a novel scanning technique for the LPBF of Fe-based nanocrystalline alloys, which have low glass forming ability to improve soft-magnetic behaviour as well as bulk density. Additionally, to comprehend microstructural change, amorphous phase content and particle size distribution of the α -Fe(Si) phase (main phase in the microstructure) were measured.

This chapter also was published in the “*Advanced Engineering Materials*” as a research paper. The details are as follows;

Enhancing soft-magnetic properties of Fe-based nanocrystalline materials with a novel double-scanning technique

Merve G. Ozden, Nicola A. Morley *Advanced Engineering Materials* 2023, 2300700.

<https://doi.org/10.1002/adem.202300700>

Chapter 7 provides a summary of the findings and draws conclusions from the research. It also discusses potential future research directions.

The review paper (Chapter 3) contained the working principle and details of laser powder bed fusion technique (LPBF). Similarly, the material characterization techniques utilized in this thesis were explained in the experimental procedure part of each research paper (Chapter 4, 5 and 6). For the methodology of the thesis, it is recommended to refer to those chapters.

References

- [1] J. Silveyra, E. Ferrara, D. Huber and T. Monson, “Soft magnetic materials for a sustainable and electrified world,” *Science*, vol. 362, no. 6413, p. 418, 2018.
- [2] H. Lasgari, D. Chu, S. Xie, H. Sun, M. Ferry and S. Li, “Composition dependence of the microstructure and soft magnetic properties of Fe-based amorphous/nanocrystalline alloys: a review study,” *J. Non-Cryst. Solids*, vol. 391, pp. 61-82, 2014.
- [3] L. Shi and K. Yao, “Composition design for Fe-based soft magnetic amorphous and nanocrystalline alloys with high Fe content,” *Materials and Design*, vol. 189, p. 108511, 2020.
- [4] D. Azuma, N. Ito and M. Ohta, “Recent progress in Fe-based amorphous and nanocrystalline soft magnetic materials,” *Journal of Magnetism and Magnetic Materials*, vol. 501, p. 166373, 2020.
- [5] X. Tong, Y. Zhang, Y. Wang, X. Liang, K. Zhang, F. Zhang, Y. Cai, H. Ke, G. Wang, J. Shen, A. Makino and W. Wang, “Structural origin of magnetic softening in a Fe-based amorphous alloy upon annealing,” *Journal of Materials Science and Technology*, vol. 96, pp. 233-340, 2022.

- [6] G. Herzer, "Modern soft magnets: Amorphous and nanocrystalline materials," *Acta Materialia*, vol. 61, pp. 718-734, 2013.
- [7] N. Kone and T. Hua, "Preparation and Study of the Crystallization Behavior of the Fe₈₇Zr₇B_{5-x} Nanocrystalline Soft-Magnetic Alloys," *Journal of Energy and Power Engineering*, vol. 14, pp. 100-110, 2020.
- [8] D. Erutin, A. Popovich and V. Sufiiarov, "Selective Laser Melting of (Fe-Si-B)/Cu Composite: Structure and Magnetic Properties Study," *Metals*, vol. 13, p. 428, 2023.
- [9] D. Erutin, E. Borisov, A. Popovich and V. Sufiiarov, "Magnetic anisotropy of a selective laser melted Fe-Si-B alloy," *Journal of Physics: Conference Series*, vol. 2361, p. 012011, 2022.
- [10] S. Madge and A. Greer, "Laser additive manufacturing of metallic glasses: issues in vitrification and mechanical properties," *Oxford Open Material Science*, vol. 1, no. 1, p. itab015, 2021.
- [11] Z. Huo, G. Zhang, J. Han, J. Wang, S. Ma and H. Wang, "A review of the preparation, machining performance and application of Fe-based amorphous alloys," *Processes*, vol. 10, p. 1203, 2022.
- [12] P. Zhang, J. Tan, Y. Tian, H. Yan and Z. Yu, "Research progress on selective laser melting (SLM) of bulk metallic glasses (BMGs): a review," *The International Journal of Advanced Manufacturing Technology*, vol. 118, pp. 2017-2057, 2022.
- [13] T. Liu, F. Li, A. Wang, L. Xie, Q. He, J. Luan, A. He, X. Wang, C. Liu and Y. Yang, "High performance Fe-based nanocrystalline alloys with excellent thermal stability," *Journal of Alloys and Compounds*, vol. 776, pp. 606-613, 2019.
- [14] T. Liu, A. He, A. Wang, X. Wang, H. Zhang and H. Ni, "Stabilizing Fe-based nanocrystalline alloys via a high-entropy strategy," *Journal of Alloys and Compounds*, vol. 896, p. 163138, 2022.
- [15] T. Liu, A. He, F. Kong, A. Wang, Y. Dong, H. Zhang, X. Wang, H. Ni and Y. Yang, "Heterostructured crystallization mechanism and its effect on enlarging the processing window of Fe-based nanocrystalline alloys," *Journal of Material Science and Technology*, vol. 68, pp. 53-60, 2021.

- [16] J. Zhou, J. You and K. Qiu, "Advances in Fe-based amorphous/nanocrystalline alloys," *Journal of Applied Physics*, vol. 132, p. 040702, 2022.
- [17] Y. Chen, T. Ohkubo, M. Ohta, Y. Yoshizawa and K. Hono, "Three-dimensional atom probe study of Fe-B-based nanocrystalline soft magnetic materials," *Acta Materialia*, vol. 57, pp. 4463-4472, 2009.
- [18] K. Pradeep, G. Herzer, P. Choi and D. Raabe, "Atom probe tomography study of ultrahigh nanocrystallization rates in FeSiNbBCu soft magnetic amorphous alloys on rapid annealing," *Acta Materialia*, vol. 68, pp. 295-309, 2014.
- [19] L. Sun, G. Wu, Q. Wang and J. Lu, "Nanostructural metallic materials: Structures and mechanical properties," *Materials Today*, vol. 38, pp. 114-135, 2020.
- [20] M. McHenry, M. Willard and D. Laughlin, "Amorphous and nanocrystalline materials for applications as soft magnets," *Progress in Materials Science*, vol. 44, pp. 291-433, 1999.
- [21] A. Inoue, "Stabilization of metallic supercooled liquid and bulk amorphous alloys," *Acta Materialia*, vol. 48, pp. 279-306, 2000.
- [22] D. Allen, J. Foley and J. Perepezko, "Nanocrystal development during primary crystallization of amorphous alloys," *Acta Metallurgica*, vol. 46, no. 2, pp. 431-440, 1998.
- [23] Y. Xie, S. Sohn, M. Wang, H. Xin, Y. Jung, M. Shattuck, C. O'Hern, J. Schroers and J. Cha, "Supercluster-coupled crystal growth in metallic glass forming liquids," *Nature Communications*, vol. 10, no. 1, p. 915, 2019.
- [24] E. Lopatina, I. Soldatov, V. Budinsky, M. Marsilius, L. Schultz, G. Herzer and R. Schafer, "Surface crystallization and magnetic properties of Fe_{84.3}Cu_{0.7}Si₄B₈P₃ soft magnetic ribbons," *Acta Materialia*, vol. 96, pp. 10-17, 2015.
- [25] O. Motoki, Y. Yoshihito, T. Masaaki and Y. Jiro, "Effect of surface microstructure on magnetization process in Fe 80.5Cu1.5Si4B14 nanocrystalline alloys," *IEEE Transactions on Magnetics*, vol. 46, no. 2, p. 5393180, 2010.
- [26] G. Zu, X. Zhang, J. Zhao, Y. Cui, Y. Wang and Z. Jiang, "Analysis of the microstructure, texture and magnetic properties of strip casting 4.5 wt.% Si non-oriented electrical steel," *Materials and Design*, vol. 85, pp. 455-460, 2015.

- [27] G. Wu, K. Chan, L. Zhu, L. Sun and J. Lu, "Dual-phase nanostructuring as a route to high-strength magnesium alloys," *Nature*, vol. 545, pp. 80-83, 2017.
- [28] H. Li, A. Wang, T. Liu, P. Chen, A. He, Q. Li, J. Luan and C. Liu, "Design of Fe-based nanocrystalline alloys with superior magnetization and manufacturability," *Materials Today*, vol. 42, pp. 49-56, 2021.
- [29] M. Willard, M. Daniil and K. Knipping, "Nanocrystalline soft magnetic materials at high temperatures: A perspective," *Scr. Mater.*, vol. 67, no. 6, pp. 554-559, 2012.
- [30] L. Thorsson, M. Unosson, M. Perez-Prado, X. Jin, P. Tiberto, G. Barrera, B. Adam, N. Neuber, A. Ghavimi, M. Frey, R. Busch and I. Gallino, "Selective laser melting of a Fe-Si-Cr-B-C-based complex-shaped amorphous soft-magnetic electric motor rotor with recorded dimensions," *Materials and Design*, vol. 215, p. 110483, 2022.
- [31] S. Singh, S. Ramakrishna and R. Singh, "Material issues in additive manufacturing: A review," *Journal of Manufacturing Processes*, vol. 25, pp. 185-200, 2017.
- [32] M. Yakout, M. Elbestawi and S. Veldhuis, "A review of metal additive manufacturing technologies," *Solid State Phenomena*, vol. 278, pp. 1-14, 2018.
- [33] T. Ngo, A. Kashani, G. Imbalzano, K. Nguyen and D. Hui, "Additive manufacturing (3D printing): A review of materials, methods, applications and challenges," *Composites Part B*, vol. 143, pp. 172-196, 2018.
- [34] E. Perigo, J. Jacimovic, F. Ferre and L. Scherf, "Additive manufacturing of magnetic materials," *Additive Manufacturing*, vol. 30, p. 100870, 2019.
- [35] T. Debroy, H. Wei, J. Zuback and T. Mukherjee, "Additive manufacturing of metallic components – Process, structure and properties," *Progress in Materials Science*, vol. 92, no. 5, pp. 112-224, 2018.
- [36] Z. Mahbooba, L. Thorsson, M. Unosson, P. Skoglund, H. West, T. Horn, C. Rock, E. Vogli and O. Harrysson, "Additive manufacturing of iron-based bulk metallic glass larger than the critical casting thickness," *Applied Materials Today*, vol. 11, pp. 264-269, 2018.
- [37] L. Zrodowski, B. Wysocki, R. Wroblewski, A. Krawczynska, B. Adamczyk-Cieslak, J. Zdunek, P. Blyskun, J. Ferenc, M. Leonowicz and W. Swieszkowski,

“New approach to amorphization of alloys with glass forming ability via selective laser melting,” *Journal of Alloys and Compounds*, vol. 771, pp. 769-776, 2019.

- [38] Y. Nam, B. Koo, M. Chang, S. Yang, J. Yu, Y. Park and J. Jeong, “Selective laser melting vitrification of amorphous soft magnetic alloys with help of double-scanning- induced compositional homogeneity,” *Materials Letters*, vol. 261, p. 127068, 2020.
- [39] D. Ouyang, W. Xing, N. Li, Y. Li and L. Liu, “Structural evolutions in 3D-printed Fe-based metallic glass fabricated by selective laser melting,” *Additive Manufacturing*, vol. 23, pp. 246-252, 2018.
- [40] Y. Zhou, Y. Wu, K. Li, C. Tan, Z. Qiu and D. Zeng, “Selective laser melting of crack-free Fe-based bulk metallic glass via chessboard scanning strategy,” *Materials Letters*, vol. 272, p. 127824, 2020.
- [41] X. Nong, X. Zhou and Y. Ren, “Fabrication and characterization of Fe-based metallic glasses by selective laser melting,” *Optics and Laser Technology*, vol. 109, pp. 20-26, 2019.
- [42] S. Alleg, R. Drablia and N. Fenineche, “Effect of the laser scan rate on the microstructure, magnetic properties and the microhardness of selective laser melted FeSiB,” *Journal of Superconductivity and Novel Magnetism*, vol. 31, pp. 3565-3577, 2018.
- [43] H. Jung, S. Choi, K. Prashanth, M. Stoica, S. Scudino, S. Yi, U. Kuhn, D. Kim, K. Kim and J. Eckert, “Fabrication of Fe-based bulk metallic glass by selective laser melting: A parameter study,” *Materials and Design*, vol. 86, pp. 703-708, 2015.

2. Theoretical Background

2.1 Fundamentals of Magnetism

Magnets have been known to humans for centuries, initially as permanent magnets. Later on, they were used for navigation purposes as compass needles since magnets have a natural tendency to align themselves in the north-south direction, with the earth magnetic field.

Classical electrodynamics attributes the origin of magnetism to electric current. The two types of electric charges, called "positive" and "negative," that are present in nature and exhibit attraction and repulsion. Similarly, magnetic poles with the same polarity repel while those with opposite polarity attract each other. One of the fundamental distinctions between electric charges and magnetic poles is that electric charges can be isolated as positive or negative charges, while the same cannot be done with magnetic poles. In a single magnet, one end is its north pole, and the other end is its south pole. If a magnet is broken, it generates two smaller magnets, each having both a north pole and a south pole. Therefore, the term magnetic "dipole" is used to describe a magnet [1].

When an electric charge is in motion through a wire, it creates an electric current. It has been observed that these currents generate magnetic forces. A basic magnet can be envisioned as a flat coil carrying a current, which is referred to as a magnetic dipole. The north and south poles of the magnet are positioned in the opposite planes of the coil and are determined by the direction of the current. The direction of the current can be determined using the right-hand rule, where the fingers of the right-hand point in the direction of the current, and the thumb shows the north pole (Figure 2.1(a)). The magnetic field created by this dipole emerges from the axis of the coil from the north pole. This idea of magnetic fields can be generalized, and it is not always necessary to refer to a single dipole. A magnetic field can also be created by a single straight current-carrying wire. In such a case, the wire will produce a magnetic field around itself (as shown in Fig. 2.1(b)) [2, 3].

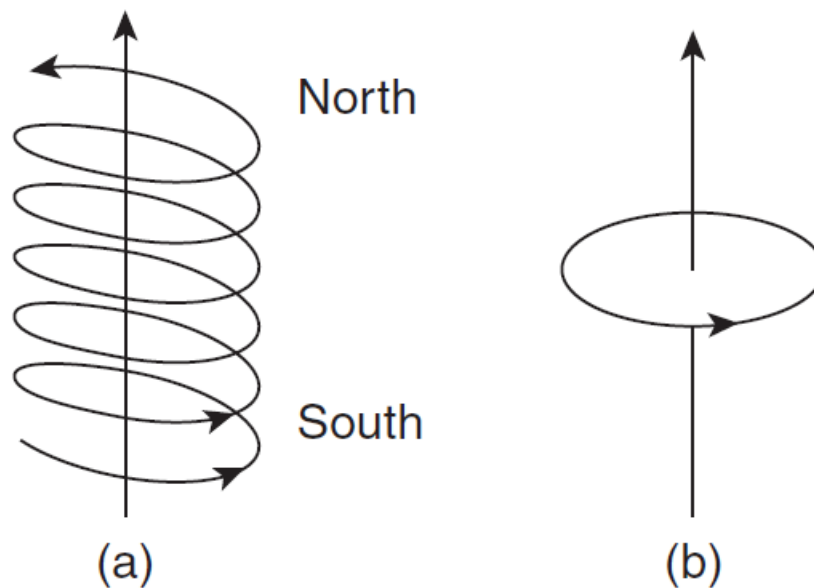


Figure 2.1: The figures depicted in (a) and (b) demonstrate the flow of electric current in a solenoid and a wire carrying current, respectively, and the corresponding magnetic fields generated [4].

At the atomic level, the majority of magnetic dipoles are created by electrons. Quantum mechanically, electrons possess two types of angular momenta. The first is orbital angular momentum, which can be envisioned classically as their movement around the nucleus, similar to how the Earth orbits around the sun. This produces a magnetic field much like a coil carrying current. The second source of atomic magnetism is the intrinsic property of electrons known as "spin." In a simplified classical sense, spin can be conceptualized as a particle, such as an electron, which rotates around an axis that passes through its centre of mass, much like the rotation of the Earth around its own axis. Additionally, this spin generates its own magnetic field, which is related to an angular momentum (Figure 2.2) [5].

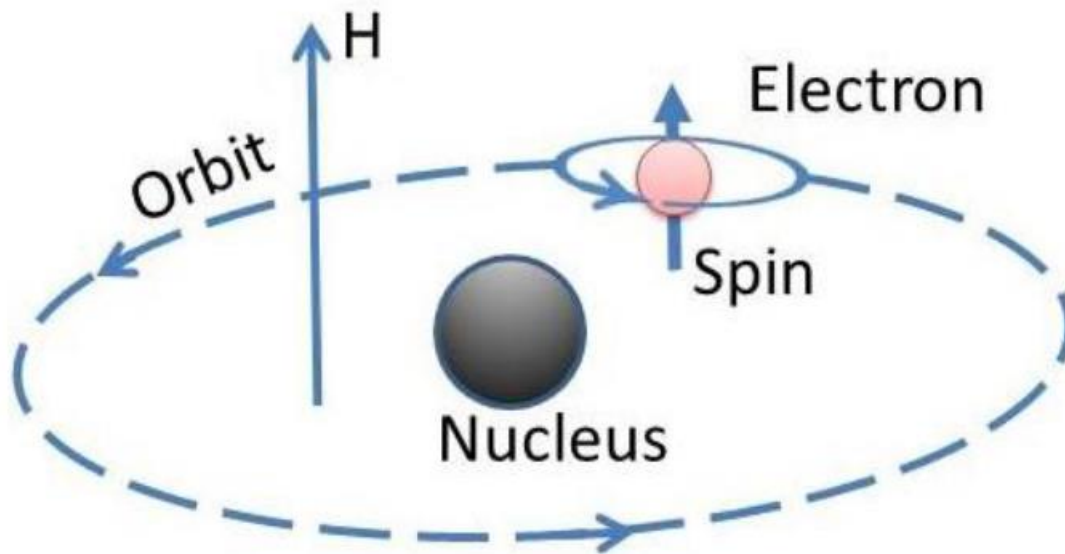


Figure 2.2: The Diagram illustrating the movements of an electron for both spin and orbital moments (H is magnetic field) [6].

When considering an atom, its magnetic property can be attributed to the net angular momentum of all the electrons, which includes both their spin and orbital contributions. If the net angular momentum of all the electrons is not zero, it would result in the atom behaving like a tiny magnet with a magnetic moment, which is a quantity that depends on the value of the net angular momentum. This magnetic moment determines the force between the gradient of the magnetic field and the tiny magnet. Alternatively, the magnetic moment (m) of a current loop carrying a current I and having an area A can be defined as:

$$m = IA \quad (2.1)$$

The SI (Système international) unit of m is the Am^2 (electromagnetic units) whereas in cgs (centimetre gram second) unit, m is in emu [7, 8].

2.2 Magnetization and Magnetic Materials

2.2.1 Magnetic Induction and magnetization

The effect of a magnetic field, H , on a substance is referred to as its magnetic induction, B . The relationship between B and H depends on the material's characteristics. B may be a linear function of H in some materials, including free space. However, in most cases, it is a lot more complex, and the relationship may be multi-valued. The equation describing the relationship between B and H , in cgs units, is as follows:

$$B = H + 4\pi M \quad (2.2)$$

Chapter 2 – Theoretical Background

where M is the magnetization, described as the magnetic moment per unit volume (**cgs unit (M)**: emu/cm³, **cgs unit (H)**: Oersted and **cgs unit (B)**: Gauss),

$$M = \frac{m}{V} \quad (2.3)$$

Magnetization is a material's property influenced by the magnetic moments of the constituent atoms, ions, or molecules, as well as by the way these dipole moments interact with one another.

The relationship among B , H and M in SI units can be expressed as:

$$B = \mu_0(H + M) \quad (2.4)$$

Where μ_0 is the permeability of free space and weber/Am or henry/m in SI units. M and H have the same unit as A/m. Therefore, B is expressed as tesla (T) or weber/m² in SI units [9].

2.2.2 Flux Density

The magnetic induction (B), also known as the magnetic flux density, is related to the magnetic flux (ϕ) within the medium.

$$B = \frac{\phi}{A} = M\mu_0 \text{ (inside the material, where } H = 0) \quad (2.5)$$

$$H = \frac{\phi}{A} \text{ (in free space)} \quad (2.6)$$

Generally, the magnetic flux density within a material differs from that of outside. In fact, magnetic materials can be categorized based on the disparity between their internal and external flux. If the flux density inside the material is lower than the outside, the material is classified as diamagnetic such as bismuth and helium. These materials have a tendency to repel or resist the magnetic field from entering their interior. It is well-known that the atoms or ions that constitute diamagnetic materials possess zero magnetic dipole moment. When the flux density within the material is marginally greater than the external flux density, the material is categorized as either paramagnetic like Na and Al or antiferromagnetic like MnO and FeO. In several paramagnetic and antiferromagnetic materials, the individual ions or atoms possess a magnetic dipole moment. For paramagnets, the magnetic dipole moments of constituent atoms or ions are oriented randomly (Figure 2.3(a)), while in antiferromagnets, they are aligned antiparallel to each other (Figure 2.3 (b)). As a result, the net magnetization of both types of materials is zero. Lastly, if the magnetic flux density inside a material is significantly greater than that outside, the material is classified as either ferromagnetic or ferrimagnetic. Ferromagnetic materials have their constituent atoms' magnetic dipole moments aligned in the same direction (Figure

2.3(c)), leading to a significantly large net magnetic moment. Ferrimagnets are akin to antiferromagnets in that their dipoles align in opposite directions, but the magnitudes of some dipole moments are greater than others (Figure 2.3(d)), leading to a resultant net magnetic moment. Ferromagnets and ferrimagnets have a tendency to confine magnetic flux to their interiors [7, 8, 10, 11].

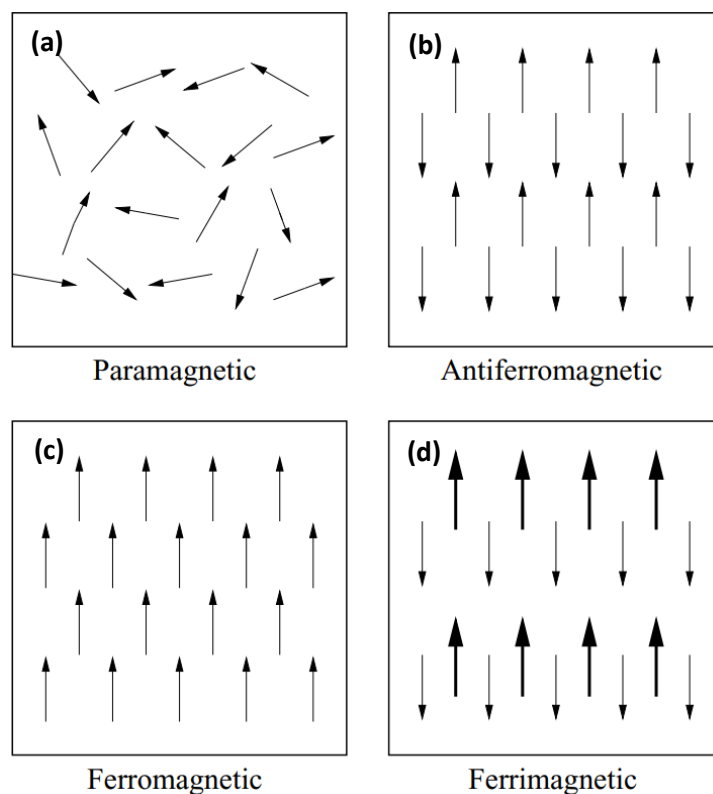


Figure 2.3: The magnetic dipole ordering in the different type of magnetic materials: (a) paramagnetic, (b) antiferromagnetic, (c) ferromagnetic and (d) ferrimagnetic materials [7].

2.2.3 Susceptibility and permeability

The characteristics of a material are determined not just by its magnetic induction or magnetization, but also by the manner in which these values change in response to a magnetic field.

The measure of how easily a material reacts to an externally applied magnetic field is represented by the susceptibility (X), defined as the ratio of M to H ;

$$X = \frac{M}{H} \left(\frac{emu}{cm^3 Oe} \right) \quad (2.7)$$

The permeability (μ), on the other hand, refers to the material's ability to allow magnetic fields to pass through it, defined as the ratio of B to H ;

$$\mu = \frac{B}{H} \left(\frac{Gauss}{Oe} \right) \quad (2.8)$$

Chapter 2 – Theoretical Background

A material with a high permeability tends to concentrate a significant amount of flux density within its interior. Using equation 2.2 provides the relationship between X and μ .

$$\mu = 1 + 4\pi X \quad (2.9)$$

It should be noted that in SI units, X is a dimensionless quantity, whereas μ is measured in the unit of henry/metre. The relationship between them in SI units can be expressed as:

$$\frac{\mu}{\mu_0} = 1 + X \quad (2.10)$$

The graphs depicting the relationship between M or B and H are commonly referred to as magnetization curves, which are unique to each material [12].

Figure 2.4(a) displays schematic plots of the magnetization (M) of diamagnetic, paramagnetic, and antiferromagnetic materials as a function of the applied field (H). Linear M - H curves characterize those materials. A significant amount of applied field is necessary to produce slight changes in magnetization, and no residual magnetization is present when the applied field is removed. Diamagnetic materials have negative slopes on their M - H curves, leading to small negative susceptibility and slightly less than 1 permeability values. On the other hand, paramagnetic and antiferromagnetic materials have positive slopes and small positive susceptibility and slightly greater than 1 permeability values [4, 5, 8].

The magnetization curves for ferrimagnets and ferromagnets are presented in Figure 2.4(b). It's important to note that the scales on the axes are entirely different from those in Figure 2.4(a). In this case, a much smaller external field produces a significantly larger magnetization. Additionally, the magnetization reaches a saturation point, meaning that a further increase in field results in a very slight increase in magnetization. The susceptibility and permeability are large and positive, and they both depend on the applied field. Furthermore, even after the field is reduced to zero, the magnetization does not drop to zero. The occurrence known as hysteresis is of great significance in technological fields. For instance, the ability of ferromagnetic and ferrimagnetic materials to preserve their magnetization in the absence of an external field makes them ideal for permanent magnet production [8].

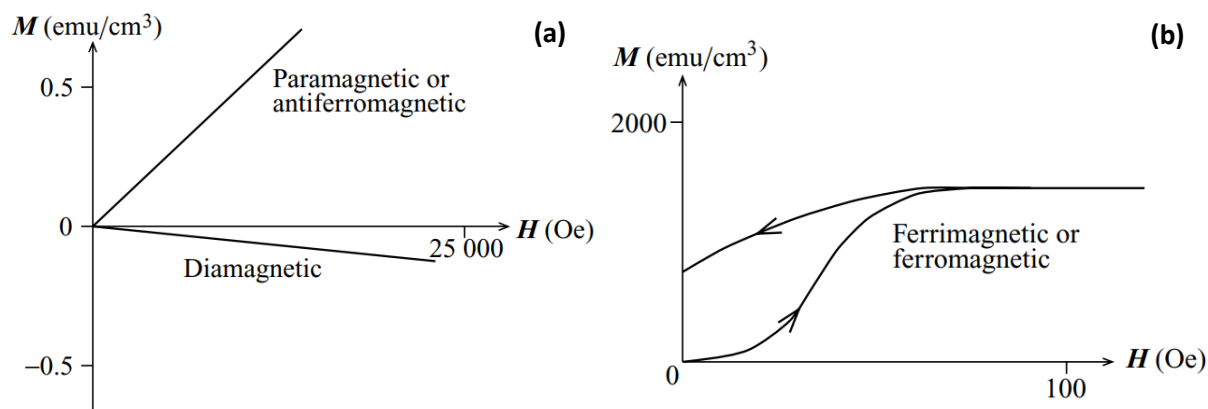


Figure 2.4: The magnetization curves for (a) diamagnets, paramagnets and antiferromagnets, and (b) ferrimagnets and ferromagnets [7, 8].

2.2.4 The ferromagnetic hysteresis loops

A crucial practical aspect of any ferromagnetic material is its non-linear and irreversible response to a magnetic field (H), as seen in the change in magnetization (M). This behaviour can be represented by the hysteresis loop. The material reacts to the applied magnetic field H , not to the magnetic flux density (internal field) B . The originators of the B -field include: (1) electric currents that flow through conductors; (2) charges in motion, which comprise an electric current; and (3) magnetic moments, which are comparable to current loops. On the other hand, H is generated by conduction currents and external magnets. For this reason, in the magnetization process, H is typically considered as the independent variable. The magnetization, M , is then plotted against H , and the magnetic flux density B is calculated using Equation (2.4). To trace a hysteresis loop, the magnitude of the applied field must be comparable to that of the magnetization so that the applied field reveals the pre-existing spontaneous ferromagnetic order at the level of microscopic domains. The schematic of the hysteresis loop shown in Figure 2.5 illustrates those domain structures. When an external magnetic field H is applied to a ferromagnetic material, it affects and eliminates the microstructure of ferromagnetic domains that were magnetized in different directions, ultimately revealing the saturation (spontaneous) magnetization (M_s). After the external field is removed, a remanence magnetization (M_r), remains within the material. The amount of reverse field required to reduce the magnetization to zero is called the coercivity or coercive field (H_c) [13, 14].

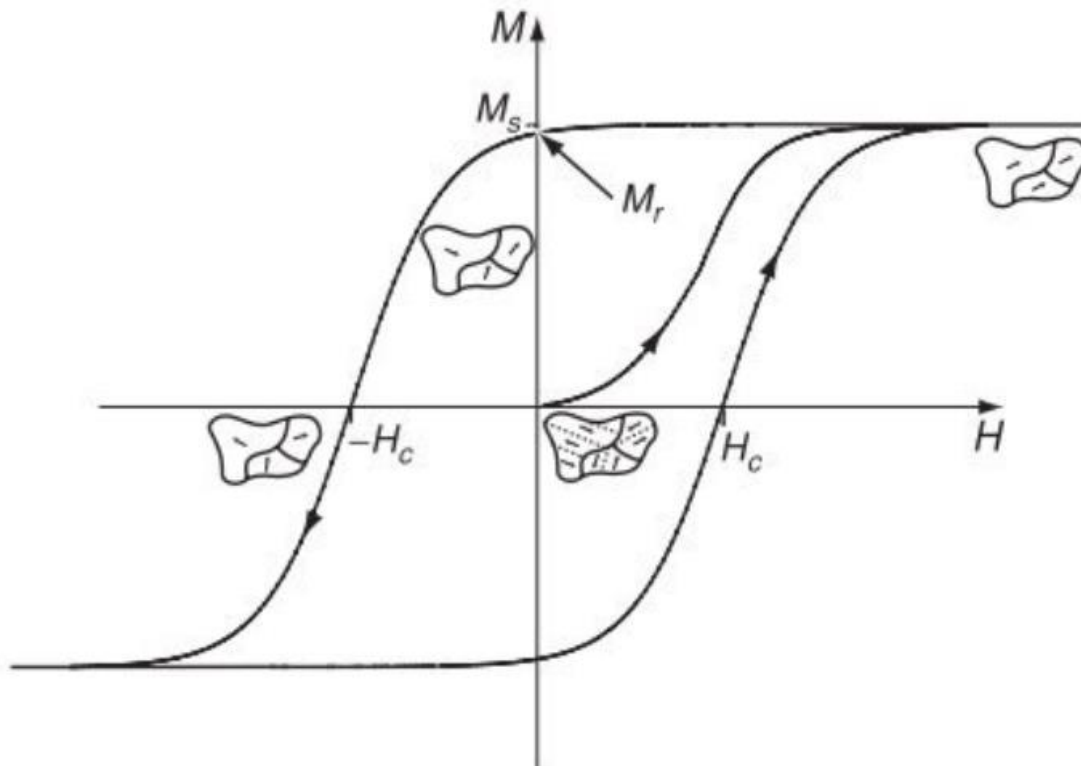


Figure 2.5: The schematic illustration of a typical ferromagnetic hysteresis loop [13].

Hard magnetic materials exhibit broad, square-shaped M - H loops and are ideal for producing permanent magnets as they maintain their magnetized state even after the applied field is removed, once magnetized with an applied external field (H). Soft magnetic materials are characterized by very narrow M - H loops, making them temporary magnets. As soon as the magnetic field is removed, they lose their magnetization.

The hysteresis loop is a fundamental concept in the field of magnetism and has significant importance in technology. Physicists strive to provide a theoretical explanation for it, material scientists work towards enhancing it, and engineers utilize it for practical applications. The hysteresis loop provides information about both intrinsic and extrinsic magnetic properties. The intrinsic property is the saturation magnetization (M_s) that exists within a domain of a ferromagnet, while the properties of remanence (M_r) and coercivity (H_c) are considered extrinsic, as they rely on external factors such as the shape of the sample, the roughness of its surface, any microscopic defects, its thermal history, and the speed at which the field is swept in order to trace the loop [9, 13-16].

2.2.4.1 *Soft and hard magnetic materials*

Ferromagnetic materials can be broadly categorized as soft or hard based on their magnetization response to an applied field. The terms "soft" and "hard" refer to their magnetic properties, not their mechanical properties. Soft magnetic materials are ferromagnets that can be fully magnetized or demagnetized with relatively low magnetic fields (≤ 1500 kA/m). Their M - H loop would indicate a low H_c (≤ 1 kA/m) and M_r , resulting in a smaller loop area. Examples of such well-known materials are pure iron, steel, Fe-6.5 wt.%Si and permalloy. Soft magnetic materials are useful in high-frequency applications such as transformers, electromagnets and write heads because they have a high M_s and consume less energy (core loss) during magnetization and demagnetization cycles. However, losses resulting from eddy currents need to be minimized, which is accomplished by the usage of lamination or an insulating magnetic materials like ferrites. Soft ferromagnets do not produce a magnetic field around them as they possess significantly low M_r and are susceptible to demagnetization with little effort, making them unsuitable as permanent magnets [16-19].

On the contrary, hard magnetic materials possess a higher coercivity and remanence. This implies that they require a stronger magnetic field to saturate or demagnetize them. Due to their higher remanence, they can generate a significant magnetic field around them. In general, hard magnetic materials are preferred for permanent magnet applications such as motors, speakers, and refrigerator magnets, as they can retain their magnetization and produce a magnetic field. The maximum value of B - H in the second quadrant of the hysteresis loop is referred to as the energy product, and it is commonly measured in MGOe (cgs unit). The energy product can be used to determine the hardness of a ferromagnet. In the past, materials such as Barium or Strontium ferrites, as well as AlNiCo, were utilized as permanent magnets. However, in recent years, hard magnets such as SmCo and NdFeB have become more prevalent, due to their much larger energy products [20-22].

2.2.5 Curie temperature

The saturation (spontaneous) magnetization (M_s) resulting from the alignment of atomic magnetic moments is temperature-dependent and decreases sharply to zero when the Curie temperature (T_c) is reached. The magnetic ordering represents a thermodynamic phase transition that occurs continuously and is characterized by a λ -shaped anomaly in specific heat. This anomaly is attributed to the disorganization of the atomic dipole moment. At temperatures higher than T_c , M_s becomes zero, while at temperatures lower than T_c , M_s is reversible [4, 11].

Fe, Co, and Ni are main ferromagnetic metals with T_c of 1044 K, 1388 K, and 628 K, respectively. Among them, cobalt has the highest T_c known. Magnetite (Fe_3O_4), on the other hand, has a T_c of 856 K [13]. For applications, a $T_c \geq 800$ K is preferred.

2.2.6 Various forms of energy within magnetic materials

This section outlines various energies that are present in a magnetic material. Understanding these energies is crucial for comprehending the behaviour of magnetic materials, such as their M - H loops and the occurrence of magnetic domains.

2.2.6.1 Magnetostatic energy

When a block of ferromagnetic material is magnetized and contains only one domain, it has a magnetization at the macroscopic level. This magnetization leads the block to act as a permanent magnet, producing a magnetic field around it. Figure 2.6(a) shows an illustration of a magnetized block and its corresponding external field. It is obvious that the field acts in the opposite direction to magnetize the block from its own magnetization. Due to this phenomenon, this field known as the demagnetizing field (H_d). The magnetostatic energy (E_{ms}), is quantified using the following equation;

$$E_{ms} = \frac{1}{2} \mu_0 H_d M \quad (2.11)$$

where M refers to the magnetization and H_d is the demagnetized field generated by M ;

$$H_d = -N_d M \quad (2.12)$$

where N_d is the magnetization factor, which relies on the sample's shape and geometry. Its value can be less than or equal to 1 for any type of sample geometry.

This energy is responsible for enabling the block to perform tasks like lifting another ferromagnet against the gravitational force. By dividing the block into domains, as depicted in Fig. 2.6(b), the external demagnetizing field can be decreased, thereby reducing the magnetostatic energy. In this case, the external field is reduced, which results in the block being able to perform less work and storing less magnetostatic energy. However, the formation of domains leads to the magnetic moments at the boundary between the domains not being able to align parallel. As a result, the exchange energy of the block is increased as the principles of quantum mechanics generate an exchange energy that drives the alignment of electron spins and their magnetic dipole moments in parallel to each other [4, 14, 23-25].

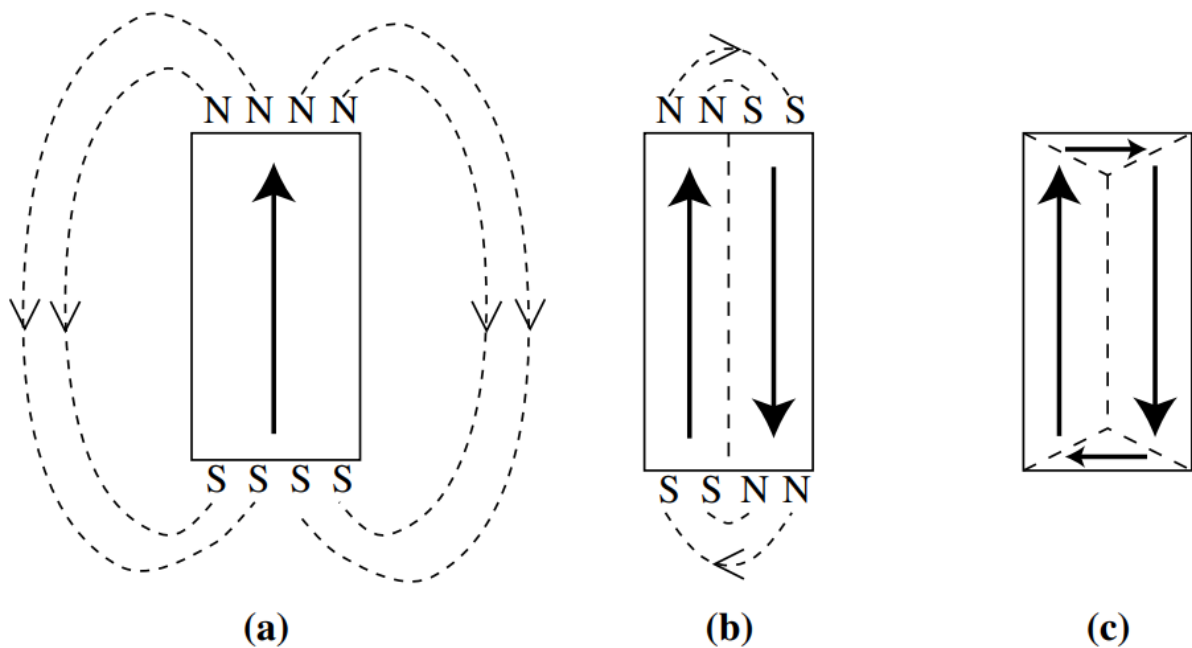


Figure 2.6: Formation of domains in a ferromagnet to decrease the magnetostatic energy [23].

In order to completely eliminate the magnetostatic energy, it is necessary to establish a domain pattern that doesn't result in any magnetic poles on the surface of the block. A possible solution for this is presented in Figure 2.6(c). However, before we can assess the feasibility of this domain pattern, it's important to have some understanding of the magneto-crystalline anisotropy energy contribution.

2.2.6.2 Magneto-crystalline anisotropy energy

Ferromagnetic crystals tend to have certain crystallographic directions where the magnetization aligns in a preferred manner. These preferred directions are referred to as the "easy" axes, since it's easier to magnetize a demagnetized sample to saturation if the external field is applied along these axes. Figure 2.7(a) depicts a graph showing the magnetization curves for a ferromagnetic single crystal when the external field is applied along the easy and hard axes. In either scenario, the ferromagnetic single crystal reaches the same saturation magnetization. However, the field applied along the hard axis requires a much greater magnitude to achieve saturation compared to the easy axis.

Each material has its own set of easy axes, which are the preferred crystallographic directions for magnetization. α -Fe (body-centred cubic (bcc)-iron) has the $\langle 100 \rangle$ direction (i.e., the cube edge) as its easy axis, which is equivalent for all six cube edge orientations as it is a cubic crystal. The body diagonal is identified as the hard axis of magnetization in α -Fe, whereas other directions like the face diagonal are considered to be intermediate.

In contrast, the preferred direction for magnetization in face-centred cubic (fcc) nickel, is the $\langle 111 \rangle$ body diagonal, while in hexagonal close-packed (hcp) cobalt, it is the $\langle 0001 \rangle$ direction. For cubic crystals such as nickel and iron, the magneto-crystalline anisotropy energy (E_{mc}) is calculated from;

$$E_{mc} = K_{mc} + K_1(\alpha_1^2\alpha_2^2 + \alpha_2^2\alpha_3^2 + \alpha_1^2\alpha_3^2) + K_2(\alpha_1^2\alpha_2^2\alpha_3^2) + \dots \quad (2.13)$$

where α_1 , α_2 and α_3 represent the direction cosines in three-dimensional space of the magnetization vector (\bar{M}), whereas K_{mc} , K_1 and K_2 are the cubic anisotropy constants.

For the uniaxial crystals such as Co-hcp structure, E_{mc} is given by;

$$E_{mc} = K_{u0} + K_{u1}\sin^2\theta + K_{u2}\sin^4\theta + \dots \quad (2.14)$$

Where θ represents the angle formed between the magnetization direction and the easy axis. K_{u0} , K_{u1} and K_{u2} refer to the uniaxial anisotropy constants.

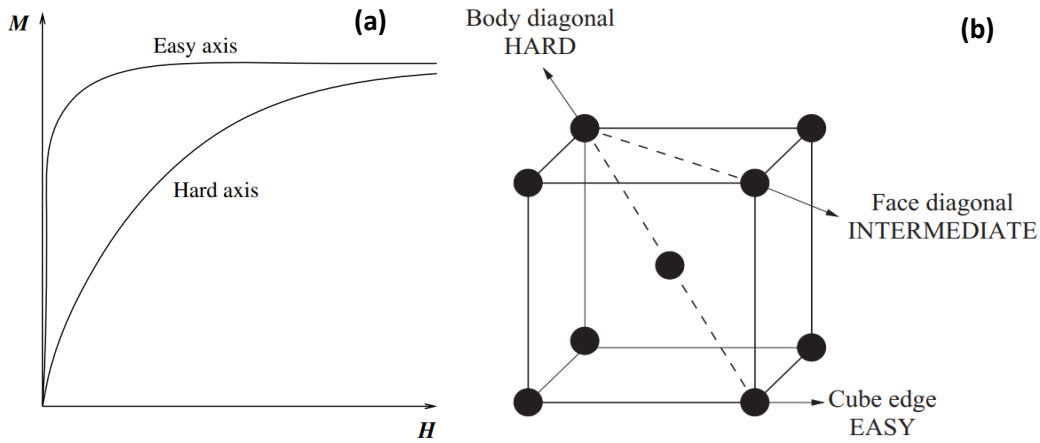


Figure 2.7: The schematics showing (a) the magnetization curves depicted for a ferromagnetic material with the magnetic field aligned along both the hard and easy directions, and (b) the hard, medium and easy magnetization directions in the unit cell of α -Fe (bcc-iron) [23].

The reason why magnetization aligns along certain crystallographic directions is due to the magnetocrystalline anisotropy, which increases when the magnetization is aligned along the hard direction as compared to the easy direction. The difference in energy per unit volume between samples that are magnetized along the easy and hard directions is known as the magnetocrystalline anisotropy energy. It can be determined by calculating the area between the hard and easy magnetization curves, such as the ones shown in Figure 2.7(a).

To minimize the energy associated with magnetocrystalline anisotropy, domains will form in a way that their magnetizations align along the easy crystallographic directions. In the case of bcc iron, a cube edge corresponds to the "vertical" axis in Figure 2.6. As α -Fe has cubic symmetry, the horizontal direction is an easy axis as well.

Consequently, the domain pattern presented in Figure 2.6(c) has a low magnetocrystalline energy.

In Figure 2.6(c), the horizontal domains that appear at the top and bottom of the crystal are referred to as "domains of closure." These domains form easily in materials that have perpendicular easy axes. This configuration is especially advantageous because it eliminates the demagnetizing field and the magnetostatic energy, without increasing the magnetocrystalline anisotropy energy.

It is worth noting that the structure of domain boundaries is influenced by the magnetocrystalline energy. Within the domain boundary region, the magnetization direction changes and is not able to be aligned along the preferred crystallographic direction. Therefore, similar to the exchange energy, the magnetocrystalline energy favours larger domains with fewer boundaries [4, 5, 23, 26].

2.2.6.3 Exchange Energy

As explained earlier, the exchange interaction in a ferromagnetic material strives to align the atomic moments in parallel to each other. Therefore, any alteration in the direction of the magnetic moments of neighbouring atoms must occur at the expense of the exchange energy. To reduce energy consumption, the magnetic moments usually remain aligned in the same direction, and any alteration in their direction occurs gradually and smoothly. The exchange energy is an extra form of energy per magnetic moment, which results in the alignment of magnetic moments within a domain [4, 27].

When two adjacent electrons have spins (S_i and S_j), the exchange energy (E_{ex}) is defined as;

$$E_{ex} = -2J_{ex}\vec{S}_i \cdot \vec{S}_j = -2J_{ex}S_iS_j \cos \varphi_{ij} \quad (2.15)$$

Where J_{ex} is the exchange constant and φ_{ij} refers to the angle between \vec{S}_i and \vec{S}_j . If J_{ex} is positive, E_{ex} attains its minimum value when the spins are parallel ($\varphi_{ij} = 0^\circ$), which is observed in ferromagnetic materials. Conversely, if the two spins are aligned antiparallel ($\varphi_{ij} = 180^\circ$), E_{ex} reaches its maximum value. In the case where J_{ex} is negative, the minimum E_{ex} is observed when the spins are antiparallel, which is the characteristic of antiferromagnetic materials.

Creating smaller magnetic domains leads to the formation of more domain walls, which results in increased exchange and magnetostatic energy. To reduce the overall energy, a domain arrangement such as the one illustrated in Figure 2.8 is adopted as a compromise [23].

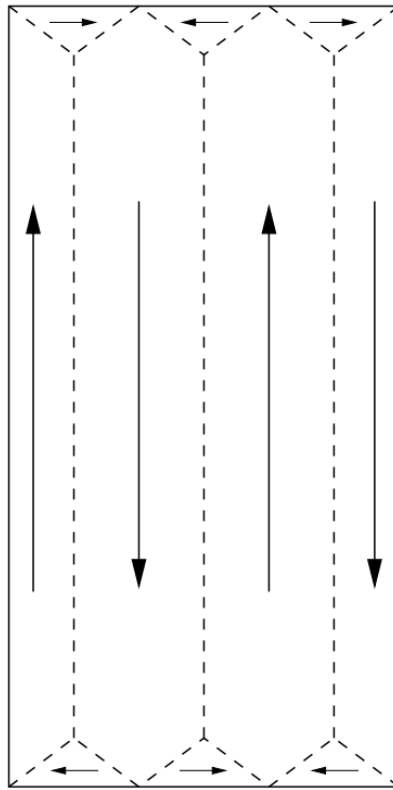


Figure 2.8: A domain configuration that minimizes the combined energy from exchange, magnetostatic, magnetocrystalline, and domain-wall effects [23].

2.2.6.4 Zeeman Energy

The magnetic moment of electrons is due to their charge and angular momentum, which is similar to the magnetic moment produced by a current of charged particles flowing in a wire loop. By observing the change in the atomic absorption spectrum in the presence of an external magnetic field, the direct evidence of that magnetic moment can be obtained. When a magnetic field is present, the energy of an electron in an atomic orbital with non-zero orbital angular momentum changes proportionally to the strength of the applied field and the orbital angular momentum. This occurrence is called the normal Zeeman effect and is observable in the absorption spectra of specific atoms, like calcium and magnesium. The Zeeman energy (E_z) can be calculated from;

$$E_z = -\mu_o MH \cos \theta \quad (2.16)$$

Where the angle θ represents the deviation between the direction of an externally applied magnetic field and the magnetization orientation of the material. It should be noted that when there is no external magnetic field applied and no demagnetizing field present, the Zeeman energy is equal to zero [11, 28-30].

2.2.7 Random anisotropy model

When a continuous magnetic material has spins that are exchange-coupled and experience a local magnetic anisotropy with random orientation, two significant effects take place. Firstly, when the length scale of the microstructure is smaller than the exchange length (L_{ex}), the magnetization experiences an anisotropy that is reduced from its local value (K_{loc}) due to exchange averaging over the random local anisotropy:

$$\langle K \rangle \approx K_{loc} \left(\frac{l}{L} \right)^{3/2} \quad (2.17)$$

The second effect that occurs is that the magnetization exhibits alignment consistency over a distance of L ($=L_{ex}$) and can span from the length scale of the random anisotropy (l) to significantly larger values. This range is determined by the ratio of the exchange stiffness (A) to the magnitude of the local anisotropy (K_{loc}).

$$L \approx L_{ex} = \frac{16A^2}{9K_{loc}^2 l^3} \quad (2.18)$$

In the current scenario, the random local anisotropy refers to that of each single domain nanoparticle. When nanocrystalline particles are included in a composite, their behaviour is influenced not only by their particle size and anisotropy but also by the characteristics of the inter-granular phase. If the inter-granular material is non-magnetic, the nanocrystals behave similar to single domain particles, interacting only through their weak magnetic dipole fields, resulting in a weak local anisotropy. When the inter-granular phase is magnetic (which is the case for nanocrystalline magnetic alloys; the inter-granular phase is the amorphous phase embedded in the matrix), the behaviour is determined by Equations (2.17) and (2.18). The resulting magnetism can be either hard or soft, and it depends on various factors, including the strength of the magnetic anisotropy, the particle size, and the strength of the exchange coupling among them. In this case, the magnitude of the local anisotropy is strong [31-33].

2.2.7.1 Random anisotropy model in nanocrystalline alloys

The significance of exchange couplings between ferromagnetic-ferromagnetic or antiferromagnetic-ferromagnetic in nanostructured materials cannot be overstated. The strength and even the sign of the coupling between the spins in magnetic particles or layers of different materials can vary based on their exchange interaction, material properties, and thickness.

In situations where there is random anisotropy, the effective anisotropy is decreased by averaging K_{loc} over L_{ex} of the magnetic moments, as shown in Equation (2.17). For nanocrystalline materials, K_{loc} is applicable over the entire nanocrystal volume, and

the suitable length scale for the random anisotropy change (l) is determined by the size of the inter-particle layer. If K_{loc} is significantly stronger than the anisotropy of the inter-granular amorphous matrix (K_{am}), the change in the direction of magnetization occurs across the inter-granular phase between the surfaces of the particles. Alternatively, if K_{loc} is similar to K_{am} , then the change occurs over a larger length [31].

Herzer [34] proposed that the expression for the exchange length (Equation 2.18) should incorporate the average anisotropy of a nanocrystalline material ($\langle K \rangle$) instead of the local anisotropy (K_{loc}). This is because the exchange length is mostly defined in the amorphous matrix between the nanocrystalline particles, where the direction of magnetization changes the most, rather than in the interior of the particles where K_{loc} is uniform. Herzer [35] also discovered that the exchange-averaged anisotropy of a nanostructured material, which governs the magnetic properties, particularly the coercivity, varies as the sixth power of the size of the inter-particle layer (l).

$$\langle K \rangle \approx 0.32 \left(\frac{K_1^4}{A^3} \right) l^6 \quad (2.19)$$

The coercivity of nanostructured materials is restricted by a particular equation, $H_c \leq \frac{2\langle K \rangle}{M_s}$, leading to a variety of coercivities that depend on the microstructure length scale. The sixth-power relationship with the microstructure length scale controls the magnetic properties, particularly the coercivity, of nanostructured materials. This relationship explains the sharp increase in coercivity observed in a nanostructured system with variable length scale. In this system, the steep line follows D^6 , which is consistent with the assumption that l is proportional to D . Therefore, the coercivities of nanostructured materials are much lower than those of microcrystalline samples composed of the same crystallite, depending on the scale (l) of the nanostructure [36-39].

a. Magneto-crystalline anisotropy for Fe-based nanocrystalline alloys

The magneto-crystalline anisotropy constant (K_1) of the α -FeSi 20 at.%, the constituent phase, remains relatively high at approximately 8 kJ/m³ [40]. However, this value alone cannot account for the observed low coercivity and high initial permeability in the nanocrystalline material. The key to comprehension lies in acknowledging that the size of the grains is smaller than the length associated with ferromagnetic exchange [41];

$$L_{ex}^0 = \left(\frac{A}{K_1} \right)^{1/2} \quad (2.20)$$

Chapter 2 – Theoretical Background

L_{ex}^0 value of 35 nm represents the minimum range (for Fe-based nanocrystalline alloys) within which the magnetic moments are compelled to align in parallel due to exchange interaction. As a result, the magnetization cannot align with the randomly oriented easy axis of each individual grain. Consequently, the effective anisotropy is a result of averaging the anisotropy values from multiple grains, resulting in a reduction in magnitude. The random anisotropy model provides an explanation for how the magneto-crystalline anisotropy is averaged out in the material. This leads to the determination of the average anisotropy $\langle K \rangle$ that is relevant to the magnetization process, which is expressed as follows;

$$\langle K \rangle \approx K_1 \left(\frac{D}{L_{ex}^0} \right)^6 = K_1^4 \frac{D^6}{A^3} \quad (2.21)$$

As long as the grain size (D) remains smaller than the ferromagnetic exchange length (35 nm), the average anisotropy $\langle K \rangle$ is expected to be negligible. For example, for grain sizes of 10 nm, the estimated average anisotropy is approximately 4 J/m³, which is significantly lower than the local magneto-crystalline anisotropy 8000 J/m³ [42]. The use of high-resolution Kerr-effect studies on nanocrystalline Fe_{73.5}Cu₁Nb₃Si_{13.5}B₉ has provided valuable insights [43]. These studies have demonstrated the presence of exceptionally wide domain walls, approximately 2 μm in thickness. This observation serves as a clear indication of the material's low effective anisotropy.

The dependence of $\langle K \rangle$ on grain size (D^6) is clearly evident in the coercivity data for grain sizes smaller than approximately 40 nm (Figure 2.9). The initial permeability, in turn, exhibits an inverse relationship with $\langle K \rangle$, indicating a $1/D^6$ dependence [44]. The coercivity's dependence on the $1/D$ for larger grain sizes demonstrates the conventional understanding that excellent soft magnetic properties are achieved with larger grains ($D > 100 \mu\text{m}$). As a result, reducing the particle size to the scale of the domain wall width leads to an increase in coercivity (H_c) up to a maximum value, which is influenced by the existing anisotropies [45].

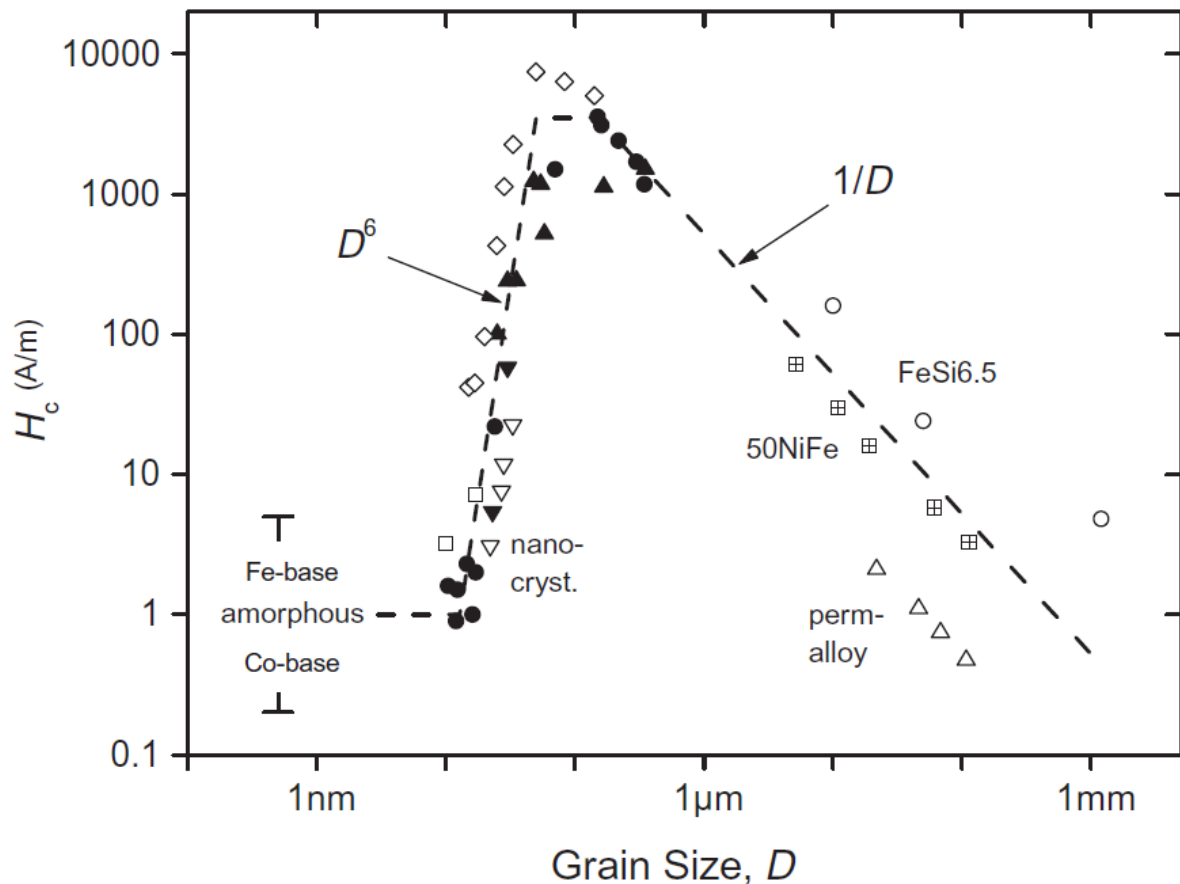


Figure 2.9: The relationship between coercivity (H_c) and grain size (D) investigated for different soft magnetic metallic alloys [38].

2.2.8 Effect of oxygen content on the soft-magnetic performance of amorphous/nanocrystalline materials

The materials' purity and the vacuum conditions in industrial settings do not meet the high standards observed in laboratories. This limitation hinders the widespread industrialization of research findings, with metallic glasses (MGs) serving as a prime example. MGs have garnered significant research interest [46, 47] since their initial synthesis in 1967 due to their exceptional soft magnetic [48], mechanical, and chemical properties [49-51], as well as their relatively cost-effective production [52]. Laboratories have developed numerous large-sized MGs following the discovery of bulk metallic glasses (BMGs) in 1995 [53], with expectations of their potential applications in structural and surface coating materials [54, 55].

Nevertheless, the actual number of BMGs suitable for industrial manufacturing remains highly limited, and their applications, especially in structural roles, are rarely documented. The demanding processing requirements for producing BMGs, which involve operating under high vacuum conditions and using high purity feedstock materials to mitigate the adverse effects of oxygen and unwanted inclusions, result in

increased production costs and pose a significant obstacle to the industrialization of the BMGs [56].

The detrimental impact of inclusions on the final properties of BMGs is well-known as these inclusions promote heterogeneous nucleation and degrade the mechanical, chemical, and soft magnetic performance of the BMGs [57, 58]. However, the role of oxygen in the formation of MGs has been a subject of controversy for over two decades [59-62]. Johnson *et al.* [63] discovered that oxygen has an adverse effect on glass formation because it promotes the evolution of harmful oxides and metastable phases acting as sites for heterogeneous nucleation. Meanwhile, Gebert *et al.* [64] proposed that the presence of oxide impurities alters the crystallization process from a single stage to a multi-stage process, consequently reducing the supercooled liquid region. In contrast, several studies demonstrated that a certain amount of oxygen content can actually facilitate the glass formation [65-68]. Furthermore, it's worth noting that the oxygen levels can exhibit considerable variation among samples, even when they have similar compositions [69]. For instance, Ponnambalam *et al.* [70] measured oxygen concentrations as low as 50 parts per million (ppm) or less in the $\text{Fe}_{48}\text{Cr}_{15}\text{Mo}_{14}\text{Y}_2\text{C}_{15}\text{B}_6$ glassy alloy. This level is approximately 20 to 50 times lower than the oxygen content observed in similar MGs developed by Lu *et al.* [71].

Although there is a controversy regarding the effect of oxide inclusions on the glass formation, their influence on magnetic properties of the glassy alloys is relatively well-established. It was suggested that a minimal oxygen content can lead to an increase in the complexity of atomic clusters' composition, consequently elevating the system's configuration entropy. Oxygen has the capacity to enhance resistance to crystallization by inhibiting the formation of competing phases and stabilizing the liquid state through the reduction of the liquidus temperature [66]. In this case, the produced part becomes fully amorphous, which causes the magnetic properties to remain unaffected from the oxygen concentration [72]. On the other hand, dissolved oxygen in liquid alloy tends to bond with other elements and forming oxides, which are considered as impurities in the microstructure. The reduction in coercivity (H_c) and the rise in effective permeability in BMGs with low oxygen content, when contrasted with those containing high oxygen levels, can be readily comprehended. In glassy alloys with high oxygen content, heterogeneous crystallization significantly increases magnetic anisotropy, while impurities serve as pinning centres for magnetic domains, resulting in an increase of coercive field [73-77]. Furthermore, an increase in Curie temperature (T_c) and a marginal decrease in saturation magnetization (M_s) were observed in BMGs having lower oxygen concentration [78, 79].

2.3 Additive Manufacturing of Soft Magnetic Materials

Additive manufacturing (AM) is in a state of constant evolution, driven by advancements in printing technologies. However, achieving a one-step fabrication of electrical machines remains a challenging goal due to the need for the usage of both hard and soft magnetic materials, along with the incorporation of copper wire. One clear advantage that AM brings is the streamlining of production processes, resulting in significantly faster core fabrication times for these machines. To illustrate, manufacturing a stator plate through conventional machining, electrical discharge machining (EDM), and milling processes is estimated to take over 4 months, whereas 3D printing can produce the same component within just 1 week, as depicted in Figure 2.10 [80]. The elimination of traditional tooling and processes is anticipated to lead to substantial cost reductions in fabrication.

AM provides the capability to easily build thin-walled hollow structures using novel materials having high electrical resistivity. This opens up significant opportunities for reducing core losses [81]. Even intricate core designs, such as those involving continuous skewing and complex flux paths integrated with cooling channels [82], can be realized, leading to more efficient designs that offer considerable cost and weight gain while also minimizing the wastage of critical materials. Moreover, AM's ability to combine different metal powders, higher-quality alloys, and binding agents allows for the enhancement of material properties by precisely controlling grain orientation and the quality of soft magnetic materials in specific sections of machine components [83].

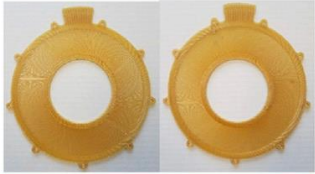
	Concept A - Stator Plates from Cobalt-Iron Alloy	Concept B - Stator Plates from Cirlex	Concept B - Stator Plates from Ultem1010
			
Fabrication Method	Machine/EDM	Machine/Mill	3D Print/FDM
Fabrication Time	4+ months	3 months	1 week (92.3% reduction)
Fabrication Costs	\$21,400	\$19,870	\$1,000
Material Costs	\$600	\$330	\$0 (included in fab.)
Total Costs	\$22,000	\$20,200	\$1,000 (95.0% reduction)

Figure 2.10: NASA's assessment of the time and expenses associated with manufacturing a stator plate [80].

Soft magnetic materials (SMMs) offer a broad spectrum of choices, each with significantly varying performance characteristics. Table 2.1 provides a comprehensive

overview of diverse SMMs, including Fe–Si, Fe–Ni, Fe–Co, soft magnetic composites (SMCs), soft ferrites and amorphous/nanocrystalline SMMs, along with their relevant magnetic properties crucial for industrial applications, such as saturation magnetization (M_s), relative permeability (μ_r), and core resistivity (r). These materials can be fabricated in different forms through AM techniques like laser powder bed fusion (LPBF), directed energy deposition (DED), fused deposition modelling (FDM) and/or binder jetting technology (BJT). The information presented in this table provides invaluable information for comprehending the distinctions in properties among different soft magnetic materials, aiding in the suitable selection for the design and production of electromagnetic devices.

Table 2.1: Key magnetic properties of the SMMs featured in the reviewed articles, along with the corresponding AM methods employed.

SMMs	M_s (T)	μ_r	r ($\mu\Omega\text{cm}$)	AM	Ref.
Fe-(2.9-3.7) Si	2.1, 1.1	25	20-50	LPBF, BJT, FDM and DED	[84-97]
Fe-(6.5-6.9) Si	1.9	11000	85	LPBF, EBPBF, DED and BJT	[96, 98-111]
Fe-Ni	0.6-1.1	8000-100000	-	LPBF, DED and FDM	[112-130]
Fe-Co	2.4-2.5	20000-60000	45	LPBF and DED	[131-139]
SMCs	0.5-1.3	6000-100000	120-130	LPBF, FDM and DED	[140-146]
Soft Ferrites	0.32-0.545	350-20000	10^7 - 10^9	UV-assisted 3D printing and FDM	[127, 147-149]

2.3.1 Fe-Si alloys

Within the family of engineering soft magnetic alloys, Fe-Si holds a significant and well-established position in both technical and market domains. It finds extensive use in applications such as transformers, particularly when utilizing the grain-oriented class, as well as in industrial motors and generators, often referred to as non-grain oriented electrical steel. The success of Fe-Si in these applications can be attributed to its exceptional combination of high electrical resistivity, ease of processing, and cost-effectiveness [150]. At present, the Fe-3.2Si alloy with low silicon content can be processed using a conventional cold rolling technique and accounts for nearly 90% of low-frequency electric machines. However, to make the high-silicon content Fe-Si alloy suitable for high-frequency electrical machines, it must exhibit high permeability and electrical resistivity. Increasing the silicon content in the alloy offers an advantage in terms of mass density, but this advantage is counterbalanced by a reduction in

saturation magnetization and an increase in brittleness due to the formation of chemically ordered phases (B_2 and DO_3) during slow cooling. To prevent these issues, melt-spinning and rapid quenching of Fe-Si ribbons have been employed, which also enhance the properties of high-silicon (approximately 6.5 at.%) steel [151, 152]. Up to this point, expensive processes such as chemical vapour deposition and diffusion siliconizing, involving annealing, have been used to prevent the formation of these phases in the conventional manufacturing process and to avoid cracking during cold rolling [153].

Additive manufacturing (AM) offers a solution to these challenges by enabling the production of electrical machine cores through the printing of atomized, amorphous Fe-Si alloy powder. Subsequently, the printed component can be annealed at a lower temperature to prevent the formation of unwanted phases. Some of the initial experiments in additive manufacturing (AM) of Fe-Si components were conducted by Garibaldi *et al.* [99], who conducted a series of investigations into the 3D printing of Fe-Si alloy with a 6.9 wt.% silicon content using LPBF. In one of these works, the effect of laser energy input on the microstructures, and the magnetic properties of the Fe-Si alloy was studied. The printing process took place under an argon atmosphere (with oxygen levels below 0.4%) on a heated platform at 473 K, which helped minimise thermal expansion gradients. The best magnetic properties were obtained with a maximum relative permeability of 5300, a coercivity of 49 A/m, and power losses of 4 W/kg (measured at 50 Hz and 1 T) for the sample processed using a laser power of 70 W, a laser scan speed of 250 mm/s, and thermally treated in an argon environment at 973 K. This thermal treatment step induced modifications in the magnetization curve due to stress relief.

Employing LPBF under pre-established conditions, nearly fully dense components were achieved, typically exhibiting elongated grains along the build direction, likely due to heat extraction. The produced specimens predominantly consisted of a single ferritic phase, lacking phase ordering, with a crystallographic $\langle 001 \rangle$ fibre texture that was discernible in pole figures. It was found that increasing the laser energy input can transform this $\langle 001 \rangle$ fibre texture into a cube texture [98]. After annealing at 1423 K, recrystallized microstructure possessed a great majority of equiaxed grains [100].

Most recently, electron beam powder bed fusion (EBPBF) [109, 111] and BJT [90, 110] have been employed to overcome the brittleness issue and prevent crack formation. It is proposed that the low preheating temperature during the LPBF process resulted in crack formation in 3D printed $\text{Fe}_{93.5}\text{Si}_{6.5}$ (wt.%) alloys, leading to a deterioration in both mechanical and magnetic properties [83, 108]. Elevating the processing

temperature in the EBPBF method is effective in mitigating thermal stresses and preventing crack formation in the specimens. Yang *et al.* [109] have previously shown the successful production of dense Fe_{93.5}Si_{6.5} (wt.%) components without cracks, achieving a remarkable relative density of up to 99.99% through EBPBF. Furthermore, EBPBF is deemed well-suited for the fabrication of fragile Fe_{93.5}Si_{6.5} (wt.%) components with intricate geometries, delivering excellent magnetic performance across various frequency ranges [83, 154]. In another study [111], two hatching techniques, namely 'radial hatching' and 'circle hatching,' were utilized to EBPBF-process toroidal Fe_{93.5}Si_{6.5} (wt.%) parts. The samples produced with circle hatching exhibited higher relative permeability (964 at 50 Hz), lower coercivity (11.95 A/m at 50 Hz), resulting in a higher maximum magnetic flux density (0.603 T at 50 Hz) and reduced hysteresis losses, thus leading to lower power losses (0.03 W/kg at 50 Hz). This favourable outcome is attributed to the ideal alignment between the circular pattern generated by the circle hatching approach and the magnetic field lines' path in the shape of enclosed circles. This alignment facilitates the magnetization-demagnetization process.

Alternatively, nearly 99% dense near-net shape Fe-6Si parts with no cracks was fabricated via BJT with M_s of 1.83 T, H_c of 31.83 A/m, electrical resistivity of 98 $\mu\Omega\cdot\text{cm}$ and an ultimate tensile strength of 434 MPa [110]. BJT was also utilized to investigate the influence of sintering temperature variation, change in Si content and B addition as a sintering additive on magnetic properties [90]. It was concluded that at a sintering temperature of 1200 °C, Fe-5wt.%Si alloy with the addition of 0.25% boron demonstrated a significantly larger grain size, enhanced bulk density, and the presence of ordered phases. This combination yielded the most appealing results in terms of H_c (69.6 A/m) and permeability (reaching 3475 H/m) among all the tested samples.

2.3.2 Fe-Ni alloys

In the 1910s, Gustav Elmen identified a nickel-rich alloy known as permalloy, with a nickel concentration of 78.5%. Permalloys are renowned for their excellent soft magnetic properties, including low losses, high initial permeability (6,000 – 10,000), and a favourable response to magnetic field annealing [155]. However, they have a lower saturation induction compared to silicon steels and are generally more expensive. The maximum permeability (in the range of 40,000 – 120,000) is achieved within a relatively narrow range, typically around 75% to 80% nickel, leading most commercial permalloys to adhere to this composition. Attaining the maximum permeability in permalloys is also dependent upon suitable heat treatment, which necessitates precise cooling within appropriate temperature ranges at the designated

rates. Another notable group of Fe-Ni alloys includes the 'supermalloys,' distinguished by their high nickel content at approximately 78%, alongside 5.0% molybdenum, iron, and a minor manganese component. These alloys also exhibit remarkable soft magnetic characteristics, encompassing exceptional initial permeability (50,000 – 150,000), low losses, and a strong response to magnetic field annealing. Achieving the maximum permeability (from 600,000 to 1,200,000) with supermalloys also requires precise heat treatment, involving specific temperature ranges and controlled cooling rates. While supermalloys may entail a higher cost compared to permalloys and silicon steels, their exceptional properties position them as a promising substitute for high-frequency electrical machines [125, 156-158].

Permalloys, owing to their remarkable permeability, have been successfully produced with various AM techniques for magnetic shielding structures, microwave applications, and power electronics. One of these AM methods, known as directed energy deposition (DED), distinguishes itself by not requiring a powder bed, in contrast to other conventional powder-based AM techniques. Mikler *et al.* effectively employed DED to fabricate diverse permalloys with 30% iron content, using a blend of elemental powders as feedstock without the need for pre-alloying [116]. Permalloys have also been generated with a powder blend of nickel and iron using LPBF by Schonrath *et al.* [157]. The raw materials in the form of powders were commercially available, high-purity substances that had not undergone pre-alloying. These powders adhered to the standard 78.5% nickel composition, with particle sizes ranging from 5 to 55 μm . These powders were mixed using the Turbula principle at 30 revolutions per minute for 30 minutes, ensuring homogeneity as confirmed by energy-dispersive X-ray analysis. Although feedstock processing and the creation of electrical cores and conductive windings were carried out using FDM, it's worth noting that the feedstock's relative permeability (10-20 up to 10 MHz) was significantly low [127-130].

2.3.3 Fe-Co alloys

Fe-Co alloys are renowned for their highest maximum saturation magnetization (2.43 T at room temperature for Fe₆₅Co₃₅ alloy) and Curie temperature (1000 - 1500 K [159]) among all soft magnetic families. These materials excel in applications requiring high magnetic moments and elevated Curie temperatures. However, owing to the presence of Co, their higher cost restricts their predominant use to specialized applications and low mass-production, such as in aerospace applications, justifying their expense due to the lighter weight they offer [160-162].

Fe-Co alloys, with their notably higher maximum flux density compared to other soft magnetic materials, enable the design of electrical machines whose size and weight can be greatly lowered. The most famous commercially available forms are Permendur [163], Supermendur [164], and Hiperco [131] with a composition closely approximating 49% iron, 49% cobalt, and 2% vanadium.

Fewer instances of AM-processed Fe-Co-based soft magnetic alloys can be found in the literature (Table 2.1). A recent study by Babuska *et al.* [165] reported the LPBF processing of a ductile Fe₅₀Co₅₀ binary alloy, which exhibited a remarkable 250% to 300% increase in yield strength and high ductility (35%) in tension. A substantial enhancement in mechanical properties was also observed in the DED-processed samples with the unique multiscale microstructures. Kustas *et al.* [131] indicated the DED producibility of an alloy equivalent to Hiperco. Fine equiaxed columnar grains were found in the microstructures of as-built samples. These transformed into a heterogeneous, bimodal grained microstructure when the as-built samples were subjected to annealing at 1111 K for 2 hours. This helped to reduce the coercivity (H_c) from 995 A/m to 401 A/m, increase the maximum permeability (μ_{max}) from 518 to 1615 and enhance the full-field induction (B_{40}) to 2.29 T, which was comparable to those fabricated through traditional powder metallurgy ($H_c = 90\text{-}200$ A/m, $\mu_{max} = 4000\text{-}8000$ and $B_{40} = 2.2\text{-}2.3$ T [166, 167, 132]). In the work, gas-atomized and pre-alloyed Fe-Co-1.5V was utilized as the feedstock powder to produce both thick-walled and thin-walled concentric cylinders. In another study, Kustas *et al.* [137] established that it was possible to suppress the formation of the chemically ordered B_2 phase with the help of well-controlled cooling rate during DED processing. This was achieved by changing the main process parameters: laser power, build speed and interlayer interval time. Geng *et al.* [168] also used DED to synthesize Fe_{1-x}Co_x bulk samples and performed high throughput characterization to investigate structural and magnetic properties. The Curie temperature, saturation magnetization, and magnetocrystalline anisotropy were found to be dependent on the concentration of cobalt (Co). With high Co concentrations, the Curie temperature rises to its maximum value of 1120°C.

2.3.4 Soft Magnetic Composites (SMCs)

Soft magnetic composites (SMCs) consist of insulated magnetic particles and are often formed into desired geometrical shapes through high-pressure consolidation. The term 'SMCs' covers amorphous soft magnets, magnetic wires, and powder-based magnets [169]. These materials have played a pivotal role in the manufacturing of near-net-shaped electrical cores using traditional methods [170]. The uniform distribution of magnetic particles in soft magnetic electrical cores results in

mechanically smooth torque without ripples. The insulation coating improves the electrical resistance of the laminates, thereby reducing losses caused by eddy currents. However, it does come at the cost of diminishing the mechanical and magnetization strength of the electrical components. In addition to providing insulation, the compacted particles create enclosed air gaps, significantly increasing electrical resistivity. SMCs need ideally to be manufactured using high-magnetic materials such as Fe, Fe₃P, Fe-Si, and Fe-Co alloys [171]. One notable advantage of employing AM to SMCs is the ability to obtain more intricate and complex geometries compared to conventional methods.

To illustrate, Khatri *et al.* [144] employed a unique approach in the creation of soft magnets. Instead of directly 3D-printing the soft magnetic powder, the researchers initially blended ABS with approximately 40% by volume of stainless-steel filler with a micrometre-scale particle size distribution. Subsequently, a laser was utilized to melt the polymer, forming intricate soft magnetic shapes. While the magnetic filler enhanced the magnetic properties, it simultaneously led to a decrease in mechanical performance. Despite this unideal combination of polymer and magnetic powder, it could serve as an initial foundation for the further improvement of complex-shaped soft magnets, especially for applications in sensing. Additional examples encompass composite transformers [142], magnetic composites incorporating magnetic nanoparticles and photopolymers [145], as well as composites manufactured through Fused Deposition Modelling (FDM) for radar wave-absorbing structures [146].

Another example of such an alloy is FINEMET alloys [172], as mentioned in Chapter 1, they exhibit excellent soft magnetic properties such as extremely high permeability (ranging from 40,000 to 100,000), and notably high electrical resistivity. Considerable effort has been dedicated to the DED processing of Fe-Si-B-Cu-Nb soft magnetic alloys, with a focus on achieving a uniform chemical composition throughout the entire part or creating functionally graded soft magnetic materials. Borkar *et al.* and Conteri *et al.* successfully produced solid net-shaped parts by using DED [140, 141]. Their research revealed that, for those alloys, the printing speed has a more pronounced impact on the magnetic properties compared to laser power; this trend is observed in other soft magnetic materials as well. Furthermore, their work indicated the feasibility of attaining semi-hard magnetic characteristics in Fe-Si-B-Cu-Nb alloys by controlling the printing parameters. This capability to fabricate functionally graded magnetic materials holds the potential for the applications like high-power and signal transformers.

2.3.5 Soft Ferrites

Soft magnetic ferrites are mostly low coercivity ceramics with crystalline spinel structures, comprising magnetite (Fe_3O_4) and elements such as nickel-zinc (NiZn), manganese-zinc (MnZn), or cobalt-zinc (CoZn) [173]. These materials were recognized as promising soft magnetic substances with high electrical resistivity in the late 1940s. Due to their elevated resistivity, ferrites have proven to be highly valuable in high-frequency electrical components, including transformer cores and inductive toroidal cores for antennas [171].

While soft magnetic ferrites offer numerous advantages, their processability can possess challenges due to their brittleness, limitations in achieving intricate shapes, dimensional tolerances, and constraints in terms of size and density [174, 175]. Nevertheless, progress in AM techniques have unlocked new possibilities for their effortless processing and subsequent utilization in electric machines. This is evident in the work of Liu *et al.* [147, 148], who created a UV-curable Ni-Zn paste and employed a direct-extrusion 3D printer to build parts. Their relative permeability was in the range of 63 and 103 and their resonance frequency exceeded 30 MHz, which are nearly the same as those of commercial Ni-Zn ferrite cores. Furthermore, Andrews *et al.* [176] processed a toroid using Ni-Zn-Cu/Fe-oxide ceramic powder through LPBF and obtained notably high permeability values in the resulting samples. Their study also underscored the critical importance of parameter selection, heat treatment and the weight percentage of ferrite in lowering porosity content and enhancing magnetic properties.

2.4 Additive Manufacturing of Amorphous Alloys

The amorphous systems that have been most extensively studied include those based on Fe [177-179], Zr [180-183], Cu [184], Ti [185], Al [186, 187], and the results regarding vitrification are somewhat inconsistent. Before delving into the specifics, it's beneficial to examine the key process parameters in additive manufacturing (AM). Chapter 3 provides an explanation of laser additive manufacturing (LAM) processes; LPBF and DED. The critical experimental parameters in LPBF are namely laser power (P), laser scan speed (v), hatch spacing (h), and layer thickness (t) [188]. The volumetric energy density (E) combines all these parameters into Equation (2.22) [189].

$$E = \frac{P}{vht} \quad (2.22)$$

E signifies the heat introduced into the powder bed, and a higher E results in improved densification of a LPBF-processed part.

Chapter 2 – Theoretical Background

The cooling rate during the solidification of a small melt volume is described by Equation (2.23), which is derived from the Rosenthal equation for a moving point heat source [190, 191].

$$\frac{dT}{dt} = \frac{2\pi kv}{\alpha P} (T_m - T_0)^2 \quad (2.23)$$

Here, the instantaneous cooling rate (dT/dt) is determined by factors such as thermal conductivity (k), laser scan speed (v), laser power (P), laser absorption coefficient (α), and the melting temperature (T_m) alongside the ambient temperature (T_0).

It's important to highlight the significance of α , as it influences both the cooling rate and the efficiency of LAM processes. A material having a lower α necessitates a higher energy density (E), assuming other factors are constant, to attain an equivalent level of densification. Consequently, this lowers the efficiency of the LAM process. α is contingent on the material, the laser wavelength, and the laser intensity employed [192].

Analysing Equations (2.22) and (2.23) indicates that, for a specific material, from the process parameters P and v exert contrasting effects on both E and dT/dt . A higher P/v ratio brings about an increase in E and a reduction in the cooling rate. Nevertheless, the small melt volume can result in solidification occurring at relatively rapid cooling rates ($\sim 10^3 - 10^4$ K/s). This speed is generally adequate for achieving vitrification in alloys with good glass forming ability (GFA), given their lower critical cooling rate (R_c), which is less than 10^3 K/s [180, 190, 193]. Only alloys having poor GFA may require a higher cooling rate.

In contrast to findings in early works conducted using Fe-based BMGs [45, 57], research on a $Zr_{52.5}Cu_{17.9}Ni_{14.6}Al_{10}Ti_5$ glassy alloy revealed that E not only influences densification but also plays a role in vitrification [189]. Higher E facilitates densification, but when E exceeds 15 J/mm³, the increased heat input tends to promote crystallization in the microstructure. It was also shown that at the same E , bulk density varies with different P . Consequently, while E is commonly utilized as a parameter, it alone is not enough to fully characterize the final properties of a LAM-processed component. The laser power itself impacts densification for a specified E , as highlighted in research on crystalline Al-Si alloys by Eckert's team [194].

Pauly *et al.* [189] propose that an elevated E causes the overheating of the molten material, lowering in the cooling rate and hence, promoting partial crystallization. Indeed, a certain level of superheat was observed to impede vitrification, potentially due to a decrease in the actual cooling rate or an increase in the dissolved oxygen

Chapter 2 – Theoretical Background

concentration in the molten alloy, thereby diminishing GFA itself [195]. Notably, crystallization takes place non-uniformly, with samples containing fully amorphous pockets encircled with regions that are partially crystalline [189]. A similar non-uniform crystallization phenomenon was also reported in Zr-Ti-Cu-Ni-Al and Zr-Cu-Ni-Al amorphous alloys. Current views suggest that a sample produced using LPBF consists of two distinct regions: melt-pool zone and heat-affected zone (HAZ) [182, 183, 196-199]. As explained in detail in Chapter 4, the cooling rate in the melt-pools is sufficiently high to enable vitrification, whereas the HAZ exhibit partial crystallinity, stemming from the reheating of the pre-existing amorphous phase when the laser beam scans an adjacent area on the powder bed [197, 198].

Intriguingly, not all amorphous alloys undergo crystallization in the HAZ, and fully glassy alloys have been successfully fabricated through LPBF, as seen in Fe-based [200], Zr-based [201, 202], and Ti-based [185] alloys. This raises the issue about which factors control the microstructural development during the LPBF process. It can be answered with the heating cycles and its relationship to the Time-Temperature-Transformation (TTT) diagram for the supercooled liquid. Figure 2.11 illustrates a schematic TTT diagram having three overlaid curves. Curve A, corresponding to the critical cooling rate (R_c), symbolizes the solidification process in the melt-pool zone, occurring rapidly enough to prevent crystallization. Curve B represents a reheating cycle in the HAZ, where the pre-existing amorphous phase does not intersect the TTT curves, thereby suppressing crystallization in the HAZ. Lastly, curve C shows a heating cycle crossing the TTT curve, resulting in a partially crystalline HAZ [203].

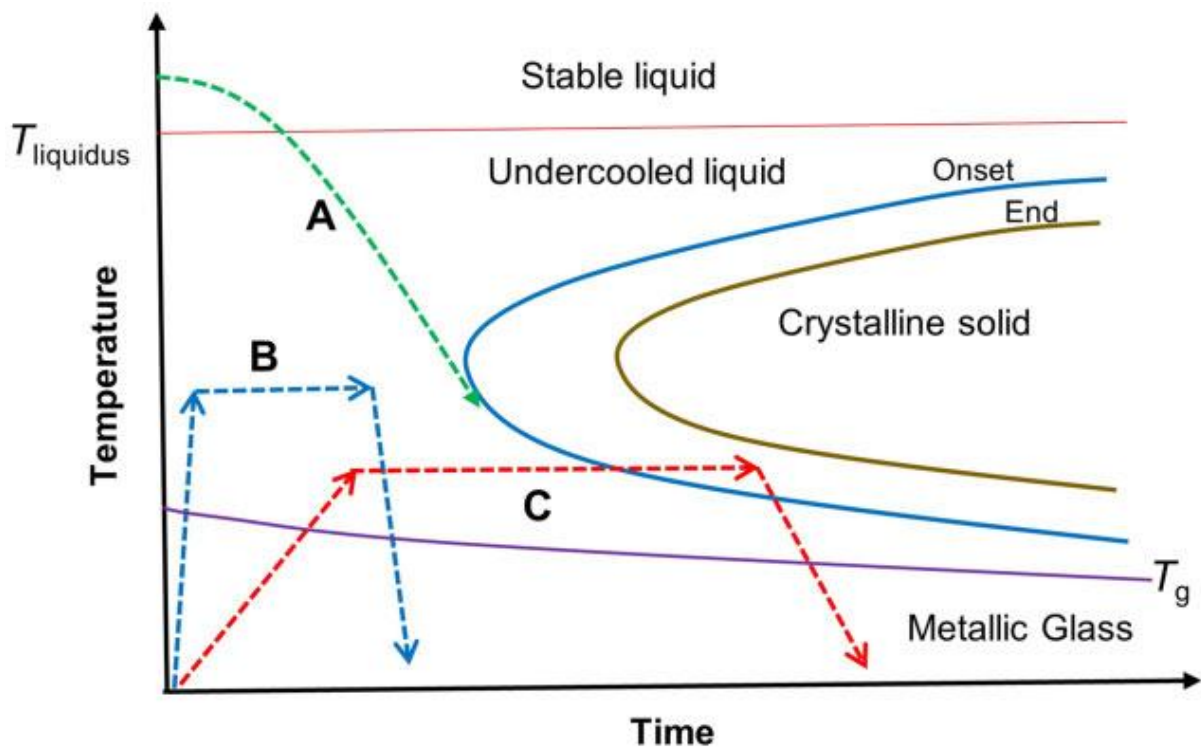


Figure 2.11: An illustrative Time-Temperature-Transformation (TTT) diagram detailing the crystallization process of a BMG [203].

Another factor that can decrease thermal stability during reheating, even in an alloy possessing high GFA, is the separation of the supercooled liquid into two unstable amorphous phases, each with compositions less resistant to crystallization [204].

Additionally, it is well-established that oxygen contamination significantly decreases the GFA of Ti-, Zr- and Hf-based BMGs [59, 60, 193]. Oxygen exerts this effect by lowering the thermal stability of Zr-based BMGs through forming phases including the 'big-cube phase,' which develops with a low nucleation barrier [205]. As reported in Reference [193], the starting powders used in LAM tend to react with oxygen during the production process. As a result, the produced BMGs may contain a higher oxygen content than the feedstock powders, making the HAZs in processed BMGs more prone to crystallization. The impact of oxygen content is likely dependent on the reactivity of the glassy alloy; for instance, Zr-based BMGs exhibit greater susceptibility compared to Fe-based amorphous alloys [68]. This discrepancy could elucidate the presence of crystalline HAZs in Zr-based BMGs [189] beyond a critical value of E , while Fe-based amorphous alloys can remain entirely amorphous across the wide range of E values applied [206]. Yavari *et al.* [207] have demonstrated that the development of equilibrium phases during devitrification can be preceded by the formation of readily nucleating metastable crystalline phases. This might not occur during the rapid quenching process, which implies that low-temperature metastable

phases with a minimal nucleation barrier might make a leftward shift in the TTT curve, causing the formation of a crystalline HAZ in LAM-processed BMGs.

2.5 Future Trends and Challenges

In general, defects (cracks and pores), impurities such as oxides, and residual stresses present in the microstructure hinders the rotation of magnetic domains, leading to a reduction the saturation magnetization (M_s) and an increase in coercivity (H_c) of Fe- and Co-based amorphous alloys [38]. Both the Curie temperature (T_c) and M_s of a glassy alloy depend on the chemical composition and the number of Bohr magnetons in the parts. The development of structural defects resulting from AM processes like microcracks and micropores serves to not only restrict the rotation and movement of magnetic domain walls but also lowers the number of Bohr magnetons per unit volume. This brings about a decline in magnetostriction, introducing stress-induced magnetic anisotropy and consequently decreasing M_s and increasing H_c [206].

Although certain soft magnetic amorphous/nanocrystalline alloys, including the commercially available FeSiBCuNb alloys (FINEMET™), demonstrate excellent soft magnetic behaviour, either amorphous or nanocrystalline alloys produced through additive manufacturing are not yet commercially available, as they are still on the research level [141]. Substantial crystallization and the segregation of alloying elements in AM pose significant challenges in producing BMGs using conventional alloying systems currently available, particularly those exhibiting low glass-forming ability (GFA) [140, 141]. Zrodowski *et al.* [208] succeeded to achieve 89.6% amorphous content of LPBF-processed FeSiBCrC alloy with low GFA by using a novel scanning strategy. Also, relatively low coercivity (238 A/m) was obtained after employing stress-relief annealing to the as-printed samples, despite the low bulk density (94%). Most recently, a “record-large” amorphous rotor with a complex 3D geometry was successfully manufactured via LPBF process by using the same alloy system (FeSiBCrC) [209]. It possesses good magnetic properties (M_s : 1.29 T, H_c : 510 A/m, magnetic susceptibility: 9.17) as well as high hardness (877 HV) and electrical resistivity (178.2 $\mu\Omega$.cm). In addition, the amorphization degree was moderate (70%). Therefore, LAM holds great promise as a future technology for producing large-scale amorphous soft-magnetic components.

Figure 2.12 outlines key aspects of the AM process for BMGs. Their thermal stability and glass transition temperature are notably influenced by both chemical composition and impurities. It is crucial to control impurities to ensure adherence to the desired composition. Careful consideration and optimization of process parameters are essential to achieve the necessary critical cooling rate, preventing crystallization and

facilitating the formation of an amorphous structure. In general, decreasing the energy density in the LPBF process for amorphous alloys can minimize the risk of heat accumulation and enhance the cooling rate to prevent crystallization. Currently, the majority of the research and development on LAM of BMGs is concentrated on Zr-based metallic glasses due to their high Glass-Forming Ability (GFA) and intrinsic ductility, which tends to tolerate any residual thermal stresses resulting from the process. Nevertheless, most of the BMGs produced through LAM commonly experience challenges such as microcracking and partial crystallization in the HAZ. Employing a pulsed laser source instead of a continuous one or increasing the duration between fusing the deposited layer and the subsequent layer is an effective strategy for elevating the cooling rate, thereby suppressing crystallization. It is important to note, however, that this strategy is applicable only to alloys with high GFA and thermal stability and they generally contain costly elements such as B and Zr [210].

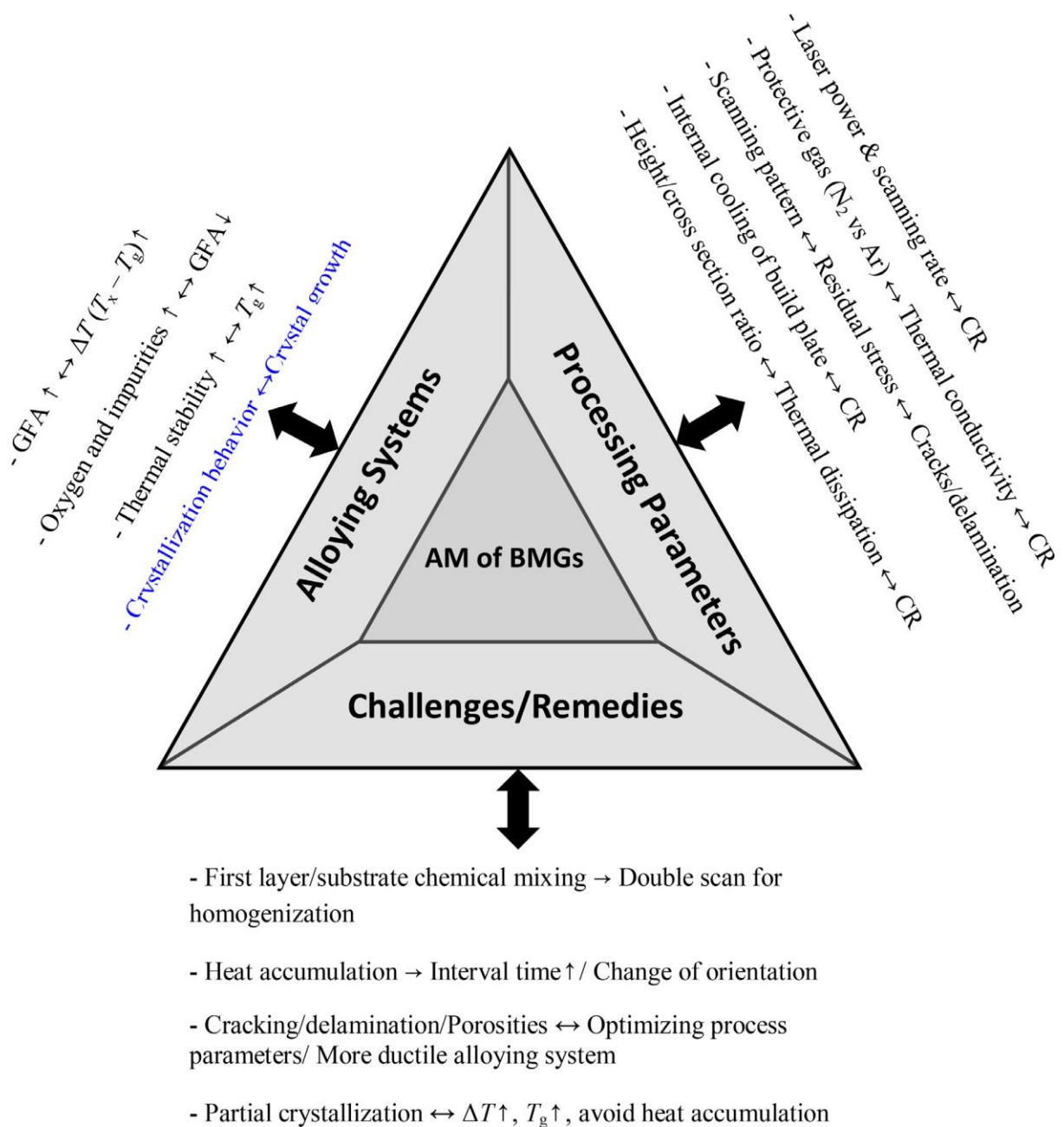


Figure 2.12: Key aspects of LAM for BMGs (CR: cooling rate, GFA: glass forming ability, T_x : crystallization temperature and T_g : glass transition temperature) [210].

References

- [1] D. Jiles, *Introduction to Magnetism and Magnetic Materials*, Boca Raton: Chapman & Hall/CRC Press, 2016.
- [2] S. McGrayne, B. Bleaney, E. Suckling, E. Kashy and F. Robinsin, *Magnetism*, United Kingdom: Encyclopedia Britannica, 2016.
- [3] E. Purcell, *Electricity and Magnetism*, New York: McGraw-Hill, 1963.
- [4] S. Prasad and S. Piramanayagam, "Fundamentals of Magnetism," in *Developments in Data Storage: Materials Perspective*, Singapore, John Wiley & Sons, Inc, 2012, pp. 10-32.
- [5] J. Suits, "The Fundamentals of Magnetism," in *Magnetic Disk Drive Technology: Heads, Media, Channel, Interfaces, and Integration*, New Jersey, Wiley-IEEE Press, 1997, pp. 13-41.
- [6] Q. Aldulaim, *Magnetic and Mechanical Properties of Magnetostrictive FeGaSiB Films*, Sheffield: PhD Thesis, University of Sheffield, 2018.
- [7] N. Spaldin, "Review of basic magnetostatics," in *Magnetic Materials: Fundamentals and Device Applications*, Cambridge, Cambridge University Press, 2003, pp. 1-10.
- [8] B. Cullity and C. Graham, "Definitions and Units," in *Introduction to Magnetic Materials*, Hoboken, New Jersey, Wiley-IEEE Press, 2009, pp. 1-21.
- [9] R. O'Handley, "Introduction and Overview," in *Modern Magnetic Materials: Principles and Applications*, New York, John Wiley & Sons, Inc, 2000, pp. 1-28.
- [10] D. Jiles, "Magnetization and Magnetic Moment," in *Introduction to Magnetism and Magnetic Materials*, Boca Rotan, CRC Press, Taylor & Francis Group, 2016, pp. 31-58.
- [11] E. Torre, "Physics of Magnetism," in *Magnetic Hysteresis*, Piscataway, New Jersey, Wiley-IEEE Press, 1999, pp. 1-30.
- [12] A. Morrish, "The Magnetic Field," in *The Physical Principles of Magnetism*, Piscataway, New Jersey, Wiley-IEEE Press, 2001, pp. 1-30.

Chapter 2 – Theoretical Background

- [13] J. Coey, "Introduction," in *Magnetism and Magnetic Materials*, Cambridge, Cambridge University Press, 2010, pp. 1-23.
- [14] J. Coey, "Magnetostatics," in *Magnetism and Magnetic Materials*, Cambridge, Cambridge University Press, 2010, pp. 24-61.
- [15] N. Spaldin, "Magnetization and Magnetic Materials," in *Magnetic Materials: Fundamentals and Device Applications*, Cambridge, Cambridge University Press, 2003, pp. 11-17.
- [16] S. Zurek, *Characterization of Soft Magnetic Materials under Rotational Magnetisation*, Boca Raton: CRC Press, Taylor and Francis Group, 2017.
- [17] G. Ouyang, X. Chen, Y. Liang, C. Macziewski and J. Cui, "Review of Fe-6.5 wt%Si high silicon steel—A promising soft magnetic material for sub-kHz application," *Journal of Magnetism and Magnetic Materials*, vol. 481, pp. 234-250, 2019.
- [18] T. Zhang and J. Tian, *Soft Magnetic Materials*, Zurich: Trans Tech Publications Ltd, 2011.
- [19] Institute of Physics, *Soft magnetic materials used in industry*, London: Institute of Physics, 1953.
- [20] J. Coey, "Perspective and Prospects for Rare Earth Permanent Magnets," *Engineering*, vol. 6, no. 2, pp. 119-131, 2020.
- [21] J. Coey, "Hard Magnetic Materials: A perspective," *Advances in Magnetism*, vol. 47, no. 12, pp. 4671-4681, 2011.
- [22] J. Mohapatra, X. Liu, P. Joshi and J. Liu, "Hard and semi-hard Fe-based magnetic materials," *Journal of alloys and Compounds*, vol. 955, p. 170258, 2023.
- [23] N. Spaldin, "Ferromagnetic domains," in *Magnetic Materials: Fundamentals and Device Applications*, Cambridge, Cambridge University Press, 2003, pp. 73-88.
- [24] R. O'Handley, "Magnetostatics," in *Modern Magnetic Materials: Principles and Applications*, New York, John and Wiley Sons, Inc., 2000, pp. 29-64.
- [25] D. Jiles, "Magnetic Domains," in *Introduction to Magnetism and Magnetic Materials*, Boca Raton, CRC Press, 2016, pp. 131-154.

Chapter 2 – Theoretical Background

- [26] B. Cullity and C. Graham, "Magnetic Anisotropy," in *Introduction to Magnetic Materials*, Piscataway, New Jersey, Wiley-IEEE, 2009, pp. 197-239.
- [27] D. Jiles, "Domain Walls," in *Introduction to Magnetism and Magnetic Materials*, Boca Raton, CRC Press, Taylor and Francis Group, 2016, pp. 155-174.
- [28] N. Spaldin, "Atomic origins of magnetism," in *Magnetic Materials: Fundamentals and Device Applications*, Cambridge, Cambridge University Press, 2003, pp. 18-34.
- [29] D. Garcia-Gonzalez and M. Hossain, "Microstructural modelling of hard-magnetic soft materials: Dipole–dipole interactions versus Zeeman effect," *Extreme Mechanics Letters*, vol. 48, p. 101382, 2021.
- [30] D. Jiles, "Electronic Magnetic Moments," in *Introduction to Magnetism and Magnetic Materials*, Boca Raton, CRC Press, Taylor & Francis Group, 2016, pp. 259-286.
- [31] R. O'Handley, "Magnetism in Small Structures: Exchange Coupling and nanocrystals," in *Modern Magnetic Materials: Principles and Applications*, New York, A Wiley-Interscience Publication, 2000, pp. 432-468.
- [32] J. Coey, "Nanoscale Magnetism," in *Magnetism and Magnetic Materials*, Cambridge, Cambridge University Press, 2010, pp. 264-304.
- [33] T. Bitoh, A. Makino, A. Inoue and T. Masumoto, "Random Anisotropy Model for Nanocrystalline Soft Magnetic Alloys with Grain-Size Distribution," *Materials Transactions*, vol. 44, no. 10, pp. 2011-2019, 2003.
- [34] G. Herzer, "On the theoretical understanding of nanocrystalline soft magnetic materials," *Journal of Materials Engineering and Performance*, vol. 2, pp. 193-197, 1993.
- [35] G. Herzer, "Grain structure and magnetism of nanocrystalline ferromagnets," *IEEE Transactions on Magnetics*, vol. 25, no. 5, pp. 3327-3329, 1989.
- [36] G. Herzer, "Nanocrystalline soft magnetic materials," *Physica Scripta*, vol. T49, pp. 307-314, 1993.
- [37] G. Herzer, "Soft Magnetic Nanocrystalline Materials," *Scripta Metallurgica et Materialia*, vol. 33, no. 10/11, pp. 1741-1756, 1995.

- [38] G. Herzer, "Modern soft magnets: Amorphous and nanocrystalline materials," *Acta Materialia*, vol. 61, pp. 718-734, 2013.
- [39] R. Alben, J. Becker and M. Chi, "Random anisotropy in amorphous ferromagnets," *Journal of Applied Physics*, vol. 49, pp. 1653-1658, 1978.
- [40] G. Herzer, "Grain size dependence of coercivity and permeability in nanocrystalline ferromagnets," *IEEE Transactions on Magnetics*, vol. 26, no. 5, pp. 1397-1402, 1990.
- [41] G. Herzer, "Magnetization process in nanocrystalline ferromagnets," *Materials Science and Engineering*, vol. A133, pp. 1-5, 1991.
- [42] G. Herzer, "Nanocrystalline soft magnetic materials," *Journal of Magnetism and Magnetic Materials*, vol. 112, pp. 258-262, 1992.
- [43] R. Schafer, A. Hubert and G. Herzer, "Domain observation on nanocrystalline material," *Journal of Applied Physics*, vol. 69, pp. 5325-5327, 1991.
- [44] G. Herzer, "Anisotropies in soft magnetic nanocrystalline alloys," *Journal of Magnetism and Magnetic Materials*, vol. 294, pp. 99-106, 2005.
- [45] G. Herzer, "Soft Magnetic Nanocrystalline Materials," *Scripta Metallurgica et Materialia*, vol. 33, no. 10/11, pp. 1741-1756, 1995.
- [46] Q. Yu, X. Wang, H. Lou, Q. Cao and J. Jiang, "Atomic packing in Fe-based metallic glasses," *Acta Mater.*, vol. 102, pp. 116-124, 2016.
- [47] P. Duwez and S. Lin, "Amorphous ferromagnetic phase in iron-carbon-phosphorus alloys," *J. Appl. Phys.*, vol. 38, no. 10, pp. 4096-4097, 1967.
- [48] J. Dai, Y. Wang, L. Yang, G. Xia, Q. Zeng and H. Lou, "Structural aspects of magnetic softening in Fe-based metallic glass during annealing," *Scr. Mater.*, vol. 127, pp. 88-91, 2017.
- [49] J. Wang, Y. Liu, M. Chen, G. Xie, D. Louzguine-Luzgin, A. Inoue and J. Perepezko, "Rapid degradation of azo dye by Fe-based metallic glass powder," *Adv. Funct. Mater.*, vol. 22, no. 12, pp. 2567-2570, 2012.

Chapter 2 – Theoretical Background

- [50] S. Pang, T. Zhang, K. Asami and A. Inoue, "Synthesis of Fe-Cr-Mo-C-B-P bulk metallic glasses with high corrosion resistance," *Acta Mater.*, vol. 50, no. 3, pp. 489-497, 2002.
- [51] W. Yang, H. Liu, Y. Zhao, A. Inoue, K. Jiang, J. Huo, H. Ling, Q. Li and B. Shen, "Mechanical properties and structural features of novel Fe-based bulk metallic glasses with unprecedented plasticity," *Sci. Rep.*, vol. 4, p. 6233, 2014.
- [52] J. Gao, Z. Chen, Q. Du, H. Li, Y. Wu, H. Wang, X. Liu and Z. Lu, "Fe-based bulk metallic glass composites without any metalloids elements," *Acta Mater.*, vol. 61, no. 9, pp. 3214-3223, 2013.
- [53] A. Inoue, Y. Shinohara and J. Gook, "Thermal and magnetic properties of bulk Fe-based glassy alloys prepared by copper mould casting," *Mater. Trans. JIM*, vol. 36, no. 12, pp. 1427-1433, 1995.
- [54] Z. Lu, C. Liu, J. Thompson and W. Porter, "Structural amorphous steels," *Phys. Rev. Lett.*, vol. 92, no. 24, p. 245503, 2004.
- [55] S. Zhang, J. Wu, W. Qi and J. Wang, "Effect of porosity defects on the long-term corrosion behaviour of Fe-based amorphous alloy coated mild steel," *Corrosion Sci.*, vol. 110, pp. 57-70, 2016.
- [56] W. Yang, Q. Wang, H. Ling, H. Liu, L. Xue, Y. He, Q. Li and B. Shen, "Oxygen-driven impurities scavenging before solidification of Fe-based metallic glasses," *Journal of Alloys and Compounds*, vol. 773, pp. 401-412, 2019.
- [57] M. Fujikura, H. Sawari and T. Sato, "Influence of Sn addition on the magnetic properties of amorphous Fe-Si-B alloys containing Ti," *J. Magn. Magn. Mater.*, vol. 1996, no. 160, pp. 289-290, 1996.
- [58] H. Li, J. Gao, S. Wang, S. Yi and Z. Lu, "Formation, crystallization behaviour, and soft magnetic properties of FeCSiBP bulk metallic glass fabricated using industrial raw materials," *Metall. Mater. Trans. A*, vol. 43, no. 8, pp. 2615-2619, 2011.
- [59] X. Lin, W. Johnson and W. Rhim, "Effect of oxygen impurity on crystallization of an undercooled bulk glass forming Zr-Ti-Cu-Ni-Al alloy," *Mater. Trans. JIM*, vol. 38, no. 5, pp. 473-477, 1997.

Chapter 2 – Theoretical Background

- [60] B. Murty, D. Ping, K. Hono and A. Inoue, "Influence of oxygen on the crystallization behaviour of Zr₆₅Cu_{27.5}Al_{7.5} and Zr_{66.7}Cu_{33.3} metallic glasses," *Acta Mater.*, vol. 48, no. 15, pp. 3985-3996, 2000.
- [61] J. Cheng, G. Chen, C. Liu and Y. Li, "Innovative approach to the design of low-cost Zr-based BMG composites with good glass formation," *Sci. Rep.*, vol. 3, p. 2097, 2013.
- [62] C. Liu, M. Chisholm and M. Miller, "Oxygen impurity and microalloying effect in a Zr-based bulk metallic glass alloy," *Intermetallics*, vol. 10, no. 11, pp. 1105-1112, 2002.
- [63] R. Conner, R. Maire and W. Johnson, "Effect of oxygen concentration upon the ductility of amorphous Zr₅₇Nb₅Al₁₀Cu_{15.4}Ni_{12.6}," *Mater. Sci. Eng. A*, vol. 419, no. 1-2, pp. 148-152, 2006.
- [64] A. Gebert, J. Eckert and L. Schultz, "Effect of oxygen on phase formation and thermal stability of slowly cooled Zr₆₅Al_{7.5}Cu_{17.5}Ni₁₀ metallic glass," *Acta Mater.*, vol. 46, no. 15, pp. 5475-5482, 1998.
- [65] D. Sordélet, X. Yang, E. Rozhkova, M. Besser and M. Kramer, "Oxygen-stabilized glass formation in Zr₈₀Pt₂₀ melt-spun ribbons," *Appl. Phys. Lett.*, vol. 83, no. 1, p. 69, 2003.
- [66] H. Li, J. Gao, Z. Jiao, Y. Wu and Z. Lu, "Glass-forming ability enhanced by proper additions of oxygen in a Fe-based bulk metallic glass," *Appl. Phys. Lett.*, vol. 95, no. 16, p. 161905, 2009.
- [67] Y. Wang, H. Yang, G. Lim and Y. Li, "Glass formation enhanced by oxygen in binary Zr-Cu system," *Scr. Mater.*, vol. 62, no. 9, pp. 682-685, 2010.
- [68] C. Chang, J. Zhang, B. Shen, W. Wang and A. Inoue, "Pronounced enhancement of glass-forming ability of Fe-Si-B-P bulk metallic glass in oxygen atmosphere," *J. Mater. Res.*, vol. 29, no. 10, pp. 1217-1222, 2014.
- [69] J. Pan, Q. Chen, N. Li and L. Liu, "Formation of centimetre Fe-based bulk metallic glasses in low vacuum environment," *J. Alloys Compd.*, vol. 463, no. 1-2, pp. 246-249, 2008.

Chapter 2 – Theoretical Background

- [70] V. Ponnambalam, S. Poon and G. Shiflet, "Fe-Mn-Cr-Mo-(Y,Ln)-C-B (Ln = Lanthanides) bulk metallic glasses as formable amorphous steel alloys," *J. Mater. Res.*, vol. 19, no. 10, pp. 3046-3052, 2011.
- [71] Z. Lu, C. Liu and W. Porter, "Role of yttrium in glass formation of Fe-based bulk metallic glasses," *Appl. Phys. Lett.*, vol. 83, no. 13, p. 2581, 2003.
- [72] Y. Liu, S. Niu, F. Li, Y. Zhu and Y. He, "Preparation of amorphous Fe-based magnetic powder by water atomization," *Powder Technology*, vol. 213, pp. 36-40, 2011.
- [73] T. Bitoh, A. Makino, A. Inoue and A. Greer, "Large bulk soft magnetic ((Fe_{0.5}Co_{0.5})_{0.75}B_{0.20}Si_{0.05})₉₆Nb₄ glassy alloy prepared by B₂O₃ flux melting and water quenching," *Appl. Phys. Lett.*, vol. 88, p. 182510, 2006.
- [74] T. Bitoh and D. Shibata, "Constant permeability of (Fe_{0.75}B_{0.20}Si_{0.05})₉₆Nb₄ bulk metallic glass prepared by B₂O₃ flux melting and Cu-mould casting," *J. Appl. Phys.*, vol. 105, pp. 07A312-313, 2009.
- [75] B. Neamtu, T. Marinca, I. Chicinas, O. Isnard, F. Popa and P. Pascuta, "Preparation and soft magnetic properties of spark plasma sintered compacts based on Fe-Si-B glassy powder," *Journal of Alloys and Compounds*, vol. 600, pp. 1-7, 2014.
- [76] X. Yang, J. Liu, X. Cui, G. Jin, Z. Liu, Y. Chen and X. Feng, "Effect of remelting on microstructure and magnetic properties of Fe-Co-based alloys produced by laser additive manufacturing," *Journal of Physics and Chemistry of Solids*, vol. 130, pp. 210-216, 2019.
- [77] Y. Liu, Y. Yi, W. Shao and Y. Shao, "Microstructure and magnetic properties of soft magnetic powder cores of amorphous and nanocrystalline alloys," *Journal of Magnetism and Magnetic Materials*, vol. 330, pp. 119-133, 2013.
- [78] T. Bitoh, A. Makino and A. Inoue, "Origin of low coercivity of (Fe_{0.75}B_{0.15}Si_{0.10})_{100-x}Nb_x (x = 1-4) glassy alloys," *J. Appl. Phys.*, vol. 99, p. 08F102, 2006.
- [79] J. Pang, A. Wang, S. Yue, F. Kong, K. Qiu, C. Chang, C. Wang and C. Liu, "Fluxing purification and its effect on magnetic properties of high-Bs FeBPSiC

Chapter 2 – Theoretical Background

amorphous alloy,” *Journal of Magnetism and Magnetic Materials*, vol. 433, pp. 35-41, 2017.

- [80] A. Krings, A. Boglietti, A. Cavagnino and S. Sprague, “Soft magnetic material status and trends in electric machines,” *IEEE Trans. Ind. Electron*, vol. 64, no. 3, pp. 2405-2414, 2017.
- [81] J. Lai, A Study of the Fabrication of Thin Lamination Stator Cores by the Uniform Droplet Spray Process, Thesis: Massachusetts Institute of Technology, 1997.
- [82] T. Wakisaka, Y. Kurosaki and S. Arai, “Electrical Steel Sheet for Traction Motor of Hybrid/Electrical Vehicles,” *Nippon Steel Technical Report*, vol. 103, pp. 116-120, 2013.
- [83] T. Lamichhane, L. Sethuraman, A. Dalagan, H. Wang, J. Keller and M. Paranthaman, “Additive manufacturing of soft magnets for electrical machines - a review,” *Materials Today Physics*, vol. 15, p. 100255, 2020.
- [84] A. Andreiev, K. Hoyer, D. Dula, F. Hengsbach, M. Haase, J. Gierse, D. Zimmer, T. Troster and M. Schaper, “Soft-Magnetic Behaviour of Laser Beam Melted FeSi₃ Alloy with Graded Cross-Section,” *J. Mater. Process. Technol.*, vol. 296, p. 117183, 2021.
- [85] M. Quercio, F. Galbusera, E. Poskovic, F. Franchini, L. Ferraris, A. Canova, A. Gruosso, A. Demir and B. Previtali, “Functional Characterization of L-PBF Produced FeSi_{2.9} Soft Magnetic Material,” in *In Proceedings of the 2022 International Conference on Electrical Machines (ICEM)*, Valencia, Spain, 2022.
- [86] A. Selema, M. Beretta, M. Van Coppenolle, H. Tiismus, A. Kallaste, M. Ibrahim, M. Rombouts, J. Vleugels, L. Kestens and P. Sergeant, “Evaluation of 3D-Printed Magnetic Materials for Additively-Manufactured Electrical Machines,” *J. Magn. Mater.*, vol. 569, p. 170426, 2023.
- [87] M. Haines, F. List, K. Carver, D. Leonard, A. Plotkowski, C. Fancher, R. Dehoff and S. Babu, “Role of Scan Strategies and Heat Treatment on Grain Structure Evolution in Fe-Si Soft Magnetic Alloys Made by Laser-Powder Bed Fusion,” *Addit. Manuf.*, vol. 50, p. 102578, 2022.

Chapter 2 – Theoretical Background

- [88] V. Martin, F. Gillon, D. Najjar, A. Benabou, J. Witz, M. Hecquet, P. Quaegebeur, M. Meersdam and D. Auzene, “MIM-like Additive Manufacturing of Fe₃Si Magnetic Materials,” *J. Magn. Magn. Mater.*, vol. 564, p. 170104, 2022.
- [89] H. Tiismus, A. Kallaste, M. Naseer, T. Vaimann and A. Rassolkin, “Design and Performance of Laser Additively Manufactured Core Induction Motor,” *IEEE Access*, vol. 10, p. 50137–50152, 2022.
- [90] G. Kumari, T. Pham, H. Suen, T. Rahman, P. Kwon, S. Foster and C. Boehlert, “Improving the Soft Magnetic Properties of Binder Jet Printed Iron-Silicon Alloy through Boron Addition,” *Mater. Chem. Phys.*, vol. 296, p. 127181, 2023.
- [91] N. Kang, Q. Li, M. El Mansori, B. Yao, F. Ma, X. Lin and H. Liao, “Laser Powder Bed Fusion Processing of Soft Magnetic Fe–Ni–Si Alloys: Effect of Hot Isostatic Pressing Treatment,” *Chin. J. Mech. Eng. Addit. Manuf. Front.*, vol. 1, p. 100054, 2022.
- [92] F. Bernier, M. Ibrahim, M. Mihai, Y. Thomas and J. Lamarre, “Additive manufacturing of soft and hard magnetic materials used in electrical machines,” *Metal Powder Report*, vol. 75, no. 6, pp. 334-343, 2020.
- [93] S. Gao, H. Liao, X. Yan, Q. Xie, C. Chang, B. Lu, X. Zhang, N. Fenineche and M. Liu, “Magnetic and mechanical properties of additive manufactured Fe-3wt.% Si material,” *Journal of Magnetism and Magnetic Materials*, vol. 580, p. 170907, 2023.
- [94] X. Shen, F. Meng, K. Lau, P. Wang and C. Lee, “Texture and microstructure characterizations of Fe-3.5wt%Si soft magnetic alloy fabricated via laser powder bed fusion,” *Materials Characterization*, vol. 189, p. 112012, 2022.
- [95] K. Sun, F. Li, C. Rong and L. Zuo, “Direct energy deposition applied to soft magnetic material additive manufacturing,” *Journal of Manufacturing Processes*, vol. 84, pp. 162-173, 2022.
- [96] H. Tiismus, A. Kallaste, A. Rassolkin and T. Vaimann, “Preliminary analysis of soft magnetic material properties fro additive manufacturing of electrical machines,” *Key Engineering Materials*, vol. 799, pp. 270-275, 2019.
- [97] S. Gao, X. Yan, C. Chang, E. Aubry, M. Liu, H. Liao and N. Fenineche, “Effect of laser energy density on surface morphology, microstructure, magnetic

Chapter 2 – Theoretical Background

- properties of selective laser melted Fe-3wt.% Si alloys,” *Journal of Materials Engineering and Performance*, vol. 30, p. 5020–5030, 2021.
- [98] M. Garibaldi, I. Ashcroft, J. Lemke, M. Simonelli and R. Hague, “Metallurgy of High-Silicon Steel Parts Produced Using Selective Laser Melting,” *Acta Mater.*, vol. 110, pp. 207-216, 2016.
- [99] M. Garibaldi, I. Ashcroft, N. Hillier, S. Harmon and R. Hague, “Relationship between Laser Energy Input, Microstructures and Magnetic Properties of Selective Laser Melted Fe-6.9%wt Si Soft Magnets,” *Mater. Charact.*, vol. 143, pp. 144-151, 2018.
- [100] M. Garibaldi, I. Ashcroft, J. Lemke, M. Simonelli and R. Hague, “Effect of Annealing on the Microstructure and Magnetic Properties of Soft Magnetic Fe-Si Produced via Laser Additive Manufacturing,” *Scr. Mater.*, vol. 142, pp. 121-125, 2018.
- [101] M. Zaied, A. Ospina-Vargas, N. Buiron, J. Favergeon and N. Fenineche, “Additive Manufacturing of Soft Ferromagnetic Fe 6.5%Si Annular Cores: Process Parameters, Microstructure, and Magnetic Properties,” *IEEE Trans. Magn.*, vol. 58, p. 2001420, 2022.
- [102] D. Schino and G. Stornelli, “Additive Manufacturing: A New Concept for End Users. The Case of Magnetic Materials,” *Acta Metall. Slovaca*, vol. 28, pp. 208-211, 2022.
- [103] A. Faba, F. Riganti Fulginei, S. Quondam Antonio, G. Stornelli, A. Di Schino and E. Cardelli, “Hysteresis Modelling in Additively Manufactured FeSi Magnetic Components for Electrical Machines and Drives,” *IEEE Transactions on Industrial Electronics*, vol. 71, no. 3, pp. 2188-2197, 2023.
- [104] G. Stornelli, A. Faba, A. Di Schino, P. Folgarait, M. Ridolfi, E. Cardelli and R. Montanari, “Properties of Additively Manufactured Electric Steel Powder Cores with Increased Si Content,” *Materials*, vol. 14, no. 6, p. 1489, 2021.
- [105] G. Stornelli, M. Ridolfi, P. Folgarait, J. De Nisi, D. Corapi, C. Repitsch and A. Di Schino, “Feasibility Assessment of Magnetic Cores through Additive Manufacturing Techniques,” *Metall. Ital.*, vol. 113, pp. 50-63, 2021.

Chapter 2 – Theoretical Background

- [106] N. Seiler, D. Kolb, J. Schanz, D. Goll and H. Riegel, "Influence of Modulated Laser Power on the Surface Topography and Microstructure in the Laser Powder Bed Fusion Process," *Procedia CIRP*, vol. 111, pp. 693-696, 2022.
- [107] A. Agapovichev, A. Khaimovich, Y. Erisov and M. Ryazanov, "Investigation of Soft Magnetic Material Fe-6.5Si Fracture Obtained by Additive Manufacturing," *Materials*, vol. 15, p. 8915, 2022.
- [108] D. Goll, D. Schuller, G. Martinek, T. Kunert, J. Schurr, C. Sinz, T. Schubert, T. Bernthaler, H. Riegel and G. Scheider, "Additive Manufacturing of Soft Magnetic Materials and Components," *Additive Manufacturing*, vol. 27, pp. 428-439, 2019.
- [109] J. Yang, Z. Fu, J. Ye, D. Kubrich and C. Korner, "Electron beam-based additive manufacturing of Fe_{93.5}Si_{6.5} (wt.%) soft magnetic material with controllable magnetic performance," *Scripta Materialia*, vol. 210, p. 114460, 2022.
- [110] C. Cramer, P. Nandwana, J. Yan, S. Evans, A. Elliott, C. Chinnasamy and M. Paranthaman, "Binder jet additive manufacturing method to fabricate near net shape crack-free highly dense Fe-6.5 wt.% Si soft magnets," *Heliyon*, vol. 5, p. e02804, 2019.
- [111] J. Yang, Z. Fu and C. Korner, "Structure design of soft magnetic materials using electron beam based additive manufacturing," *Advanced Materials*, vol. 35, p. 2300837, 2023.
- [112] V. Chaudhary, N. Sai Kiran Kumar Yadav, S. Mantri, S. Dasari, A. Jagetia, R. Ramanujan and R. Banerjee, "Additive Manufacturing of Functionally Graded Co-Fe and Ni-Fe Magnetic Materials," *J. Alloys Compd.*, vol. 823, p. 153817, 2020.
- [113] V. Chaudhary, T. Borkar, C. Mikler, B. Gwalani, D. Choudhuri, V. Soni, T. Alam, R. Ramanujan and R. Banerjee, "Additively Manufactured Functionally Graded FeNi Based High Entropy Magnetic Alloys," in *In Proceedings of the 2018 IEEE International*, Singapore, 2018.
- [114] M. Yi, B. Xu and O. Gutfleisch, "Computational Study on Microstructure Evolution and Magnetic Property of Laser Additively Manufactured Magnetic Materials," *Comput. Mech.*, vol. 64, pp. 917-935, 2019.

Chapter 2 – Theoretical Background

- [115] C. Mikler, V. Chaudhary, T. Borkar, V. Soni, D. Choudhuri, R. Ramanujan and R. Banerjee, "Laser Additive Processing of Ni-Fe-V and Ni-Fe-Mo Permalloys: Microstructure and Magnetic Properties," *Mater. Lett.*, vol. 192, pp. 9-11, 2017.
- [116] C. Mikler, V. Chaudhary, T. Borkar, V. Soni, D. Jaeger, X. Chen, R. Contieri, R. Ramanujan and R. Banerjee, "Laser Additive Manufacturing of Magnetic Materials," *JOM*, vol. 69, pp. 532-543, 2017.
- [117] V. Chaudhary, S. Mantri, R. Ramanujan and R. Banerjee, "Additive Manufacturing of Magnetic Materials," *Prog. Mater. Sci.*, vol. 114, p. 100688, 2020.
- [118] J. Yang, Q. Zhu, Z. Wang, F. Xiong, Q. Li, F. Yang, R. Li, X. Ge and M. Wang, "Effects of Metallurgical Defects on Magnetic Properties of SLM NiFeMo Permalloy," *Mater. Charact.*, vol. 197, p. 112672, 2023.
- [119] B. Li, W. Zhang, W. Fu and F. Xuan, "Laser Powder Bed Fusion (L-PBF) 3D Printing Thin Overhang Walls of Permalloy for a Modified Honeycomb Magnetic-Shield Structure," *Thin-Walled Struct.*, vol. 182, p. 110185, 2023.
- [120] E. Kim, F. Haftlang, S. Ahn, H. Kwon, G. Gu and H. Kim, "Mechanical and Magnetic Properties of Soft Magnetic Fe–Ni Permalloy Produced by Directed Energy Deposition Processes," *J. Mater. Sci.*, vol. 57, pp. 17967-17983, 2022.
- [121] E. Kim, F. Haftlang, S. Ahn, G. Gu and H. Kim, "Effects of Processing Parameters and Heat Treatment on the Microstructure and Magnetic Properties of the In-Situ Synthesized Fe-Ni Permalloy Produced Using Direct Energy Deposition," *J. Alloys Compd.*, vol. 907, p. 164415, 2022.
- [122] F. Haftlang, E. Kim and H. Kim, "Crystallographic-Orientation-Dependent Magnetic Properties of Fe–Ni Permalloy in-Situ Alloyed Using Additive Manufacturing," *J. Mater. Process. Technol.*, vol. 309, p. 117733, 2022.
- [123] A. Mohamed, J. Zou, R. Sheridan, K. Bongs and M. Attallah, "Magnetic Shielding Promotion via the Control of Magnetic Anisotropy and Thermal Post Processing in Laser Powder Bed Fusion Processed NiFeMo-Based Soft Magnet," *Additive Manufacturing*, vol. 32, p. 101079, 2020.
- [124] C. Mikler, V. Chaudhary, V. Soni, B. Gwalani, R. Ramanujan and R. Banerjee, "Tuning the phase stability and magnetic properties of laser additively

processed Fe-30at%Ni soft magnetic alloys,” *Materials Letters*, vol. 199, pp. 88-92, 2017.

- [125] B. Li, W. Fu, H. Xu, B. Qian and F. Xuan, “Additively manufactured Ni-15Fe-5Mo permalloy via selective laser melting and subsequent annealing for magnetic-shielding structures: Process, microstructural and soft-magnetic characteristics,” *Journal of Magnetism and Magnetic Materials*, vol. 494, p. 165754, 2020.
- [126] S. Firdosy, N. Ury, K. Dang, P. Narvaez, R. Dillon and V. Ravi, “Additively manufactured high permeability Fe-Ni alloys and novel bi-metallic magnetic shields,” *Journal of Magnetism and Magnetic Materials*, vol. 584, p. 171049, 2023.
- [127] C. Ding, L. Liu, Y. Mei, K. Ngo and G. Lu, “Magnetic paste as feedstock for additive manufacturing of power magnetics,” in *2018 IEEE Applied Power Electronics Conference and Exposition (APEC)*, San Antonio, TX, USA, 2018.
- [128] Y. Arbaoui, P. Agaciak, A. Chevalier, V. Laur, A. Maalouf, J. Ville, P. Roquefort, T. Aubry and P. Queffelec, “3D printed ferromagnetic composites for microwave applications,” *Journal of Materials Science*, vol. 52, pp. 4988-4996, 2017.
- [129] Y. Yan, J. Moss, K. Ngo, Y. Mei and G. Lu, “Additive Manufacturing of Toroid Inductor for Power Electronics Applications,” *IEEE Transactions on Industry Applications*, vol. 53, no. 6, pp. 5709-5714, 2017.
- [130] Y. Yan, K. Ngo, Y. Mei and G. Lu, “Additive Manufacturing of Magnetic Components for Power Electronics Integration,” in *2016 International Conference on Electronics Packaging (ICEP)*, Hokkaido, Japan, 2016.
- [131] A. Kustas, D. Susan, K. Johnson, S. Whetten, M. Rodriguez, D. Dagele, J. Micheal, D. Keicher and N. Argibay, “Characterization of the Fe-Co-1.5V Soft Ferromagnetic Alloy Processed by Laser Engineered Net Shaping (LENS),” *Addit. Manuf.*, vol. 21, pp. 41-52, 2018.
- [132] R. Sundar and S. Deevi, “Soft Magnetic FeCo Alloys: Alloy Development, Processing, and Properties,” *Int. Mater. Rev.*, vol. 50, pp. 157-192, 2005.

- [133] G. Sreenivasulu, U. Laletin, V. Petrov, V. Petrov and G. Srinivasan, "A Permendur-Piezoelectric Multiferroic Composite for Low-Noise Ultrasensitive Magnetic Field Sensors," *Appl. Phys. Lett.*, vol. 100, p. 173506, 2012.
- [134] T. Lindroos, T. Riipinen, S. Metsa-Kortelainen, J. Pippuri-Makelainen and A. Manninen, "Lessons Learnt—Additive Manufacturing of Iron Cobalt Based Soft Magnetic Materials," *J. Magn. Magn. Mater.*, vol. 563, p. 169977, 2022.
- [135] T. Riipinen, J. Pippuri-Makelainen, Z. Que, S. Metsa-Kortelainen, A. Antikainen and T. Lindroos, "The Effect of Heat Treatment on Structure and Magnetic Properties of Additively Manufactured Fe-Co-V Alloys," *Mater. Today Commun.*, vol. 36, p. 106437, 2023.
- [136] M. Nartu, S. Dasari, A. Sharma, V. Chaudhary, S. Varahabhatla, S. MAntri, E. Ivanov, R. Ramanujan, N. Dahotre and R. Banerjee, "Reducing Coercivity by Chemical Ordering in Additively Manufactured Soft Magnetic Fe–Co (Hiperco) Alloys," *J. Alloys Compd.*, vol. 861, p. 157998, 2021.
- [137] A. Kustas, C. Fancher, S. Whetten, D. Dagel, J. Micheal and D. Susan, "Controlling the Extent of Atomic Ordering in Intermetallic Alloys through Additive Manufacturing," *Addit. Manuf.*, vol. 28, pp. 772-780, 2019.
- [138] S. Li, K. Lau, D. Wu, F. Wei, M. Lin, A. Cheong, P. Wang, C. Tan and U. Ramamurty, "3D printing of ductile equiatomic Fe-Co alloy for soft magnetic applications," *Additive Manufacturing*, vol. 47, p. 102291, 2021.
- [139] T. Riipinen, S. Metsa-Kortelainen, T. Lindroos, J. Keranen, A. Manninen and J. Pippuri-Makelainen, "Properties of soft magnetic Fe-Co-V alloy produced by laser powder bed fusion," *Rapid Prototyping Journal*, vol. 25, no. 4, pp. 699-707, 2019.
- [140] T. Borkar, R. Conteri, X. Chen, R. Ramanujan and R. Banerjee, "Laser Additive Processing of Functionally-Graded Fe–Si–B–Cu–Nb Soft Magnetic Materials," *Mater. Manuf. Process.*, vol. 32, pp. 1581-1587, 2017.
- [141] R. Conteri, T. Borkar, S. Nag, D. Jaeger, X. Chen, R. Ramanujan and R. Banerjee, "Laser Additive Processing of Fe-Si-B-Cu-Nb Magnetic Alloys," *J. Manuf. Process.*, vol. 29, pp. 175-181, 2017.

Chapter 2 – Theoretical Background

- [142] L. Bollig, P. Hilpisch, G. Mowry and B. Nelson-Cheeseman, “3D printed magnetic polymer composite transformers,” *Journal of Magnetism and Materials*, vol. 442, pp. 97-101, 2017.
- [143] L. Bollig, M. Patton, G. Mowry and B. Nelson-Cheeseman, “Effects of 3-D printed structural characteristics on magnetic properties,” *IEEE Transactions on Magnetics*, vol. 53, no. 11, p. 2300806, 2017.
- [144] B. Khatri, K. Lappe, D. Noetzel, K. Pursche and T. Hanemann, “A 3D-Printable Polymer-Metal Soft-Magnetic Functional Composite—Development and Characterization,” *Materials*, vol. 11, no. 2, p. 189, 2018.
- [145] N. Lowa, J. Fabert, D. Gutkelch, H. Paysen, O. Kosch and F. Wiekhorst, “3D-printing of novel magnetic composites based on magnetic nanoparticles and photopolymers,” *J. Magn. Magn. Mater.*, vol. 469, pp. 456-460, 2019.
- [146] X. Guan, X. Xu, R. Kuniyoshi, H. Zhou and Y. Zhu, “Electromagnetic and mechanical properties of carbonyl iron powders-PLA composites fabricated by fused deposition modeling,” *Materials Research Express*, vol. 5, no. 11, p. 115303, 2018.
- [147] L. Liu, T. Ge, K. Ngo, Y. Mei and G. Lu, “Ferrite Paste Cured with Ultraviolet Light for Additive Manufacturing of Magnetic Components for Power Electronics,” *IEEE Magn. Lett.*, vol. 9, p. 5102705, 2018.
- [148] L. Liu, T. Ge, Y. Yan, K. Ngo and G. Lu, “UV-Assisted 3D-Printing of Soft Ferrite Magnetic Components for Power Electronics Integration,” in *In Proceedings of the 2017 International Conference on Electronics Packaging (ICEP)*, Yamagata, Japan, 2017.
- [149] Y. Wang, F. Castles and P. Grant, “3D Printing of NiZn ferrite/ABS Magnetic Composites for Electromagnetic Devices,” *MRS Online Proceedings Library*, vol. 1788, pp. 29-35, 2015.
- [150] E. Perigo, J. Jacimovic, F. Ferre and L. Scherf, “Additive manufacturing of magnetic materials,” *Additive Manufacturing*, vol. 30, p. 100870, 2019.
- [151] Y. Ouyang, B. Jensen, W. Tang, K. Dennis, C. Macziewski, S. Thimmaiah, Y. Liang and J. Cui, “Effect of wheel speed on magnetic and mechanical properties

Chapter 2 – Theoretical Background

of melt spun Fe-6.5 wt.% Si high silicon steel," *AIP Advances*, vol. 8, p. 056111, 2018.

- [152] Y. Takada, M. Abe, S. Masuda and J. Inagaki, "Commercial scale production of Fe-6.5 wt. % Si sheet and its magnetic properties," *Journal of Applied Physics*, vol. 64, pp. 5367-5369, 1988.
- [153] H. Haji, K. Okada, T. Hiratani, M. Abe and M. Ninomiya, "Magnetic properties and workability of 6.5% Si steel sheet," *Journal of Magnetism and Magnetic Materials*, vol. 160, pp. 109-114, 1996.
- [154] C. Korner, "Additive manufacturing of metallic components by selective electron beam melting – a review," *International Materials Reviews*, vol. 61, no. 5, pp. 361-377, 2016.
- [155] M. Ghassemi, "High power density technologies for large generators and motors for marine applications with focus on electrical insulation challenges," *High Voltage*, vol. 5, no. 1, pp. 7-14, 2020.
- [156] S. Maklakov, A. Naboko, S. Maklakov, S. Bobrovskii, V. Polozov, P. Zezyulina, A. Osipov, I. Ryzhikov, K. Rozanov, D. Filimonov, K. Pokholok, I. Iakubov and A. Lagarkov, "Amorphization of thin superalloy films Ni₇₉Fe₁₇Mo₄ with oxygen during magnetron sputtering," *Journal of Alloys and Compounds*, vol. 854, p. 157097, 2021.
- [157] H. Schonrath, M. Spasova, S. Kilian, R. Meckenstock, G. Witt, J. Sehrt and M. Farle, "Additive Manufacturing of Soft Magnetic Permalloy from Fe and Ni Powders: Control of Magnetic Anisotropy," *J. Magn. Magn. Mater.*, vol. 478, pp. 274-278, 2019.
- [158] T. Waeckerle, A. Demier, F. Godard and H. Fraise, "Evolution and Recent Developments of 80%Ni Permalloys," *J. Magn. Magn. Mater.*, vol. 505, p. 166635, 2020.
- [159] L. Rohman, A. Arkundato, Y. Mulyani and D. Djuhana, "Magnetic susceptibility and curie temperature of Co_{1-x}Fe_x alloy nanocube and nanosphere using micromagnetic simulation," *Journal of Physics: Conference Series*, vol. 1825, p. 012003, 2021.

Chapter 2 – Theoretical Background

- [160] E. Atzeni and A. Salmi, "Economics of additive manufacturing for end-useable metal parts," *Int. J. Adv. Manuf. Technol.*, vol. 62, no. 9, pp. 1147-1155, 2012.
- [161] R. Major and C. Orrock, "High saturation ternary cobalt-iron basalt alloys," *IEEE Trans. Magn.*, vol. 24, no. 2, pp. 1856-1858, 1988.
- [162] N. Sun and S. Wang, "Soft high saturation magnetization (Fe/sub0.7/Co/sub0.3/)/sub1-x/N/sub x/thin films for inductive write heads," *IEEE Trans. Magn.*, vol. 36, no. 5, pp. 2506-2508, 2000.
- [163] Y. Ustinovshikov and S. Tresheva, "Character of transformations in Fe-Co system," *Materials Science and Engineering: A*, vol. 248, no. 1-2, pp. 238-244, 1998.
- [164] H. Gould and D. Wenny, "Supermendur: a new rectangular-loop magnetic material," *Electr. Eng.*, vol. 76, no. 3, pp. 208-211, 1957.
- [165] T. Babuska, M. Wilson, K. Johnson, S. Whetten, J. Curry, J. Rodelas, C. Atkinson, P. Lu, M. Chandross, B. Krick, J. Micheal, N. Argibay, D. Susan and A. Kustas, "Achieving high strength and ductility in traditionally brittle soft magnetic intermetallics via additive manufacturing," *Acta Materialia*, vol. 180, pp. 149-157, 2019.
- [166] R. Fingers, R. Carr and Z. Turgut, "Effect of aging on magnetic properties of Hiperco® 27, Hiperco® 50, and Hiperco 50 HS® alloys," *Journal of Applied Physics*, vol. 91, no. 10, pp. 7848-7850, 2002.
- [167] R. Yu, S. Basu, L. Ren, Y. Zhang, A. Parvizi-Majidi, K. Unruh and J. Xiao, "High temperature soft magnetic materials: FeCo alloys and composites," *IEEE Transactions on Magnetics*, vol. 36, no. 5, pp. 3388-3393, 2000.
- [168] J. Geng, I. Nlebedim, M. Besser, E. Simsek and R. Ott, "Bulk Combinatorial Synthesis and High Throughput Characterization for Rapid Assessment of Magnetic Materials: Application of Laser Engineered Net Shaping (LENS)," *JOM*, vol. 68, pp. 1972-1977, 2016.
- [169] R. Hasegawa, "Design and fabrication of new soft magnetic materials," *J. Non-Cryst. Solids*, vol. 329, no. 1, pp. 1-7, 2003.

Chapter 2 – Theoretical Background

- [170] S. Yoshida, T. Mizushima, T. Hatanai and A. Inoue, "Preparation of new amorphous powder cores using Fe-based glassy alloy," *IEEE Trans. Magn.*, vol. 36, no. 5, pp. 3424-3429, 2000.
- [171] J. Silveyra, E. Ferrara, D. Huber and T. Monson, "Soft magnetic materials for a sustainable and electrified world," *Science*, vol. 362, p. 6413, 2018.
- [172] Y. Yoshizawa, S. Oguma and K. Yamauchi, "New Fe-based soft magnetic alloys composed of ultrafine grain structure," *J. Appl. Phys.*, vol. 64, no. 10, pp. 6044-6049, 1988.
- [173] E. Peng, X. Wei, T. Heng, U. Garbe, D. Yu and J. Ding, "Ferrite-based soft and hard magnetic structures by extrusion free-forming," *RSC Adv.*, vol. 7, no. 43, pp. 27128-27138, 2017.
- [174] H. Rimal, G. Stornelli, A. Faba and E. Cardelli, "Macromagnetic Approach to the Modelling in Time Domain of Magnetic Losses of Ring Cores of Soft Ferrites in Power Electronics," *IEEE Trans. Power Electron*, vol. 38, pp. 3559-3568, 2023.
- [175] K. Sharma, N. Aggarwal, N. Kumar and A. Sharma, "A Review Paper: Synthesis Techniques and Advance Application of Mn-Zn Nano-Ferrites," *Mater. Today, Proc.*, p. In Press, 2023.
- [176] C. Andrews, M. Chatham, S. Dorman, I. McCue, J. Sopciask and M. Taheri, "Additive Manufacturing of NiZnCu-Ferrite Soft Magnetic Composites," *J. Mater. Res.*, vol. 36, pp. 3579-3590, 2021.
- [177] B. Zeng, Y. Zhou, J. Smugeresky and E. Lavernia, "Processing and Behaviour of Fe-Based Metallic Glass Components via Laser-Engineered Net Shaping," *Metallurgical and Materials Transactions A*, vol. 40, no. 5, pp. 1235-1245, 2009.
- [178] S. Pauly, L. Lober, R. Petters, M. Stoica, S. Scudino, U. Kuhn and J. Eckert, "Processing metallic glasses by selective laser melting," *Materials Today*, vol. 16, no. 1-2, pp. 37-41, 2013.
- [179] V. Balla and A. Bandyopadhyay, "Laser processing of Fe-based bulk amorphous alloy," *Surf Coatings Technol.*, vol. 205, pp. 2661-2667, 2010.

Chapter 2 – Theoretical Background

- [180] X. Li, M. Roberts, S. O’Keeffe and T. Sercombe, “Selective laser melting of Zr-based bulk metallic glasses: Processing, microstructure and mechanical properties,” *Materials and Design*, vol. 112, pp. 217-226, 2016.
- [181] C. Zhang, X. Li, S. Liu, H. Liu, L. Yu and L. Liu, “3D printing of Zr-based bulk metallic glasses and components for potential biomedical applications,” *Journal of Alloys and Compounds*, vol. 790, pp. 963-973, 2019.
- [182] Y. Ge, X. Chen and Z. Chang, “The forming and crystallization behaviours of Zr₅₀Ti₅Cu₂₇Ni₁₀Al₈ bulk amorphous alloy by laser additive manufacturing,” *Mater Express*, vol. 10, pp. 1155-1160, 2020.
- [183] C. Yang, C. Zhang, W. Xing and L. Liu, “3D printing of Zr-based bulk metallic glasses with complex geometries and enhanced catalytic properties,” *Intermetallics*, vol. 94, pp. 22-28, 2018.
- [184] S. Kim, G. Park, H. Kim, A. Lee, H. Oh, C. Lee and M. Lee, “Micro-deposition of Cu-based metallic glass wire by direct laser melting process,” *Materials Letters*, vol. 202, pp. 1-4, 2017.
- [185] L. Deng, S. Wang, P. Wang, U. Kuhn and S. Pauly, “Selective laser melting of a Ti-based bulk metallic glass,” *Materials Letters*, vol. 212, pp. 346-349, 2018.
- [186] X. Li, C. Kang, H. Huang, L. Zhang and T. Sercombe, “Selective laser melting of an Al₈₆Ni₆Y_{4.5}Co₂La_{1.5} metallic glass: Processing, microstructure evolution and mechanical properties,” *Materials Science and Engineering: A*, vol. 606, pp. 370-379, 2014.
- [187] X. Li, C. Kang, H. Huang and T. Sercombe, “The role of a low-energy-density re-scan in fabricating crack-free Al₈₅Ni₅Y₆Co₂Fe₂ bulk metallic glass composites via selective laser melting,” *Materials and Design*, vol. 63, pp. 407-411, 2014.
- [188] C. Yap, C. Chua, Z. Dong, Z. Liu, D. Zhang, L. Loh and S. Sing, “Review of selective laser melting: Materials and applications,” *Applied Physics Reviews*, vol. 2, no. 4, p. 041101, 2015.
- [189] S. Pauly, C. Schricker, S. Scudino, L. Deng and U. Kuhn, “Processing a glass-forming Zr-based alloy by selective laser melting,” *Materials and Design*, vol. 135, pp. 133-141, 2017.

Chapter 2 – Theoretical Background

- [190] P. Bordeenithikasem, D. Hofmann, S. Firdosy and N. Ury, "Controlling microstructure of FeCrMoBC amorphous metal matrix composites via laser directed energy deposition," *Journal of Alloys and Compounds*, vol. 857, p. 157537, 2020.
- [191] M. Tang, C. Pistorius, S. Narra and J. Beuth, "Rapid Solidification: Selective Laser Melting of AlSi10Mg," *JOM*, vol. 68, pp. 960-966, 2016.
- [192] E. Schubert and H. Bergmann, "Rapidly solidified surface layers by laser melting," in *Rapidly Solidified Alloys: Processes, Structures, Properties & Applications*, New York, Marcel Dekker Inc., 1993, pp. 195-230.
- [193] V. Pacheco, D. Karlsson, J. Marattukalam, M. Stolpe, B. Hjorvarsson, U. Jansson and M. Sahlberg, "Thermal stability and crystallization of a Zr-based metallic glass produced by suction casting and selective laser melting," *Journal of Alloys and Compounds*, vol. 825, p. 153995, 2020.
- [194] K. Prashanth, S. Scudino, T. Maity, J. Das and J. Eckert, "Is the energy density a reliable parameter for materials synthesis by selective laser melting?" *Materials Research Letters*, vol. 5, no. 6, pp. 386-390, 2017.
- [195] J. Mao, H. Zhang, H. Fu, A. Wang, H. Li and Z. Hu, "The Effects of Casting Temperature on the Glass Formation of Zr-Based Metallic Glasses," *Advanced Engineering Materials*, vol. 11, no. 12, pp. 986-991, 2010.
- [196] X. Lin, Y. Zhang, G. Yang, X. Gao, Q. Hu, J. Yu, L. Wei and W. Huang, "Microstructure and compressive/tensile characteristic of large size Zr-based bulk metallic glass prepared by laser solid forming," *Journal of Materials Science & Technology*, vol. 35, no. 2, pp. 328-335, 2019.
- [197] Y. Lu, H. Zhang, H. Li, H. Xu, G. Huang, Z. Qin and X. Lu, "Crystallization prediction on laser three-dimensional printing of Zr-based bulk metallic glass," *Journal of Non-Crystalline Solids*, vol. 461, pp. 12-17, 2017.
- [198] D. Ouyang, N. Li, W. Xing, J. Zhang and L. Liu, "3D printing of crack-free high strength Zr-based bulk metallic glass composite by selective laser melting," *Intermetallics*, vol. 90, pp. 128-134, 2017.

Chapter 2 – Theoretical Background

- [199] D. Ouyang, N. Li and L. Liu, "Structural heterogeneity in 3D printed Zr-based bulk metallic glass by selective laser melting," *Journal of Alloys and Compounds*, vol. 740, pp. 603-609, 2018.
- [200] N. Luo, C. Scheitler, N. Ciftci, F. Galgon, Z. Fu, V. Uhlenwinkel, M. Schmidt and C. Korner, "Preparation of Fe-Co-B-Si-Nb bulk metallic glasses by laser powder bed fusion: Microstructure and properties," *Materials Characterization*, vol. 162, p. 110206, 2020.
- [201] P. Bordeenithikasem, M. Stolpe, A. Elsen and D. Hoffman, "Glass forming ability, flexural strength, and wear properties of additively manufactured Zr-based bulk metallic glasses produced through laser powder bed fusion," *Additive Manufacturing*, vol. 21, pp. 312-317, 2018.
- [202] J. Shi, S. Ma, S. Wei, J. Best, M. Stolpe and B. Markert, "Connecting structural defects to tensile failure in a 3D-printed fully-amorphous bulk metallic glass," *Materials Science and Engineering: A*, vol. 813, p. 141106, 2021.
- [203] S. Madge and A. Greer, "Laser additive manufacturing of metallic glasses: issues in vitrification and mechanical properties," *Oxford Open Materials Science*, vol. 1, no. 1, pp. 1-13, 2021.
- [204] J. Löffler and W. Johnson, "Model for decomposition and nanocrystallization of deeply undercooled $Zr_{41.2}Ti_{13.8}Cu_{12.5}Ni_{10}Be_{22.5}$," *Appl Phys Lett*, vol. 76, pp. 3394-3396, 2000.
- [205] M. Baricco, S. Spriano, I. Chang, M. Petrzehik and L. Battezzati, "'Big cube' phase formation in Zr-based metallic glasses," *Materials Science and Engineering: A*, Vols. 304-306, pp. 305-310, 2001.
- [206] H. Jung, S. Choi, K. Prashanth, M. Stoica, S. Scudino, S. Yi, U. Kuhn, D. Kim, K. Kim and J. Eckert, "Fabrication of Fe-based bulk metallic glass by selective laser melting: A parameter study," *Materials & Design*, vol. 86, pp. 703-708, 2015.
- [207] A. Yavari, A. Le Moulec, W. Botta, A. Inoue, P. Rejmankova and A. Kvick, "In situ crystallization of $Zr_{55}Cu_{30}Al_{10}Ni_5$ bulk glass forming from the glassy and undercooled liquid states using synchrotron radiation," *Journal of Non-Crystalline Solids*, vol. 247, no. 1-3, pp. 31-34, 1999.
- [208] L. Zrodowski, B. Wysocki, R. Wroblewski, A. Krawczynska, B. Adamczyk-Cieslak, J. Zdunek, P. Blyskun, J. Ferenc, M. Leonowicz and W. Swieszkowski,

Chapter 2 – Theoretical Background

“New approach to amorphization of alloys with low glass forming ability via selective laser melting,” *Journal of Alloys and Compounds*, vol. 771, pp. 769-776, 2019.

[209] L. Thorsson, M. Unosson, M. Perez-Prado, X. Jin, P. Tiberto, G. Barrera, B. Adam, N. Neuber, A. Ghavimi, M. Frey, R. Busch and I. Gallino, “Selective laser melting of a Fe-Si-Cr-B-C-based complex-shaped amorphous soft-magnetic electric motor rotor with record dimensions,” *Materials and Design*, vol. 215, p. 110483, 2022.

[210] H. Lashgari, M. Ferry and S. Li, “Additive manufacturing of bulk metallic glasses: Fundamental principle, current/future developments and applications,” *Journal of Materials Science & Technology*, vol. 119, pp. 131-149, 2022.

Laser Additive Manufacturing of Fe-Based Magnetic Amorphous Alloys

Merve G. Özden * and Nicola A. Morley

Department of Material Science and Engineering, University of Sheffield, Sheffield S1 3JD, UK.

* Correspondence: mgozden1@sheffield.ac.uk

Citation: Özden, M.G.; Morley, N.A. Laser Additive Manufacturing of Fe-Based Magnetic Amorphous Alloys. *Magnetochemistry* 2021, 7, 20.

<https://doi.org/10.3390/magnetochemistry7020020>

Copyright: © 2021 by the authors. Licensee MDPI, Basel, Switzerland. This article is an open access article distributed under the terms and conditions of the Creative Commons Attribution (CC BY) licence (<https://creativecommons.org/licenses/by/4.0/>).

Abstract

Fe-based amorphous materials offer new opportunities for magnetic sensors, actuators, and magnetostrictive transducers due to their high saturation magnetostriction ($\lambda_s = 20\text{--}40$ ppm) and low coercive field compared with polycrystalline Fe-based alloys, which have high magnetostriction but large coercive fields and Co-based amorphous alloys with small magnetostriction ($\lambda_s = -3$ to -5 ppm). Additive layer manufacturing (ALM) offers a new fabrication technique for more complex net-shaping designs. This paper reviews the two different ALM techniques that have been used to fabricate Fe-based amorphous magnetic materials, including the structural and magnetic properties. Laser powder bed fusion (LPBF)—a powder-bed fusion technique—and laser engineered net shaping (LENS)—a directed energy deposition method—have both been utilised to fabricate amorphous alloys, owing to their high availability and low cost within the literature. Two different scanning strategies have been introduced by using the LPBF technique. The first strategy is a double-scanning strategy, which gives rise to maximum relative density of 96% and corresponding magnetic saturation of 1.22 T. It also improved the glassy phase content by an order of magnitude of 47%, as well as improving magnetic properties (decreasing coercivity to 1591.5 A/m and increasing magnetic permeability to around 100 at 100 Hz). The second is a novel scanning strategy, which involves two-step melting: preliminary laser melting and short pulse amorphization. This increased the amorphous phase fraction to a value of up to 89.6%, and relative density up to 94.1%, and lowered coercivity to 238 A/m. On the other hand, the LENS technique has not

been utilised as much as LPBF in the production of amorphous alloys owing to its lower geometric accuracy (0.25 mm) and lower surface quality, despite its benefits such as providing superior mechanical properties, controlled composition, and microstructure. As a result, it has been commonly used for large parts with low complexity and for repairing them, limiting the production of amorphous alloys because of the size limitation. This paper provides a comprehensive review of these techniques for Fe-based amorphous magnetic materials.

Keywords: Laser powder bed fusion; laser engineered net shaping; 3D printing; magnetic glassy alloys; bulk metallic glasses.

3.1 Introduction

Functional magnetic materials (FMMs) have gained considerable interest for advanced engineering devices owing to their technical benefits for energy conversion, harvesting, transmission, sensing/actuation [1], and more recently for magnetic refrigeration applications, based on their magnetocaloric effects [2]. Fe-based soft magnetic materials are of great importance for sensors, transformers, and inductive devices because of their superior magnetic properties such as outstanding magnetic permeability, low coercivity, and good corrosion resistance [3-6].

In general, Fe-based soft magnetic alloys are used in two distinct categories of applications:

- i. For producing and utilising electromagnetic energy: due to their low cost and ecological reasons, the usage of soft magnetic materials comprises an important part of these applications because they have high magnetic permeability, low energy losses and high magnetic saturation. Fe-Si-based alloys are considered as the most representative materials for this area.
- ii. For signal processing: Fe-Ni-based alloys are usually used in informatics, electronics, transducers, magnetic recording heads, microwave installations and so on [7].

In the last two decades, significant progress has been achieved in the understanding of alloy design in an attempt to enhance the glass forming ability (GFA) of soft magnetic amorphous materials [8]. Therefore, many new bulk amorphous alloys with large GFA and good magnetic properties have been reported [9-14]. Casting methods including injection moulding have been used for the production of magnetic bulk metallic glasses (BMG). Zhang *et al.* utilised casting technique to fabricate glassy toroidal cores having good magnetic properties [15]. They consisted of $\text{Fe}_{66}\text{Co}_{10}\text{Mo}_{3.5}\text{P}_{10}\text{C}_4\text{B}_4\text{Si}_{2.5}$ BMG with an outer diameter of 10 mm and inner diameter of

6 mm and showed low coercivity (1.0 A/m), high maximum magnetic permeability (450,000), low core loss (0.4 W/kg at 50 Hz) and maximum magnetic flux density (1 T) [15]. Nevertheless, dimensional limitations and poor mechanical properties restrict the use of casting techniques in the production of bulk metallic alloys.

Alternatively, to manufacture three-dimensional (3D) amorphous magnetic parts, powder metallurgy (PM), especially hot pressing and spark plasma sintering, has been extensively exploited [16-18]. To reduce the possibility of the deterioration of magnetic softness because of partial crystallisation in the amorphous matrix, it is necessary that consolidation behaviour and thermal stability of the glassy structure at elevated temperatures is controlled [19]. It is promising that the limitations of conventional techniques can be overcome by using additive manufacturing (AM) in the production of glassy magnetic alloys, which is discussed in detail in Section 3.3. This section also mentions the use of powder-bed fusion and directed energy deposition techniques in the fabrication of amorphous magnetic Fe-based alloys, and the effects of process parameters on the final magnetic and mechanical properties. To emphasise the importance of the amorphous magnetic materials, their properties are analysed and compared with those of polycrystalline materials in Section 3.2.

3.2 Amorphous Fe-Based Magnetic Alloys

Amorphous alloys for soft magnetic applications are often fabricated by rapid solidification of the melt [20, 21]. They are generally prepared with the nearly 20% addition of metalloids (Si, B, Al, C and P) for Fe-based and Co-based alloys [7]. Si and B are important metalloids for glass formation and the amorphous structure stabilisation [21, 22]. Typical chemical compositions are such that the combined compositions of Fe, Co, Ni elements are 70–85 atomic (at.) % and those of Si and B are 15–30 at. % in total. However, magnetic glassy alloys have a wide variety of compositions. This allows for a large range of soft magnetic properties to be achieved, which depend upon the demands of the application [23].

In magnetic amorphous alloys, the microstructure lacks atomic long-range order and only exhibits short-range order, which is essentially random atomic arrangement of the liquid melt solidified at a cooling rate of $10^5 - 10^6$ K/s. As a result, there are no crystallite-related defects including grain boundaries and dislocations, leading to a decrease in coercivity (see Figure 3.1) [24].

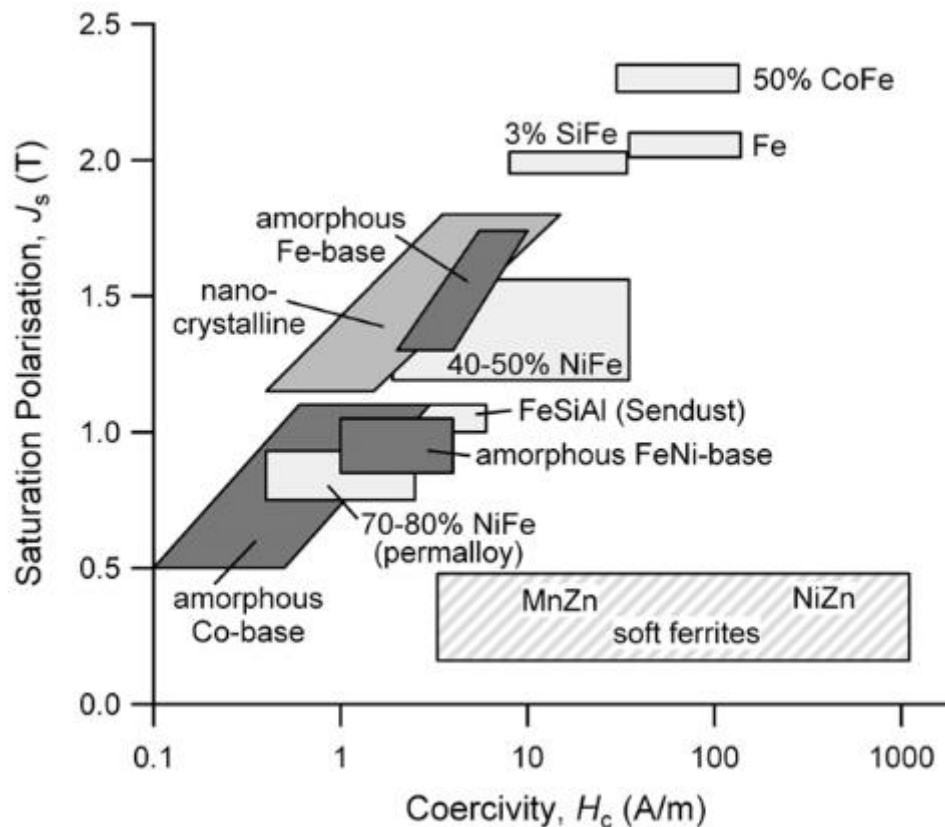


Figure 3.1: Comparison of the magnetic properties of soft magnetic materials (reprinted with the permission from [23], Elsevier, 2013).

Amorphous Fe-based alloys, based on inexpensive raw materials, have relatively high saturation magnetisation (see Figure 3.1) and high magnetostriction [23], which makes them promising candidates for sensors and actuators [25-29].

A nanocrystalline structure with favourable soft magnetic properties typically develops when the amorphous state undergoes primary crystallization of bcc-Fe phase (Crystallization temperature (T_x) \approx 773 K and melting temperature (T_m) \approx 1773 K), also known as α -Fe, before the formation of intermetallic phases including Fe_3B ($T_x \approx$ 823 K, $T_m =$ 1420 K) or Fe_2B ($T_x \approx$ 1013 K, $T_m =$ 1662 K). Two typical binary phase diagrams of Fe-Si-B alloy system are given in Figure 3.2. Achieving a microstructure on the nanoscale requires an exceptionally high nucleation rate and slow growth of the bcc-Fe crystallite precipitates. The originally proposed and minimally altered optimal alloy composition is $\text{Fe}_{73.5}\text{Cu}_1\text{Nb}_3\text{Si}_{13.5}\text{B}_9$ (at. %), which can be regarded as a typical Fe-Si-B metallic glass composition with small additions of Cu and Nb (or other group IV-VI elements). The combined inclusion of Cu and Nb plays a crucial role in shaping the distinct nanocrystalline structure: Cu promotes the nucleation of bcc-Fe nanograins, while Nb hinders their coarsening and concurrently restrains the formation of boride compounds [11, 23].

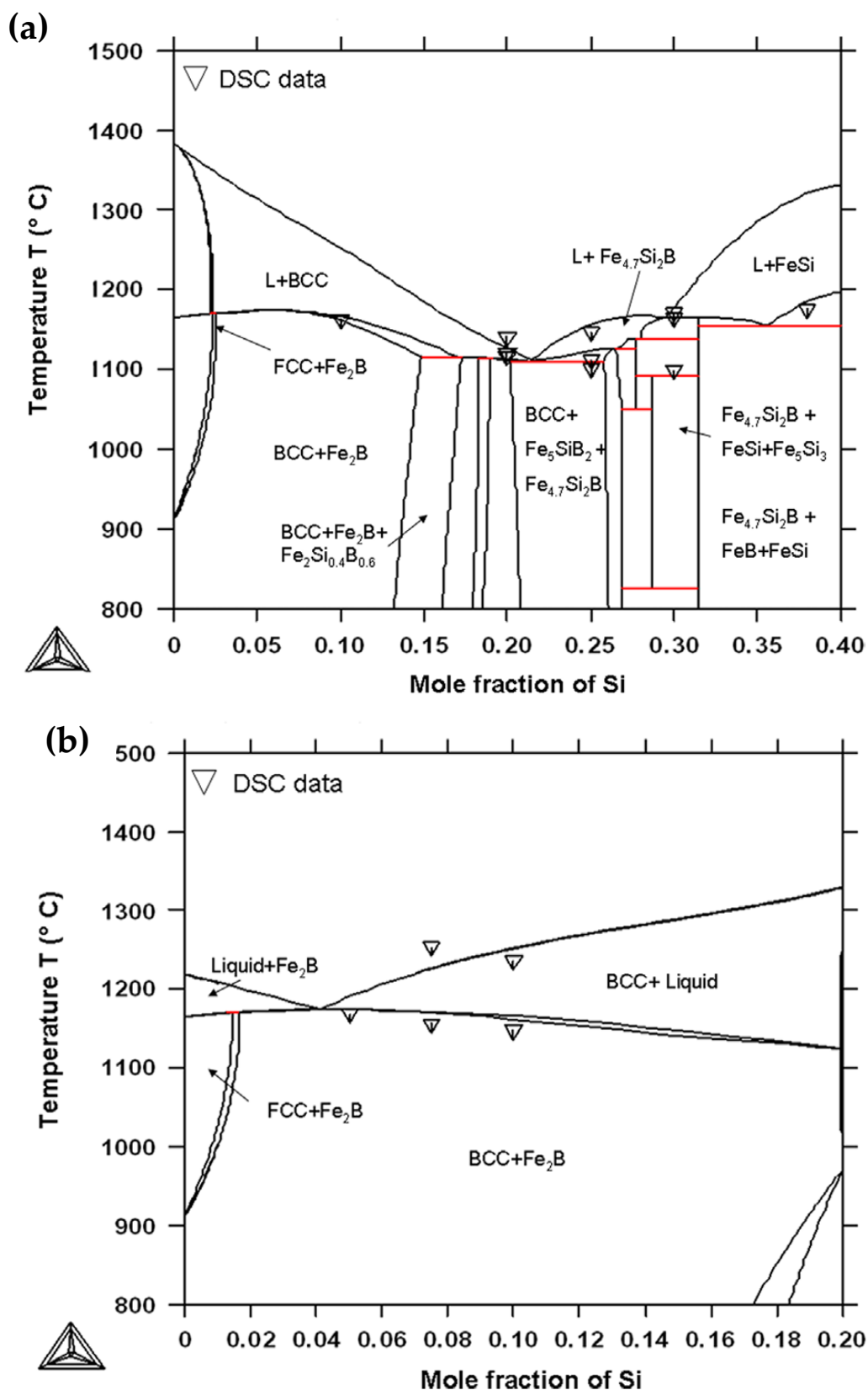


Figure 3.2: The binary phase diagrams of Fe-Si-B alloys systems at (a) the boron mole fraction of 0.10 and (b) the iron mole fraction of 0.80 [30].

Figure 3.3 illustrates the relationship between the saturation magnetostriction constant and Si content for the FeCuNbSiB alloy system. The saturation magnetostriction (λ_s) has the highest value and is virtually independent of Si composition for the amorphous structure, different from the nanocrystalline state where magnetostriction is significantly dependent on the Si concentration and its maximum value is as nearly half that of the amorphous structure.

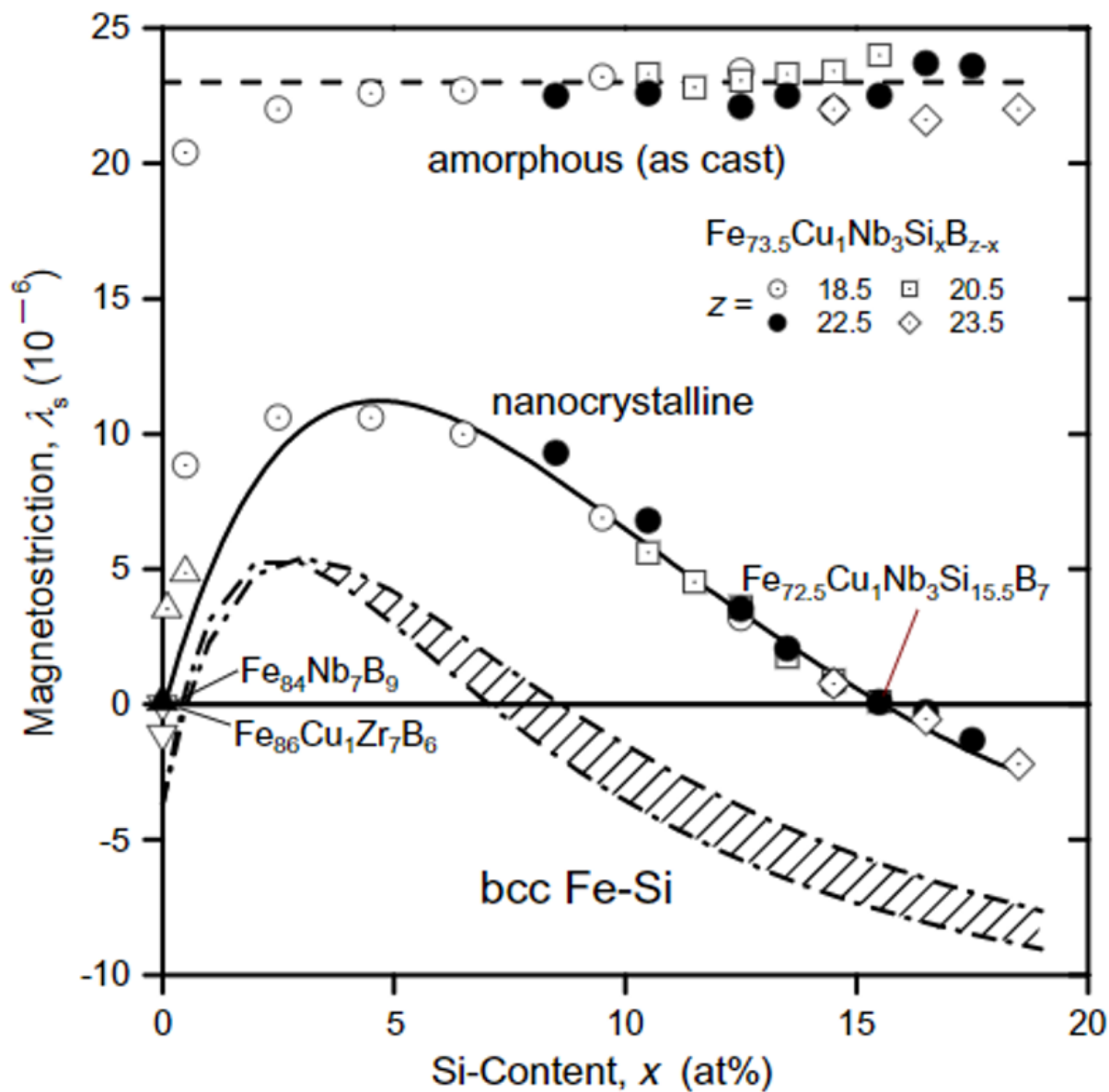


Figure 3.3: The saturation magnetostriction constant (λ_s) of $\text{Fe}_{96-z}\text{Cu}_1\text{Nb}_3\text{Si}_x\text{B}_{z-x}$ alloys as a function of Si content for the amorphous and nanocrystalline states (reprinted with the permission from [23], Elsevier, 2013).

Figure 3.4 indicates the change in the saturation polarisation (J_s) and the magnetostriction constant (λ_s) of amorphous magnetic alloys as a function of Fe, Ni and Co content. Fe-rich alloys possess the highest saturation polarisation and

saturation magnetisation constant, decreasing as Co and Ni concentration increases. J_s for amorphous materials is usually lower than polycrystalline ones (Figure 3.1) because of the addition of nonmagnetic metalloids (Si and B) required for glass formation [23].

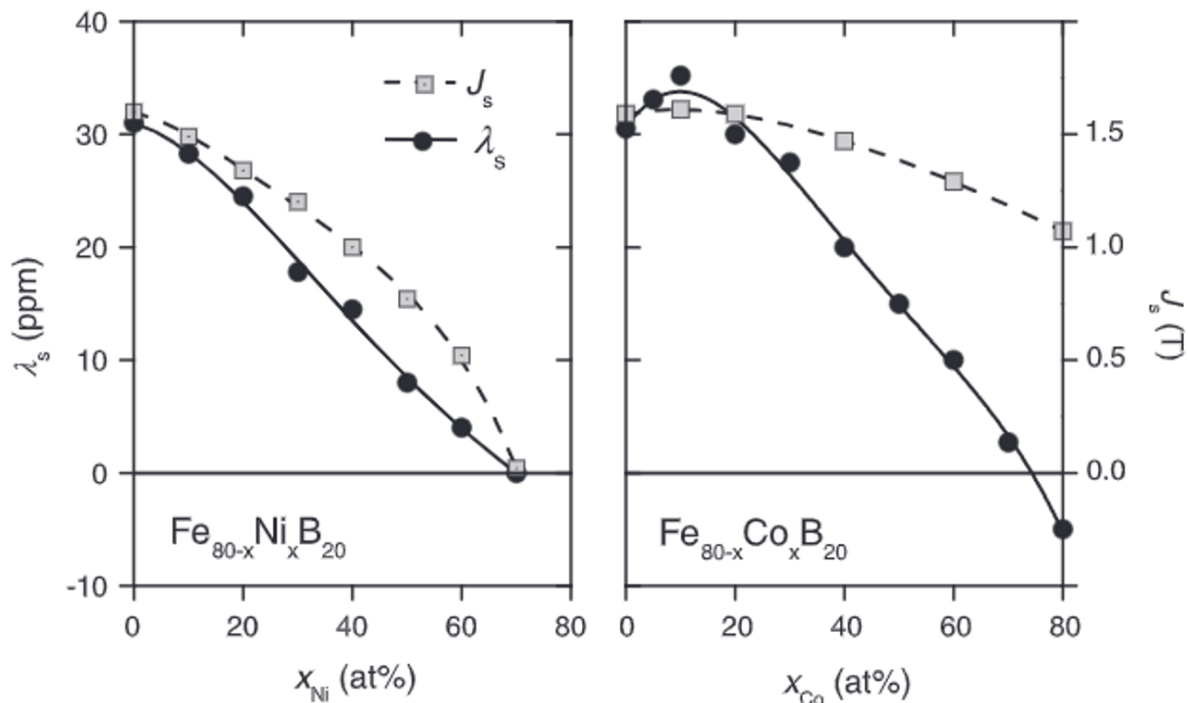


Figure 3.4: Saturation magnetisation J_s (dashed lines) and saturation magnetostriction λ_s (full lines) of amorphous Fe-Ni-based and Fe-Co-based alloys with changing Ni and Co content, respectively (reprinted with the permission from [23], Elsevier, 2013).

The saturation magnetostriction of Fe-based amorphous alloys is typically positive, ≈ 20 – 40 ppm, on the other hand for Co-based amorphous alloys, it is typically negative, ≈ -5 to -3 ppm. The increase in λ_s with lowering Ni concentration is linked to a concurrent increase in J_s ($|\lambda_s| \propto J_s^2$). Therefore, near zero λ_s at high Ni concentrations only occur as the system becomes paramagnetic [23].

Fe-B alloys with a saturation flux density higher than 1.5 T were the first metallic glass developed for the fabrication of distribution transformers. The addition of Si gave a higher thermal stability without any reduction in the saturation flux density, producing the ternary alloy $Fe_{82}B_{12}Si_6$. However, this is prone to material oxidation due to air pockets forming during the production process, lowering magnetic flux density, and increasing total losses. $Fe_{81.5}B_{13.5}Si_3C_2$ was developed to overcome these limitations [7].

Fe-Si-B glassy alloys possess six times fewer energy losses than traditional Fe-Si alloys at industrial frequencies. In fact, $Fe_{79}B_{13}Si_8$ has a higher Curie temperature without changing core losses and flux density, compared with Fe-3%Si alloys in the fabrication

of power transformers [7]. Therefore, they are competitive for applications where Fe-Si alloys are traditionally used.

After rapidly quenching amorphous alloys, internal residual stresses are developed in the structure, altering the magnetic behaviour (increasing coercivity and reducing permeability) due to the emergence of magnetocrystalline anisotropy. Strain relief annealing has been employed below the crystallisation temperature not only to achieve higher permeability, lower energy losses and smaller coercivity (see Table 3.1), but also to improve mechanical properties by allowing atomic arrangement over a short distance. Table 3.1 clearly shows that although as-cast alloys exhibit very soft magnetic behaviour, strain relief annealing considerably allows the enhancement of magnetic properties (reducing coercivity, increasing permeability) by relieving the internal residual strains. Amorphous alloys with a wide variety of magnetic properties can be fabricated by annealing in the existence of an applied magnetic field [31].

Table 3.1: Magnetic properties of amorphous alloys under direct current (DC) applications (reprinted with the permission from [31], CRC Press, 2016).

Alloy	Shape	As cast			Annealed		
		H_c (A/m)	M_r/M_s	μ_{max} (10^3)	H_c (A/m)	M_r/M_s	μ_{max} (10^3)
Fe ₈₀ B ₂₀	Toroid	6.4	0.51	100	3.2	0.77	300
Fe ₄₀ Ni ₄₀ P ₁₄ B ₆	Toroid	4.8	0.45	58	1.6	0.71	275
Fe ₂₉ Ni ₄₄ P ₁₄ B ₆ Si ₂	Toroid	4.6	0.54	46	0.88	0.70	310
Fe _{4.7} Co _{70.3} Si ₁₅ B ₁₀	Strip	1.04	0.36	190	0.48	0.63	700
(Fe _{0.8} Ni _{0.2}) ₇₈ Si ₈ B ₁₄	Strip	1.44	0.41	300	0.48	0.95	2000
Fe ₈₀ P ₁₆ C ₃ B	Toroid	4.96	0.4	96	4.0	0.42	130

There are a few limitations of using amorphous magnetic materials in certain applications. Firstly, their low saturation magnetisation restricts their usage in heavy current density engineering. Secondly, their core losses start to rise rapidly at high flux densities. For this reason, they have more use in low-power, low-current applications, and specialised small-device applications where transformers are required with moderate flux densities. In these applications, amorphous magnetic materials can be used successfully instead of nickel-iron alloys including permalloy. Amorphous magnetic materials, being manufactured in large quantities, have been utilised in pulsed-power transformers, magnetic sensors, magnetostrictive transducers and communication equipment [31].

3.3 Additive Manufacturing of Amorphous Fe-Based Magnetic Alloys

Additive manufacturing (AM) includes a number of production techniques where components with a variety of structures and complex geometries are manufactured in a layer-by-layer manner directly from 3D model data [32-36]. The introduction of AM has influenced the whole fabrication field by making the design easy and simplifying the production process, enabling rapid production without needing major change in the fabrication step [37, 38]. The economic advantage of AM is revealed especially in low-volume production [38].

Several Fe-based magnetic materials produced by additive manufacturing have been studied owing to their wide range of potential applicability in the energy area [39-45]. Additive manufacturing of amorphous Fe-based magnetic materials is focused on within this review paper. From the range of AM techniques, powder-bed fusion and direct energy deposition have been used for this purpose. This section reviews the AM of amorphous magnetic materials for different laser-based AM techniques, including the research carried out and the advantages and disadvantages of each method [1, 46-50]. A summary table is given at the end of the section.

3.3.1. Powder Bed Fusion

In the powder-bed fusion process, a thin layer (typically 20–100 μm) of very fine powder (with particle size in the range of 20–50 μm) [51] is spread closely packed on a platform. This is where the powder is then fused together with a laser beam or an electron beam. Once the fusion of one layer is completed, another layer of powder is rolled on top of the previous layer and melted together till the targeted 3D part is obtained (Figure 3.5). Powder size distribution and packing both influence significantly the density of the printed component, thus are the most critical factors, along with laser process parameters (laser scan speed, laser power, pulse duration and spot diameter), to the efficiency of this technique [52]. Selective laser sintering (SLS), used generally for various polymers and for some metals with the help of sacrificial binder materials, and laser powder bed fusion (LPBF), utilised only for certain metals are the two powder-bed fusion processes, which use a laser. In the SLS process, only sintering occurs between powder particles once temperature is increased with a high-power laser above the softening point of polymers. On the other hand, in LPBF technique, a relatively higher-powered laser is exploited to fully melt metallic powder instead of sintering it. Electron-beam melting (EBM) exploits an electron beam to melt the metal powder. Unlike SLS, in the LPBF and EBM processes, the laser/electron beams can fully melt the metal powder and fuse them together, leading to exceptional mechanical properties [53].

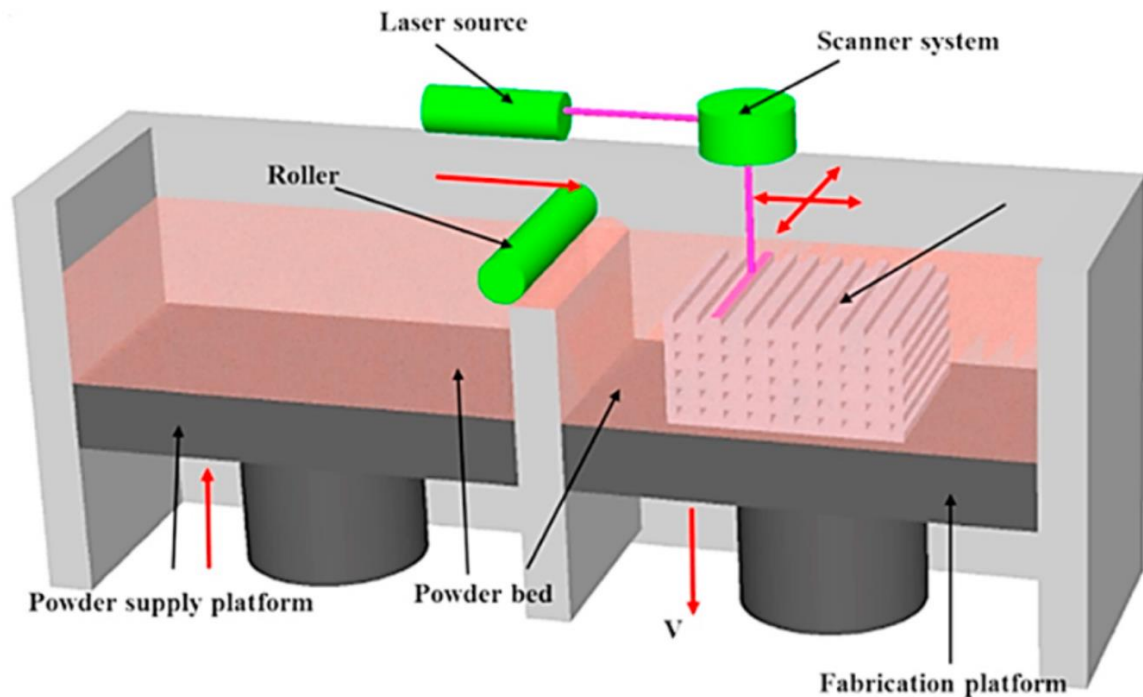


Figure 3.5: Schematic illustration of powder bed fusion [35].

In the literature, LPBF has been widely utilised to produce amorphous magnetic materials due to their low cost and high availability. Different materials and applications that exploit LPBF have been reviewed in detail [54]. It is indicated that during LPBF processes, solidification takes place relatively fast with typical cooling rates of $10^3 - 10^4$ K/s, fast enough to prevent crystallisation, [55, 56] even though the cooling rate is dependent on the process parameters [57]. For this reason, LPBF is a promising technique to produce bulk amorphous parts.

Fabrication of Fe-based bulk metallic glass with LPBF has been studied firstly by Jung *et al.* [8]. $\text{Fe}_{68.3}\text{C}_{6.9}\text{Si}_{2.5}\text{B}_{6.7}\text{P}_{8.7}\text{Cr}_{2.7}\text{Mo}_{2.5}\text{Al}_{2.1}$ (at. %) amorphous powder with different sizes in the range of $75 \mu\text{m}$ and $150 \mu\text{m}$ was prepared using gas atomisation. The cylindrical specimens with a diameter of 2 mm and height of 6 mm were built with the LPBF technique. The microstructure of the final part was composed of a mixture of amorphous and $\alpha\text{-Fe}$, $\gamma\text{-Fe}$ and Fe_{23}B_6 crystalline phases, which are associated with impurities accidentally included in the master alloy. Also, the effect of the laser power (P) and scan speed (v) on the density of the final part and magnetic properties were examined in this study. It was concluded that at high scan speeds ($v > 2500$ mm/s), bulk parts could not be generated because the powder bed did not have sufficient energy input during the LPBF process, which resulted in incomplete melting and poor inter-particle bonding [58-60]. At lower v and higher P , enhanced melting and consolidation of powder brings about the formation of LPBF specimens having high relative densities (Figure 3.6). To achieve relative densities higher than 99%, it is vital

that v lowers to 1500 mm/s and P is higher than 300 W. Moreover, hysteresis loops of the atomised powder and LPBF specimens produced with different scan speeds obtained are illustrated in Figure 3.7. It shows that the saturation magnetisation of all three samples is nearly the same within experimental error. The intrinsic magnetic properties including saturation magnetisation (M_s) are dependent on the atomic configuration and the composition of the soft amorphous magnetic materials [61], indicating that amorphous structures of the LPBF specimens are identical to those of the starting atomised powder in this study.

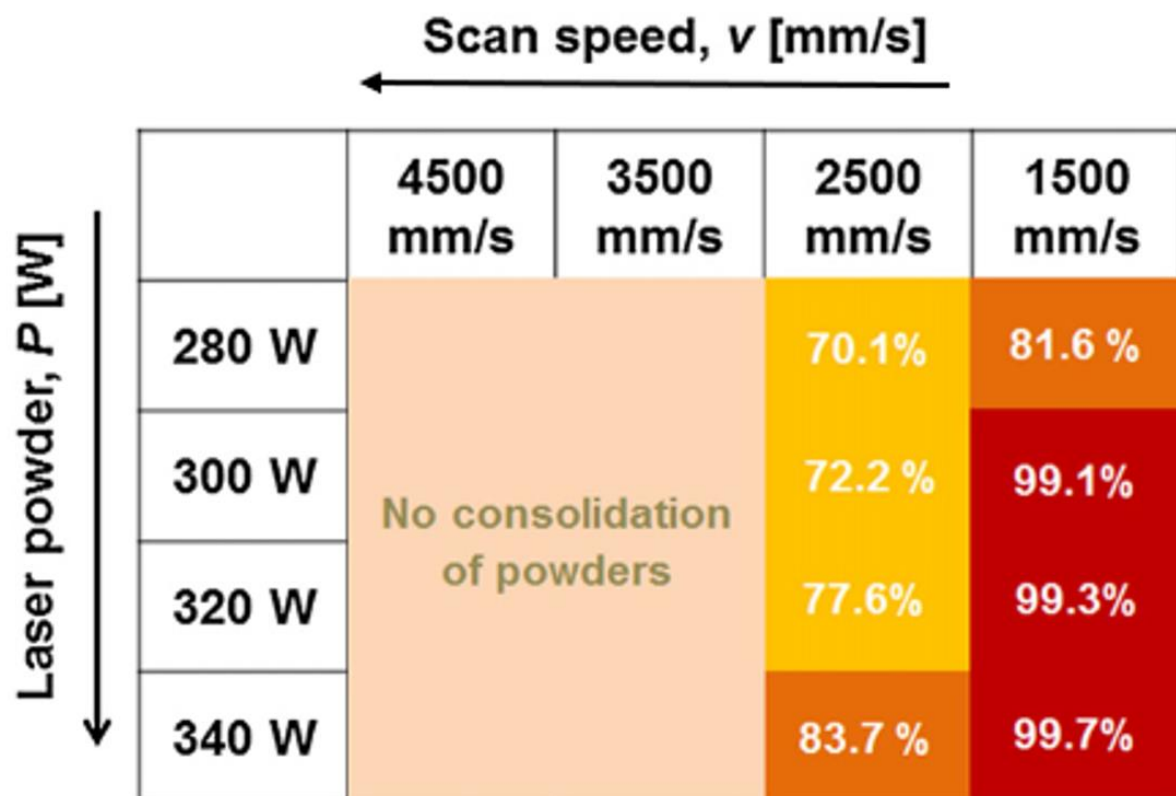


Figure 3.6: Relative density map of the laser powder bed fusion (LPBF)-processed $\text{Fe}_{68.3}\text{C}_{6.9}\text{Si}_{2.5}\text{B}_{6.7}\text{P}_{8.7}\text{Cr}_{2.7}\text{Mo}_{2.5}\text{Al}_{2.1}$ specimens as a function of power and scan speed, the values of which increase in the directions of the arrows. Figure taken from and reprinted with the permission from [8], Elsevier, 2015 (Common Grading Scale (CGS) to The International System of Units (SI) conversion $1 \text{ emu/g} = 1 \text{ Am}^2/\text{kg}$ and $1 \text{ Oe} = 79.6 \text{ A/m}$).

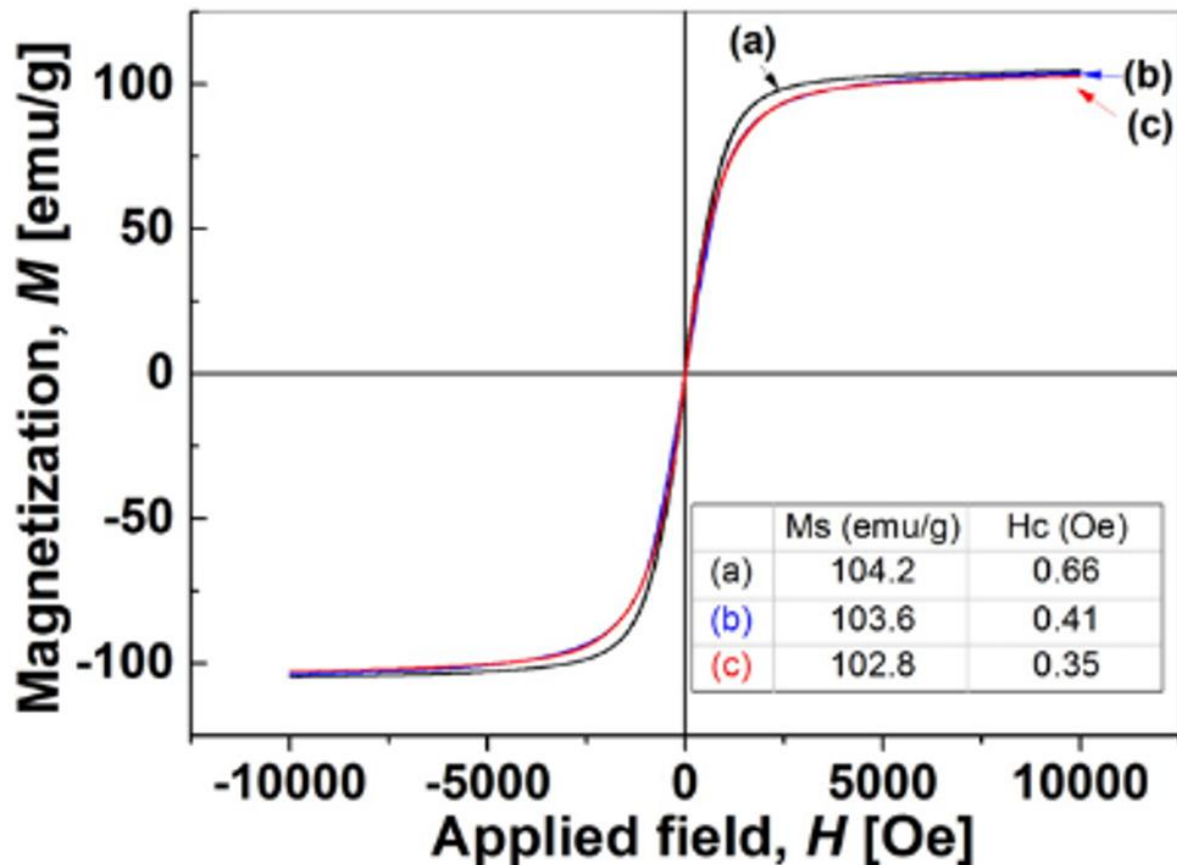


Figure 3.7: Hysteresis M-H loops of (a) parent atomised powder and LPBF-processed $\text{Fe}_{68.3}\text{C}_{6.9}\text{Si}_{2.5}\text{B}_{6.7}\text{P}_{8.7}\text{Cr}_{2.7}\text{Mo}_{2.5}\text{Al}_{2.1}$ specimens generated with (b) $v = 2500$ mm/s and $P = 340$ W and (c) $v = 1500$ mm/s and $P = 340$ W, reprinted with the permission from [8], Elsevier, 2015 (CGS to SI conversion $1 \text{ emu/g} = 1 \text{ Am}^2/\text{kg}$ and $1 \text{ Oe} = 79.6 \text{ A/m}$).

Mahbooba *et al.* tried to fabricate Fe-based BMG samples larger than critical casting thickness with LPBF by using gas-atomised FeCrMoB powder with a nominal particle-size distribution of 20–80 μm [62]. It was reported that the thicknesses of the produced fully amorphous specimens (15 mm) were much more than the critical casting thickness (1 mm) in all dimensions. In addition, it was found that the change in the LPBF parameters was not enough to prevent stress-induced micro-cracking because of rapid solidification and the brittle nature of BMGs. A low concentration of localised and isotropic nanograins, as shown in Figure 3.8, was present in the microstructure of the produced part due to mechanical stress-induced crystallisation. Furthermore, a mechanical test revealed that the Young's modulus of the LPBF bulk FeCrMoCB alloy (220 GPa) was fairly close to the modulus of the cast amorphous alloys with similar composition (190–220 GPa) [63]. This means that amorphous materials having larger than their casting critical thickness can be fabricated using LPBF with mechanical properties competing with those of cast amorphous alloys.

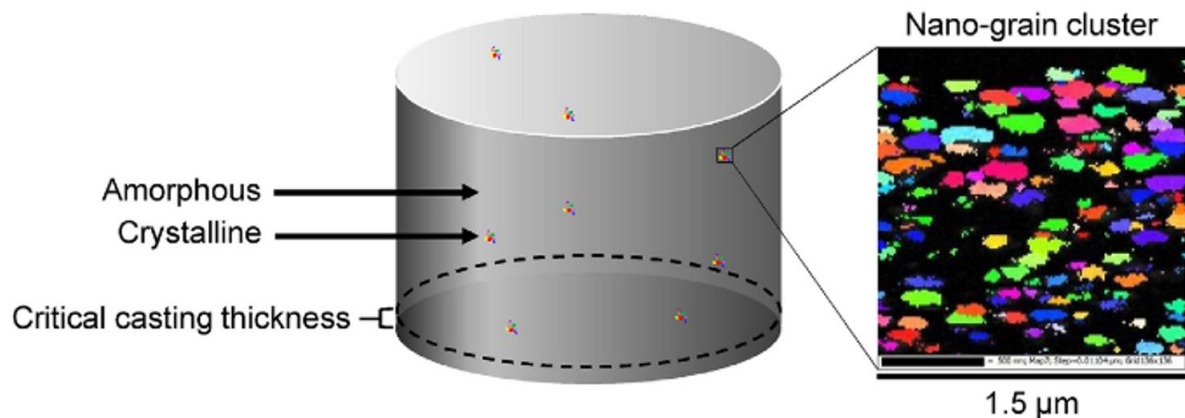


Figure 3.8: Nanograin clusters in the cylinder: Electron backscatter diffraction (EBSD) micrograph showing a nanograin cluster in the FeCrMoCB bulk cylinder (reprinted with the permission from [62], Elsevier, 2018).

As mentioned in Section 3.2, Fe-Si-B BMGs have attracted much attention as technological materials resulting from their outstanding soft ferromagnetic properties, great amorphous phase forming ability (APFA) and exceptional mechanical properties [64, 65]. Consequently, it is possible to use them as core materials sensors [66], biosensors [67] and distribution transformers. Mostly, the high APFA of Fe-B alloys enables the formation of the amorphous phase and Si makes additional contribution to it. A fully amorphous phase is achieved within the range of 5–26 at. % B and 0–29 at. % Si [68]. Accordingly, $\text{Fe}_{92.4}\text{Si}_{3.1}\text{B}_{4.5}$ alloy was produced with LPBF with a laser scan speed of 100–150 mm/s and laser power of 90 W by using gas-atomised powder having particle sizes less than 30 μm , purchased from NANOVAL company as $\text{Fe}_{92.4}\text{Si}_{3.1}\text{B}_{4.5}$ amorphous powder [69]. Nanocrystalline $\alpha\text{-Fe}_{0.95}\text{Si}_{0.05}$ and Fe_2B phases in an amorphous $\varepsilon\text{-FeSi}$ type matrix were observed in the microstructure. The immoderate number of impurity atoms in the interstitial sites is linked to the formation of the amorphous $\varepsilon\text{-FeSi}$ type structure by distorting the crystal lattice locally. The strong attraction between Fe and Si atoms indicates that APFA may be comparatively high in the Si composition above 20 at. % Si [68]. Furthermore, the large negative heat of mixing between constituents (-26 kJ/mol for Fe-Si and -38 kJ/mol for Fe-B alloys [70]) allows short-range order in the liquid upon laser melting. The crystallite sizes of $\alpha\text{-Fe}_{0.95}\text{Si}_{0.05}$ and Fe_2B , retained from the starting powder, decreases with increasing laser scan speed due to the high solidification rate ($10^6\text{--}10^8$ K/s). Such a fast solidification of droplets hinders the nucleation and growth of the crystallites, bringing about the amorphous structure. On the other hand, it is found that lower laser scan speeds of 100 mm/s and 400 mm/s enable denser microstructure, having lower porosity.

The change in the relative proportions of the phases as a function of laser scan speed (Figure 3.9(a)) depicts the variation in composition during the LPBF process and therefore the atomic motion between distinct phases for $\text{Fe}_{92.4}\text{Si}_{3.1}\text{B}_{4.5}$ alloys. The relative ratios of $\epsilon\text{-FeSi}$ type amorphous and $\alpha\text{-Fe}_{0.95}\text{Si}_{0.05}$ phases show an antagonist behaviour in which the maximum relative ratio of $\epsilon\text{-FeSi}$ amorphous phase represents a minimum fraction of $\alpha\text{-Fe}_{0.95}\text{Si}_{0.05}$ phase in the sample produced by using laser scan speed of 400 mm/s in this study. Consequently, it can be said that 400 mm/s is the optimum laser scan speed considering the process parameters used in this study to achieve both densification and high amorphous phase fractions for Fe-Si-B alloys. Furthermore, hardness was measured by a Vickers microhardness tester with a load of 100 gr. The high microhardness values (1654–2273 HV) were observed, linking to the crystallite size refinement as well as the dissolution of boron into the amorphous matrix. Those microhardness values are much higher than those of the $\text{Fe}_{70}\text{Si}_{10}\text{B}_{20}$ produced by the modified melt spinning technique (830–110 HV) [65].

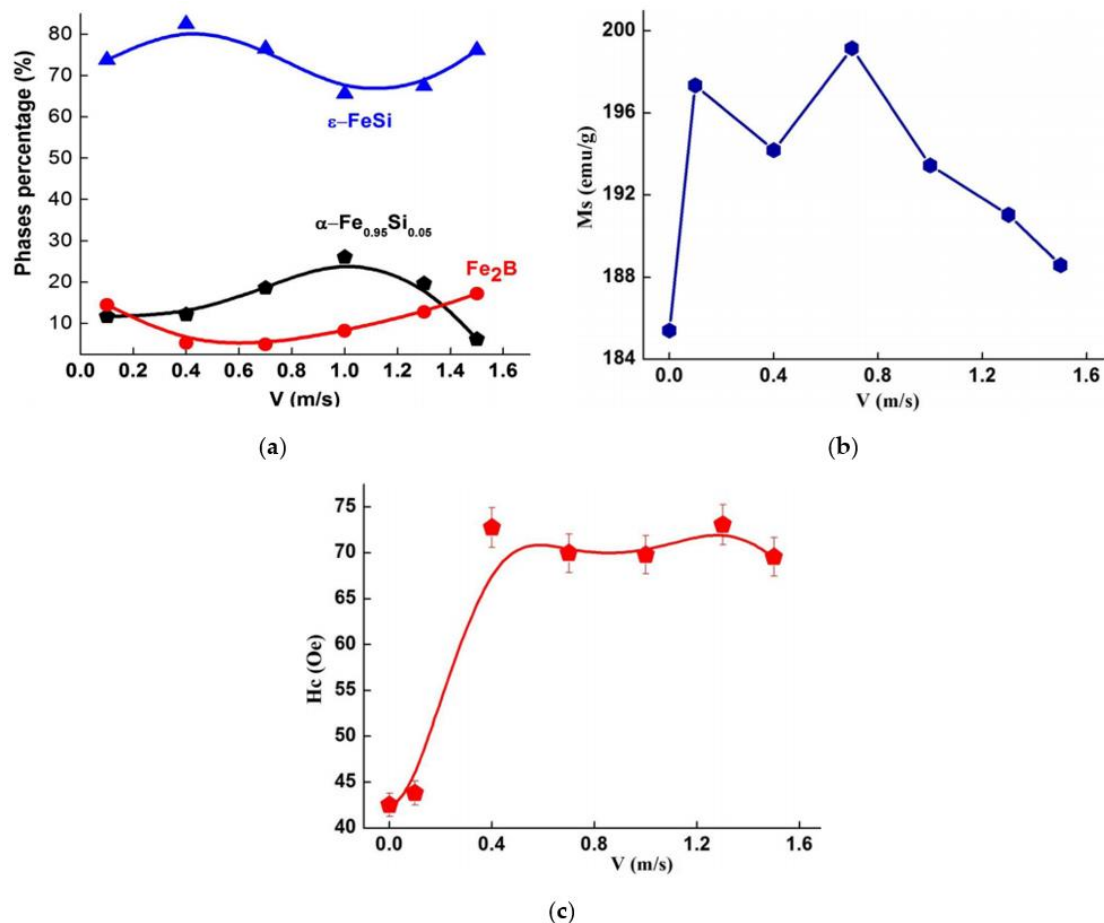


Figure 3.9: (a) Evolution of the relative proportions of the phases, (b) saturation magnetisation alterations and (c) coercivity changes of the LPBF-processed $\text{Fe}_{92.4}\text{Si}_{3.1}\text{B}_{4.5}$ specimens as a function of laser scan speed, reprinted with the permission from [69], Springer, 2018 (CGS to SI conversion 1 emu/g = 1 Am^2/kg and 1 Oe = 79.6 A/m).

In the case of the magnetic performance of the LPBF samples, it is observed that saturation magnetisation has maximum value of 199 Am²/kg for the sample fabricated with the laser scan speed of 700 mm/s and then decreases linearly to approximately 188 Am²/kg for that with 1500 mm/s as can be seen in Figure 3.9(b)). The alteration in the nearest neighbour configuration of Fe atoms with their substitution by nonmagnetic Si atoms, causes a decrease in magnetic moment per atom, thus reducing M_s . Still, the specimens fabricated by LPBF have much higher M_s values than FeSiB coatings produced by using the same starting powder (30–40 Am²/kg) [71].

How the coercivity (H_c) change with respect with to laser scanning speed is depicted in Figure 3.9(c). It is obvious that H_c increases with increasing laser scanning speed up to 400 mm/s and then levels off. Since H_c is generally associated with the size, shape, and the dispersion degree of the crystallites, including lattice distortion and internal stresses, high values of coercivity are attributed to the structural defects, such as vacancies and interstitials that originated from the laser melting process [69].

The study conducted by Ouyang *et al.* [72] confirms that the properties of LPBF-processed parts strongly depend on the mechanism of the microstructural development in amorphous alloys during the LPBF process. In this study, in order to show the effect of LPBF parameters on the microstructural evolution of Fe_{43.7}Co_{7.3}Cr_{14.7}Mo_{12.6}C_{15.5}B_{4.3}Y_{1.9} alloy, a map is made (Figure 3.10(a)). It indicates that low laser power ($P < 200$ W) and high laser scan speed ($v > 700$ mm/s) result in larger amorphous phase fractions. The relationship (Equation 3.1) between amorphous content and laser energy input is attained (Figure 3.10(b)) based on the laser energy density equation, which is presented by:

$$E_d = \frac{P}{vh d} \quad (3.1)$$

where E_d is the energy input of energy density (J/mm³), P is the laser power (W), v is the laser scan speed (mm/s), h is the hatch distance (mm) and d is the thickness of the powder layer (mm) [73-75]. It is obvious that there is a linear transition from a nearly fully crystalline structure to a fully amorphous one as the E_d decreases. This may be because as energy density decreases, the cooling rate increases, leading to amorphous structure [76].

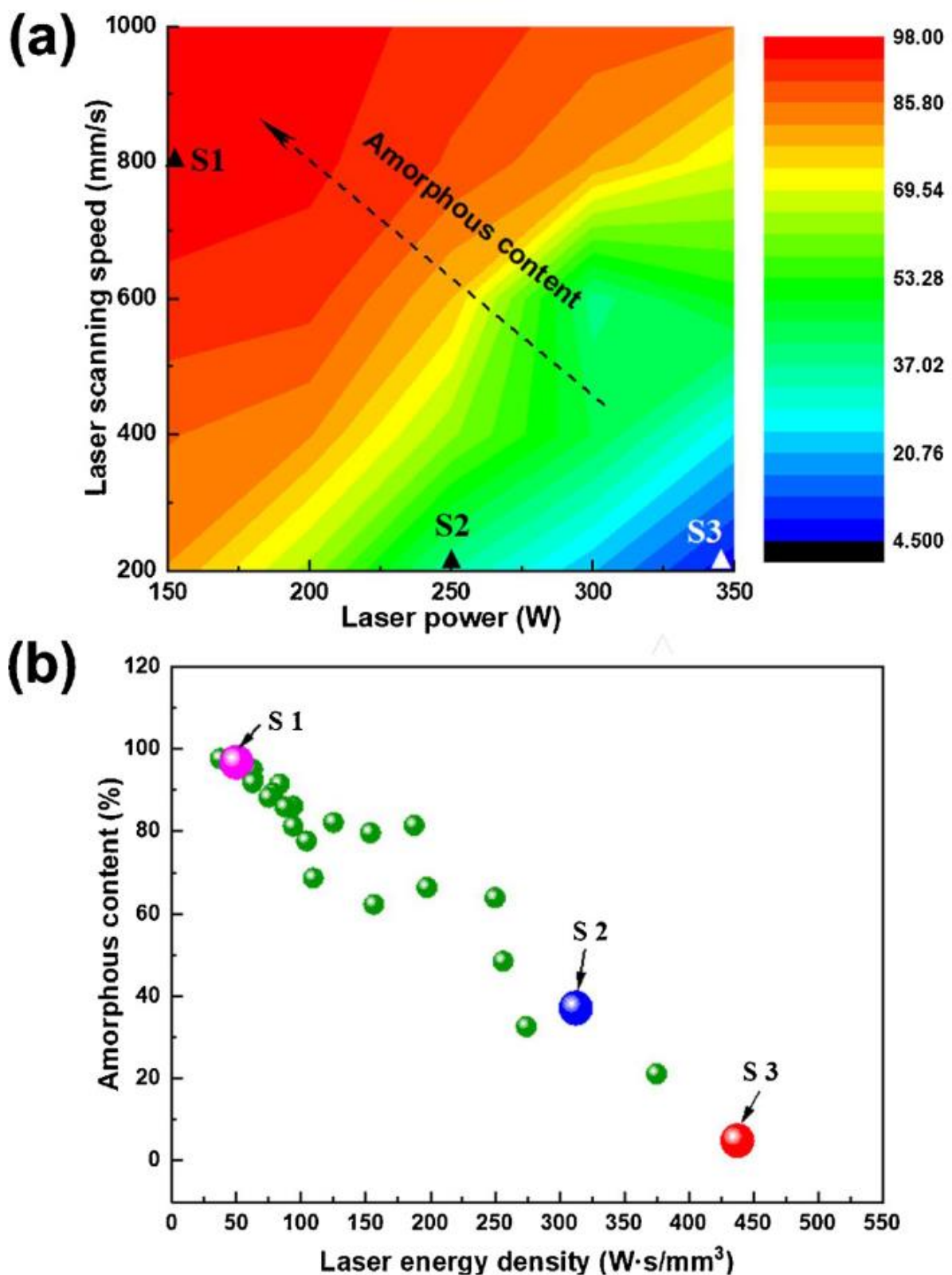


Figure 3.10: (a) Amorphous content of LPBF $Fe_{43.7}Co_{7.3}Cr_{14.7}Mo_{12.6}C_{15.5}B_{4.3}Y_{1.9}$ glassy alloys, 3D-printed by using different laser powers and laser scan speeds. The data were interpolated between the measured data points. (b) The graph compares the laser energy density and amorphous content of LPBF specimens, reprinted with the permission from [72], Elsevier, 2018 (S1, S2 and S3 have the laser energy densities of $36.8 J/mm^3$, $245.3 J/mm^3$ and $343.3 J/mm^3$).

A novel scanning strategy has been introduced for amorphization of Fe-based alloys with low glass forming ability with LPBF as well as for ensuring enhanced magnetic properties [77]. For this purpose, $\text{Fe}_{71}\text{Si}_{10}\text{B}_{11}\text{C}_6\text{Cr}_2$ (at. %) was used. The strategy comprises of (1) the preliminary laser melting the loose powder by using a checkboard strategy, (2) second melting (remelting) by random pulses (point-random (P-R) strategy) and (3) finally short-pulse amorphization as shown in Figure 3.11. In the checkboard strategy, edge length of 1 mm and laser power of 20 W with 90° rotations (a standard alternating scanning strategy) were used with an exposure time of 500 μs . In the P-R strategy, minimum distance of 1 mm between successive points and maximum laser power of 120 W was exploited. Both melting processes were carried out by using the same focal diameter of 40 μm .

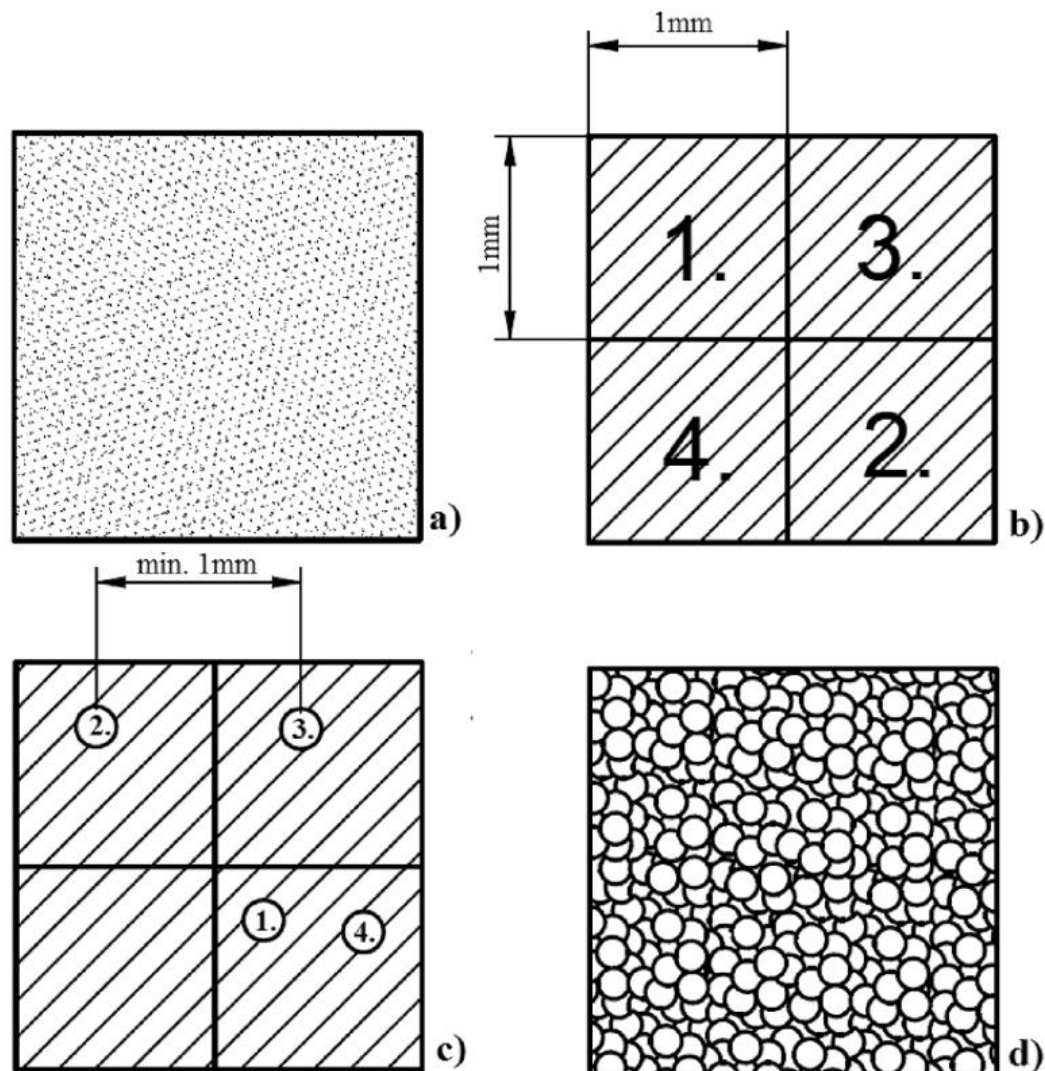


Figure 3.11: Production scheme of one layer of $\text{Fe}_{71}\text{Si}_{10}\text{B}_{11}\text{C}_6\text{Cr}_2$ alloys with the novel scanning strategy (a) loose powder, (b) preliminary laser melting of loose powder by using checkboard strategy (Sample A), (c) re-melting with P-R strategy (Sample B) – numbers stand for scanning order, (d) completely remelted layer [77].

It is reported that the novel scanning strategy has enabled the restoration of 89.6% of the amorphous structure of the parent alloy in spite of its low glass-forming ability and considerable crystallisation during the preliminary melting. After P-R scanning (second melting), the amorphous phase appears as a continuous matrix, rather than forming separate regions, as is observed in the specimens produced with a single melting. In addition, second melting increases the density of the bulk sample from 78.2% to 94.1%.

It is assumed that if the amorphous phase is heated by a laser pulse to a maximum temperature with a heating rate lower than the critical value, it devitrifies. In this study the critical heating rate was calculated as 8.77×10^6 K/s, at which the amorphous phase does not devitrify till the melting point of the material is reached. The heating rate for the preliminary melting (pulse duration (exposure time) 500 μ s) (Sample A) was estimated as 2.5×10^6 K/s, which is below the critical heating rate value. The heating rate of the second melting (P-R remelting with the pulse duration of 20 μ s) (Sample B) was approximated as 6.25×10^7 K/s, which is higher than the critical heating rate [77].

It is indicated that this strategy has a positive effect on soft magnetic properties. Coercivity was reduced substantially after the second melting (using P-R scanning) as seen in Table 3.2. Stress relief annealing at 820 K provided further reduction in coercivity. On the other hand, the M-H hysteresis loops (Figure 3.12) show that the saturation magnetisation seems to be the same for all samples except sample A within the margin of error.

Table 3.2: Coercivity of feedstock powder and melted samples of Fe₇₁Si₁₀B₁₁C₆Cr₂ (at. %) alloy (reprinted with the permission from [77], Elsevier, 2019).

Sample	Coercivity (A/m)
Powder	99
Melted once	1032
Melted twice	397
Melted twice and annealed	238

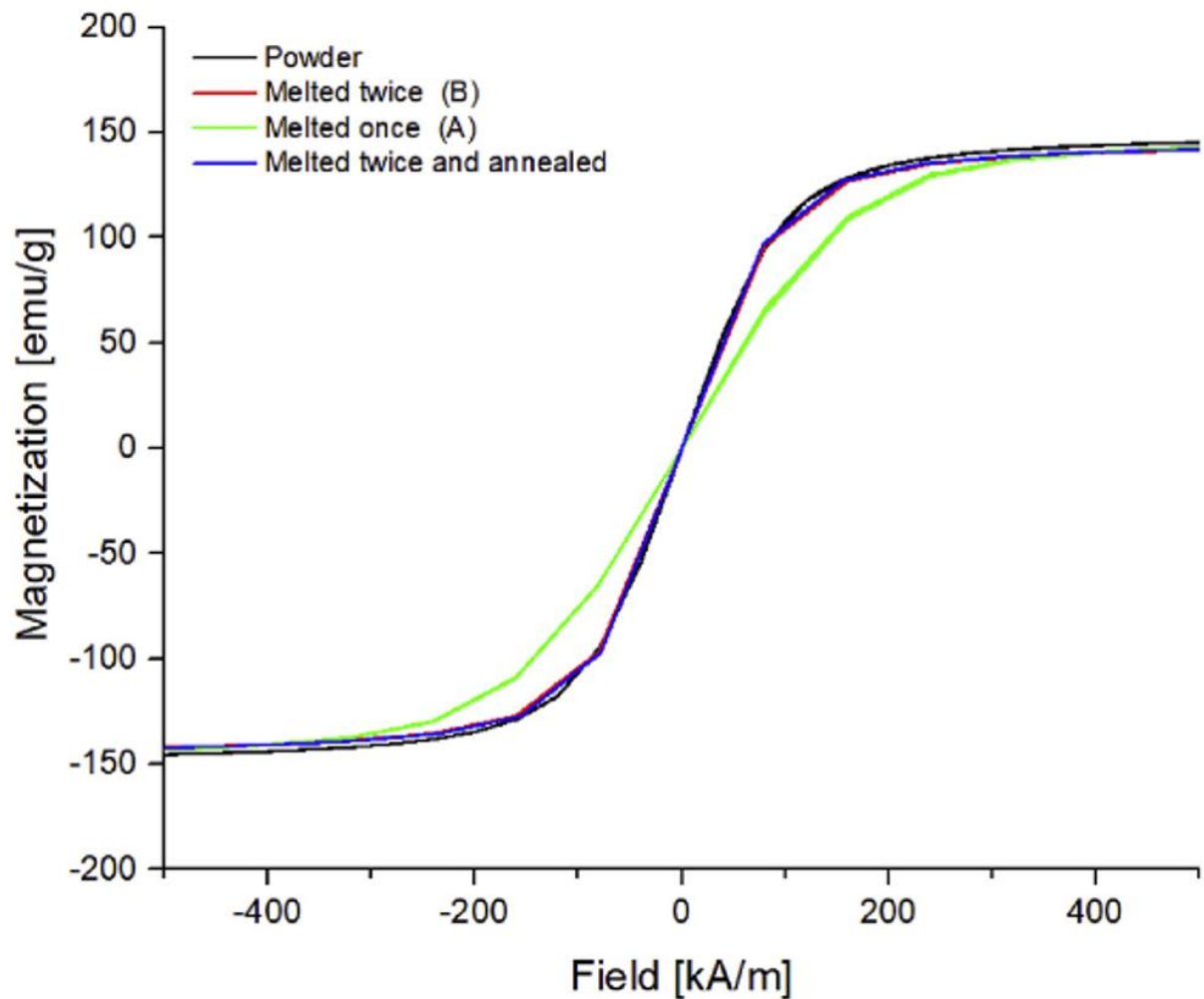


Figure 3.12: *M-H* hysteresis loops for $\text{Fe}_{71}\text{Si}_{10}\text{B}_{11}\text{C}_6\text{Cr}_2$ parent powder, samples A (produced by melting each powder layer twice), and sample B after annealing, reprinted with the permission from [77], Elsevier, 2019 (CGS to SI conversion $1 \text{ emu/g} = 1 \text{ Am}^2/\text{kg}$ and $1 \text{ Oe} = 79.6 \text{ A/m}$).

Most recently, Nam *et al.* have utilised a similar scanning technique as in Reference [77], referred to as the double-scan strategy, to achieve full verification and densification of Fe-based BMGs having high magnetic saturation [76]. In the double-scan strategy, before the coating of a subsequent powder layer over the build area, every $\text{Fe}_{73.7}\text{Si}_{11}\text{B}_{11}\text{C}_2\text{Cr}_{2.28}$ amorphous powder layer was rescanned (remelted) with the linear scan method using the same laser power and laser scan speed as the first laser scanning. In this study, they compared the double-scanning strategy with a single scan in terms of relative density (Figure 3.13(b)), transverse rupture strength (TRS) (Figure 3.13(c)) and magnetic properties as a function of laser energy density, calculated using equation 3.1. It was found that double scanning enables effective shrinkage of voids formed because of partial melting of powder (Figure 3.13(d)), resulting in a relative density of maximum 96% and corresponding to the mechanical strength (TRS) of 75

MPa. This was achieved at the highest E_d of 37.5 J/mm^3 (high power of 90 W and low scanning speed of 1200 mm/s) as it is shown in Figure 3.13(d).

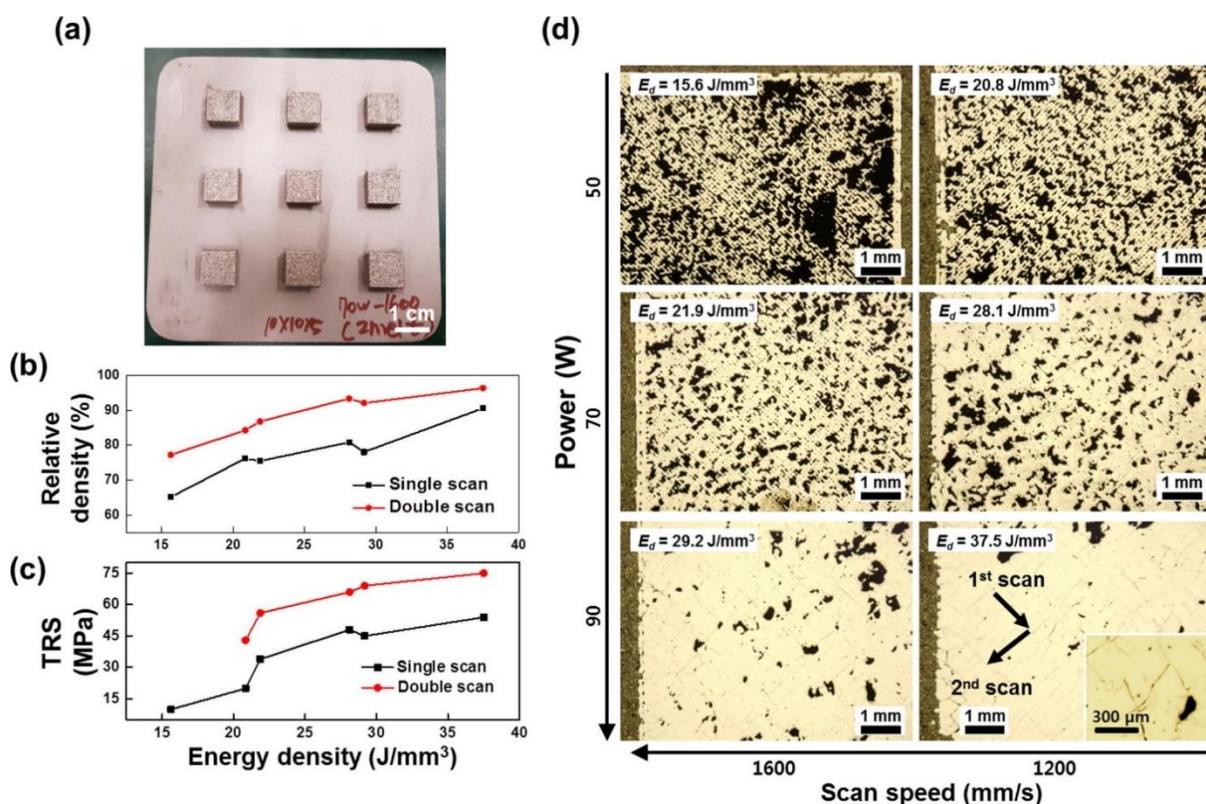


Figure 3.13: The graph of (a) macroscopic photograph of 3D-printed $\text{Fe}_{73.7}\text{Si}_{11}\text{B}_{11}\text{C}_2\text{Cr}_{2.28}$ alloys, (b) relative density and (c) transverse rupture strength (TRS) versus laser energy density and (d) optic microscope images of double-scanned alloys (reprinted with the permission from [76], Elsevier, 2020).

From the graphs in Figure 3.14, it is obvious that double scanning improves magnetic properties significantly. Magnetic saturation has a linear dependence on the E_d and a maximum M_s value of 1.22 T was attained with double scanning. Coercivity tends to increase with increasing E_d because higher E_d provides enough time for crystals to nucleate and grow, by lowering the cooling rate. This leads to a reduction in the amorphous fraction (f_{am}), which was found to be 47% for E_d of 29.2 J/mm^3 . X-ray powder diffraction (XRD) results (Figure 3.15) show that the intensity of the $\alpha\text{-Fe}$ crystallite peak lowers as E_d decreases, implying that the fraction of the crystallite phase reduces.

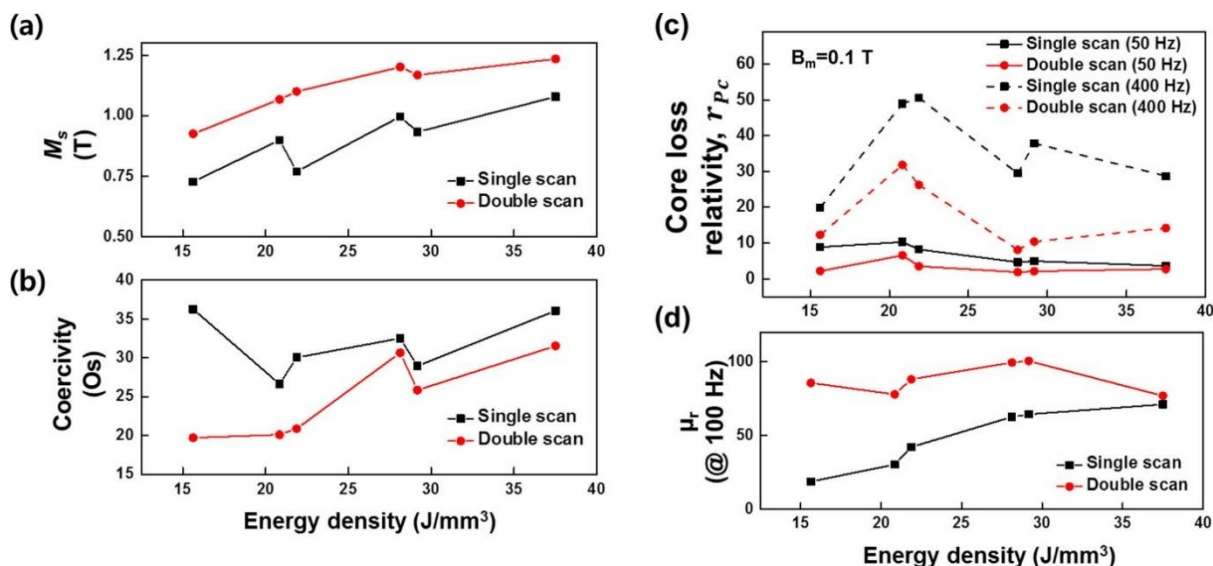


Figure 3.14: The graph of (a) magnetic saturation (M_s), (b) coercivity (in Oe), (c) core loss relativity and (d) relative permeability, μ_r , taken as at 100 Hz frequency (@ 100 Hz) versus laser power density for 3D-printed $Fe_{73.7}Si_{11}B_{11}C_2Cr_{2.28}$ alloys (reprinted with the permission from [76], Elsevier, 2020).

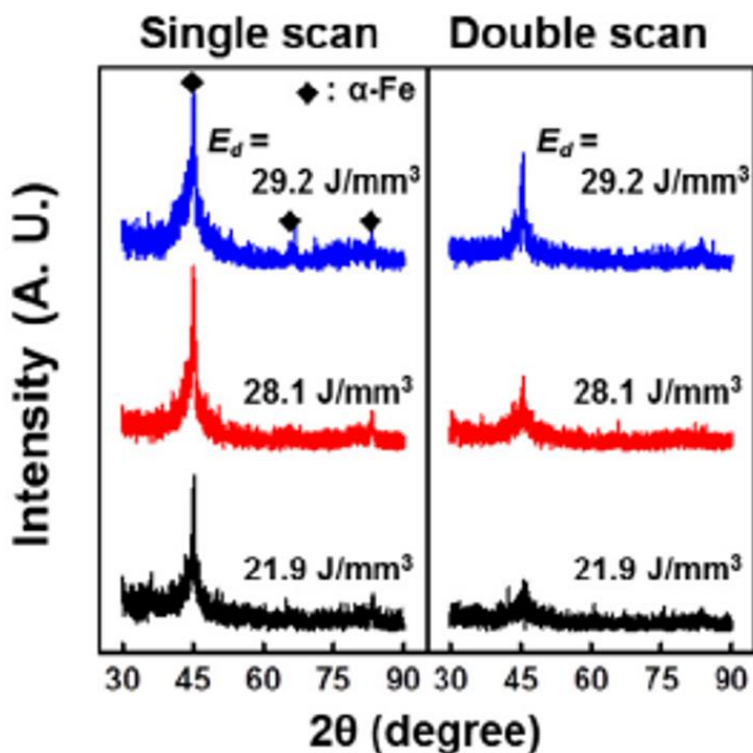


Figure 3.15: X-ray powder diffraction (XRD) patterns of 3D-printed $Fe_{73.7}Si_{11}B_{11}C_2Cr_{2.28}$ alloys with different laser energy density (reprinted with the permission from [76], Elsevier, 2020).

In conclusion, LPBF has been successfully used to produce Fe-based BMGs because it provides high cooling rates 10^3 – 10^4 K/s [55] but depends strongly on the process parameters used such as laser power and laser scan speed [57]. Low laser power and high laser scan speed leads to low energy input onto the powder, causing high cooling

rate. Although decreasing the energy input, enables an increase in the amorphous fraction of the magnetic alloy, it adversely affects full densification, which requires a high energy density. Hence, low energy input results in poor mechanical properties (hardness and mechanical strength). It is crucial that optimum process parameters are defined for both full densification and amorphous structure. The studies indicate that double scanning (remelting) helps to increase the glassy phase content and relative density and improve soft magnetic and mechanical properties [76].

3.3.2 Direct Energy Deposition

Direct energy deposition (DED) has been utilised for fabricating high-performance super-alloys. It contains several techniques, which are laser-engineered net shaping (LENS), laser solid forming (LSF), directed light fabrication (DLF), direct metal deposition (DMD), electron-beam AM (EBAM), and wire and arc AM (WAAW). In DED, laser or electron beams are used as a source of energy, which is directed onto a specific location of the substrate and exploited to melt feedstock materials (wires or powder) at the same time. Then, the molten materials are deposited and fused onto the substrate. This process continues layer by layer until the 3D part is built (Figure 3.16) [78]. Differently from LPBF, DED has no powder bed, and the feedstock is melted, then deposited into substrate in a layer-by-layer manner, enabling both multiple materials and multiple axis deposition simultaneously.

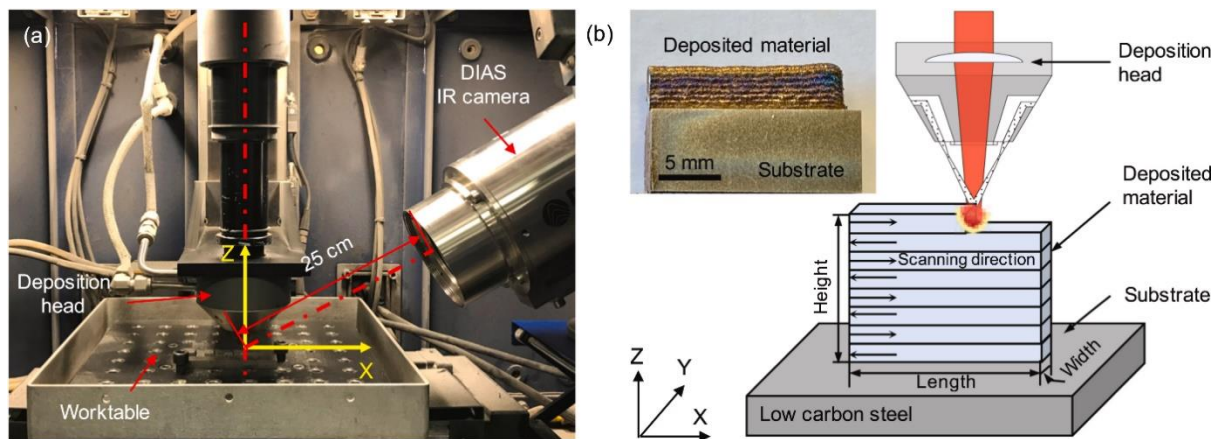


Figure 3.16: (a) The experimental setup and (b) the schematics of the laser-engineered net shaping (LENS) process (reprinted with the permission from [79], Elsevier, 2020).

The LENS technique generally has been utilised to produce Fe-based BMGs because it provides (i) a high cooling rate (10^3 – 10^5 K/s) [80], (ii) less dilution at the substrate-layer interface, restricting crystallisation and (iii) tailorable process parameters with net shape production ability [81].

To prevent crystallisation in BMGs during the LENS process, laser power, laser scan speed and substrate temperature are the main parameters that can be controlled. The total heat input per unit area, I , is utilised to combine first two parameters along with the beam diameter as follows:

$$I = \frac{P}{vD} \quad (3.2)$$

where P is the laser power (W), v is the laser scanning speed (mm/s), and D is the laser beam diameter on the substrate (mm) [82]. It is obvious from Equation 3.2 that reducing laser power and increasing laser scanning speed brings about a lower heat input [83], similarly to the LPBF process as mentioned in Section 3.3.1. The lower the heat input, the higher the cooling rate due to high thermal gradients, which restricts crystallisation. Moreover, in order to maintain high cooling rates and obtain BMGs with maximum amorphous content, it is crucial that substrate temperature is kept as low as possible.

There are two ways to estimate the cooling rate during LENS processing. First one includes the use of the following equation:

$$\frac{dT}{dt} = RG \quad (3.3)$$

where dT/dt (K/s) is the cooling rate, R (mm/s) is the solidification velocity and G (K/mm) is the local thermal gradient [84]. Through experiments, it has been presented that R is in the order of the laser scanning speed (v) [85], which is 20 mm/s in the study by Balla *et al.* [81], and G is approximately 100 K/mm [80]. Hence, by using this study, the cooling rate in the melt zone calculated using Equation (3.3) is approximated to be 2000 K/s, which is more than enough to produce an amorphous NSSHS7574 alloy with a critical cooling rate of 610 K/s [86]. Still, in order to make better estimations of cooling rates, it is necessary to take into consideration the substrate or prior deposit temperature, temperature change in the melt zone, laser input and the thermal conductivity of substrate and deposited alloys. Despite the complicated physics of laser surface melting [87, 88], improved approximation of cooling rates during laser surface melting can be achieved by using the Rosenthal solution for a mobile heat source Equation 3.4, as presented by Steen [88].

$$\frac{dT}{dt} = -2\pi k \left(\frac{v}{Q}\right) \Delta T^2 \quad (3.4)$$

where k is the thermal conductivity of the substrate (W/mm.K), v is the laser scan speed (mm/s), Q is the laser power (W) and ΔT is the temperature range during cooling (K). It confirms that reducing the laser power and increasing the laser scan speed provides a higher cooling rate during laser-based additive manufacturing processes (Equation 3.4). In addition, by using Equation 3.4, the cooling rates were quantified for different substrate/prior deposit temperature, which indicates that the

cooling rate increases when the prior deposit temperature decreases (Equation 3.4) [81].

In the production of Fe-based amorphous alloys with LENS, the initial attempt was made by Balla and Bandyopadhyay [81], who used a gas-atomised NanoSteel NSSHS7574 glass-forming alloy powder of $\text{Cr}_{<25}\text{Mo}_{<15}\text{W}_{<10}\text{C}_{<3}\text{Mn}_{<5}\text{Si}_{<2}\text{B}_{<5}\text{Fe}_{\text{balance}}$ (at. %) with a particle size in the range of 53 and 180 μm . Laser power of 250 W and laser scan speed of 20 mm/s were chosen to reduce heat input and to melt amorphous powder. In addition, even though no direct technique exists to control substrate and prior deposit temperature during the LENS process, in order to keep substrate temperature/prior deposit temperature low, a five-seconds delay was inserted between each successive layer with argon gas flowing through the powder delivery nozzles.

In this study, the cooling rate for the NSSHS7574 alloy was approximated to be in the range of 3.38×10^3 and 1.72×10^3 K/s using Equation 3.4, which is higher than the critical cooling rate (610 K/s) required for complete amorphisation of NSSHS7574 alloy. Even though theoretically the process parameters used in this study are ideal to obtain full amorphous alloys, XRD (Figure 3.17), differential scanning calorimetry (DSC) (Figure 3.18) and microstructural analysis (Figure 3.19) of the 3D-printed alloy exhibit partial crystallisation/incomplete amorphization. It is thought that the reason for that is the coarse feedstock powder (53–108 μm), only partially melted during deposition because of the low heat input (14 J/mm²). Those partially melted particles are found in the deposit with a melted and resolidified surface having amorphous structure, surrounded with crystalline features as shown in Figure 3.19. It was concluded that to obtain fully amorphous alloys with the help of the LENS technique, the use of a finer starting powder would enable complete melting with the same process parameters, or increasing the heat input would allow for melting particles completely without influencing negatively the critical cooling rate needed to achieve full amorphization [81].

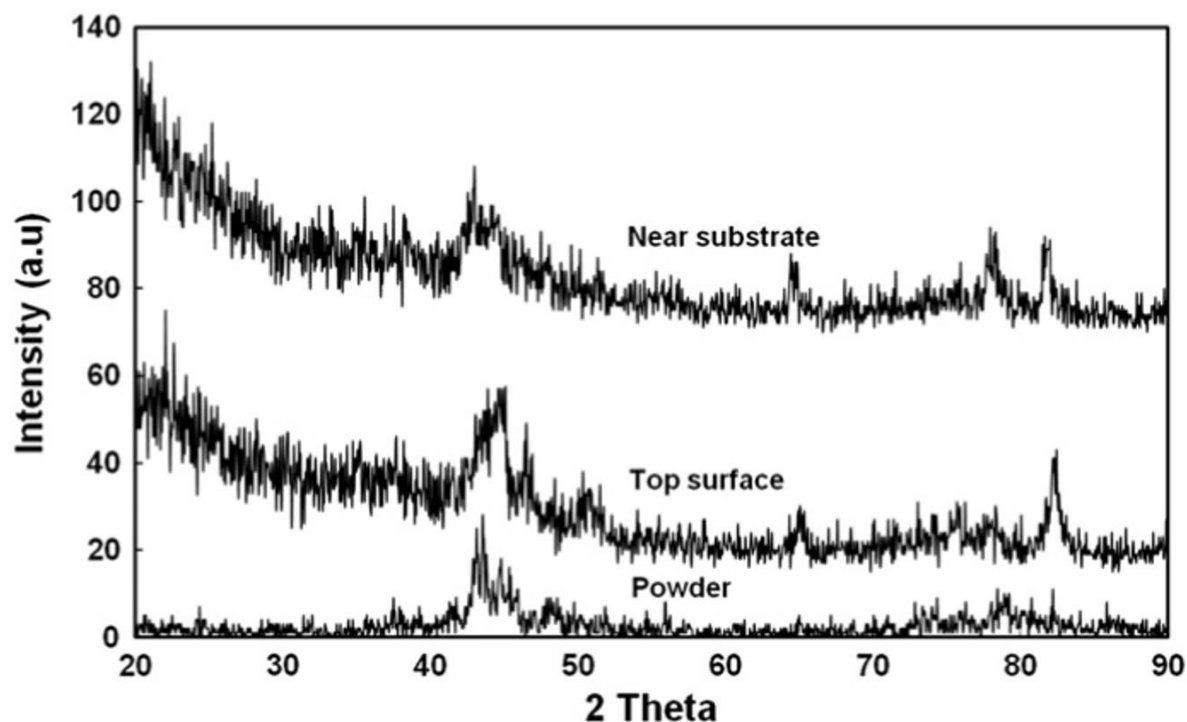


Figure 3.17: XRD patterns of the top surface (15 mm for substrate) and near substrate (0.8 mm from substrate) of LENS processed Fe-based BMGs compared to NSSHS7574 starting powder [81].

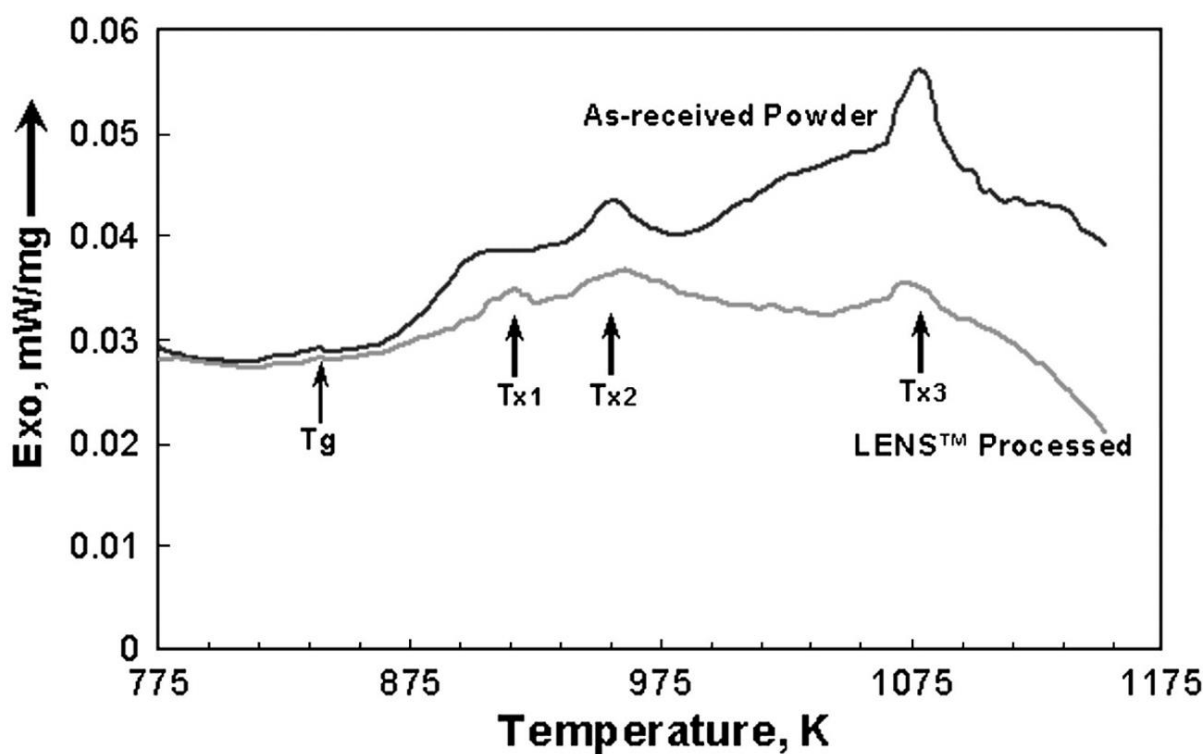


Figure 3.18: Differential scanning calorimetry (DSC) curves of the feedstock powder and the 3D-printed NSSHS7574 alloy, depicting three crystallisation peaks with three-stage crystallisation behaviour, reprinted with the permission from [81], Elsevier, 2010 (T_g is glass transition temperature and T_{x1} , T_{x2} and T_{x3} are crystallisation temperatures, showing that the material undergoes a three-stage crystallisation process upon heating).

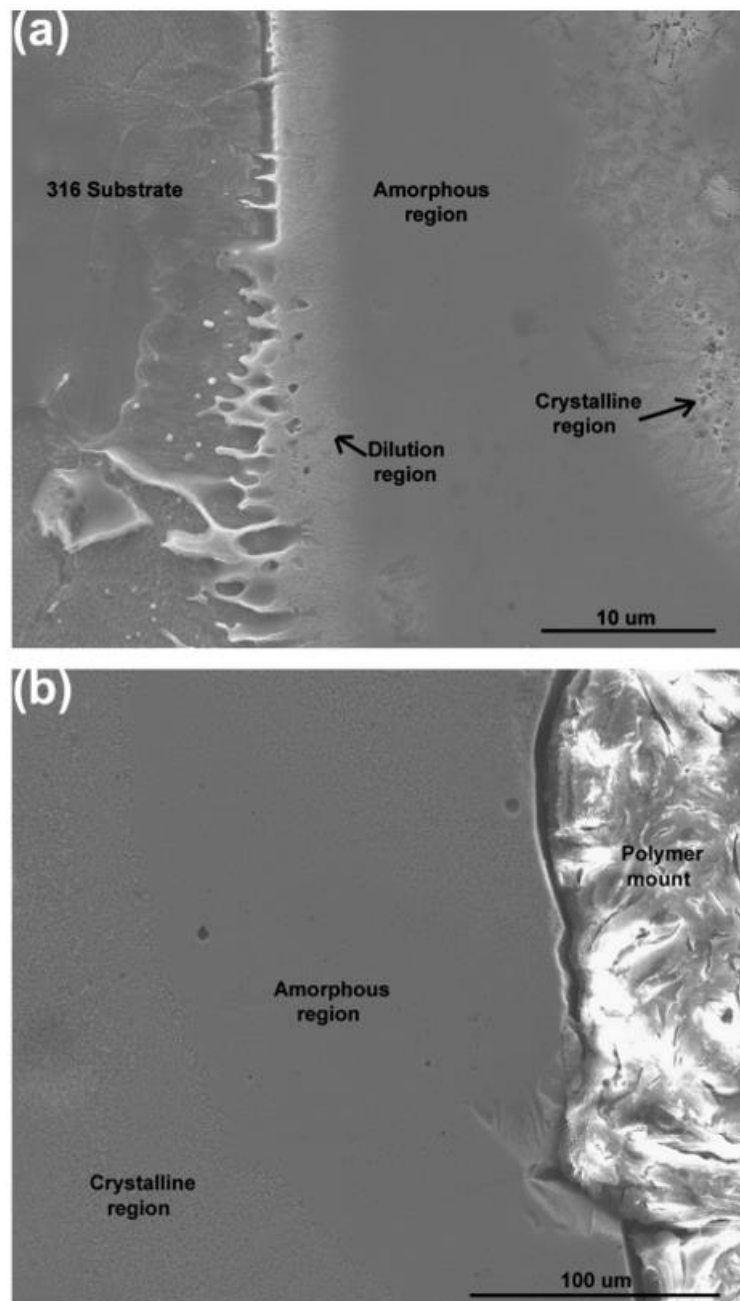


Figure 3.19: Cross-sectional SEM micrographs of 3D-printed NSSHS7574 alloy (a) demonstrating exceptional interfacial bonding between substrate and the produced alloy (b) the microstructure at the top region of the bulk specimen (reprinted with the permission from [81], Elsevier, 2010).

Borkar *et al.* produced a compositionally graded Fe-Si-B-Nb-Cu alloy with varying Si/B ratios by using the LENS technique [5]. It was observed that dendrite formation occurred in the amorphous matrix, which is associated with constitutional supercooling because of the compositional differences between the crystal and amorphous matrix [89-91]. The partitioning of Si at the interface of α -Fe/amorphous matrix causes the constitutional supercooling, promoting the dendrite formation owing to interfacial instability. Furthermore, it was found that Fe-Si-B-Nb-Cu alloy

with a Si/B ratio of around 1.7 showed considerably low coercivity (1512 A/m) and higher magnetic saturation (143 Am²/kg) compared with the other FeSiBNbCu samples with different Si/B ratios.

The effect of laser process parameters on the hardness of Fe-based BMGs produced by LENS was studied by Xie *et al.* [92], who used Fe₄₁Co₇Cr₁₅Mo₁₄C₁₅B₆Y₂ (at. %) amorphous spherical powder and different laser energy densities. The variation in hardness as a function of laser energy density (LED) is illustrated in Figure 3.20. It is obvious that hardness increases as LED lowers. The use of the lowest energy density of 30 J/mm led to the highest hardness of 1263.7 HV. This value is significantly close to the hardness of cast Fe₄₁Co₇Cr₁₅Mo₁₄C₁₅B₆Y₂ amorphous alloy (1253 HV) [93], which suggests that the printed specimen retained a certain amount of its amorphous phase.

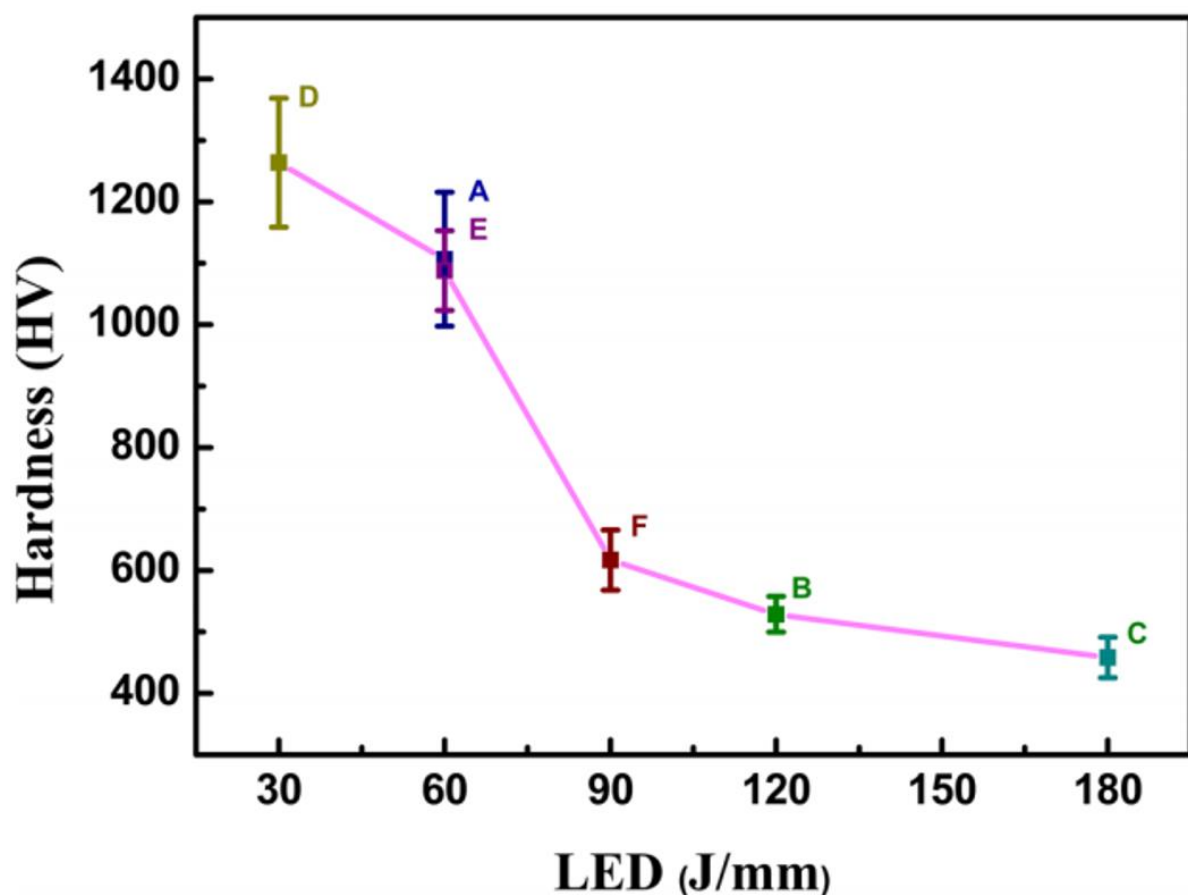


Figure 3.20: Hardness of the LENS-processed Fe₄₁Co₇Cr₁₅Mo₁₄C₁₅B₆Y₂ amorphous alloys as a function of laser energy density (LED) (A, B, C, D, E and F denote Fe₄₁Co₇Cr₁₅Mo₁₄C₁₅B₆Y₂ samples that were produced using different laser parameters, i.e., laser energy density (LED). A and E have the same LED; however, for A, $P = 300$ W and $v = 5$ mm/s and for E, $P = 600$ W and $v = 10$ mm/s, for B: $P = 600$ W and $v = 5$ mm/s, for C: $P = 900$ W and $v = 5$ mm/s, for D: $P = 300$ W and $v = 10$ mm/s and for F: $P = 900$ W and $v = 10$ mm/s) (reprinted with the permission from [92], Springer, 2019).

In general, the LENS technique has not been much used in the production of magnetic amorphous alloys because it has lower geometric accuracy (0.25 mm) and lower surface quality, requiring post-processing [94] and can only fabricate less complicated components compared with LPBF [78]. Consequently, LENS is commonly utilised for large parts with low complexity [35] and for repairing them [95], which restricts the fabrication of amorphous alloys by LENS due to their size limitation. All the drawbacks aside, the benefit of using LENS is the ability to produce parts with superior mechanical properties, controlled composition, and microstructure [35]. As explained in this section, generating amorphous alloys with the LENS technique is possible by lowering laser energy input (low laser power and high scan speed similar to LPBF) and reducing substrate/prior deposit temperature.

Table 3.3 gives a summary of the different materials and AM techniques described in this paper. It is observed that Fe-based magnetic alloys with various amorphous content up to 100% can be produced by the LPBF technique by changing process parameters. It can be said that even though both of the elemental compositions and powder sizes of the feedstock powder in [76, 77] are quite similar to each other, the LPBF processes alloys have different amorphous phase fractions and magnetic properties due to the different process parameters and scanning strategy, as mentioned in Section 3.3.1. This means that laser process parameters and scanning strategy play critical roles in the production of amorphous alloys with laser additive manufacturing. From the perspective of magnetic properties, while the produced alloy in [8] possesses relatively low magnetic saturation and coercivity, the glassy alloy in Ref. [69] has relatively high saturation magnetisation and coercivity. This may be due to the different alloy design and composition, process parameters or problems that occurred during the production, causing structural defects. It is indicated in Table 3.3 that LPBF-processed glassy alloy ($\text{Fe}_{71}\text{Si}_{10}\text{B}_{11}\text{C}_6\text{Cr}_2$ (at. %)) has the best soft magnetic properties (that is, high saturation magnetisation and low coercivity) resulting from the double scanning strategy (remelting) carried out during the LPBF process. The last three rows in Table 3.3 represent the Fe-based amorphous materials produced by the LENS technique. As stated before, the LENS technique has not been studied extensively in fabricating amorphous alloys due to the process-related problems. Considering the hardness values of the FeCrMoCB alloy produced by LPBF [62] and the $\text{Fe}_{41}\text{Co}_7\text{Cr}_{15}\text{Mo}_{14}\text{C}_{15}\text{B}_6\text{Y}_2$ (at. %) alloy fabricated by LENS [92], it can be said that LENS provides more mechanical strength than the LPBF technique.

Chapter 3 – Literature Review Paper

Table 3.3: Amorphous content, magnetic and mechanical properties of Fe-based alloys produced by laser additive manufacturing, also showing process parameters and powder size of starting powder.

Alloy	Powder Size (μm)	Technique	Process Parameters		Amorphous content (%)	Magnetic Properties			Reference
			P (W)	v (m/s)		M_s	H_c (A/m)	Hardness (HV)	
$\text{Fe}_{68.3}\text{C}_{6.9}\text{Si}_{2.5}\text{B}_{6.7}\text{P}_{8.7}\text{Cr}_{2.3}\text{Mo}_{2.5}\text{Al}_{2.1}$	<150	LPBF	340	1.5, 2.5	Unknown	102.8, 103.6 Am^2/kg	27.9 31.6	-	[8]
FeCrMoCB	<80	LPBF	80-200	0.8-5	100 ^a	-	-	902	[62]
$\text{Fe}_{92.4}\text{Si}_{3.1}\text{B}_{4.5}$	< 30	LPBF	90	0.1-1.5	70-80	188.6-199 Am^2/kg	3485.5-5809.2	1654-2273	[69]
$\text{Fe}_{43.7}\text{Co}_{7.3}\text{Cr}_{14.7}\text{Mo}_{12.6}\text{C}_{15.5}\text{B}_{4.3}\text{Y}_{1.9}$ (at.%)	< 33	LPBF	150-350	0.2-1	4.96-100	-	-	-	[72]
$\text{Fe}_{71}\text{Si}_{10}\text{C}_6\text{Cr}_2$ (at.%)	~24.5	LPBF	Max 120	-	89.6	~150 Am^2/kg	238	-	[77]
$\text{Fe}_{73.7}\text{Si}_{11}\text{B}_{11}\text{C}_2\text{Cr}_{2.28}$	~25	LPBF	50, 70, 90	1.2, 1.6	47	1.22 T ($\text{kg}/\text{s}^2\text{A}$)	1591.5-2387.3	-	[76]
Fe-Si-B-Nb-Cu	<150	LENS	-	-	-	118-150 Am^2/kg	1273.2-3819.7	-	[5]
$\text{Cr}_{<25}\text{Mo}_{<15}\text{W}_{<10}\text{C}_{<3}\text{Mn}_{<5}\text{Si}_{<2}\text{B}_{<5}\text{Fe}_{\text{balance}}$ (at. %)	<180	LENS	250	0.02	-	-	-	1421 \pm 101	[81]
$\text{Fe}_{41}\text{Co}_7\text{Cr}_{15}\text{Mo}_{14}\text{C}_{15}\text{B}_6\text{Y}_2$ (at.%)	-	LENS	300, 600, 900	0.005, 0.01	-	-	-	1263.7	[92]

^a According to the XRD analysis, the part is fully amorphous.

3.4 Conclusions

This paper provides a review of laser additive manufacturing found in the literature for Fe-based amorphous alloys. The literature demonstrates that laser additive manufacturing, which contains directed energy deposition and powder-bed fusion, is a promising process to produce Fe-based glassy alloys with good soft magnetic properties. The LPBF technique from the powder-bed fusion category and the LENS technique from the directed energy deposition category have been used for that purpose within the literature, resulting from their high availability, low cost and being less time-consuming compared with the conventional techniques that have been used to produce amorphous alloys, such as casting. In both techniques, amorphous alloys were manufactured by altering the process parameters. Generally, low energy input, achieved via low laser power and high laser scanning speed, brings about increased amorphous phase content due to a higher cooling rate, but decreases relative density and deteriorates mechanical properties. To overcome this limitation, the double scanning (remelting) strategy has been employed, which results in enhancing both magnetic and mechanical properties. Additionally, in the LENS process, it is also necessary to consider the substrate/prior deposit temperature, to ensure that it is kept as low as possible to obtain a high cooling rate. LPBF has been utilised more than LENS in the fabrication of Fe-based amorphous alloys, since LENS is not preferred for the production of small parts because of low geometric accuracy and poor surface quality. This contradicts with the size limitation of glassy alloys owing to their high critical cooling rates.

References

- [1] E. Perigo, J. Jacimovic, F. Garcia Ferre and L. Scherf, "Additive Manufacturing of magnetic materials," *Additive Manufacturing*, vol. 30, p. 100870, 2019.
- [2] V. Franco, J. Blazquez, J. Ipus, J. Law, L. Moreno-Ramirez and A. Conde, "Magnetocaloric effect: From materials research to refrigeration devices," *Progress in Materials Science*, vol. 93, pp. 112-232, 2018.
- [3] C. Smith, S. Katakam, S. Nag, Y. Zhang, J. Law, R. Ramanujan and R. Banerjee, "Comparison of the crystallisation behaviour of Fe-Si-B-Cu and Fe-Si-B-Cu-Nb-based amorphous soft magnetic alloys," *Metallurgical and Materials Transactions A*, vol. 45, no. 7, pp. 2998-3009, 2014.

- [4] F. Wan, A. He, J. Zhang, J. Song, A. Wang, C. Chang and X. Wang, "Development of FeSiBNbCu nanocrystalline soft magnetic alloys with high Bs and good manufacturability," *Journal of Electronic Materials*, vol. 45, pp. 4913-4918, 2016.
- [5] T. Borkar, R. Conteri, X. Chen, R. Ramanujan and R. Banerjee, "Laser additive processing of functionally-graded Fe–Si–B–Cu–Nb soft magnetic materials," *Materials and Manufacturing Processes*, vol. 32, no. 14, pp. 1581-1587, 2017.
- [6] X. Yang, X. Cui, G. Jin, J. Liu, Y. Chen and Z. Liu, "Soft magnetic property of (Fe₆₀Co₃₅Ni₅)₇₈Si₆B₁₂Cu₁Mo₃ alloys by laser additive manufacturing," *Journal of Magnetism and Magnetic Materials*, vol. 466, pp. 75-80, 2018.
- [7] H. Gavrilă and V. Ionita, "Crystalline and Amorphous Soft Magnetic Materials and Their Applications - Status of Art and Challenges," *Journal of Optoelectronics and Advanced Materials*, vol. 4, no. 2, pp. 173-192, 2002.
- [8] H. Jung, S. Choi, K. Prashanth, M. Stoica, S. Scudino, S. Yi, U. Kuhn, D. Kim, K. Kim and J. Eckert, "Fabrication of Fe-based bulk metallic glass by selective laser melting: A parameter study," *Materials and Design*, vol. 86, pp. 703-708, 2015.
- [9] J. Wang, R. Li, N. Hua, L. Huang and T. Zhang, "Ternary Fe–P–C bulk metallic glass with good soft-magnetic and mechanical properties," *Scripta Materialia*, vol. 65, no. 6, pp. 536-539, 2011.
- [10] M. Shi, Z. Liu and T. Zhang, "Effects of metalloid B addition on the glass formation, magnetic and mechanical properties of FePCB bulk metallic glasses," *Journal of Material Science and Technology*, vol. 31, no. 5, pp. 493-497, 2015.
- [11] Z. Li, A. Wang, C. Chang, Y. Wang, B. Dong and S. Zhou, "FeSiBPNbCu alloys with high glass-forming ability and good soft magnetic properties," *Intermetallics*, vol. 54, pp. 225-231, 2014.
- [12] K. Alvarez, J. Martin, M. Ipatov and J. Gonzalez, "Soft magnetic amorphous alloys (Fe-rich) obtained by gas atomisation technique," *Journal of Alloys and Compounds*, vol. 735, pp. 2646-2652, 2018.
- [13] L. Jeziorski, M. Nabialek, M. Szota and M. Dospial, "Method of continuous casting of amorphous metallic materials based on iron," *Archives of Foundry Engineering*, vol. 11, no. 4, pp. 69-72, 2011.

- [14] M. Nabialek, P. Pietrusiewicz, M. Dospial, M. Szota, K. Bloch, K. Gruzka, K. Ozga and S. Garus, "Effect of manufacturing method on the magnetic properties and formation of structural defects in Fe₆₁Co₁₀Y₈Zr₁B₂₀ amorphous alloy," *Journal of Alloys and Compounds*, vol. 615, pp. 51-55, 2014.
- [15] M. Zhang, F. Kong, A. Wang and C. Chang, "Soft magnetic properties of bulk FeCoMoPCBSi glassy core prepared by copper mould casting," *Journal of Applied Physics*, vol. 111, no. 7, pp. 07A312-07A312-3, 2012.
- [16] Y. Kim, D. Jang, H. Seok and K. Kim, "Fabrication of Fe–Si–B based amorphous powder cores by cold pressing and their magnetic properties," *Material Science and Engineering A*, vol. 449, pp. 389-393, 2007.
- [17] S. Ishihara, W. Zhang, H. Kimura, M. Omori and A. Inoue, "Consolidation of Fe–Co–Nd–Dy–B glassy powders by spark-plasma sintering and magnetic properties of the consolidated alloys," *Materials Transactions*, vol. 44, pp. 138-143, 2003.
- [18] S. Yoshida, T. Mizushima, A. Makino and A. Inoue, "Structure and soft magnetic properties of bulk Fe–Al–Ga–P–C–B–Si glassy alloys prepared by consolidating amorphous powders," *Material Science and Engineering A*, Vols. 304-306, pp. 1019-1022, 2001.
- [19] A. Inoue, "Stabilization of metallic supercooled liquid and bulk amorphous alloys," *Acta Materialia*, vol. 48, pp. 279-306, 2000.
- [20] R. Cahn, *Rapidly solidified alloys*, New York: Marcel Dekker Inc., 1993.
- [21] H. Davies and M. Gibbs, "Volume 4: Novel Materials," in *Handbook of Magnetism and Advanced Magnetic Materials*, London, John Wiley and Sons, 2007.
- [22] R. Boll, H. Hilzinger and H. Warlimont, *The magnetic, chemical and structural properties of glassy metallic alloys*, Boca Raton, FL: CRC Press, 1983.
- [23] G. Herzer, "Modern soft magnets: Amorphous and nanocrystalline materials," *Acta Materialia*, vol. 61, pp. 718-734, 2013.
- [24] S. Katakam, J. Hwang, S. Paital, R. Banerjee, H. Vora and N. Dahotre, "Laser-induced thermal and spatial nanocrystallization of amorphous Fe–Si–B alloy," *Scripta Materialia*, vol. 66, pp. 538-541, 2012.

- [25] R. Elhajjar, C. Law and A. Pegoretti, "Magnetostrictive polymer composites: Recent advances in materials, structures and properties," *Progress in Materials Science*, vol. 97, pp. 204-229, 2018.
- [26] S. Na, J. Galuardi and A. Flatau, "Consolidation of magnetostrictive (001)-oriented Fe-Ga flakes for 3D printing powder materials," in *IEEE International Magnetism Conference (INTERMAG)*, Dublin, 2017.
- [27] A. Al-Taher, R. Reiss, A. Lafferty, S. Hayes, N. Lupu, I. Murgulescu and N. Morley, "Magnetostrictive Materials for aerospace applications," *Journal of Physics: Conference Series*, vol. 903, p. 012010, 2017.
- [28] K. Hathaway and A. Clark, "Magnetostrictive Materials," *Materials Research Society Bulletin*, vol. 18, no. 4, pp. 34-41, 1993.
- [29] C. Moron, C. Cabrera, A. Moron, A. Garcia and M. Gonzalez, "Magnetic Sensors Based on Amorphous Ferromagnetic Materials: A Review," *Sensors*, vol. 15, pp. 28340-28366, 2015.
- [30] M. Poletti and L. Battezzati, "Assessment of the ternary Fe-Si-B phase diagram," *CALPHAD: Computer Coupling of Phase Diagrams and Thermochemistry*, vol. 43, pp. 40-47, 2013.
- [31] D. Jiles, *Introduction to Magnetism and Magnetic Materials*, third edition, New York: CRC Press: Taylor and Francis Group, 2016.
- [32] Z. Sun, X. Tan, S. Tor and W. Yeong, "Selective laser melting of stainless steel 316L with low porosity and high build rates," *Materials and Design*, vol. 104, pp. 197-204, 2016.
- [33] S. Sing, J. An, W. Yeong and F. Wiria, "Laser and electron-beam powder-bed additive manufacturing of metallic implants: a review on processes, materials and designs," *Journal of Orthopaedic Research*, vol. 34, pp. 369-385, 2016.
- [34] J. Lee and W. Yeong, "Design and printing strategies in 3D bioprinting of cell-hydrogels: a review," *Advanced Healthcare Materials*, vol. 5, pp. 2856-2865, 2016.
- [35] T. Ngo, A. Kashani, G. Imbalzano, K. Nyugen and D. Hui, "Additive manufacturing (3D printing): A review of materials, methods, applications and challenges," *Composite Part B*, vol. 143, pp. 172-196, 2018.

- [36] S. Singh, S. Ramakrishna and R. Singh, "Material issues in additive manufacturing: A review," *Journal of Manufacturing Processes*, vol. 25, pp. 184-200, 2017.
- [37] T. Campbell, C. Williams, O. Ivanona and B. Garrett, "Could 3D Printing Change the World, in: Technologies, Potential, and Implications of Additive Manufacturing," in *Atlantic Council*, Washington, DC, 2011.
- [38] G. Goh, S. Agarwala, G. Goh, V. Dikshit, S. Sing and W. Yeong, "Additive manufacturing in unmanned aerial vehicles (UAVs): Challenges and potential," *Aerospace Science and Technology*, vol. 63, no. 140-151, pp. 140-151, 2017.
- [39] A. Taylor, C. Cuervo, D. Arnold and L. Velasquez-Garcia, "Fully 3D-Printed, Monolithic, Mini Magnetic Actuators for Low-Cost, Compact Systems," *Journal of Microelectromechanical Systems*, vol. 28, no. 3, pp. 481-493, 2019.
- [40] M. Pattron, P. Ryan, T. Calascione, N. Fischer, A. Morgenstern, N. Stenger and B. Nelson-Cheeseman, "Manipulating magnetic anisotropy in fused filament fabricated parts via macroscopic shape, mesoscopic infill orientation, and infill percentage," *Additive Manufacturing*, vol. 27, pp. 482-488, 2019.
- [41] A. Diaz-Garcia, J. Law, A. Cota, A. Bellido-Correa, J. Ramirez-Rico, R. Schafer and V. Franco, "Novel procedure for laboratory scale production of composite functional filaments for additive manufacturing," *Materials Today Communications*, vol. 24, p. 101049, 2020.
- [42] L. Bollig, M. Patton, G. Mowry and B. Nelson-Cheeseman, "Effects of 3-D Printed Structural Characteristics on Magnetic Properties," *IEEE Transactionson on Magnetism*, vol. 53, no. 11, p. 2300806, 2017.
- [43] Y. Arbaoui, P. Agaciak, A. Chevalier, V. Laur, A. Maalouf, J. Ville, P. Roquefort, T. Aubry and P. Queffelec, "3D printed ferromagnetic composites for microwave applications," *Journal of Material Science*, vol. 52, pp. 4988-4966, 2017.
- [44] S. Fafenrot, N. Grimmelsmann, M. Wortmann and A. Ehrmann, "Three-Dimensional (3D) Printing of Polymer-Metal Hybrid Materials by Fused Deposition Modelling," *Materials*, vol. 10, p. 1199, 2017.

- [45] V. Chaudhary, S. Mantri, R. Ramanujan and R. Banerjee, "Additive manufacturing of magnetic material," *Progress in Material Science*, vol. 114, p. 100688, 2020.
- [46] B. Zhang, N. Fenineche, L. Zhu, H. Liao and C. Coddet, "Studies of magnetic properties of permalloy (Fe-30%Ni) prepared by SLM technology," *Journal of Magnetism and Magnetic Materials*, vol. 324, pp. 495-500, 2012.
- [47] C. Mikler, V. Chaudhary, T. Borkar, V. Soni, D. Jaeger, X. Chen, R. Contleri, R. Ramanujan and R. Banerjee, "Laser additive manufacturing of magnetic materials," *Journal of The Minerals, Metals and Materials Society*, vol. 69, no. 3, pp. 532-543, 2017.
- [48] A. Kustas, D. Susan, K. Johnson, S. Whetten, M. Rodriguez, D. Dagel, J. Micheal, D. Keicher and N. Argibay, "Characterization of the Fe-Co-1.5V soft magnetic alloy processed by laser engineered net shaping (LENS)," *Additive Manufacturing*, vol. 21, pp. 41-52, 2018.
- [49] D. Goll, D. Schuller, G. Martinek, T. Kunert, J. Schurr, C. Sinz, T. Schubert, T. Bernthaler, H. Riegel and G. Scheider, "Additive manufacturing of soft magnetic materials and components," *Additive Manufacturing*, vol. 27, pp. 428-439, 2019.
- [50] N. Kang, M. El Mansori, F. Guittonneau, H. Liao, Y. Fu and E. Aubry, "Controllable mesostructured, magnetic properties of soft magnetic Fe-Ni-Si by using selective laser melting from nickel coated high silicon steel powder," *Applied Surface Science*, vol. 455, pp. 736-741, 2018.
- [51] X. Song, W. Zhai, R. Huang, J. Fu, M. Fu and F. Li, "Metal-Based 3D-Printed Micro Parts & Structures," *Encyclopedia of Materials: Metals and Alloys*, vol. 4, pp. 448-461, 2022.
- [52] B. Utela, D. Storti, R. Anderson and M. Ganter, "A review of process development steps for new material systems in three dimensional printing (3DP)," *Journal of Manufacturing Processes*, vol. 10, no. 2, pp. 96-104, 2008.
- [53] H. Lee, C. Lim, M. Low, N. Tham, V. Murukeshan and Y. Kim, "Lasers in additive manufacturing: a review," *International Journal of Precision Engineering and Manufacturing-Green Technology*, vol. 4, no. 3, pp. 307-322, 2017.

- [54] C. Yap, C. Chua, Z. Dong, Z. Liu, D. Zhang, L. Loh and S. Sing, "Review of selective laser melting: materials and applications," *Applied Physics Reviews*, vol. 2, no. 4, p. 041101, 2015.
- [55] S. Pauly, L. Lober, R. Petters, M. Stoica, S. Scudino, U. Kuhn and J. Eckert, "Processing metallic glasses by selective laser melting," *Materials Today*, vol. 16, no. 1, pp. 37-41, 2013.
- [56] B. Zheng, Y. Zhou, J. Smugeresky and E. Lavernia, "Processing and behaviour of Fe-based metallic glass components via laser-engineered net shaping," *Metallurgical and Materials Transactions A*, vol. 40, pp. 1235-1245, 2009.
- [57] D. Gu, W. Meiners, K. Wissenbach and R. Poprawe, "Laser additive manufacturing of metallic components: materials, processes and mechanisms," *International Materials Reviews*, vol. 57, pp. 133-164, 2012.
- [58] M. Khan and P. Dickens, "Selective laser melting (SLM) of pure gold," *Gold Bulletin*, vol. 43, pp. 114-121, 2010.
- [59] R. Dayal, "Numerical Modelling of Processes Governing Selective Laser Sintering," PhD Thesis Technische Universitat Darmstadt, 2014.
- [60] P. Yuan and D. Gu, "Molten pool behaviour and its physical mechanism during selective laser melting of TiC/AlSi10Mg nanocomposites: simulation and experiments," *Journal of Physics D: Applied Physics*, vol. 48, p. 035303, 2015.
- [61] F. Luborsky, *Amorphous Metal Alloys*, London, UK: Butterworths, 1983.
- [62] Z. Mahbooba, L. Thorsson, M. Unosson, P. Skoglund, H. West, T. Horn, C. Rock, E. Vogli and O. Harryson, "Additive manufacturing of an iron-based bulk metallic glass larger than the critical casting thickness," *Applied Materials Today*, vol. 11, pp. 264-269, 2018.
- [63] C. Suryanarayana and A. Inoune, "Iron-based bulk metallic glasses," *International Materials Reviews*, vol. 58, pp. 131-166, 2013.
- [64] Y. Efimov, G. Mukhin, E. Lazarev, N. Korotkov, L. Ryabtsev, V. Dmitriev and T. Frolova, "The structure of rapidly hardened Fe-Si-B alloys," *Russ. Metallurgy*, vol. 4, pp. 167-173, 1986.

- [65] M. Haginora, A. Inonue and T. Masu, "Mechanical properties of FeSiB amorphous wires produced by in-rotating-water spinning method," *Metallurgical and Materials Transactions A*, vol. 13, pp. 373-382, 1982.
- [66] Y. Suwa, S. Agatsuma, S. Hashi and K. Ishiyama, "Study of strain sensor using FeSiB magnetoresistive thin films," *IEEE Transactions on Magnetics*, vol. 46, no. 2, pp. 666-669, 2010.
- [67] S. Li, S. Horikawa, M. Park, Y. Chai, V. Vodyanoy and B. Chi, "Amorphous metallic glass biosensors," *Intermetallics*, vol. 30, pp. 80-85, 2012.
- [68] A. Inoue, M. Komuro and T. Masumoto, "Fe-Si-B amorphous alloys with high silicon concentration," *Journal of Materials Science*, vol. 19, p. 4125, 1984.
- [69] S. Alleg, R. Drablia and N. Fenineche, "Effect of the Laser Scan Rate on the Microstructure, Magnetic Properties, and Microhardness of Selective Laser-Melted FeSiB," *Journal of Superconductivity and Novel Magnetism*, vol. 31, pp. 3565-3577, 2018.
- [70] F. de Boer, R. Boom, W. Mattens, A. Miedema and A. Niessen, *Cohesion in Metals*, Amsterdam: North-Holland, 1988.
- [71] S. Dong, B. Song, X. Zhang, C. Deng, N. Fenineche, B. Hansz, H. Liao and C. Coddet, "Fabrication of FeSiB magnetic coatings with improved saturation magnetization by plasma spray and dry-ice blasting," *Journal of Alloys and Compounds*, vol. 584, pp. 254-260, 2014.
- [72] D. Ouyang, W. Xing, L. Ning, Y. Li and L. Liu, "Structural evolutions in 3D-printed Fe-based metallic glass fabricated by selective laser melting," *Additive Manufacturing*, vol. 23, pp. 246-252, 2018.
- [73] S. Pauly, C. Schricker, S. Scudino, L. Deng and U. Kuhn, "Processing a glass-forming Zr-based alloy by selective laser melting," *Materials and Design*, vol. 135, pp. 133-141, 2017.
- [74] K. Prashanth, S. Scudino, T. Maity, J. Das and J. Eckert, "Is the energy density a reliable parameter for materials synthesis by selective laser melting?," *Materials Research Letters*, vol. 5, no. 6, pp. 386-390, 2017.

- [75] L. Carter, X. Wang and N. Read, "Process optimization of selective laser melting using energy density model for nickel based superalloys," *Materials Science and Technology*, vol. 32, pp. 1-5, 2015.
- [76] Y. Nam, B. Koo, M. Chang, S. Yang, J. Yu, Y. Park and J. Jeong, "Selective laser melting vitrification of amorphous soft magnetic alloys with help of double-scanning-induced compositional homogeneity," *Materials Letters*, vol. 261, p. 127068, 2020.
- [77] L. Zrodowski, B. Wysocki, R. Wroblewski, A. Krawczynska, B. Adamczyk-Cieslak, J. Zdunek, P. Blyskun, J. Ferenc, M. Leonowicz and W. Swieszkowski, "New approach to amorphization of alloys with low glass forming ability via selective laser melting," *Journal of Alloys and Compounds*, vol. 771, pp. 769-776, 2019.
- [78] I. Gibson, D. Rosen and B. Stucker, "Directed energy deposition processes," in *Additive manufacturing technologies: 3D printing, rapid prototyping, and direct digital manufacturing*, New York, Springer, 2015, pp. 245-268.
- [79] Z. Zhang, Z. Liu and D. Wu, "Prediction of melt pool temperature in directed energy deposition using machine learning," *Additive Manufacturing*, vol. 37, p. 101692, 2020.
- [80] W. Hofmeister, M. Griffith, M. Ensz and J. Smugeresky, "Solidification in direct metal deposition by LENS processing," *Journal of The Minerals, Metals and Materials Society*, vol. 53, no. 9, pp. 30-34, 2001.
- [81] V. Balla and A. Bandyopadhyay, "Laser processing of Fe-based bulk amorphous alloy," *Surface & Coatings Technology*, vol. 205, pp. 2661-2667, 2010.
- [82] J. Mazumder, A. Schifferer and J. Choi, "Direct materials deposition: designed macro and microstructure," *Materials Research Innovations*, vol. 3, no. 3, pp. 118-131, 1999.
- [83] W. Kurz, C. Bezencon and M. Gaumann, "Columnar to equiaxed transition in solidification processing," *Science and Technology of Advanced Materials*, vol. 2, pp. 185-191, 2001.

- [84] S. Bontha, N. Klingbeil, P. Kobryn and H. Fraser, "Thermal process maps for predicting solidification microstructure in laser fabrication of thin-wall structures," *Journal of Materials Processing Technology*, vol. 178, pp. 135-142, 2001.
- [85] M. Gaumann, S. Henry, F. Cleton, J. Wagniere and W. Kurz, "Epitaxial laser metal forming: analysis of microstructure formation," *Materials Science and Engineering A*, vol. 271, pp. 232-241, 1999.
- [86] J. Farmer, J. Haslam, S. Day, T. Lian, C. Saw, P. Hailey, J. Choi, R. Rebak, N. Yang, J. Payer, J. Perepezko, K. Hildal, E. Lavernia, L. Ajdelsztajn, D. Branagan, E. Buffa and L. Aprigliano, "Corrosion resistance of thermally sprayed high-boron iron-based amorphous-metal coatings: Fe_{49.7}Cr_{17.7}Mn₁₉Mo_{7.4}W_{1.6}B_{15.2}C_{3.8}Si_{2.4}," *Journal of Materials Research*, vol. 22, no. 8, pp. 2297-2311, 2007.
- [87] R. Vilar , "Laser Alloying and Laser Cladding," *Materials Science Forum*, vol. 301, pp. 229-252, 1999.
- [88] W. Steen and J. Mazumder, *Laser Material Processing*, London: Springer-Verlag, 2010.
- [89] Y. Zhang and R. Ramanujan, "The effect of niobium alloying additions on the crystallisation of a Fe–Si–B–Nb alloy," *Journal of Alloys and Compounds*, vol. 403, no. 1, pp. 197-205, 2005.
- [90] Y. Zhang and R. Ramanujan, "Characterization of the effect of alloying additions on the crystallisation of an amorphous Fe_{73.5}Si_{13.5}B₉Nb₃Cu₁ alloy," *Intermetallics*, vol. 14, no. 6, pp. 710-714, 2006.
- [91] Y. Zhang and R. Ramanujan, "A study of the crystallisation behaviour of an amorphous Fe_{77.5}Si_{13.5}B₉ alloy," *Materials Science and Engineering: A*, vol. 416, no. 1, pp. 161-168, 2006.
- [92] F. Xie, Q. Chen, J. Gao and Y. Li, "Laser 3D Printing of Fe-Based Bulk Metallic Glass: Microstructure Evolution and Crack Propagation," *Journal of Materials Engineering and Performance*, vol. 28, no. 6, pp. 3478-3486, 2019.
- [93] Q. Chen, J. Shen, D. Zhang, H. Fan and J. Sun, "Mechanical Performance and Fracture Behaviour of Fe₄₁Co₇Cr₁₅Mo₁₄Y₂C₁₅B₆ Bulk Metallic Glass," *Journal of Materials Research* , vol. 22, no. 2, pp. 358-363, 2007.

Chapter 3 –Literature Review Paper

- [94] A. Dehghanhadikolaei, N. Namdari, B. Mohammadian and B. Fotovvati, "Additive Manufacturing Methods: A Brief Overview," *Journal of Scientific and Engineering Research*, vol. 5, no. 8, pp. 123-131, 2018.
- [95] K. Wong and A. Hernandez, "A Review of Additive Manufacturing," *International Scholarly Research Network: ISRN Mechanical Engineering*, vol. 2012, p. 208760, 2012.

Chapter 4: Research Paper 1

This chapter contains the initial research step to optimize the laser powder bed fusion technique for Fe-based nanocrystalline alloys. To obtain information about the process, it investigates the effect of volumetric energy input to powder bed on the final properties (bulk density, saturation magnetization and coercivity) as the energy input combines the main process parameters: laser power, laser scan speed, hatch spacing and layer thickness. To comprehend their influence, different combinations were used to produce Fe-based nanocrystalline samples.

Optimising Laser Additive Manufacturing Process for Fe-based Nano-crystalline Magnetic Materials

Merve G. Ozden^{1,*} and Nicola A. Morley¹

¹ Department of Material Science and Engineering, University of Sheffield, Sheffield, S1 3JD, UK, mgozden1@sheffield.ac.uk

* Correspondence: mgozden1@sheffield.ac.uk

Citation: Ozden, M.G., Morley, N.A. Optimising Laser Additive Manufacturing Process for Fe-based Nano-crystalline Magnetic Materials. *Journal of Alloys and Compounds* 2023, 960, 170644. <https://doi.org/10.1016/j.jallcom.2023.170644>.

Copyright: © 2023 by the authors. Published by Elsevier B.V. This is an open access article under the CC BY-NC-ND license (<http://creativecommons.org/licenses/by-nc-nd/4.0/>).

Abstract

Fe-based amorphous magnetic alloys offer new opportunities for magnetic sensors, actuators and magnetostrictive transducers due to their high saturation magnetostriction ($\lambda_s = 20\text{-}40$ ppm) compared with that of amorphous Co-based alloys ($\lambda_s = -3$ to -5 ppm). Due to the conventional production limitations of Fe-based glassy alloys, including dimensional limitations and poor mechanical properties, this has led to a search for novel fabrication techniques. Recently, the laser powder bed fusion (LPBF) technique has attracted attention for the production of Fe-based magnetic bulk metallic glasses (BMGs) as it provides high densification, which brings about excellent mechanical properties, and high cooling rate during the process. Optimization of process parameters in the LPBF technique have been studied using the volumetric energy input (E), which includes the major build parameters; laser power (P), scan speed (v), layer thickness (t) and hatch spacing (h). This study investigates how the major process parameters influence the physical and magnetic properties of LPBF-

processed Fe-based amorphous/nanocrystalline composites ($(\text{Fe}_{87.38}\text{Si}_{6.85}\text{B}_{2.54}\text{Cr}_{2.46}\text{C}_{0.77})$ (mass %)). Various process parameter combinations with P (90, 100, 120 and 150 W) and v (700, 1000 and 1300 mm/s) were applied with t of 30, 50 and 70 μm and h of 20, 30, 40, 50 and 60 μm . It was found that bulk density improves as P and t increases, v and h decreases, i.e., high E is necessary, however, 99.45% of bulk density was achieved with E of 61.22 J/mm^3 ($P=150 \text{ W}$, $v=700 \text{ mm/s}$, $h=50 \mu\text{m}$ and $t=70 \mu\text{m}$), which indicates the importance of understanding how parameters affect the specific materials. In addition, the magnetic properties differ significantly due to the nanocrystalline phases present in the microstructure, with their size depending on the process parameters considerably. Owing to the laser scanning nature, the microstructure evolves as molten pools (MP) and heat affected zones (HAZ) due to the high thermal gradient that occurred between laser tracks. MP forms around the scans, containing $\alpha\text{-Fe}(\text{Si})$ nanograins mainly, whereas HAZ generally contains Fe_2B and Fe_3Si nanocrystalline clusters. The size and quantities of those nanocrystallites determine the magnetic properties. With the same E (60 J/mm^3), v (1000 mm/s) and t (50 μm), only changing P and h caused samples to have different saturation magnetization; 206 emu/gr (P : 90 W and h : 30 μm) and 150 emu/gr (P : 150 W and h : 50 μm). In general, the saturation magnetisation, M_s of LPBF-processed samples changes between 130 and 206 emu/gr, which is much higher than that of feedstock powder (102 emu/gr) due to their nanocrystalline structures. The coercivity (H_c) is in the range of 14.55 and 34.68 Oe, which is considered high for soft-magnetic behaviour ($H_c \leq 12.5 \text{ Oe}$), resulting from the larger crystallite size and the presence of defects (pores and cracks) in the microstructure. The bivariate correlational analysis revealed that bulk density demonstrated a significant correlation with P , v , h , and E , while M_s and H_c showed significant correlations exclusively with v and P , respectively.

Keywords: Laser powder bed fusion, amorphous/nanocrystalline magnetic materials, laser additive manufacturing process optimization.

4.1 Introduction

Laser Powder Bed Fusion (LPBF) is an additive manufacturing (AM) technique, which has attracted significant attention due to its ability to produce components with complex structures and high melting points in one go [1-5]. Conventional techniques would need a series of fabrication processes, to achieve the same designs, which takes excess material, time, and energy [6]. The LPBF process methodology is to build components in a layer-by-layer fashion by selectively scanning/melting and consolidating a thin layer of powder using a laser beam [6-8].

The major build parameters commonly studied to optimise the process are laser power (P), scan speed (v), layer thickness (t) and hatch spacing (h) (Figure 4.1). Previous

studies indicate that low laser power, high laser scan speed and large layer thickness leads to insufficient energy during the melt process. This causes balling to occur during LPBF, where molten metal creates spherical drops resulting from the inadequate wetting of the molten pool with the previous layer [9]. This phenomenon prevents the forming of continuous melt lines, creating rough surfaces and large pores within the parts. Poor interlayer bonding along with thermal stresses also result in delamination, which fractures the parts [10, 11]. On the other hand, high laser power and low scan speed may cause substantial material evaporation and the keyhole effect [12]. Moreover, too large hatch spacing generally leads to a high amount of porosity in printed components as neighbouring scan lines do not melt together completely [10]. Therefore, an optimised combination of laser power, laser scan speed, layer thickness and hatch spacing is necessary for the LPBF process to successfully fabricate components with near full density [9, 13].

Soft-magnetic properties of LPBF-processed Fe-based amorphous alloys have been investigated by a few researchers. Recently, Sufiiarov *et al.* used different P from 90 W to 120 W at constant laser v and h in producing FeSiB parts [14]. However, no change in saturation magnetisation, M_s (195 emu/gr) and coercivity, H_c (48 Oe) was observed. The effect of v on the soft-magnetic behaviour of 3D-printed FeSiB [1] and FeCSiBPCrMoAl alloys [3] was also studied. While changing v (from 1500 mm/s to 2500 m/s) did not show substantial difference in the soft-magnetic properties of FeSiB alloy (M_s : 102.8, 103.6 emu/gr and H_c : 0.35, 0.41 Oe; respectively) [1], laser scan speed significantly influenced the magnetic properties of FeCSiBPCrMoAl alloy. The laser scan speed between 100-1500 mm/s at constant P (90 W), h (40 μm) and t (50 μm) were used to explore its magnetic properties. M_s improved with increasing v till 700 mm/s where it had the maximum value (199 emu/gr) due to the existence of strong magnetic coupling between nanocrystalline grains and amorphous matrix. After that point, M_s decreased linearly to 188 emu/gr ($v=1500$ mm/s). On the other hand, coercivity reached its minimum (~ 40 Oe) at v of 100 mm/s, then increases with v up to 400 mm/s and then levels off to around 70 Oe. High H_c was related to the ferromagnetic heterogeneity of the system such as the presence of hard magnetic Fe₂B phases, impeding the domain wall movement and so increasing magneto-crystalline anisotropy.

It is crucial to note that laser additive manufacturing (LAM) provides isotropic properties for Fe-based amorphous alloys in macro-scale even due to the nano-equiaxed grains and amorphous phase in the microstructure despite the directionality of the process. It is proven that LPBF-processed Fe-based glassy alloy possesses nearly same coercivity (79 Oe), saturation magnetization (162 emu/gr) and microhardness (900 HV_{0.1}) at both X (platform axes) and Z (building axes) directions [15].

Researchers have tried different scanning techniques to enhance the properties of Fe-based BMGs. Nam *et al.* utilised the double scan strategy where every powder layer is rescanned using the same laser power and laser scan speed with the first scan before spreading to the next powder layer [16]. The study also includes different laser power (50, 70 and 90 W) and laser scan speed (1200 and 1600 mm/s) along with the volumetric energy input (E), expressing the energy that the powder receives;

$$E = \frac{P}{vth} \quad (4.1)$$

Where P is laser power, v is laser scan speed, t is layer thickness and h is hatch spacing [17-19]. High E combined with double scanning improved significantly relative density of 96%, M_s of 140 emu/gr and mechanical strength of 76 MPa. While double scanning reduced coercivity (20 Oe), core losses and increased permeability, these properties were not affected by energy input substantially. Despite the good results obtained in this research, the amorphous phase fraction was low (47%). To maximise it and ensure soft-magnetic properties, a novel scanning strategy, containing two-step scanning (preliminary laser melting followed by short-pulse amorphization) was introduced [20]. The first scanning (preliminary laser melting) was performed using the checkboard strategy with the laser power of 20 W and in the second melting (short-pulse amorphization), the Point-Random (P-R) strategy with the laser power of 120 W was applied on every layer after the first melting. This strategy increased the amorphous phase content from 3.5% (after first scan) to 89.6% and relative density from 78.2% to 94.1%. Coercivity was also reduced to 5 Oe. However, the strategy did not change the saturation magnetization (150 emu/gr). Furthermore, it was shown that low E (low P and high v) can be used to increase glassy phase content since low E provides high cooling rate [21].

It was shown that the energy input significantly influences the microstructure and porosity level of the parts [22-24]. Even though researchers were able to produce Fe-based nanocrystalline alloys with good properties, the bulk density and saturation magnetization need to be improved without compromising coercivity by investigating the effects of all major build parameters; P , v , h and t . As mentioned above, the researchers focused on only laser power and laser scan speed to study the magnetic and physical properties of Fe-based amorphous alloys. However, this study includes the effects of h and t as well as P and v . The main aim is to optimise the process parameters to fabricate almost fully dense parts having high saturation magnetization (M_s) and low coercivity (H_c), which was achieved by the formations of nanocrystallites with a small quantity of an amorphous phase. For this purpose, different laser power (90, 100, 120 and 150 W), laser scan speed (700, 1000 and 1300 mm/s), layer thickness (30, 50 and 70 μm) and hatch spacing (20, 30, 40, 50 and 60 μm) were explored.

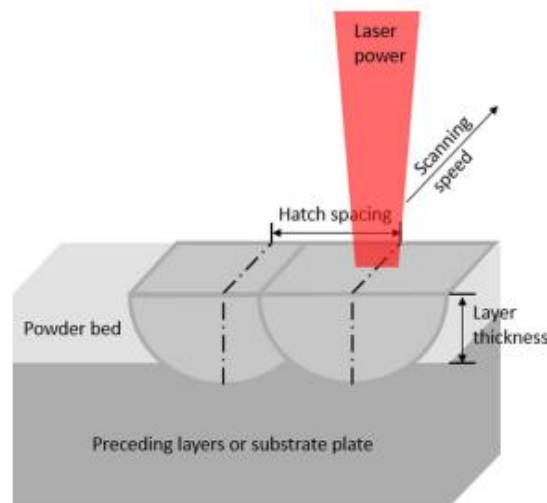


Figure 4.1: The studied processing parameters of LPBF process [13].

4.2 Material and Methods

4.2.1 Powder characterization

The amorphous soft-magnetic powder, KUAMET 6B2 ($\text{Fe}_{87.38}\text{Si}_{6.85}\text{B}_{2.54}\text{Cr}_{2.46}\text{C}_{0.77}$ (mass %)) containing 570 ppm by mass of oxygen content, was provided by Epson Atmix Corporation, Japan. Before being used in the LPBF process, the powder was characterised. This included determining the powder particle size distribution using a Mastersizer machine, the morphology via INSPECT F50 high-resolution field emission scanning electron microscope (HR-SEM), x-ray diffraction (XRD), PANalytical X'pert diffractometer), differential scanning calorimetry (DSC) analysis with a TA instrument SDT Q600 and the magnetisation hysteresis (M-H) loop at 300 K using a QD MPMS-3 magnetometer. It should be noted that all the characterization techniques were performed before powder-sieving. The results are shown in Figure 4.2. As presented in Figure 4.2(a), the powder particles exhibit near-spherical shape, which is crucial for superior flowability and spreadability over the powder bed. Furthermore, they have a narrow particle size distribution (Figure 4.2(b)) with D10, D50 and D90, indicating the sizes below which 10%, 50% and 90% of all powder particles are present, of 9.49, 23.4 and 47.5 μm , respectively. Only one broad peak in the XRD spectrum (Figure 4.2(b)) is observed, suggesting that the parent alloy is completely amorphous. The M-H loop in Figure 4.2(c) shows that the alloy has excellent soft-magnetic characteristics with M_s of 102 emu/gr and H_c of 28.51 Oe. The DSC curve in Figure 4.2(d) is composed of two consecutive exothermic and three consecutive endothermic peaks, resulting from multi-stage crystallisation and melting, respectively.

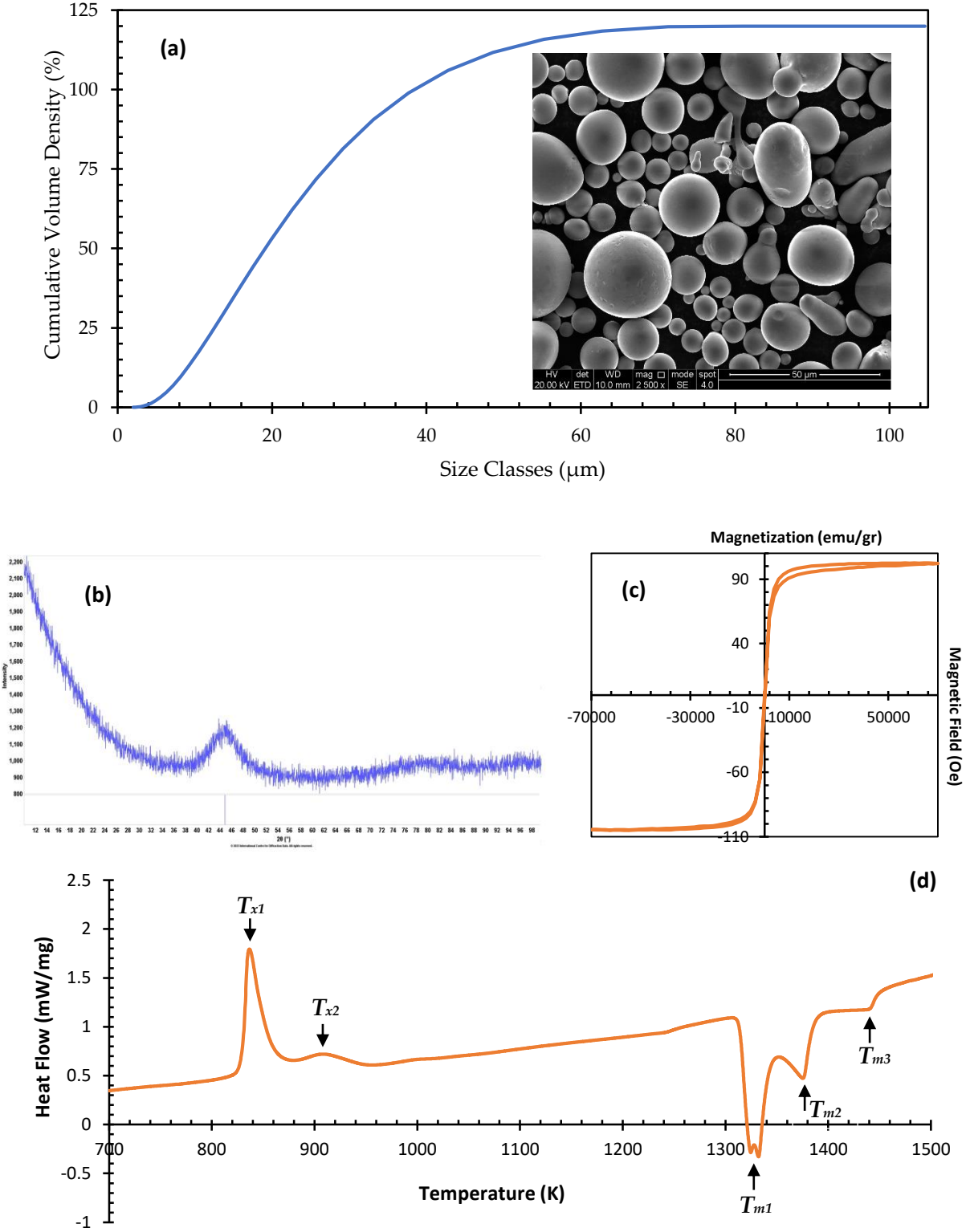


Figure 4.2: Powder characterization: (a) cumulative particle size distribution and SEM micrograph (morphology), (b) XRD pattern and (c) M-H loop and (d) DSC curve (exothermic peaks are up) of KUAMET6B2 powder (T_{x1} and T_{x2} are the crystallization temperatures, and T_{m1} , T_{m2} and T_{m3} are the melting temperatures).

4.2.2 Laser Powder Bed Fusion (LPBF) process

Before starting to print, the powder was sieved with a 53 μm mesh-size sieve to eliminate the larger powder particles and to ensure that the particle size range is 10-53 μm . This is a necessity for optimal layer deposition during the LPBF process. To produce the cylindrical samples with dimensions of 6 mm in diameter and 8 mm in height, the Aconity Mini machine was utilised. Various process parameter combinations with P of 90, 100, 120 and 150 W and v of 700, 1000 and 1300 mm/s were applied with the layer thickness of 30, 50 and 70 μm and the hatch spacing of 20, 30, 40, 50 and 60 μm . The hatch filling type was utilised with a hatch style rotation of 70° and starting angle of 22.5° . To prevent oxidation, the chamber was filled using Argon gas to keep the residual oxygen content below 0.01%.

4.2.3 Characterization of printed samples

After printing, the densities of all the samples were measured three times using the Archimedes method with distilled water and the mean density of every sample was determined. The bulk density percent of the printed specimens was calculated by using the mean densities and the theoretical density of the master alloy.

To obtain micrographs, firstly the samples were mounted in bakelite, ground and polished. Then, the polished samples were subjected to etching with 2% nital solution (98 ml HNO_3 and 2 ml ethanol) for 3 min. Then, the microstructural characterization was performed by Nikon optical microscope and INSPECT F50 HR-SEM. The transmission electron microscope (TEM) micrographs were taken at the voltage of 300 kV and the nominal magnification of X6000 by using JEOL R005 Cs Corrected TEM/STEM machine after the sample was produced with FEI Helios NanoLab G3 UC focused Ion beam (FIB) machine.

Phase analysis of the produced samples was conducted by using PANalytical X'pert diffractometer with Cu radiation ($\lambda = 1,541 \text{ \AA}$). DSC analysis was carried out with a heating rate of 20 $^\circ\text{C}/\text{min}$ up to 1400 $^\circ\text{C}$ by TA instruments SDT Q600 in order to measure the crystallisation enthalpies of the samples (ΔH_{cry}). The amorphous content ($=\Delta H_{\text{cry}}$ of LPBFed alloy/ ΔH_{cry} of starting powder) then was calculated by using the method described in these papers [16, 20, 25]. A SQUID magnetometer MPMS3 from Quantum Design was used to obtain magnetization hysteresis (M-H) loops at 300 K and examine the magnetic properties, such as saturation magnetization (M_s) and coercivity (H_c) of the as-printed alloys.

For the Design of Experiment (DoE), a bivariate correlational analysis was conducted to examine the connections among the five process parameters (E , P , v , h and t) and the three outcome variables (Bulk density, M_s and H_c).

4.3 Results and Discussion

The phase development during the LPBF process is a complicated occurrence that has to be investigated directly. Therefore, with the help of the DSC curve of the powder (Figure 4.2(d)), the crystallisation characteristics were analysed. Previous work has shown that the crystallisation of Fe-Si-B based systems generally happens in two steps, the first stage relating to the development of α -Fe solid solution followed by the decomposition of the amorphous matrix into boride, ferrite, and silicide phases [26]. The DSC curve (Figure 4.2(d)) indicates that the amorphous powder experiences a two-stage crystallisation mechanism while heating from 820 K to 960 K with a heating rate of 20 K/min. The first one ($T_{x1} = 840$ K) is associated with the α -Fe(Si) bcc phase and the second one ($T_{x2} = 910$ K) with the evolution of Fe₂B phase. Between 1300 K and 1500 K, the powder undergoes multiple melting transformations. The first endothermic peak (T_{m1}) at around 1330 K corresponds to the melting of α -Fe/Fe₂B mixture and the subsequent peak (T_{m2}) at 1380 K is linked to the melting of Fe₂B [27]. The last one (T_{m3}) at 1440 K can be attributed to the melting of Fe carbides having the highest melting point [28].

Figure 4.3 gives the XRD patterns of different LPBF printed samples with different energy densities. It is observed that bcc α -Fe(Si) and the ordered Fe₃Si phases are found together with a proportion of stable Fe₂B phase in all the samples. Low amorphous content (<10%) suggests that the amorphous phase is only present within the matrix, being retained from the parent powder. The sharp diffraction peaks represent the α -Fe(Si) phase. Owing to its large size (300-500 nm) and high amount in the microstructure, its crystallisation peaks can be seen distinctively in the XRD patterns. On the other hand, the other phase peaks are lost in the noisy background, which may be associated with small crystallite sizes and the irregularities in the polished surface such as cracks and pores.

Research conducted by Zrodowski and his team [20] pointed out that during the devitrification of Fe₇₁Si₁₀B₁₁C₆Cr₂ (at. %) amorphous powder, initially the ordered Fe₃Si phase and metastable Fe₃B phases were formed, after further heating, the metastable phases were transformed into a stable boride Fe₂B. Also, in that study, it was noted that the α -Fe(Si) phase evolves while the liquid solidifies (liquid to crystal), on the other hand, the ordered Fe₃Si phase forms while the glass phase devitrifies (glass to crystal). This explains why α -Fe(Si) and Fe₃Si phases are present together in the XRD patterns for the printed samples (Figure 4.3).

The XRD patterns suggest that all the samples produced with varying energy densities (between 48-85.71 J/mm³) possess a mixture of α -Fe(Si)/Fe₃Si and Fe₂B phases. It should be noted that there was no considerable shift of the peak positions ($\pm 0.23^\circ$), which

indicates no change in lattice parameters (no lattice expansion or contraction). Ouyang *et al.* [21] and Nam *et al.* [16] proposed that lower energy densities (low laser power and high scanning speed) lead to higher amorphous content of 3D printed Fe-based amorphous alloys. In this study, the XRD results indicate there is a tendency to decrease amorphous content with increasing energy density, except for the sample with 85.71 J/mm³ where relatively higher amorphous content was observed. This may be due to the low laser power (90 W) as stated in the other studies. Consequently, evidence suggests that low laser power and energy density can improve amorphous content.

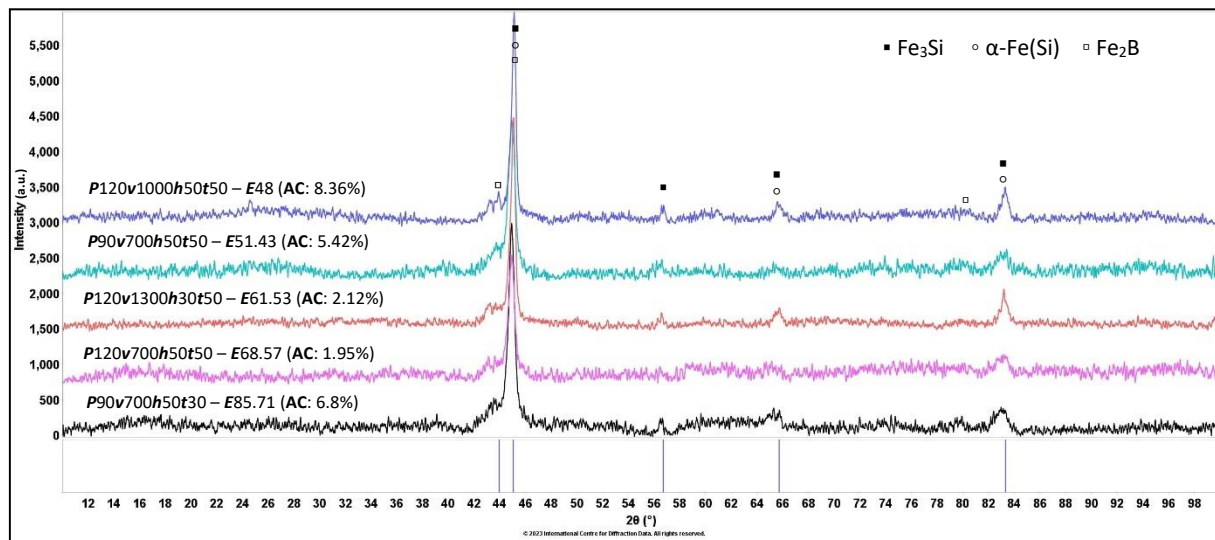


Figure 4.3: XRD patterns of the samples produced with different energy densities.

In the sample notations, P is laser power in Watt, v is laser scan speed in mm/s, h is hatch spacing in μm , t is layer thickness in μm , E is laser energy density in J/mm³ and AC represents the amorphous content.

The microstructural evolution of bulk metallic glasses (BMGs) during the LPBF process is a complex event, owing to the heterogeneous nature of the complicated thermal treatments, which develop during the printing process. The microstructure generally contains two different regions; molten pools (MP) and heat affected zone (HAZ), both of which experience a highly different cooling rate and therefore, possess different microstructure (Figure 4.4) [29]. The cooling rate decreases from the molten pool region through the HAZ due to high thermal gradients formed during laser scanning whose tracks can clearly be observed in the microstructure (Figure 4.5(a)). It is well-established that the ordered Fe₃Si phase grows as dendrites whereas the disordered α -Fe(Si) phase is observed as equiaxial grains [20] and the growth of the Fe₂B is needle-like [30]. Hence, in the MP zone, the α -Fe(Si) nanograins in the size range between 300 and 500 nm were observed (Figure 4.5(f)), whereas the HAZ contains mainly Fe₃Si nanocrystalline clusters with sizes between 30-100 nm (Figure 4.5(c)) and

Fe₂B nano-phases with the sizes of 400-600 nm (Figure 4.5(d)). The MP zone provides more supercooling than the HAZ region to nucleate and grow the disordered α -Fe(Si) phase. It was observed that in the MP zone, the grains are coarser than the HAZ region (Figure 4.5) because at high undercooling, nucleation rates decrease and the growth velocity of nucleus increases resulting from the high driving force for atomic diffusion process, that is, high supercooling [31]. This leads to the grain coarsening.

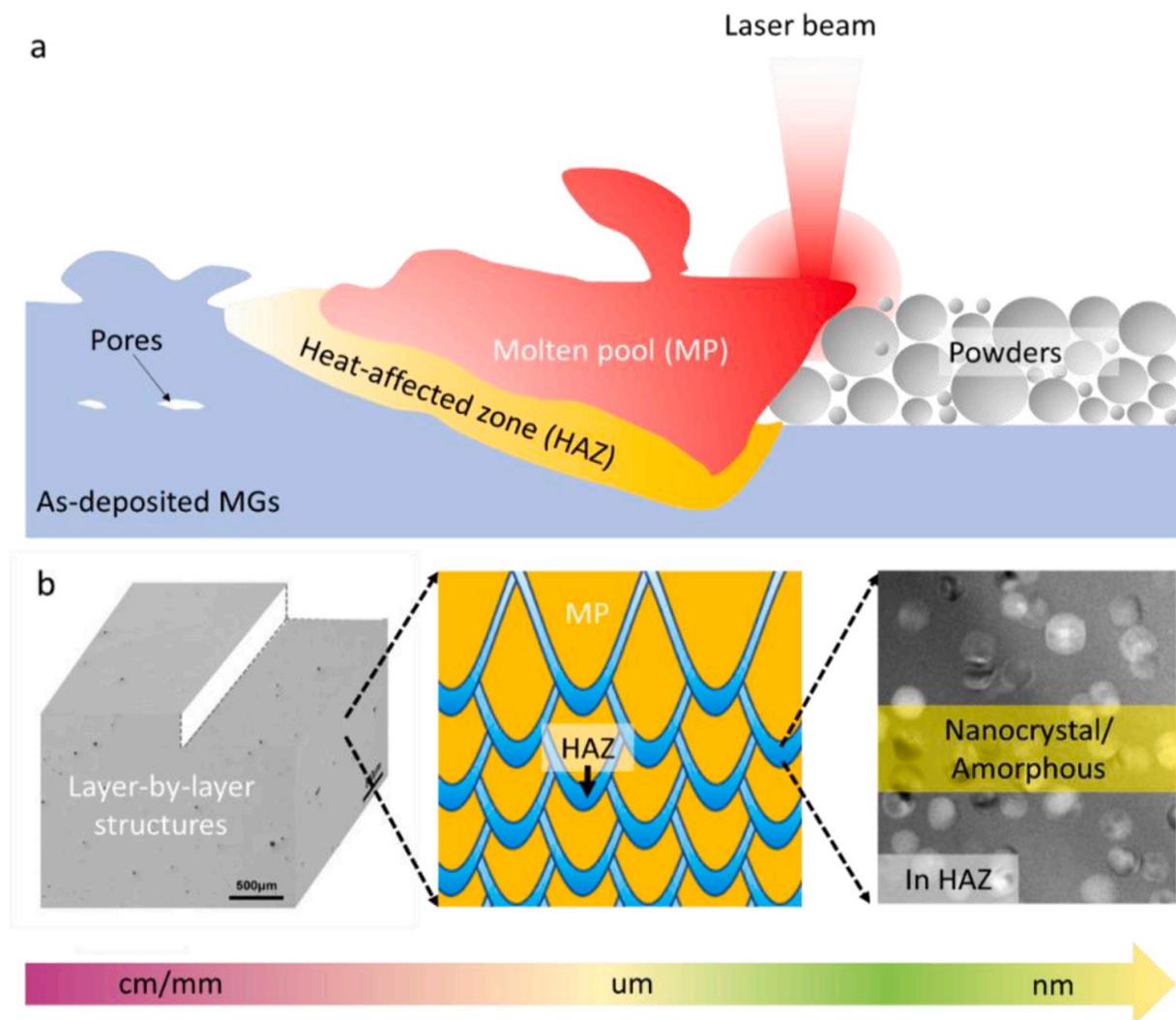


Figure 4.4: (a) Complex thermal interaction between laser beam and amorphous powder and (b) hierarchical microstructures in LPBF-processed amorphous alloys [29].

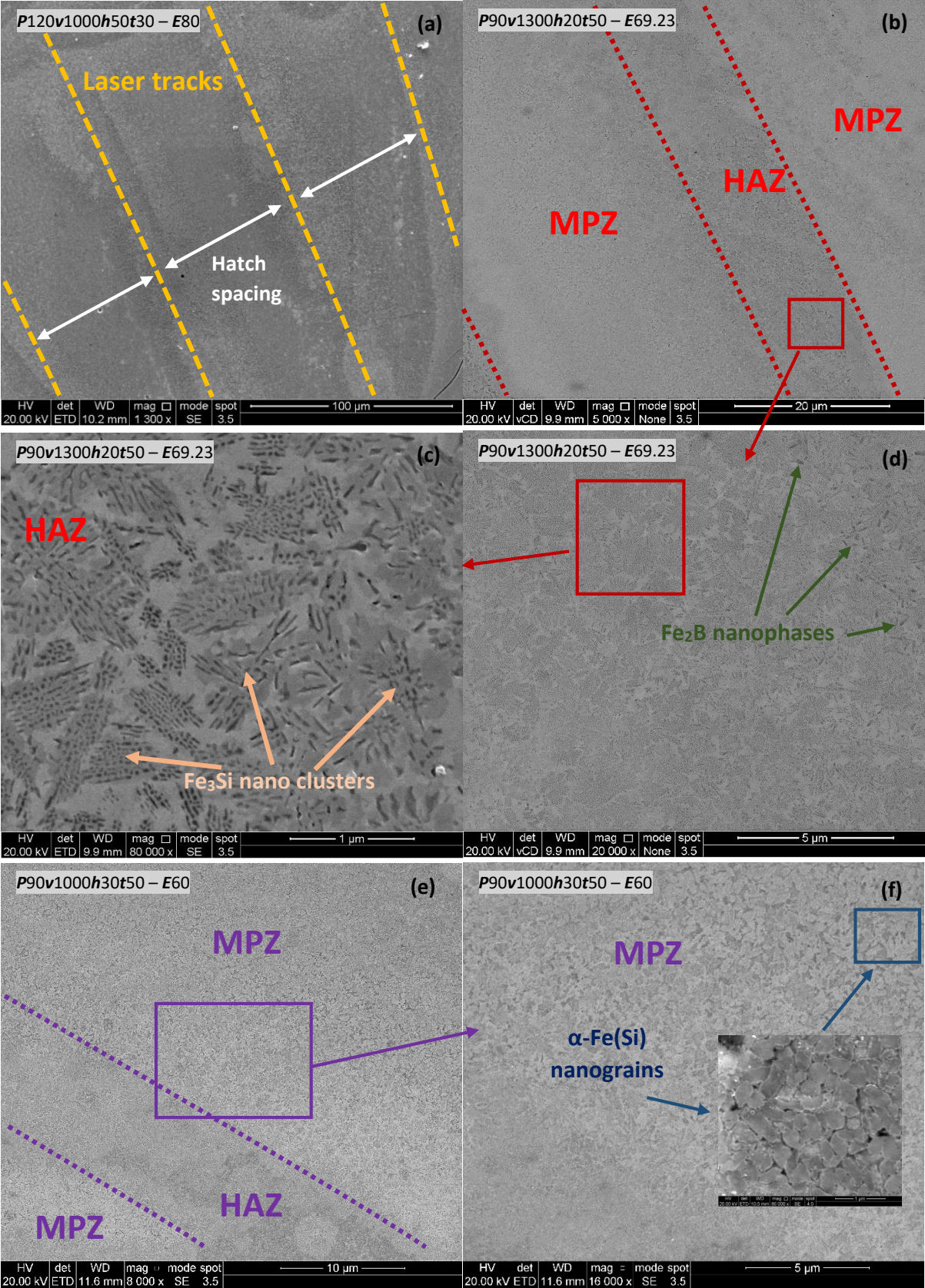


Figure 4.5: SEM micrographs of LPBF processed samples showing (a) laser scan tracks on the microstructure, (b) melt pool zone (MPZ) and heat affected zone (HAZ), (c) and (d) the microstructure in HAZ, (e) and (f) the microstructure in MPZ. In the sample notations, *P* is laser power in Watt, *v* is laser scan speed in mm/s, *h* is hatch spacing in μm, *t* is layer thickness in μm, *E* is laser energy density in J/mm³.

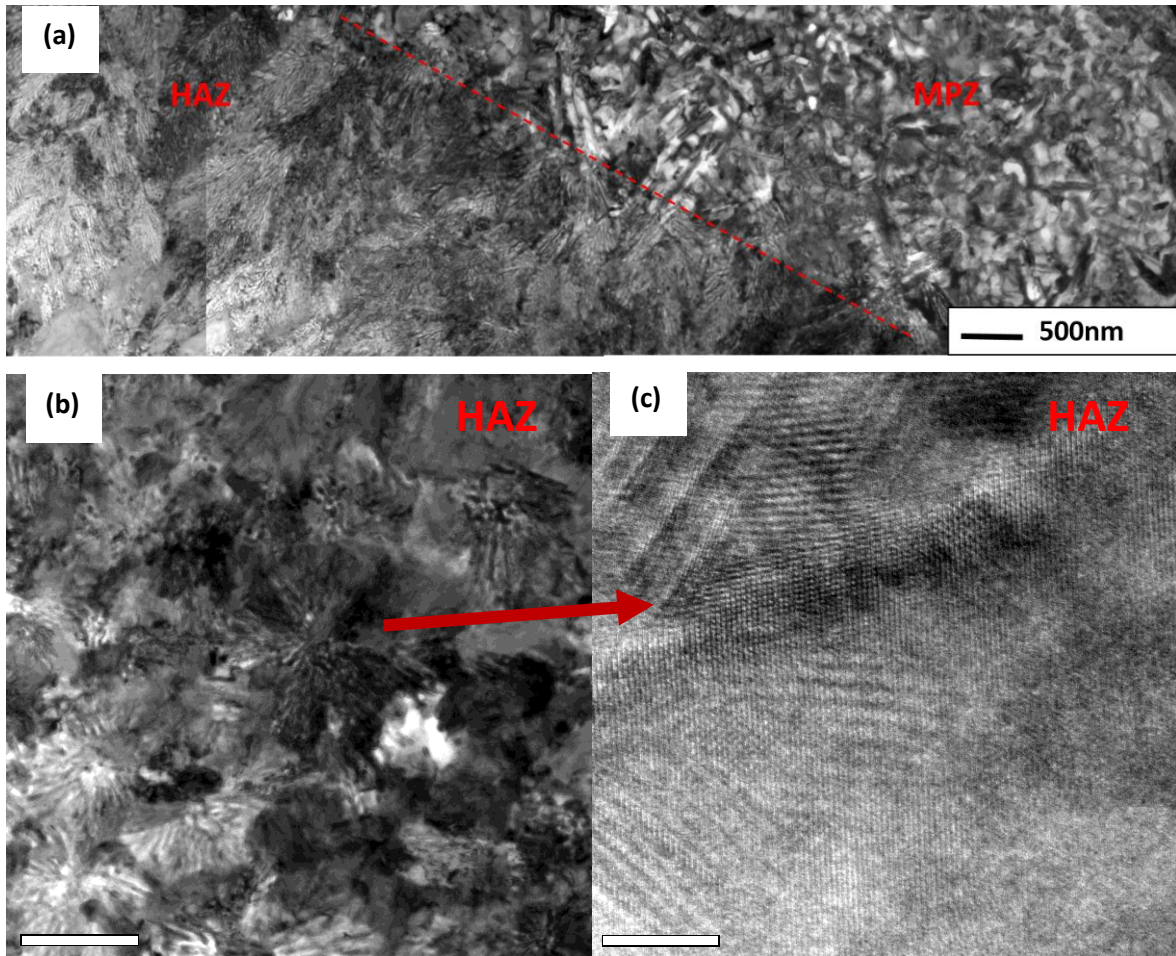


Figure 4.6: Bright-Field TEM cross-sectional micrographs of the sample produced with P of 90 W, v of 1000 mm/s, h of 20 μm , and t of 50 μm , (a) a composite image from the uppermost surface of the sample illustrating the interface between the MPZ and HAZ regions, (b) detail of the spherulitic crystal growth observed in the lower HAZ region and (c) a high resolution image from the HAZ region displaying atomic lattice structure indicative of a crystalline structure.

Cross sectional TEM imaging of the LPBF-processed sample supports the microstructure observed in the SEM images shown in Figure 4.5. Figure 4.6(a) illustrates the interface between the MPZ and under-lying HAZ region. Figure 4.6(b) shows the presence of spherulitic-like crystal growth in the lower HAZ region while the high-resolution lattice image, Figure 4.6(c), confirms the crystalline nature of this region.

Figure 4.7 illustrates how the bulk densities of the sample changes as a function of energy density. The bulk density has tendency to increase with rising energy density till around 55 J/mm³. After this, the bulk density fluctuates between 97 % and 99 %. Less than 55 J/mm³, there are a large number of pores in the microstructures because of the insufficient energy inputted to the powder bed. At the same energy densities, different bulk densities were obtained, implying that energy density is not a reliable parameter to control the porosity level in the parts. In addition, some parts printed

with varying energy densities failed during printing or fractured heavily. It was observed that high laser power of 150 W (facilitating large crack formation), high laser scan speed of 1300 mm/s (leading to balling effect) and large hatch spacing of 60 μm (insufficient overlapping between melt pools) commonly caused the failure in printing. Although utilising laser energy density to combine all major process parameters is a good way to start, their effect on the final properties should be investigated individually. Detailed discussion on the reliability of energy density as a parameter can be found elsewhere [32].

For convenience, the samples were categorised into three groups: high density (higher than 99%), moderate density (between 97% and 99%) and low density (lower than 97%). It was inferred that high bulk density was achieved only with increased layer thickness (50 and 70 μm). Thinner layer thickness resulted in the crack formation between the layers as the previous layer is subjected to too much energy. At $t = 50 \mu\text{m}$, low laser power (90 and 120 W) brings about high density, on the other hand, at $t = 70 \mu\text{m}$, high laser power (150 W) causes high density. It can be said that all these parameters are related to each other to obtain a low amount of porosity and cracks. For example, at the large layer thickness ($= 70 \mu\text{m}$), if the laser power is increased, it is a good idea to use large hatch spacing and low scan speed to achieve high density.

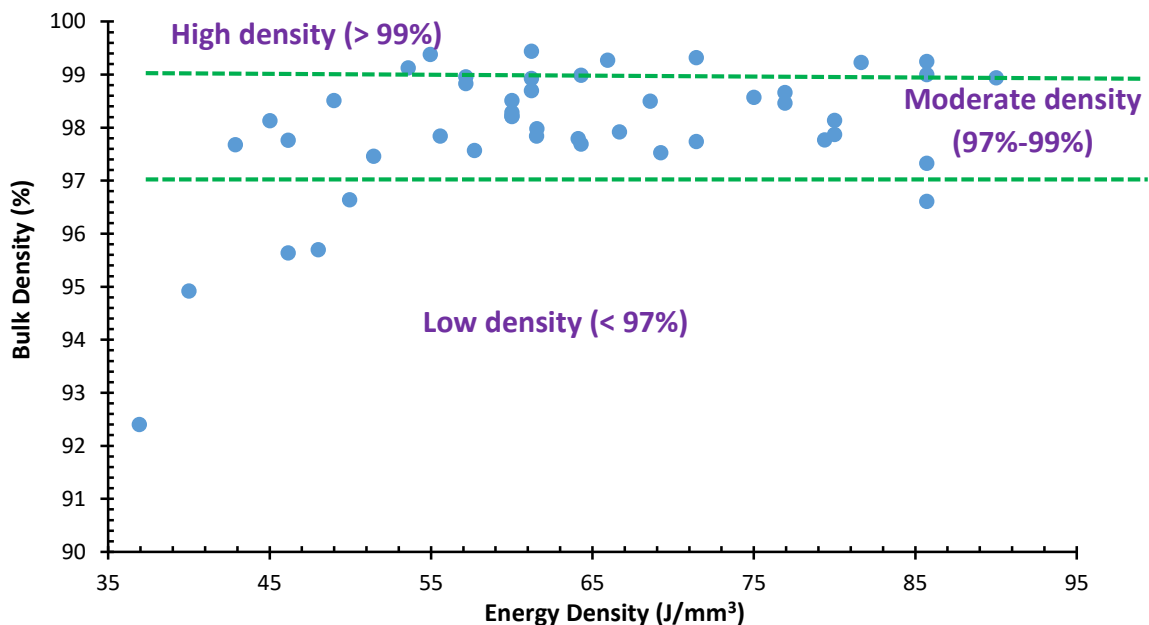


Figure 4.7: The graph of bulk density of samples as a function of different energy densities.

Figure 4.8 illustrates the variation in the bulk density as a function of P , v , h and t . In general, bulk density improves as P (Figure 4.8(a)) and t (Figure 4.8(d)) increases; v (Figure 4.8(b)) and h (Figure 4.8(c)) decreases, i.e., high E is necessary. However, 99.45% of bulk density was achieved with the E of 61.22 J/mm^3 ($P=150 \text{ W}$, $v=700 \text{ mm/s}$,

$h=50\ \mu\text{m}$ and $t=70\ \mu\text{m}$), its microstructure is in Figure 4.8(d). It seems that individual process parameters greatly influence the microstructure and bulk densities. Common defects observed in the LPDF process are pores (metallurgical and key-hole pores) and cracks. Cracks are generally formed in the HAZ region and through the melt pool because of the excessive heat applied to melt the powders. The first microstructure in Figure 4.8(d) contains relatively large cracks mainly resulting from the higher E and higher P . In addition, it was observed that pore concentration affects the crack density significantly because cracks originating from pores or outer surface of the samples, act as stress concentration points. Cracks present in the microstructure are mostly cold cracks, which is a type of solid-state cracks. They typically occur when processed components undergo cooling to reach room temperature. Irregular shrinkage, a consequence of inconsistent cooling rates and high thermal gradient during the cooling, and the poor plasticity of Fe-based BMGs leads to the accumulated residual thermal stresses in the microstructure. When these stresses exceed a threshold, these cracks tend to nucleate using free surfaces like pores and propagate through long distances. These cracks are often notable for their considerable size. The crack density was nearly the same 17 ± 2 cracks per 3 mm, except for the samples produced with high scan speed ($\geq 1000\ \text{mm/s}$) and high hatch spacing ($\geq 50\ \mu\text{m}$). The crack density then went up to 28 ± 1 cracks per 3 mm since high v and h increases porosity content owing to low E . Up to now, there are no Fe-based BMGs fabricated by laser additive manufacturing in a crack-free condition [2, 3, 33]. The problem is the high energy input and the brittle nature of metallic glasses, which is beyond the scope of this study and will be investigated further later. Moreover, this microstructure had a few nearly spherical pores instead of irregularly shaped metallurgical pores. They can be related to the gas bubbles produced by the vaporisation of constituents having low melting point (B and C) in the alloy [17]. These bubbles generally are formed in the lower region of the melt pool and cannot escape from the surface due to the high solidification rate. Therefore, they remain at the bottom of the melt pool after solidification [19, 34]. However, at high P , increasing t (lowering E) has significantly improved the microstructure Figure 4.8(d), there are relatively thin cracks and irregular shape pores, which are due to process instability such as insufficient gas flow and laser power fluctuations [17].

As P decreases to 90 W (other parameters held constant), the porosity content increases due to the weak sintering and unstable melt, as shown in Figure 4.8(a). At low laser power, the powder does not receive sufficient energy during the LPBF process, resulting in incomplete melting and poor inter-particle bonding [3]. Processing at higher scan speed ($v = 1300\ \text{mm/s}$) brings about a balling effect as mentioned in Section

4.1. It generally occurs when the length (L) to diameter (D) ratio of the melt pool rises to 2:1, which breaks the molten alloy into small drops rather than a continuous melt line and destabilises the melt pool [35]. Thus, low scan speed ($v = 700$ mm/s) led to improved sintering and consolidation of the powder, allowing the fabricated samples to have approximately 99 % density (Figure 4.8(b)).

It was also observed that high hatch spacing results in low bulk density because of the large metallurgical (process-related) pores evolving in the microstructure (Figure 4.8(c)). Increasing h may cause an un-melted powder gap between layers due to the lack of melt pool overlap (high L/D ratio of the melt pool) [17]. This increases the porosity content of the LPDF samples resulting from the unstable melt pool and un-melted powder particles. For this reason, when the hatch spacing increases, the layer thickness should be decreased to close the powder gap. In Figure 4.7(d), at high P (= 150 W), the bulk density increased by over 4% and the crack size was reduced substantially from 11.94 ± 0.69 μm to 2.58 ± 0.16 μm when t was increased from 50 μm to 70 μm . In general, the crack size was 5.71 ± 0.79 μm .

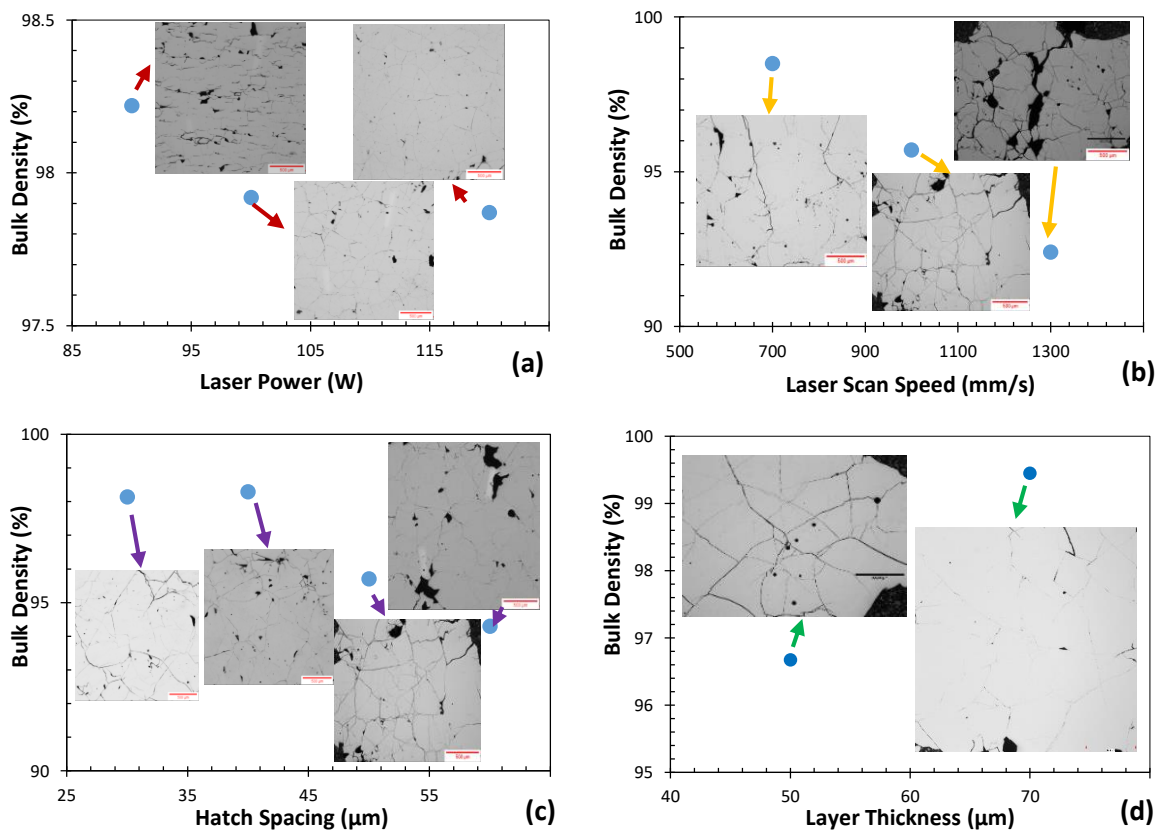


Figure 4.8: The graphs showing bulk densities of specimens fabricated by using different (a) laser power (The other parameters are constant; $v = 1000$ mm/s, $t = 30$ μm and $h = 50$ μm), (b) laser scan speed (The other parameters are constant; $P = 120$ W, $t = 50$ μm and $h = 50$ μm), (c) hatch spacing (The other parameters are constant; $P = 120$ W, $v = 1000$ mm/s and $t = 50$ μm) and (d) layer thickness (The other parameters are constant; $P = 150$ W, $v = 700$ mm/s and $h = 50$ μm).

Bulk Density variations can be seen more clearly as functions of E , P , v , h and t in Figure 4.9. Since laser power and energy density directly influence the melt-pool size and heat input to the powder bed, at low E , high P and at high E , low P provides high bulk density (Figure 4.9(a)). At high E , low P prevents excessive energy input and at low E , high P increases melt pool area to enhance overlapping between MPs. There has not been found any direct effects of E and v on bulk density (Figure 4.9(b)). High bulk density can be obtained for any v at E larger than 55 J/mm³. Likewise, if E is higher than 60 J/mm³, at least 80% of bulk density can be achieved using h in the range of 20-50 μ m (Figure 4.8(c)). Low h (< 40 μ m) brings about better results in reducing porosity. In addition, t strongly affected bulk density at E of 55-80 J/mm³, increasing t from 30 to 70 μ m increased bulk density from 97.7% to 99.4%.

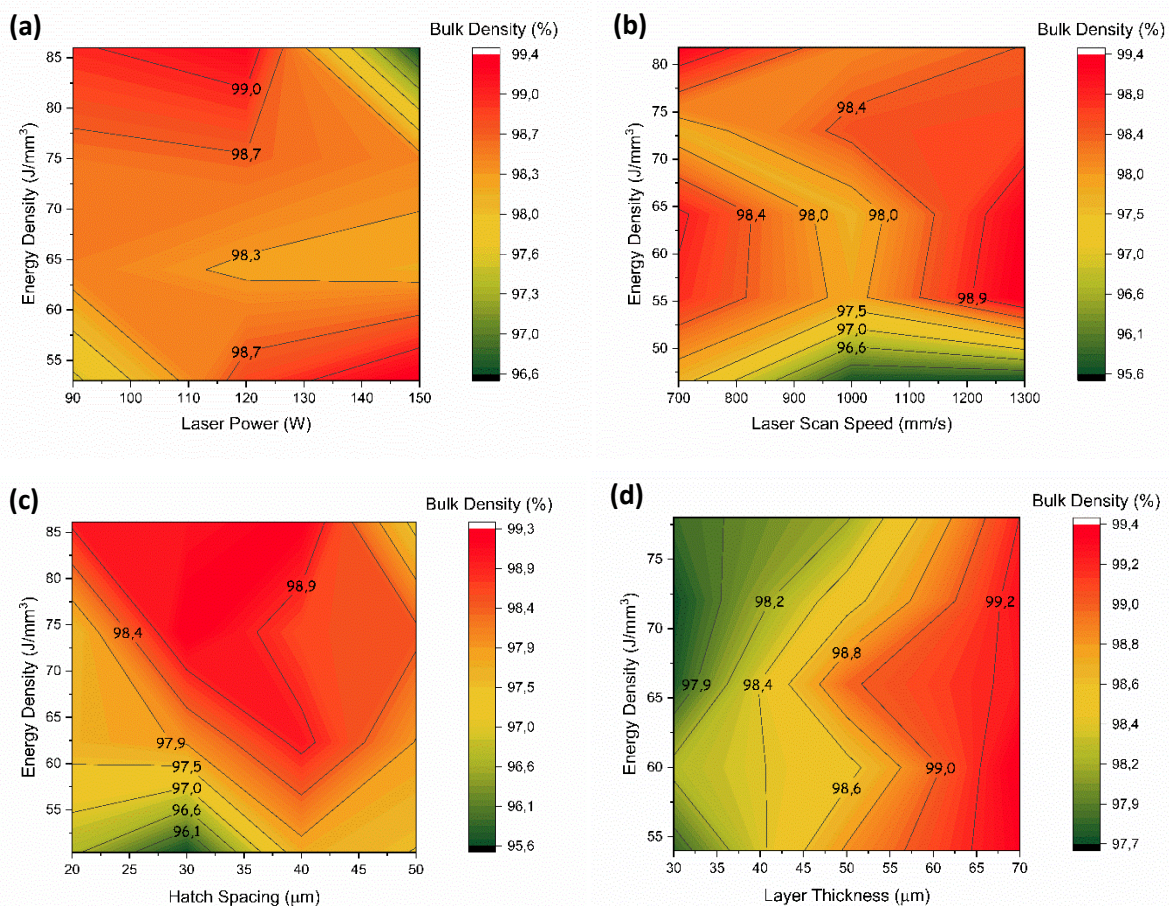


Figure 4.9: Bulk Density values of Fe-based BMG samples 3D printed by using different (a) laser power, (b) laser scan speed, (c) hatch spacing and (d) layer thickness (The bulk density values with uncertainties is presented in Appendix A).

The saturation magnetization values of the printed samples vary between 139 and 207 emu/gr (Figure 4.10), which is a lot higher than that of powder (102 emu/gr) due to the presence of nanocrystalline phases in the produced samples. As shown in Figure 4.10, there is no obvious relation between M_s and E because in soft-magnetic nanocrystalline

alloys, M_s is strongly influenced by the fraction of crystalline and amorphous phases, the structure of crystalline phases and the composition of the alloy. The most dominant factor that affects the M_s considerably is the amount of magnetic transition metals (Fe, Co, and Ni) in the alloy [37]. Since the alloy composition is the same in all LPBF-processed samples, the amount, and the distribution of the nanocrystalline phases throughout the samples changes the M_s value.

In general, Fe-based nanocrystalline alloys, which are composed of fine 10-15 nm α -Fe(Si) nano-crystallites in an amorphous matrix, separated by 1-2 nm allowing for exchange interaction, exhibit excellent soft-magnetic properties (H_c : 0.4-8 A/m, M_s : 1.3 T) [38]. In this study, magnetic saturation can go up to 1.9 T. The reason for this is thought to be the large crystallite size of the bcc-Fe(Si) phase (311.79-557.99 nm) and high exchange interaction among the magnetic phases in the microstructure (M_s (Fe₃Si): 133.5 emu/gr (1.1 T) [39], M_s (Fe₂B): 174 emu/gr (1.3 T) [40, 41] and M_s (α -Fe(Si)): 2.1 T [42]) and small amorphous phase. In this study, it was observed that as the thickness of the MP zone decreases, M_s increases, due to a short MP region creating a more homogenous microstructure (Figure 4.10). This facilitates exchange interaction between the magnetic phases at a shorter distance, so increasing M_s . Therefore, to increase saturation magnetization, one should aim to obtain homogenous microstructure for enhanced exchange interaction as well as decreasing the amorphous content. Figure 4.11 indicates that generally high E (> 80 J/mm³) leads to high M_s (> 200 emu/gr) because high E promotes crystallization, whereas low E increases amorphous content [21], which in turn, lowers M_s . In addition, based on the measurements of the MP zone, high E and P ; and low v , t and h lower the thickness of MP zone and increase M_s . By looking at Figure 4.11, it can be said that M_s has a strong dependency on P and t . Increasing E and P simultaneously till $P = 130$ W improves M_s (Figure 4.11(a)). While v and h do not seem to be controlling parameters for M_s . It was observed that the only substantial difference in M_s exists at high E (Figure 4.11(b)). At high E (≥ 75 J/mm³), high v leads to low M_s because of the large MP zone thickness. Moreover, between h of 20 and 50 μ m, it is possible to obtain high M_s (≥ 180 emu/gr) when E is higher than 80 J/mm³ (Figure 4.11(c)). At low E (≤ 70 J/mm³), layer thickness in the range of 50 and 70 μ m provides enhanced M_s (Figure 4.11(d)).

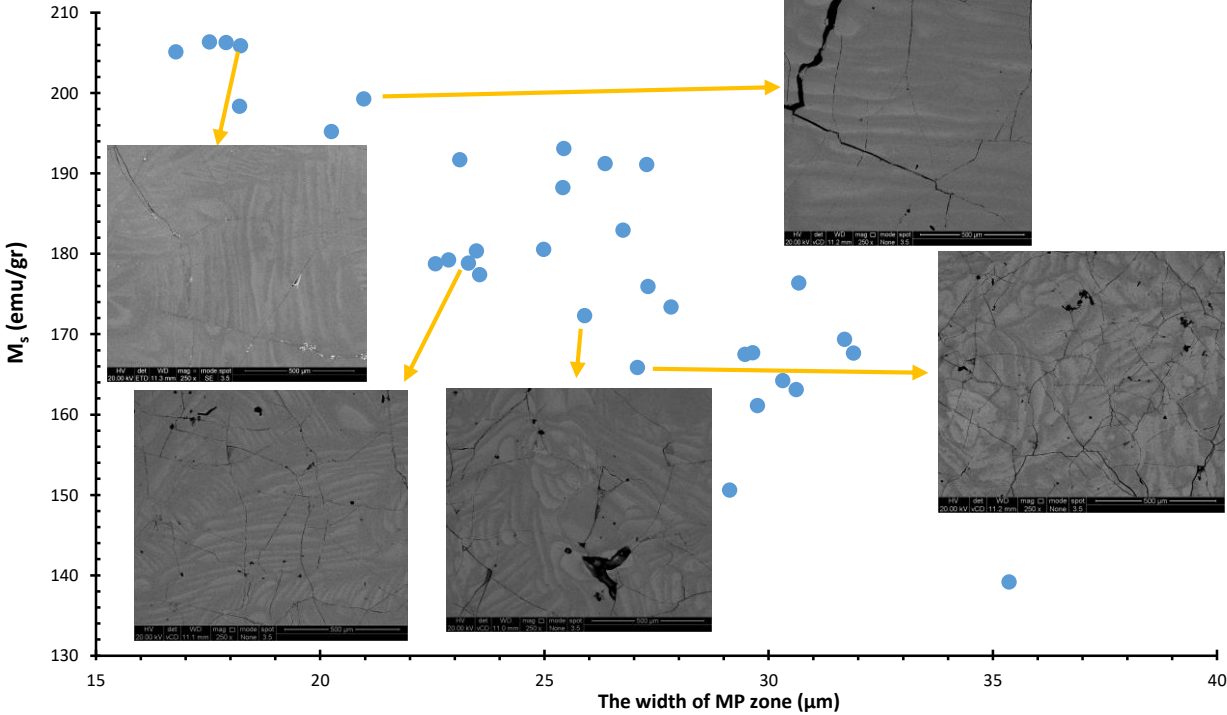


Figure 4.10: The saturation magnetization values of LPBF-processed samples as a function of the thickness of the MP zone (All of the micrographs are in the same scale with the scale bar of 500 μm and lighter and darker areas represent MP and HAZ zones, respectively).

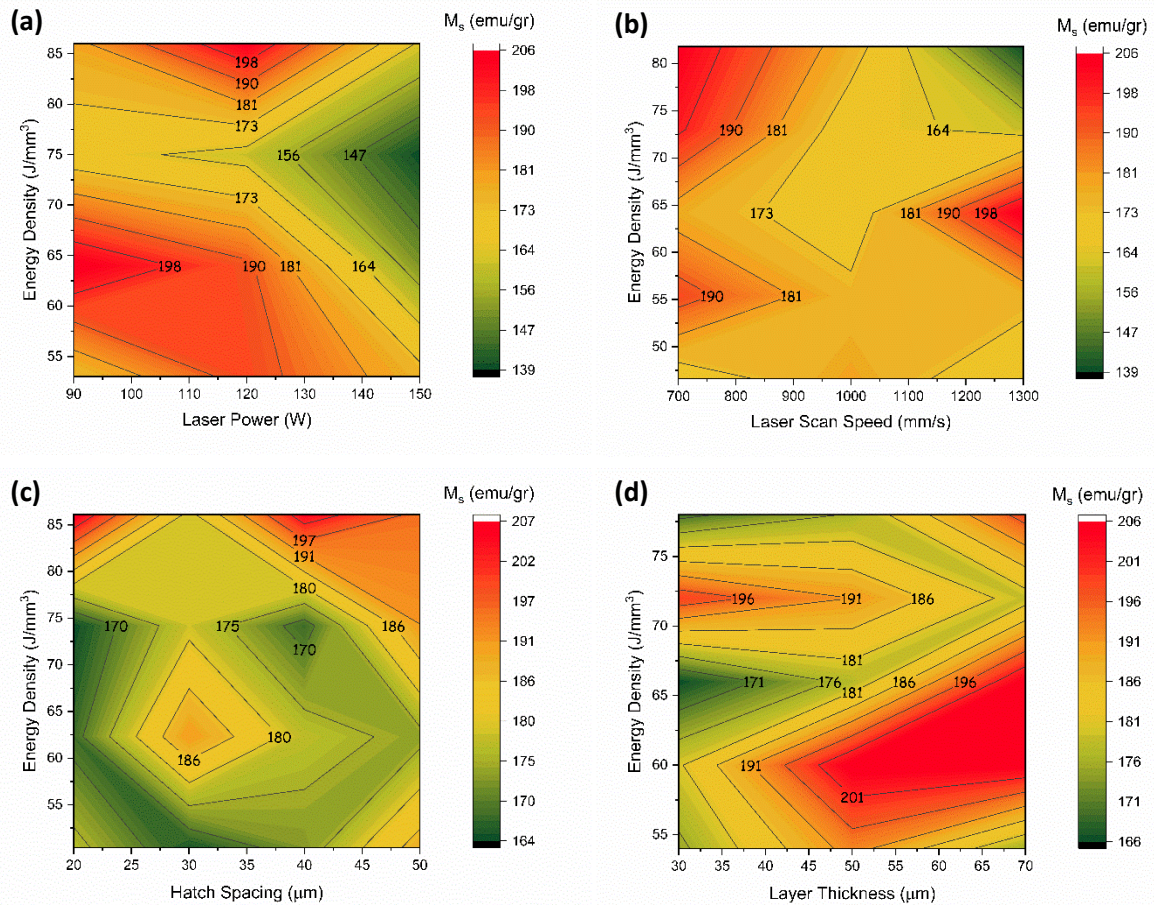


Figure 4.11: Saturation magnetization values of Fe-based amorphous samples LPBF-processed by using different (a) laser power, (b) laser scan speed, (c) hatch spacing and (d) layer thickness (The saturation magnetization values with uncertainties is presented in Appendix B).

Coercivity (H_c) is an extrinsic property (if the anisotropy is neglected due to the isotropic nature of nano features in the microstructure), which means it is affected by process-related defects (pore and cracks), impurities (oxide inclusions) and nano crystallite size. In theory, given that the maximum crystallite size (300 nm) in this study, the coercivity should be approximately 25 Oe [43]. Thus, it can be concluded that H_c is controlled by the crystallite size, as it varies between 14.55 and 34.68 Oe with porosity (Figure 4.12) and different energy densities (Figure 4.13), which is much higher than Fe-based amorphous ribbons (~ 0.04 Oe) [44, 45]. This is due to the presence of large nanocrystallites and impurities in the microstructure. As mentioned in Chapter 2, powders tend to react with oxygen during processing. Also, there is a small amount of oxygen (57×10^{-5} wt. %) in the feedstock powder composition. This causes the formation of oxide inclusions in the microstructure during printing, leading to deteriorating the magnetic properties (decreasing M_s , increasing H_c). For details, one can refer to Section 2.2.7.

Conventional techniques like strip casting and melt spinning provide a high cooling rate throughout the whole ribbons resulting from their small thickness ($\leq 100 \mu\text{m}$). As a result, fully amorphous alloys are produced, minimising coercivity. On the other hand, due to the laser scanning nature causing high thermal gradient, it is hard to maintain a high cooling rate throughout the whole microstructure. Thus, inevitably crystallites occur in the HAZ region during the LPBF process, increasing coercivity. Although Zrodowski *et al.* reduced the crystallisation by nearly 90%, coercivity was still as high as 3 Oe [20].

H_c is nearly the same as the feedstock powder (28.51 Oe), implying that powder might have nanocrystalline phase in the microstructure. Furthermore, the microstructures of the samples with high coercivity (Figure 4.12(a)) and low coercivity (Figure 4.12(b)) do not show any difference in terms of cracks and pores. If the effects of energy density and individual process parameters on H_c are considered (Figure 4.13), generally low coercivity occurs from low E when P is lower than 100 W (Figure 4.13(a)) and h is shorter than $35 \mu\text{m}$ (Figure 4.13(c)). As stated earlier, high E increases the crystallisation rate during the LPBF process [21], which in turn brings about a high number of crystallites in the microstructure thus this increases H_c . It seems that v alone does not have a significant effect on coercivity (Figure 4.13(b)) as at the same E ($= 65 \text{ J/mm}^3$), H_c is nearly the same with varying v . Similarly, t did not affect the coercivity, since H_c is in the range of 20-29 Oe for the layer thicknesses between $30\text{-}70 \mu\text{m}$ (Figure 4.13(d)). Additionally, no direct relation between E and H_c was found in Figure 4.14. It can be said that energy density alone is not a determining factor for coercivity as at the same E , different coercivity values can be observed.

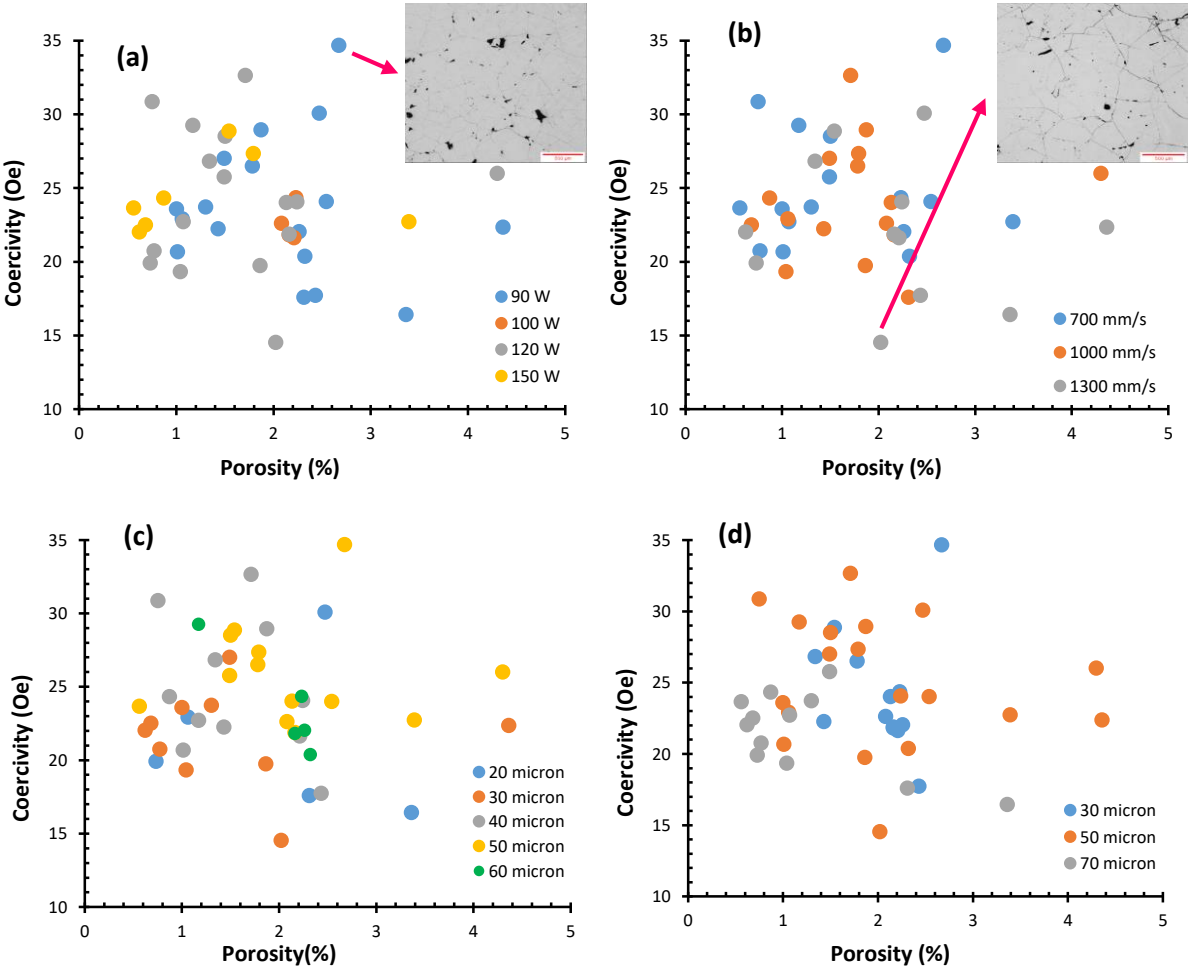


Figure 4.12: The graphs of coercivity as a function of porosity, colour-coded according to (a) laser power, (b) laser scan speed, (c) hatch spacing and (d) layer thickness.

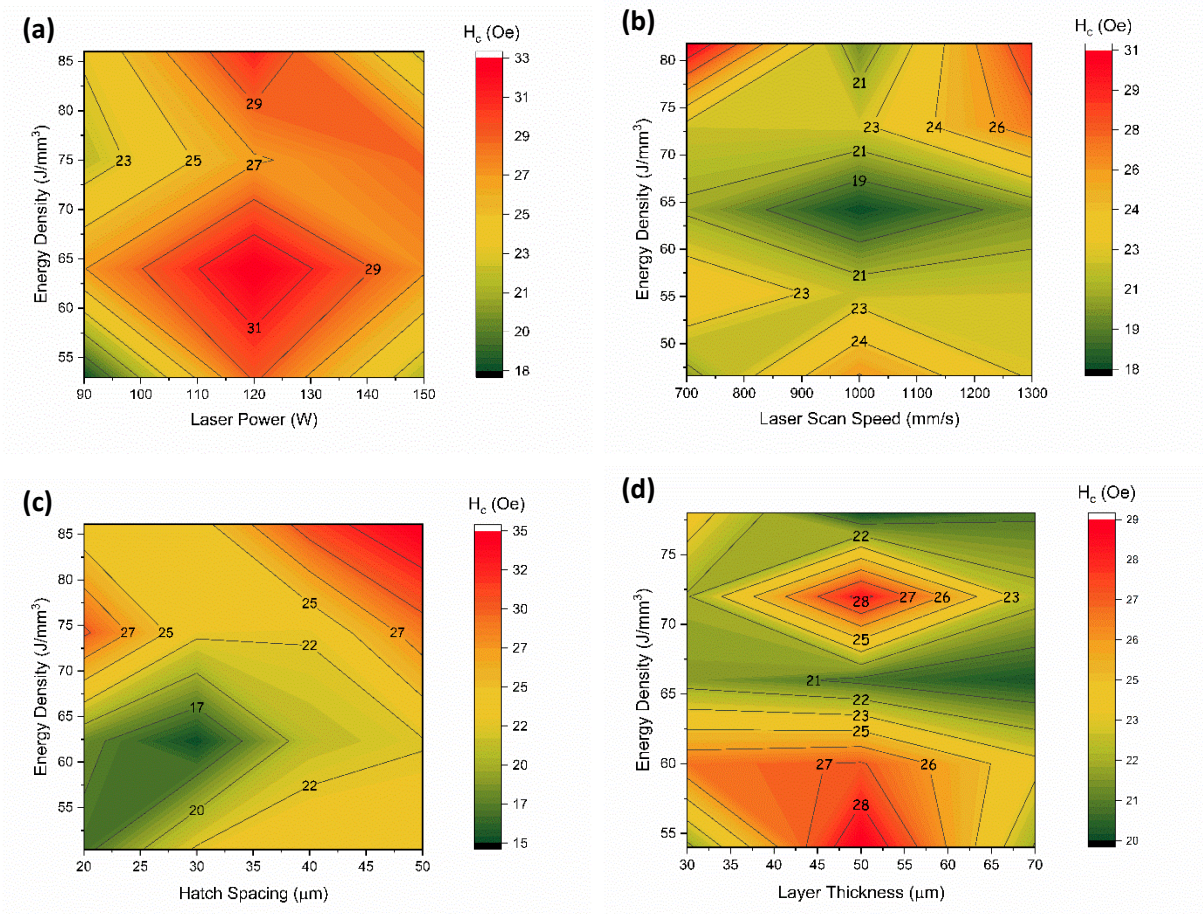


Figure 4.13: Coercivity values of Fe-based BMGs produced utilising different (a) laser power, (b) laser scan speed, (c) hatch spacing and (d) layer thickness (The coercivity values with uncertainties is presented in Appendix C).

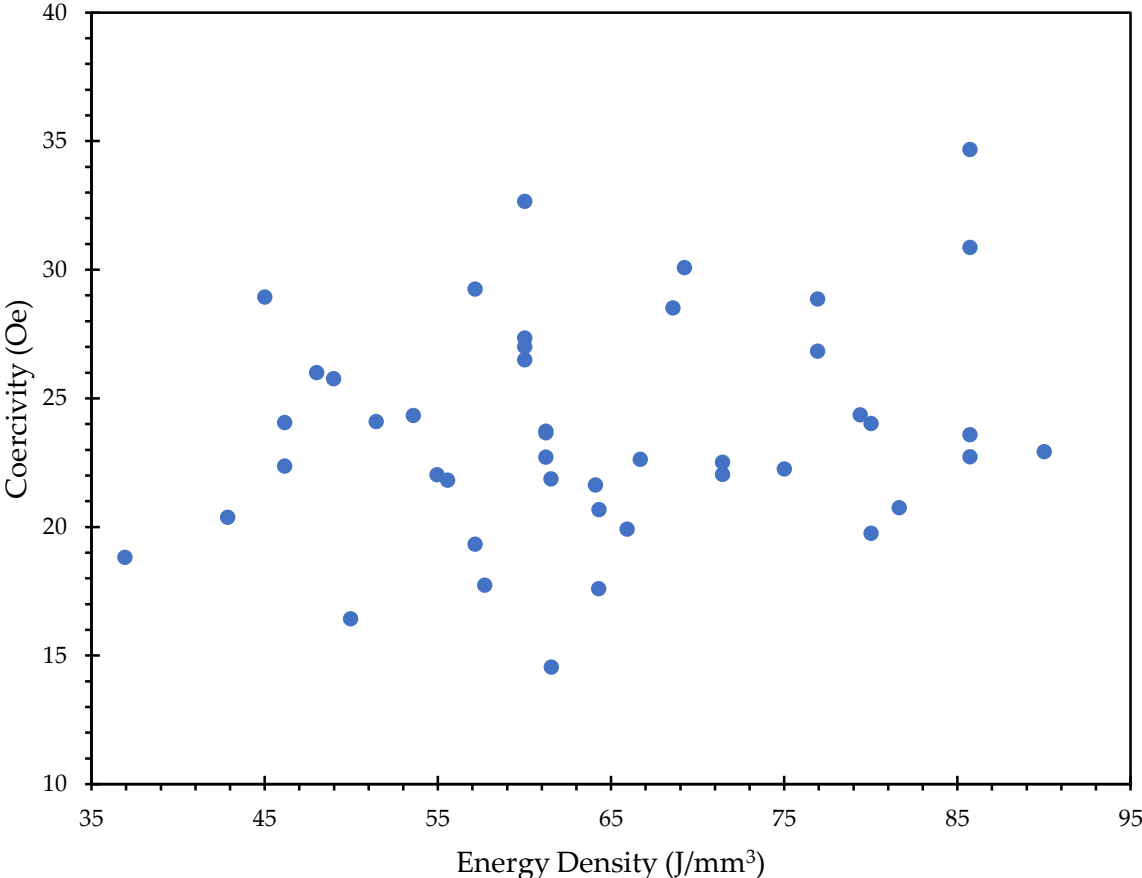


Figure 4.14: The graph showing the relationship between coercivity and energy density of LPBF-processed samples.

Table 4.1 lists the properties of the LPBF-processed Fe-based BMGs from the literature that have a similar composition with the alloy studied in this work. It is obvious that this study achieved the highest bulk density and saturation magnetization because previous researchers generally focused on the laser power and laser scan speed, whereas in this study, all major parameters were studied together. In terms of coercivity, Zrodowski *et al.* [20] introduced a novel scanning strategy involving a different hatching style (checkerboard pattern) to obtain the best result.

Table 4.1: The magnetic properties and bulk densities of Fe-based amorphous alloys processed with LPBF.

Material	M_s (emu/gr)	H_c (Oe)	Bulk Density (%)	Phases	Reference
Fe _{balance} Si ₈₋₁₀ B ₁₂₋₁₅ Cr ₂₋₃ C ₁₋₃ (wt. %)	162.24, 162.7	79.1, 78.8	-	α -Fe(Si), Fe ₃ Si, FeB and Fe ₂ B	[15]
Fe _{92.4} Si _{3.1} B _{4.5}	188.6-199	43.8-73	98.4-98.8	α -Fe(Si), and Fe ₂ B	[1]
Fe ₇₁ Si ₁₀ B ₁₁ C ₆ Cr ₂ (at. %)	~ 150	2.99-12.97	78.1-94.1	α -Fe(Si), Fe ₃ Si and Fe ₂ B	[20]
Fe _{73.7} Si ₁₁ B ₁₁ C ₂ Cr _{2.28}	0.75-1.22 T	20-37	65-96	α -Fe and intermetallic crystallites (FeSi _x and FeC _y)	[16]
Fe _{87.38} Si _{6.85} B _{2.54} Cr _{2.46} C _{0.77} (mass %)	139.2-207.27 (1.26-1.89 T)	14.55-34.68	92.4-99.45	α -Fe(Si), Fe ₃ Si and Fe ₃ B	This study

4.3.1. Design of Experiment

The strength of correlation is determined by the magnitude of the Pearson correlation coefficient (r). Guidelines provided by Cohen [48] offer a general assessment of the strength of association, suggesting that if $.1 < |r| < .3$, the association is considered small; if $.3 < |r| < .5$, the association is medium; and if $|r| > .5$, the association is strong. Table 4.2 illustrates the relationship between the five process parameters and the three material properties. A significant small correlation was observed between bulk density and the four process parameters: laser power ($r = .22$), laser scan speed ($r = .14$), hatch spacing ($r = .16$), and energy density ($r = .18$). The relationship between bulk density and laser power, hatch speed, and energy density was positive, indicating that an increase in any of these parameters led to an increase in bulk density. Conversely, the relationship between bulk density and laser scan speed was negative, indicating that an increase in laser scan speed resulted in a decrease in bulk density. Concerning the relationship between the five process parameters and saturation magnetization, a significant small correlation was observed only between saturation magnetization and laser scan speed ($r = .24$). This negative relationship indicates that an increase in laser scan speed led to a decrease in saturation magnetization (M_s) and vice versa. Finally, a significant small correlation was found between coercivity (H_c) and laser power ($r = .14$). This negative relationship suggests that an increase in laser power led to a decrease in coercivity and vice versa. There was no significant correlation between the remaining four process parameters and coercivity.

Table 4.2: Relationship between the process parameters and outcome variables

<i>Pearson's Correlations (r)</i>			
	Bulk density (%)	M_s (Am²/kg)	H_c (kA/m)
Laser power (W)	.221**	-.057	-.138*
Laser scan speed (mm/s)	-.141*	-.237**	-.117
Hatch spacing (mm)	.163*	-.015	.063
Layer thickness (mm)	-.070	.077	-.127
Energy density (J/mm³)	.179*	.042	-.045

Note: * $p \leq .05$; ** $p \leq .01$ (one -tailed).

Pearson's correlation was employed to establish the relationship between the primary laser process parameters and the resulting properties. It was observed that bulk density is significantly influenced by all process parameters except layer thickness (t). The finding that increasing laser power (P) and decreasing laser scan speed (v) lead to higher bulk density aligns with the experimental results mentioned before. However, these results indicated that increased hatch spacing (h) adversely affected bulk density when other process parameters remained constant. The statistical outcome of increased bulk density with rising h may be attributed to its dependence on other process parameters, particularly P , despite their theoretical independence. It was suggested that the optimal h value should be determined based on melt-pool size, primarily influenced by P and marginally by v as stated in Chapter 5. Like h , t is also influenced by P and v , potentially explaining the lack of a statistically significant relationship between t and the final properties.

Additionally, a significant negative correlation between saturation magnetization (M_s) and v was observed, as expected, as high v results in a high cooling rate, increasing amorphous content and reducing M_s as reported in Chapter 5. Conversely, a significant negative relationship between coercivity (H_c) and P was found instead of a positive one. Since magnetic properties (M_s and H_c) depend significantly on microstructure, including impurities, porosities, and phase presence, considering other process conditions such as chamber oxygen level and parent powder oxygen content may be crucial to understanding changes in magnetic properties. Although this study suggested that statistically, M_s is only influenced by v and H_c is only affected by P , the impact of other laser process parameters cannot be dismissed. All process conditions, in conjunction with P , v , h , and t , must be collectively considered to analyse

changes in microstructure and, consequently, magnetic behaviour. Energy density, treated as an independent variable, showed a significant correlation only with bulk density. This positive correlation complies with the experimental results.

4.4 Conclusion

In this study, $\text{Fe}_{87.38}\text{Si}_{6.85}\text{B}_{2.54}\text{Cr}_{2.46}\text{C}_{0.77}$ samples were produced using LPBF-process, using a variety of laser power, laser scan speed, layer thickness and hatch spacing. It was determined that due to the laser scanning, nanocrystalline alloys composed of metastable Fe_2B nanophase, $\alpha\text{-Fe}(\text{Si})$ and Fe_3Si nanocrystalline clusters with a small (<10%) amorphous phase were produced. The samples with the highest density were achieved at the highest layer thicknesses (70 μm), along with high laser power (120, 150 W) and low hatch spacing (20, 30 μm). It was also determined that to achieve high saturation magnetization and bulk density, a high energy density was required. This was accomplished by having high supercooling in the melt pool zone, which facilitated the formation of the disordered $\alpha\text{-Fe}$ nanograins with high magnetization. For the coercivity, it was found that it was mainly influenced by the crystallite size, rather than the pores and cracks within the sample. To achieve a low coercivity, the energy density had to be low, which decreased the crystallisation rate. Further it was determined that to obtain both high bulk density and superior soft magnetic properties (high M_s and low H_c), a layer thickness greater than 50 μm was required.

The bivariate correlational analysis revealed that bulk density exhibits a significant correlation with laser power (P), laser scan speed (v), hatch spacing (h), and energy density (E), whereas saturation magnetization (M_s) and coercivity (H_c) show significant correlations only with laser scan speed (v) and laser power (P), respectively. This discrepancy may arise from the fact that magnetic properties are heavily dependent on microstructure, and the evolution of microstructure is influenced not only by the laser process parameters examined in this study but also by other process conditions such as the oxygen level in the building chamber. Furthermore, statistically, bulk density increases with rising values of P , h , and E , and decreases with increasing v . Conversely, in the case of magnetic properties, high M_s can be achieved by low v , and low H_c results from high P . It was concluded that laser power (P) and laser scan speed (v) are the primary laser process parameters, upon which hatch spacing (h), and layer thickness (t) depend due to the control exerted by P and v on the melt-pool size.

Acknowledgment

We gratefully thank the Ministry of National Education of the Turkish Government for financial support. We also thank Dr Ian Ross and Dr Jiahui Qi for their assistance and discussions in the preparation of this manuscript.

CRedit author statement

Merve G. Ozden – Conceptualization, methodology, validation, formal analysis, investigation, resources, data curation, writing – original draft, writing – review & editing, visualisation, project administration and funding acquisition.

Nicola A. Morley – Conceptualization, methodology, resources, writing – review & editing, supervision and project administration.

References

- [1] S. Alleg, R. Drablia, N. Fenineche, Effect of the Laser Scan Rate on the Microstructure, Magnetic Properties, and Microhardness of Selective Laser-Melted FeSiB, *Journal of Superconductivity of Novel Magnetism* 31 (2018) 3565-3577.
- [2] S. Pauly, L. Lober, R. Petters, M. Stoica, S. Scudino, U. Kuhn, J. Eckert, Processing metallic glasses by selective laser melting, *Materials Today* 16 (2013) 37-41.
- [3] H. Jung, S. Choi, K. Prashanth, M. Stoica, S. Scudino, S. Yi, U. Kuhn, D. Kim, K. Kim, J. Eckert, Fabrication of Fe-based bulk metallic glass by selective laser melting: A parameter study *Materials and Design* 86 (2015) 703-708.
- [4] C. Chua, K. Leong, *3D Printing and Additive Manufacturing: Principles and Applications*, fourth ed., World Scientific Publishing Co. Pte. Ltd, Singapore, 2014.
- [5] H. Ali, H. Ghadbeigi, K. Mumtaz, Effect of scanning strategies on residual stress and mechanical properties of Selective Laser Melted Ti6Al4V, *Materials Science and engineering: A* 712 (2018) 175-187.
- [6] N. Aboulkhair, N. Everitt, I. Ashcroft, C. Tuck, Reducing porosity in AlSi10Mg parts processed by selective laser melting, *Additive Manufacturing* 1 (2014) 77-86.
- [7] B. Zhang, N. Fenineche, L. Zhu, H. Liao, C. Coddet, Studies of magnetic properties of permalloy (Fe-30%Ni) prepared by SLM technology, *Journal of Magnetism and Magnetic Materials* 32 (2012) 495-500.
- [8] I. Gibson, D. Rosen, B. Stucker, *Additive manufacturing technologies*, Springer, New York, USA, 2010.
- [9] R. Li, J. Liu, Y. Shi, L. Wang, W. Jiang, Balling behaviour of stainless steel and nickel powder during selective laser melting process, *The International Journal of Advanced Manufacturing Technology* 59 (2012) 1025-1035.

- [10] S. Das, Physical Aspects of Process Control in Selective Laser Sintering of Metals, *Advanced Engineering Materials* 5 (2003) 701-711.
- [11] N. Tolochko, S. Mozzharov, I. Yadroitsev, T. Laoui, L. Froyen, V. Titov, M. Ignatiev, Balling processes during selective laser treatment of powders, *Rapid Prototyping Journal* 10 (2004) 78-87.
- [12] P. Krakhmalev, I. Yadroitsev, Microstructure and properties of intermetallic composite coatings fabricated by selective laser melting of Ti–SiC powder mixtures, *Intermetallics* 46 (2014) 147-155.
- [13] C. Yap, C. Chua, Z. Dong, Z. Liu, D. Zhang, L. Loh, S. Sing, 2015, Review of selective laser melting: Materials and applications, *Applied Physics Reviews* 2, 041101.
- [14] V. Sufiiarov, D. Erutin, A. Kantyukov, E. Borisov, A. Popovich, D. Nazarov, 2022, Structure, Mechanical and Magnetic Properties of Selective Laser Melted Fe-Si-B Alloy, *Materials* 15, 4121.
- [15] S. Gao, X. Yan, C. Chang, E. Aubry, P. He, M. Liu, H. Liao, N. Fenineche, 2021, Microstructure and magnetic properties of FeSiBCrC soft magnetic alloy manufactured by selective laser melting, *Materials Letters* 290, 129469.
- [16] Y. Nam, B. Koo, M. Chang, S. Yang, J. Yu, Y. Park, J. Jeong, 2020, Selective laser melting vitrification of amorphous soft magnetic alloys with help of double-scanning-induced compositional homogeneity, *Materials Letter* 261, 127068.
- [17] H. Gong, K. Rafi, H. Gu, T. Starr, B. Stucker, Analysis of defect generation in Ti–6Al–4V parts made using powder bed fusion additive manufacturing processes, *Additive manufacturing* 1 (2014) 87-98.
- [18] S. Liu, H. Li, C. Qin, R. Zong, X. Fang, 2020, The effect of energy density on texture and mechanical anisotropy in selective laser melted Inconel 718, *Materials and Design* 191, 108642.
- [19] H. Gong, K. Rafi, H. Gu, J. Ram, T. Starr, B. Stucker, Influence of defects on mechanical properties of Ti-6Al-4V components produced by selective laser melting and electron beam melting, *Materials and Design* 86 (2015) 545-554.
- [20] L. Zrodowski, B. Wysocki, R. Wroblewski, A. Krawczynska, B. Adamczyk-Cieslak, J. Zdunek, P. Blyskun, M. Leonowicz, J. Ferenc, W. Swieszkowski, New approach to amorphization of alloys with low glass forming ability via selective laser melting, *Journal of Alloys and Compounds* 771 (2019) 769-776.

- [21] D. Ouyang, W. Xing, N. Li, Y. Li, L. Liu, Structural evolutions in 3D-printed Fe-based metallic glass fabricated by selective laser melting, *Additive Manufacturing* 23 (2018) 246-252.
- [22] Q. Jia, D. Gu, Selective laser melting additive manufacturing of Inconel 718 superalloy parts: Densification, microstructure and properties, *Journal of Alloys and Compounds* 585 (2014) 713-721.
- [23] D. Gu, W. Meiners, K. Wissenbach, R. Poprawe, Laser additive manufacturing of metallic components: Materials, processes and mechanisms, *International Materials Reviews* 57 (2012) 133-164.
- [24] C. Li, Y. Guo, J. Zhao, Interfacial phenomena and characteristics between the deposited material and substrate in selective laser melting Inconel 625, *Journal of Materials Processing Technology* 243 (2017) 269-281.
- [25] A. Yazdani, G. Höhne, S. Misture, O. Graeve, 2020, A method to quantify crystallinity in amorphous metal alloys: A differential scanning calorimetry study, *PLoS ONE* 15, e0234774.
- [26] D. dos Santos, D. dos Santos, Crystallisation kinetics of Fe–B–Si metallic glasses, *Journal of Non-Crystalline Solids* 304 (2002) 56-63.
- [27] R. Piccin, P. Tiberto, M. Baricco, Glass formation and magnetic characterization of (Fe₇₈B₁₄Si₈)–Nb–Y alloys, *Journal of Alloys and Compounds* 434-435 (2007) 628-632.
- [28] Z. Lu, C. Liu, J. Thompson, W. Porter, 2004, Structural Amorphous Steels, *Physical Review Letters* 92, 245503.
- [29] C. Zhang, D. Ouyang, S. Pauly, L. Liu, 2021, 3D printing of bulk metallic glasses, *Materials Science & Engineering R* 145, 100625.
- [30] J. Lentz, A. Rottger, F. Grobwendt, W. Thesien, Enhancement of hardness, modulus and fracture toughness of the tetragonal (Fe,Cr)₂B and orthorhombic (Cr,Fe)₂B phases with addition of Cr, *Materials and Design* 156 (2018) 113-124.
- [31] C. Yang, G. Yang, Y. Lu, Y. Chen, Y. Zhou, Phase selection in highly undercooled Fe-B eutectic alloy melts, *Trans. Nonferrous Met. SOC. China* 16 (2006) 39-43.
- [32] K. Prashanth, S. Scudino, T. Maity, J. Das, J. Eckert, Is the energy density a reliable parameter for materials synthesis by selective laser melting?, *Materials Research Letters* 5 (2017) 386-390.
- [33] F. Xie, Q. Chen, J. Gao, Y. Li, Laser 3D Printing of Fe-Based Bulk Metallic Glass: Microstructure Evolution and Crack Propagation, *JMEPEG* 28 (2019) 3478-3486.

- [34] L. Li, Repair of directionally solidified superalloy GTD-111 by laser-engineered net shaping, *J. Mater. Sci.* 41 (2006) 7886-7893.
- [35] M. Kahn, P. Dickens, Selective Laser Melting (SLM) of pure gold, *Gold Bulletin* 43 (2010) 114-121.
- [36] H. Gong, K. Rafi, H. Gu, T. Starr, B. Stucker, Analysis of defect generation in Ti-6Al-4V parts made using powder bed fusion additive manufacturing processes, *Additive Manufacturing* 1, (2014) 87-98.
- [37] M. A. Willard, M. Daniil, Nanocrystalline Soft Magnetic Alloys Two Decades of Progress, *Handbook of Magnetic Materials* 21 (2013) 173-342.
- [38] S. Sgobba, Physics and measurements of magnetic materials, *CERN* 4 (2010) 39-63.
- [39] Y. Jing, S. He, J. Wang, 2013, Fe₃Si nanoparticles for alternating magnetic field heating, *J. Nanopart. Res.* 15, 1517.
- [40] F. Luborsky, J. Livingston, G. Chin, Chapter 29 - Magnetic Properties of metals and alloys, *Physical Metallurgy* 3 (1996) 2501-2565.
- [41] D. Wang, L. Ma, L. Li, X. Xu, Y. Guo, S. Zhao, Characterization of Polycrystalline Fe₂B Compound with High Saturation Magnetization, *J. Supercond. Nov. Magn.* 31 (2018) 431-435.
- [42] D. Dunlop, O. Ozdemir, Magnetizations in Rocks and Minerals, *Treatise on Geophysics* 5 (2007) 277-336.
- [43] G. Herzer, Modern soft magnets: Amorphous and nanocrystalline materials, *Acta Materialia* 61 (2013) 718-734.
- [44] Z. Li, K. Yao, X. Li, X. Ni, Z. Lu, The effect of ribbon curvature on the magnetic properties of Fe-based amorphous cores, *J Mater Sci: Mater Electron* 28 (2017) 16736-16740.
- [45] F. Wang, A. Inoue, Y. Han, F. Kong, S. Zhu, E. Shalaan, F. Al-Marzouki, A. Obaid, Excellent soft magnetic Fe-Co-B-based amorphous alloys with extremely high saturation magnetization above 1.85 T and low coercivity below 3 A/m, *Journal of Alloys and Compounds* 711 (2017) 132-142.
- [46] A. Goldman, A. Kreyssig, G. Rustan, D. Quirinale, 2015, Synergistic stabilisation of metastable Fe₂₃B₆ and γ -Fe in undercooled Fe₈₃B₁₇, *Appl. Phys. Lett.* 106, 241906.

Chapter 4 – Research Paper I

- [47] M. Celikbilek, A. Ersundu, S. Aydin, Crystallisation Kinetics of Amorphous Materials, in *Advances in Crystallisation Processes*, InTech, Rijeka, 2012, pp. 127-162.
- [48] J. Cohen, *Statistical Power Analysis for the Behavioural Sciences*, Hillsdale, New Jersey: Lawrence Erlbaum Associates, Publishers, 1988.

Chapter 5: Research Paper 2

The previous chapter revealed that the soft-magnetic behaviour of Fe-based nanocrystalline alloys strongly depended on their microstructure, and energy density was not a reliable parameter to optimize their soft magnetic behaviour. For this reason, this chapter presents an investigation of the individual influences of the major process parameters (laser power, laser scan speed, hatch spacing and layer thickness) on the bulk density, microstructural evolution, saturation magnetization and coercivity of Fe-based nanocrystalline alloys. Also, how their microstructural change affects their saturation magnetization and coercivity was studied in this chapter.

Soft-Magnetic Behaviour of Fe-Based Nanocrystalline Alloys Produced Using Laser Powder Bed Fusion

Merve G. Ozden^{1,*} Felicity SHB. Freeman and Nicola A. Morley¹

¹ Department of Material Science and Engineering, University of Sheffield, Sheffield, S1 3JD, UK, mgozden1@sheffield.ac.uk

* Correspondence: mgozden1@sheffield.ac.uk

Citation: Ozden, M.G., Freeman, F.SHB. and Morley, N.A. Soft-Magnetic Behaviour of Fe-Based Nanocrystalline Alloys Produced Using Laser Powder Bed Fusion. *Advanced Engineering Materials* 2023, 25(19), 2300597. <https://doi.org/10.1002/adem.202300597>.

Copyright: © 2023 The Authors. *Advanced Engineering Materials* published by Wiley-VCH GmbH. This is an open access article under the terms of the Creative Commons Attribution-Non-commercial-No Derivations License, which permits use and distribution in any medium, provided the original work is properly cited, the use is non-commercial, and no modifications or adaptations are made.

Abstract

In this paper, an extensive experimental study is presented on the influence of the major process parameters of the Laser Powder Bed Fusion (LPBF) technique on the bulk density and soft-magnetic properties of Fe-based bulk metallic glasses (BMGs). For this purpose, 81 samples were manufactured by using the combinations of different process parameters, i.e., layer thickness (t : 50-70 μm), laser power (P : 70-130 W), laser scan speed (v : 900-1100 mm/s) and hatch spacing (h : 20-40 μm). High bulk density ($\geq 99\%$) was achieved utilising low P and v combined with low h and t in order to decrease energy input to the powder, preventing cracks associated with the brittle nature of BMGs. Furthermore, it was indicated that $h = 30 \mu\text{m}$ and $v = 1000 \text{ mm/s}$ play

a determining role in acquiring high saturation magnetization ($\geq 200 \text{ Am}^2/\text{kg}$) resulting from their influence on the thermal gradient that occurred between the two laser scans. Due to the laser scanning nature of the process, two distinct microstructures evolve, melt-pool (MP) and heat affected zone (HAZ). While MP is mainly composed of α -Fe(Si) phase, HAZ contains nanocrystalline phases (Fe_2B and Fe_3Si) in an amorphous matrix. The experimental results demonstrated that saturation magnetization (M_s) was considerably affected by the amorphous content and the quantity of nanocrystalline phases present in the microstructure.

5.1 Introduction

Ferromagnetic metallic glasses (MGs) have been studied extensively owing to their lack of crystalline defects, resulting in superior soft-magnetic properties. Crystalline-related imperfections lead to anisotropy, which in turn increases the coercive field within the material. Thus, low coercivity is achieved with a fully amorphous phase present in the material [1]. Introducing nanocrystalline phases into an amorphous matrix provides higher saturation magnetization and higher permeability (Figure 5.1), especially in Fe-based ferromagnets [2]. Their exceptional soft-magnetic properties allow them to be utilised as a magnetic core material in electromagnetic systems in order to increase their efficiency by lowering the energy losses considerably for eddy currents [3]. Recently, Thorsson *et al.* managed to produce a Fe-based nanocrystalline complex-shaped electric motor rotor with a 6 cm diameter by selective laser melting [4], enabling its users to build 3D complicated shapes in one-production step without the need of post-processing [5]. The 3D printed electric motor rotor possessed high electrical resistivity ($178.2 \mu\Omega\cdot\text{cm}$), high magnetic susceptibility (9.17), relatively high saturation magnetization (1.29 T) and relatively small coercivity (0.51 kA/m), which are the key factors for electric motors. Moreover, the electric motor rotor was fabricated with much larger than critical casting thickness (6 cm) due to the high cooling rate evolving in the whole part [4]. This can only be achieved by using laser additive manufacturing (LAM).

Laser Powder Bed Fusion (LPBF), as one of the LAM techniques, has been exploited widely for Fe-based amorphous/nanocrystalline ferromagnetic materials. LPBF, also known as selective laser melting (SLM), manufactures dense metallic components in a layer-by-layer fashion by using a focused laser beam, scanning each powder layer [6]. Figure 5.2(a) shows the main process parameters of LPBF technique. Optimization of those parameters play an important role in producing Fe-based amorphous/nanocrystalline alloys as changing parameters affects the microstructural evolution, which is complex and heterogeneous as shown in Figure 5.2(b), (c) and (d).

Because of the laser scanning nature of the LPBF process, the microstructure usually contains two distinct regions, melt pool (MP) and heat affected zones (HAZ), both of which experience different cooling rates [7]. One of the main challenges in LPBF technique is process optimization to control the microstructure of Fe-based amorphous/nanocrystalline ferromagnets in order to enhance their soft-magnetic properties.

This paper addresses this issue to comprehend how microstructural development influences magnetic properties of Fe-based alloys as well as how bulk density changes with different process parameters. To do this, all major process parameters were considered: laser power (P), laser scan speed (v), hatch spacing (h) and layer thickness (t). Researchers have generally investigated the effects of laser power and laser scan speed on the properties of Fe-based MGs [3, 8-11]. This work provides a comprehensive experimental study to optimise the LPBF process for the differing process parameters (P, v, h and t).

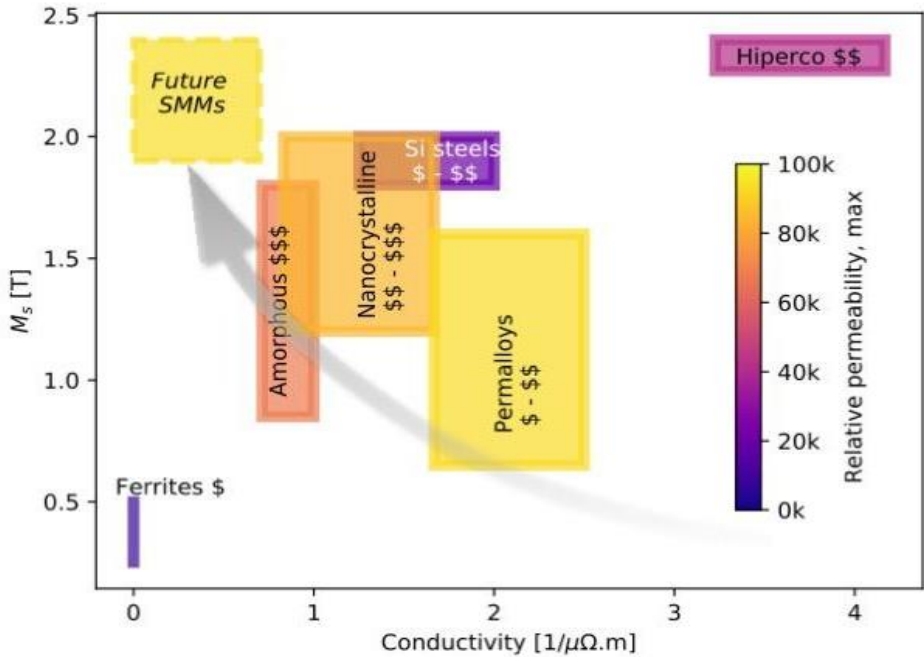


Figure 5.1: Relative permeability and saturation magnetization of soft-magnetic materials.

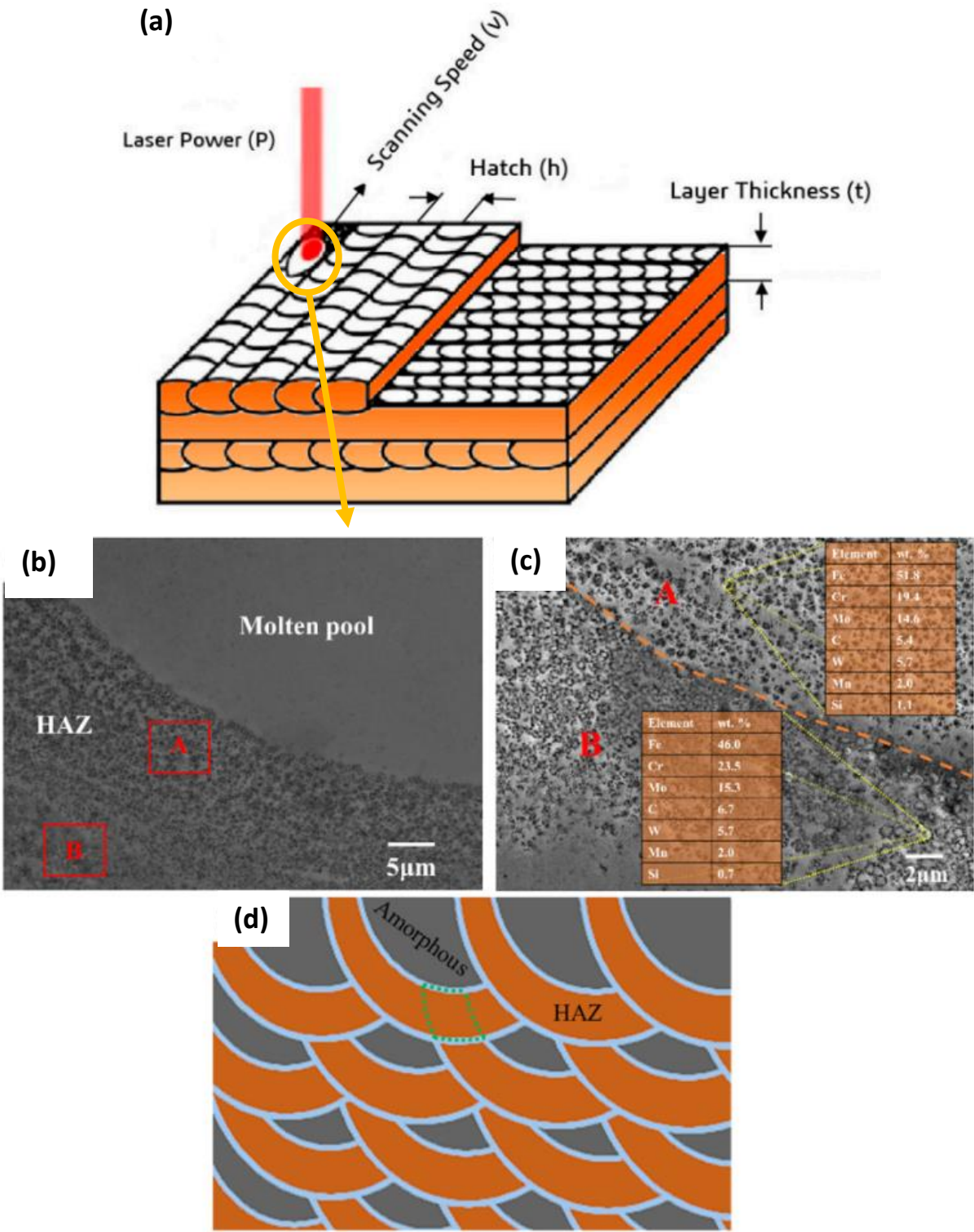


Figure 5.2: (a) The studied process parameters of LPBF technique [12], (b) the SEM microstructure of the MP and HAZ regions of the LPBF-processed FeCrMoCWMnSi amorphous alloy, (c) the HAZ microstructure of the same sample taken at higher magnification and (d) the schematic illustrations of microstructural development of BMGs during LPBF process [13].

5.2 Experimental Procedure

5.2.1 Material

The amorphous ferromagnetic powder (KUAMET 6B2 ($\text{Fe}_{87.38}\text{Si}_{6.85}\text{B}_{2.54}\text{Cr}_{2.46}\text{C}_{0.77}$ (mass %))), provided by Epson Atmix Corporation, Japan, was chosen for this study. This was because the elements within the Fe-Si-B-Cr-C system are widely available and more sustainable than its competitive materials, containing Co or rare earth materials such as Nd and Dy. The only expensive element in the alloy is boron, however with a smaller quantity (2.54%) compared to other amorphous alloys. The powder characterization results can be found in our previous work [14] (Chapter 4). According to the results, the amorphous spherical powder has a narrow particle size distribution with D10, D50 and D90 of 9.49, 23.4 and 47.5 μm , respectively. In addition, it shows soft-magnetic behaviour with saturation magnetization of 102 Am^2/kg and coercivity of 2.27 kA/m .

5.2.2 Methods

Firstly, powder sieving was carried out using a 53 μm mesh-size sieve to narrow the particle size distribution down for better spreadability and flowability over the powder bed. An Aconity Mini machine was used to print the cylindrical samples with the dimensions of 6 mm in diameter and 5 mm in height. Different combinations of process parameters were applied to study their individual effect on the properties (Appendix A). For all layer thicknesses, t (50, 60 and 70 μm), the same hatch spacing, h (20, 30 and 40 μm) and laser scan speed, v (900, 1000, 1100 mm/s) values were maintained, however, with the increasing layer thickness, it was necessary to increase laser power to obtain bulk dense parts, as stated in our previous work [14] (Chapter 4). Therefore, at $t = 50 \mu\text{m}$, $P = 70, 80$ and 90 W (Table j in Appendix D); at $t = 60 \mu\text{m}$, $P = 90, 100, 110 \text{ W}$ (Table k in Appendix D) and at $t = 70 \mu\text{m}$, $P = 110, 120$ and 130 W (Table l in Appendix D) were used. All the samples were printed using the hatch filling type with a starting angle of 22.5° and rotation of 70° after each layer and the residual oxygen content of the chamber was kept below 0.01% to prevent oxidation.

After the production of the samples, their densities were measured with an Archimedes technique set-up three times. The bulk density percentage was quantified using the mean density and the theoretical density (7.294 gr/cm^3) for every sample. Moreover, the micrographs of the samples were taken by INSPECT F50 HR-SEM after they were ground, polished and subjected to etching for 3 min with 2% nital solution (98 ml HNO_3 and 2 ml ethanol). The crystallite sizes were calculated from those micrographs using the ImageJ program. Differential scanning calorimetry (DSC) (TA instruments SDT Q600 machine) was utilised by heating the samples with a rate of 20

K/min up to 1673 K to obtain their crystallisation enthalpies. Then, the amorphous content was quantified by using the technique, described in these articles [3, 10, 15]. Finally, the magnetic properties (saturation magnetization and coercivity) were determined from magnetization hysteresis (M-H) loops, which were obtained using a SQUID magnetometer MPMS3 from Quantum Design at 300 K and fields up to 160 kA/m.

5.3 Results and Discussion

As stated in our previous work [14], due to the high thermal gradients evolved between two hatches, the cooling rate significantly differs so that four phases develop in the distance of hatch spacing (Figure 5.3). The α -Fe(Si) phase mainly evolves in the melt pool (MP) region (Figure 5.3(a) and 5.3(b)) whereas Fe₃Si nanoclusters and Fe₂B crystallites exist in the heat-affected zone (HAZ) region (Figure 5.3(f)). In the HAZ region, the presence of the ordered Fe₂B phase implies that HAZ has the equilibrium condition (slower cooling rate). Small amount of the amorphous phase content ($\leq 30\%$) suggested that it was embedded in the matrix, retained from the parent powder. Phase identification (XRD, TEM and DSC analysis) was performed in the previous study [14], where it was shown that the disordered α -Fe(Si), the ordered Fe₃Si and the stable Fe₂B phases grow as equiaxed, dendritic (star-like) and needle-like, respectively. Moreover, the size of the α -Fe(Si) phase increases from MP to the end of HAZ region (Figure 5.3(a) and (b)), which means this phase has a variety of sizes within the same MP region. For this reason, its grain size was represented as particle size distribution in the form of histogram graph in this study, where the effect of process parameters on the particle size distribution of the α -Fe(Si) phase was investigated. The thermal gradient mostly influences its amorphous content and grain size in the MP region, which in turn affects the soft-magnetic properties.

There are two types of cracks in the microstructure, based on the crack size: macro cracks (Figure 5.3(c)) and micro cracks (Figure 5.3(d)). Bigger cracks, also known as cold or crisscross cracks, occur irregular shrinkage and residual thermal stresses caused by rapid cooling, high thermal gradient, and poor ductility of BMGs [16, 17]. Microcracks generally form due to near lack of fusion (LoF) pores and/or un-melted powders at the end of melt-pool, as shown in Figure 5.3(d) [18]. The occurrence of micro-segregation during rapid solidification has been identified as a potential contributor to microcracking [19]. Micro-segregation has the capacity to expand the solidification temperature range, consequently heightening the vulnerability to solidification microcracking [20].

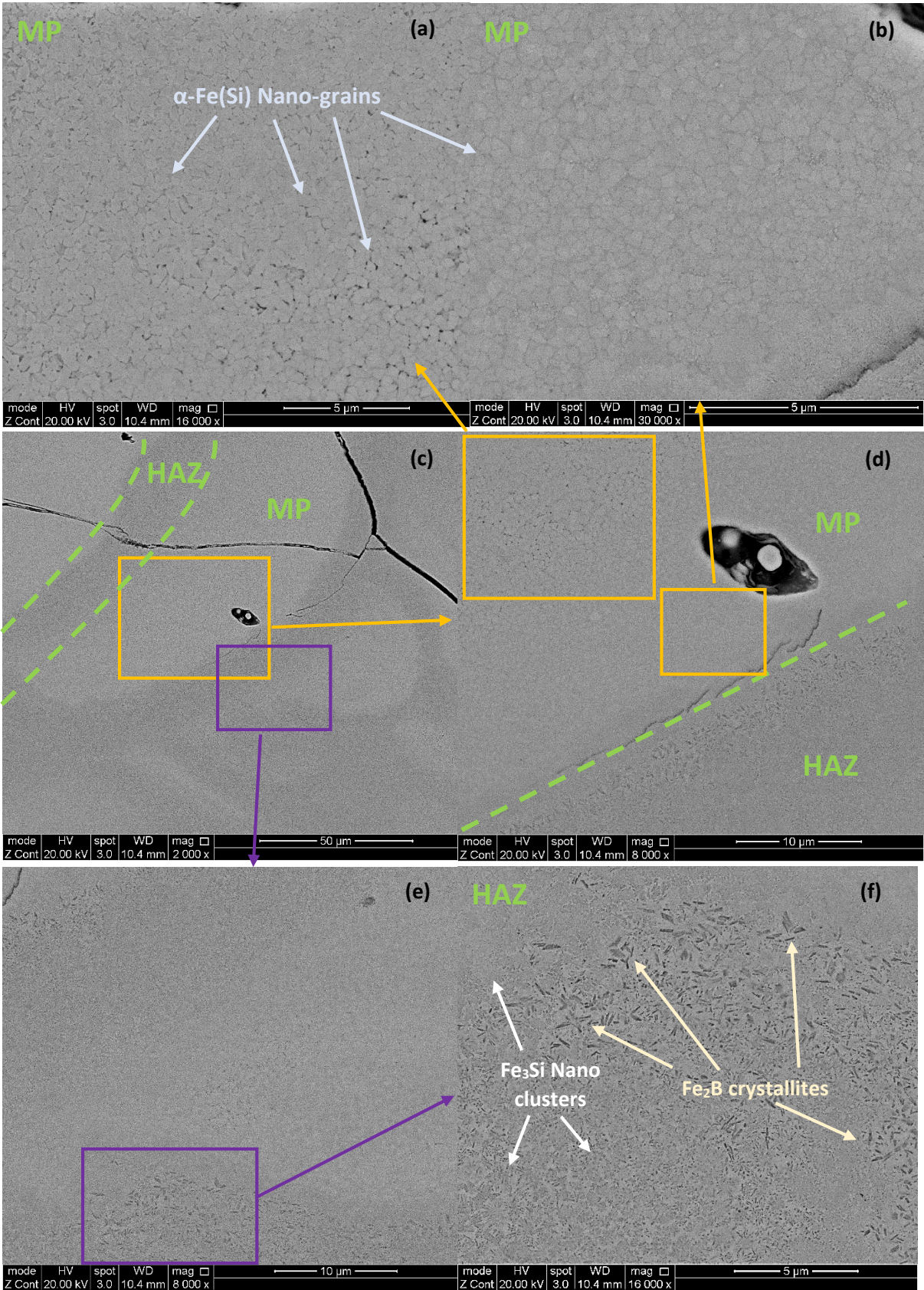


Figure 5.3: SEM micrographs of LPBF processed samples showing (a) and (b) the microstructures in melt pool zone (MP) containing α -Fe(Si) grains; (c) and (d) MP and HAZ regions at higher magnification; (e) and (f) the microstructures in heat affected zone (HAZ) composed of Fe₃Si and Fe₂B nano-phases.

Elemental analysis showed the Fe content in the samples is around 82 wt.%. The only noteworthy differences between MP and HAZ regions are that the Fe content is higher in the MP (due to amorphous and α -Fe phases) and the B content is higher in the HAZ region, because of Fe₂B phases (Table 5.1). While EDS gives the general idea about elemental compositions for comparison, it is worth mentioning that it is not reliable to investigate exact compositions resulting from the presence of B and C in the sample. Additionally, since Fe, Si and Cr possess relatively lower boiling points of 3135 K, 2628 K and 2945 K, respectively; they might evaporate during processing. This may cause a change in elemental compositions as well.

Table 5.1: EDS results of the LPBF-processed samples and their MP and HAZ regions in their microstructure.

Wt. %	General	MP	HAZ
Fe	81.9±0.4	83.0±0.9	80.8±0.8
Si	6.0±0.1	6.1±0.1	5.9±0.1
B	3.1±0.5	1.8±1.0	3.9±1.0
Cr	2.5±0.1	2.6±0.1	2.4±0.1
C	6.5±0.1	6.5±0.2	7.0±0.3

Before starting to investigate the change in magnetic properties with different process parameters, it is worth noting that in general, the saturation magnetization, M_s is influenced dominantly by the amount of magnetic transition metals (Fe, Co and Ni) because of their high magnetic moments [21]. In literature, amorphous ferromagnets containing 82 wt.% of Fe possess a saturation magnetization of 180 Am²/kg [22] (1.6 T [23, 24]). Nevertheless, it was well-established that their saturation magnetization can be enhanced considerably by nucleating nanometre-sized phases in an amorphous matrix [25-28]. However, as the grain size reaches to 100 nm, the coercive field can be 10-50 kA/m resulting from increase in the length of grain boundaries, which are crystal lattice defects [29]. It was proven that coercivity has the lowest value for the grain sizes that are either less than 40 nm or more than 100 μ m [30, 31]. Considering the crystallite sizes of bcc-Fe phases (50-1000 nm), the coercivity has a dependence of $1/D$ on the grain size (D), rather than D^6 . This means as the grain size increases, magneto-crystalline anisotropy decreases in the macroscopic scale due to the reduction in grain boundary area. Fe₂B tetragonal structure has much higher magneto-crystalline anisotropy (anisotropy constant (K_1 : 100 kJ/m³) than bcc-Fe phase (K_1 : 8 kJ/m³). Nevertheless, since the Fe₂B phase is in a small quantity in the microstructure and its size does not change considerably with different process parameters, its effect on coercivity was ignored in this study. However, to minimise the coercivity, one might consider preventing the

formation of Fe₂B phase in the microstructure. The amorphous content also changes the magnetic properties, i.e., a higher content is expected to reduce the saturation magnetization (M_s) and coercivity (H_c).

Laser power (P) is the most dominant parameter to vary the thermal profile between two laser scans. While laser power and laser scan speed (v) mainly affect cooling rate, layer thickness (t) and hatch spacing (h) influence thermal gradient. In cooling rate, temperature and time depends on P and v , respectively. Maximum nucleation rate occurs at just above the glass transition temperature and lowers quickly with increasing temperature, whereas the growth rate continues to increase, reaching its maximum at much higher temperature [32]. For this reason, low initial temperature associated with low laser power promotes nucleation while high initial temperature related to high laser power increases growth rate (grains are bigger in size, rather than increase in number). Increasing P from 90 W to 100 W increases the nucleation rate, on the other hand at $P=110$ W, growth of the nucleus is dominant (Figure 5.4(a)). At low P ($=90$ W), there are a few smaller α -Fe(Si) grains (narrow particle size distribution) in the MP region (Figure 5.4(a)), which implies high cooling rate, i.e., high amorphous content, leading to low saturation magnetization (M_s) (Figure 5.4(b)). Coercivity (H_c) is affected by not only magnetic anisotropy, but also defects in the parts. High laser power (100 W) improves the sintering of powders, lowering the porosity content and eventually decreases H_c (Figure 5.4(c)). High coercivity at $P=110$ W could be resulting from low amorphous content (Figure 5.4(b)), bigger grains (≤ 1000 nm) and wider particle size distribution (50-1000 nm) (Figure 5.4(a)).

Laser scan speed (v) impacts the time parameter in the cooling rate expression. Low v provides a long time between laser scan tracks, lowering the cooling rate and increasing the crystallisation rate at constant temperature [33]. That is why the crystallite size decreases, when the v increases from 900 mm/s (100-700 nm) to 1100 mm/s (100-600 nm) (Figure 5.5(a)). Also, decreasing the cooling rate (at $v = 900$ mm/s) leads to the low amorphous content, which brings about high M_s (Figure 5.5(b)). When other parameters are constant and moderate, increasing v brings about the balling effect (this phenomenon generally occurs at high v or large h due to unstable melt. More detailed information can be found elsewhere [34]), leading to high porosity content. Even though the crystallite size is smaller, and the amorphous content is higher at high v ($=1100$ mm/s) (Figure 5.5(b)), high coercivity is observed at this parameter, implying that the high porosity level increases the coercivity (Figure 5.5(c)). Hatch Spacing (h) and layer thickness (t) have a major effect on the thermal gradient from the MP through to the HAZ. High h and t increase the thermal gradient, lowering the cooling rate and temperature in both MP and HAZ regions. This makes nucleation

dominant overgrowth of crystallites from the crystallisation kinetics point of view. At increasing h (Figure 5.6(a)) and t (Figure 5.7(a)), the number of crystallites increases in the MP, causing high M_s despite high amorphous content (Figure 5.6(b) and 5.7(b)). Although layer thickness does not have substantial effect on the porosity and coercivity (Figure 5.7(c)), high hatch spacing lowers the bulk density by 1 % due to the balling effect (Figure 5.6(c)).

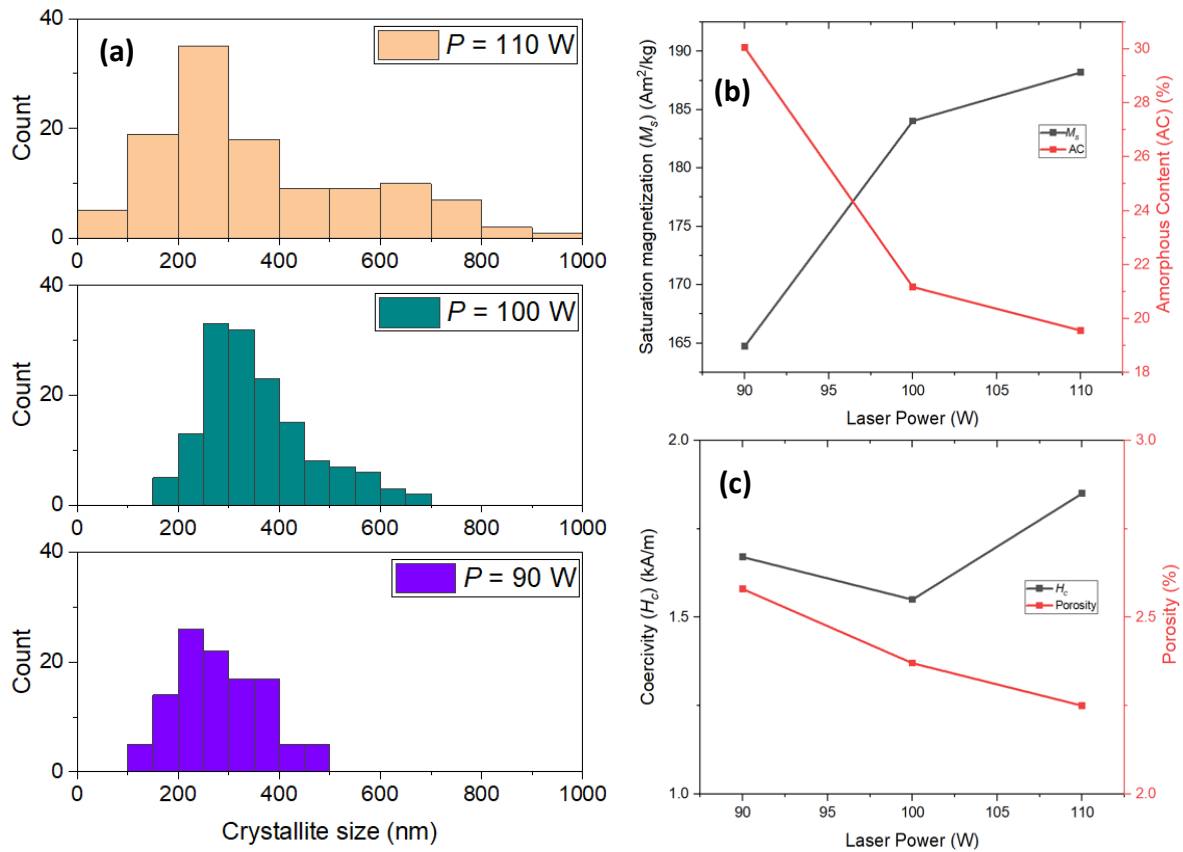


Figure 5.4: The characterization results demonstrate the effect of laser power on the microstructural and magnetic properties of 3D printed samples by using different laser power (90, 100 and 110 W) (other parameters kept constant; $v=900$ mm/s, $h=30$ μm , $t=60$ μm): (a) The histogram graphs showing α -Fe(Si) crystallite size distribution and the graphs illustrating (b) saturation magnetization and amorphous content, (c) coercivity and porosity values as a function of laser power.

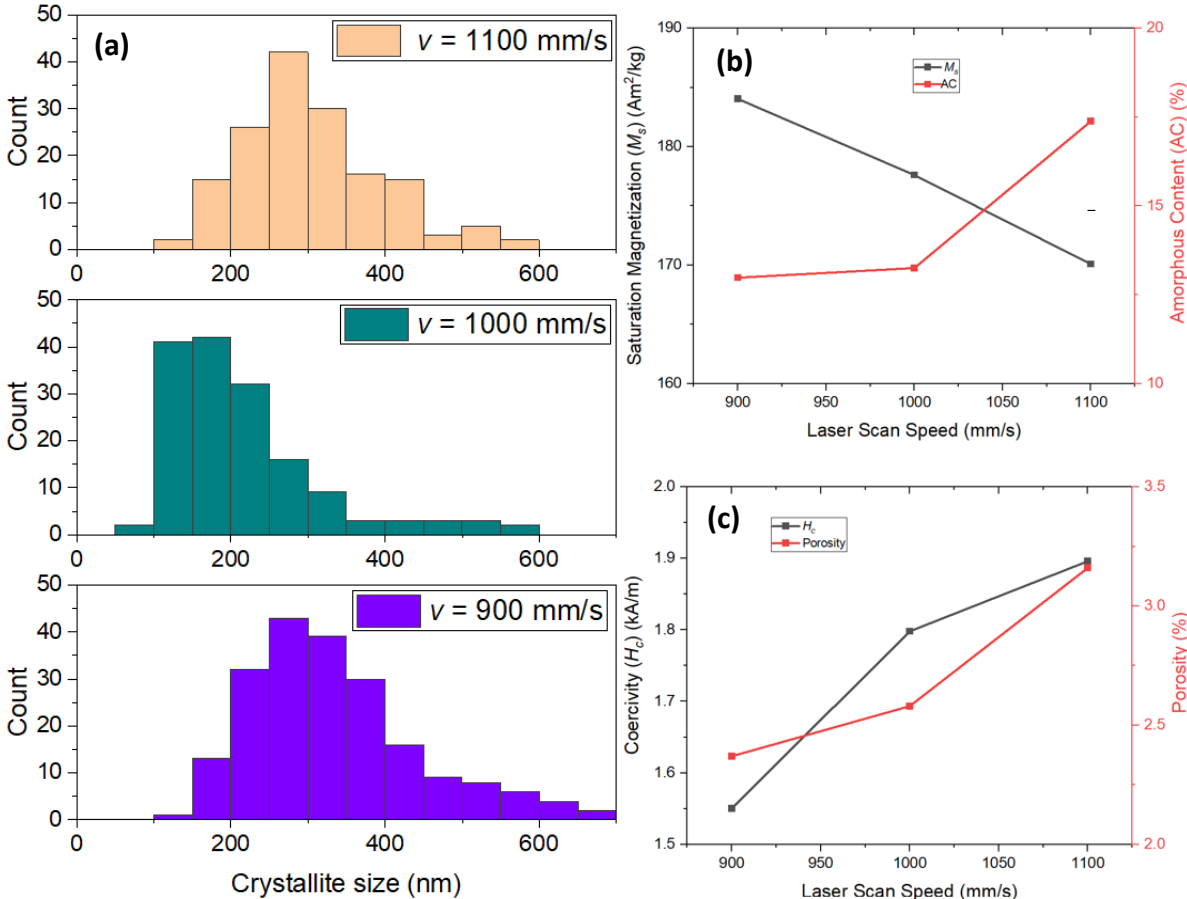


Figure 5.5: The characterization results demonstrate the effect of laser scan speed on the microstructural and magnetic properties of 3D printed samples by using different laser scan speed (900, 1000 and 1100 mm/s) (other parameters kept constant; $P=100$ mm/s, $h=30$ μm , $t=60$ μm): **(a)** The histogram graphs showing $\alpha\text{-Fe(Si)}$ crystallite size distribution and the graphs illustrating **(b)** saturation magnetization and amorphous content, **(c)** coercivity and porosity values as a function of laser scan speed.

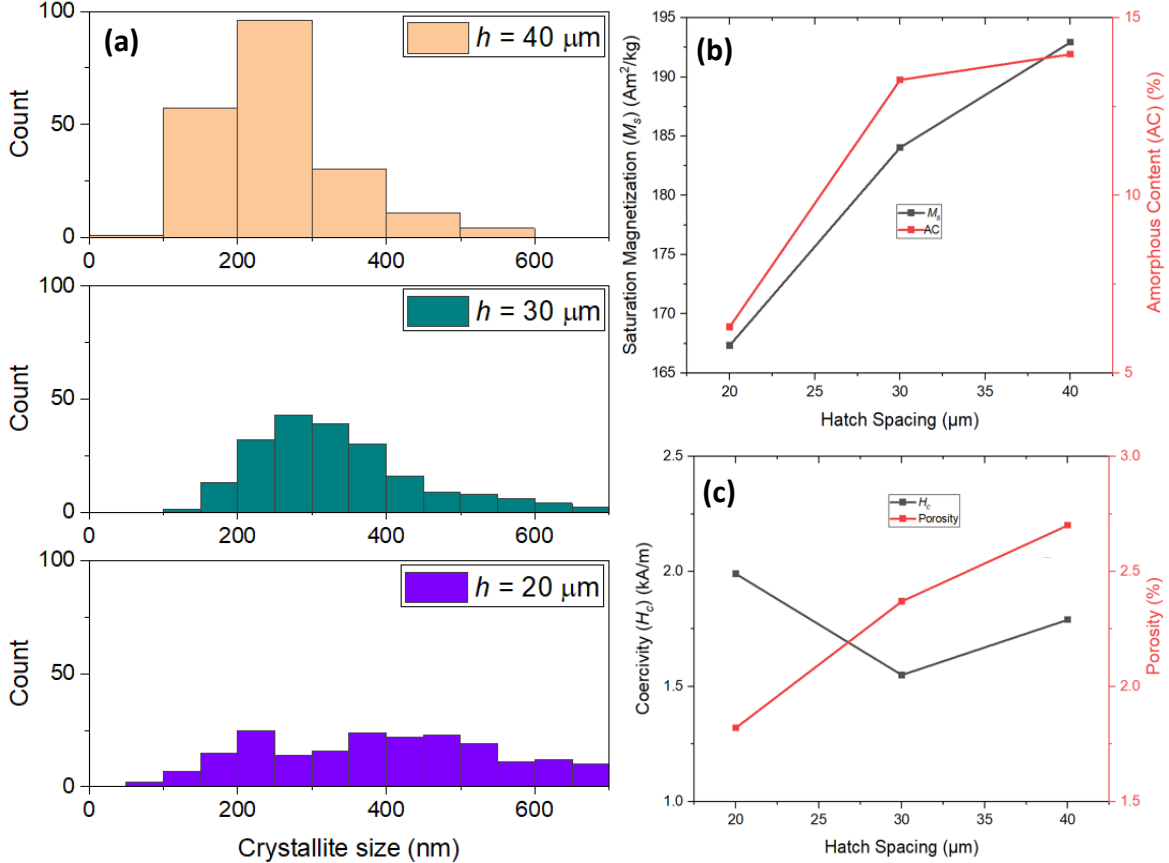


Figure 5.6: The characterization results demonstrate the effect of hatch spacing on the microstructural and magnetic properties of 3D printed samples by using different hatch spacing (20, 30 and 40 μm) (other parameters kept constant; $v=900 \text{ mm/s}$, $P=100 \text{ W}$, $t=60 \mu\text{m}$): **(a)** The histogram graphs showing α -Fe(Si) crystallite size distribution and the graphs illustrating **(b)** saturation magnetization and amorphous content, **(c)** coercivity and porosity values as a function of hatch spacing.

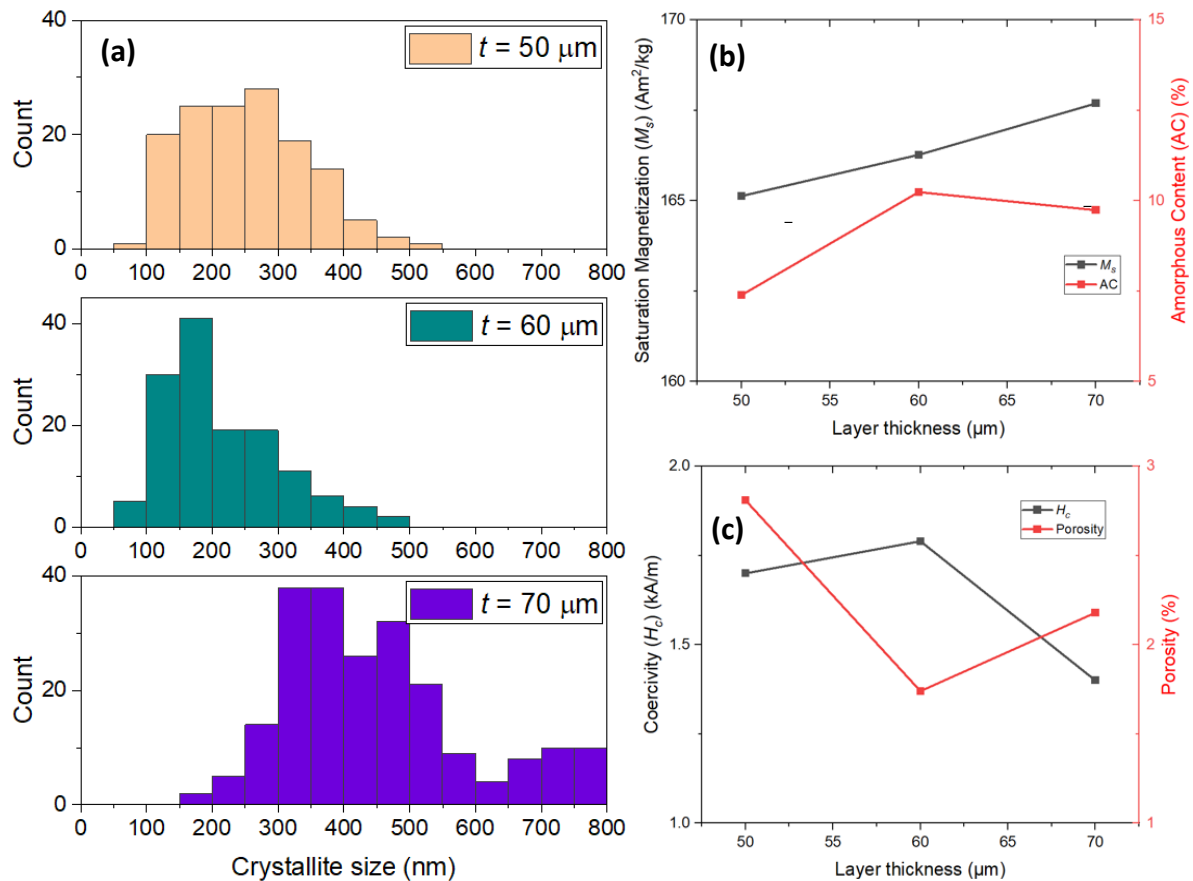


Figure 5.7: The characterization results demonstrate the effect of layer thickness on the microstructural and magnetic properties of 3D printed samples by using different layer thickness (50, 60 and 70 μm) (other parameters kept constant; $v=1000 \text{ mm/s}$, $P=90 \text{ W}$, $h=20 \mu\text{m}$): (a) The histogram graphs showing α -Fe(Si) crystallite size distribution and the graphs illustrating (b) saturation magnetization and amorphous content, (c) coercivity and porosity values as a function of layer thickness.

While investigating the laser process parameters individually gives great insight about thermal and crystallisation characteristics of the LPBF process, this is not enough in order to achieve desirable properties. All of the major process parameters must be taken into account together since they are dependent on each other.

The graphs showing the bulk density variations as a function of laser scan speed and laser power at different hatch spacing and layer thickness are presented in Figure 5.8. Black regions demonstrate low density ($\leq 96\%$). In general, high laser power creates cracks due to the brittle nature of metallic glasses, especially at high laser power ($\geq 120 \text{ W}$) and low hatch spacing ($= 20 \mu\text{m}$). In addition, the combination of laser scan speed (v), hatch spacing (h) and low laser power (P) creates an extensive balling effect resulting from the small areas of melt pools and large distances between them. This eventually leads to large metallurgical pores in the microstructure, decreasing the bulk density. However, low P brings about high bulk density (red regions) when it is used with low v , h . High v and low P provides high cooling rate, leading to high internal

thermal stresses generating cracks. They are generally formed around micropores acting as thermal stress concentrations. Also, the combination of high v and low P does not give enough heat input to the powder, resulting in incomplete melting and interparticle bonding. This increases porosity. Nevertheless, rapid cooling rate (high v) is a necessity for the development of the amorphous phase. Thus, to increase amorphous content as well as bulk density, one should consider thermal annealing as a post-process to get rid of the internal stresses or double scanning. It should contain the first scan with high E ($=P/(vth)$) to improve sintering and a second scan with low E to increase amorphous content.

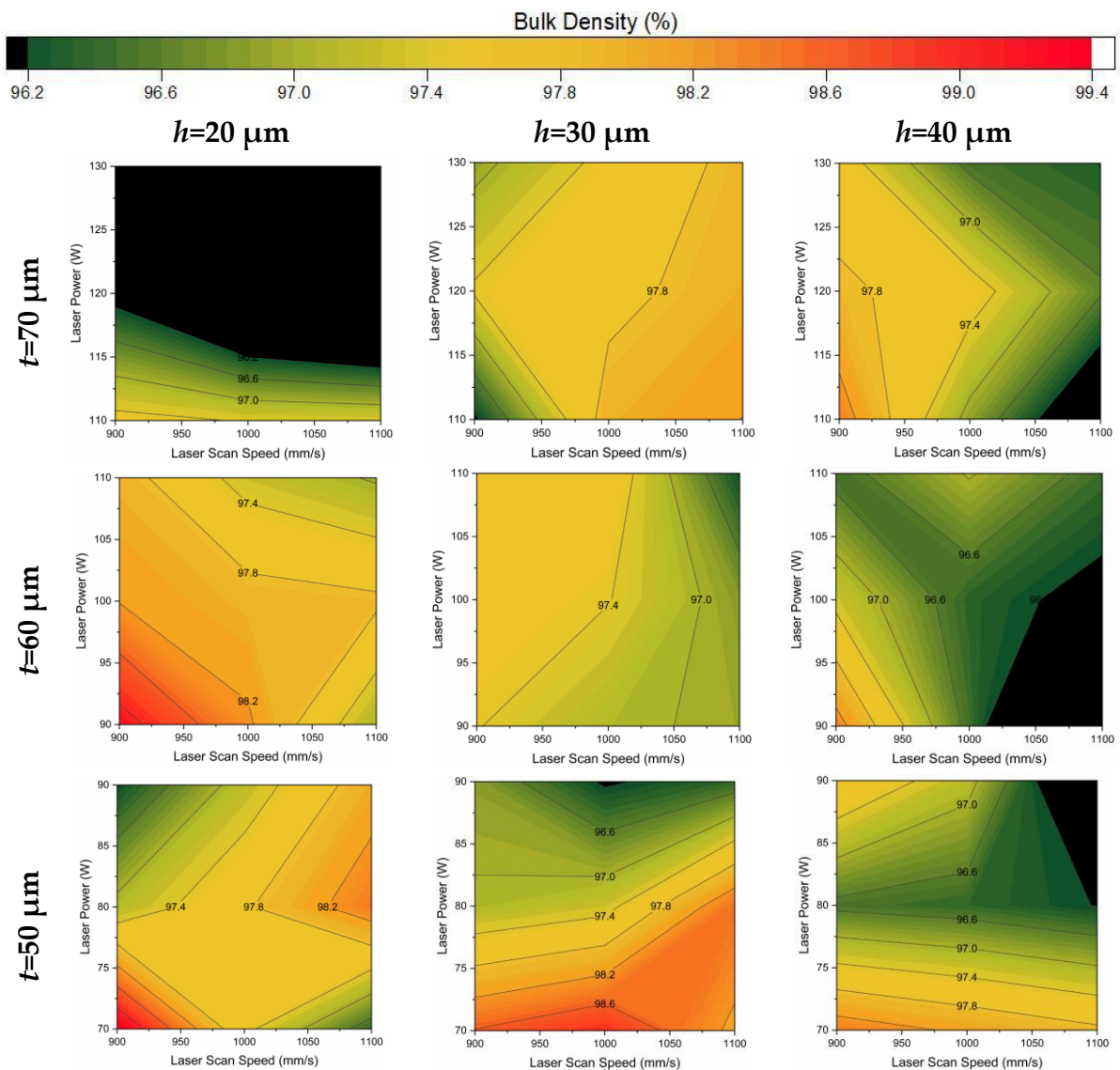


Figure 5.8: Colour-mapped graphs showing bulk density variations as a function of laser power and laser scan speed at three different layer thickness (t) and hatch spacing (h) with the scale bar on top of the graphs.

When the process parameters were investigated individually, it was observed that as P , t and h were increased and v was decreased, M_s values were enhanced. When the different combinations of process parameters were examined (Figure 5.9), conflicting results were obtained as the process parameters are intercorrelated with each other. The most distinguishable difference is that at high h , M_s worsens. Previously, it was mentioned that increasing h (at $P = 100$ W, $v = 900$ mm/s and $t = 60$ μ m) improves M_s due to the high number of crystallites. In general, high h reduces the volumetric energy input to the powder, increasing amorphous content resulting from high cooling rate. Also, it is clear that h and v are the controlling parameters for saturation magnetization as the combination of $h = 30$ μ m and $v = 1000$ mm/s gives the higher saturation magnetization at different layer thicknesses and lower powers. The reason for this could be that those parameters provide sufficient undercooling so that smaller crystallites spread in amorphous matrix at a smaller distance, which improves exchange interaction among them and increases M_s . In addition, too high v and h destabilised the melt-pools, causing thermal fluctuations.

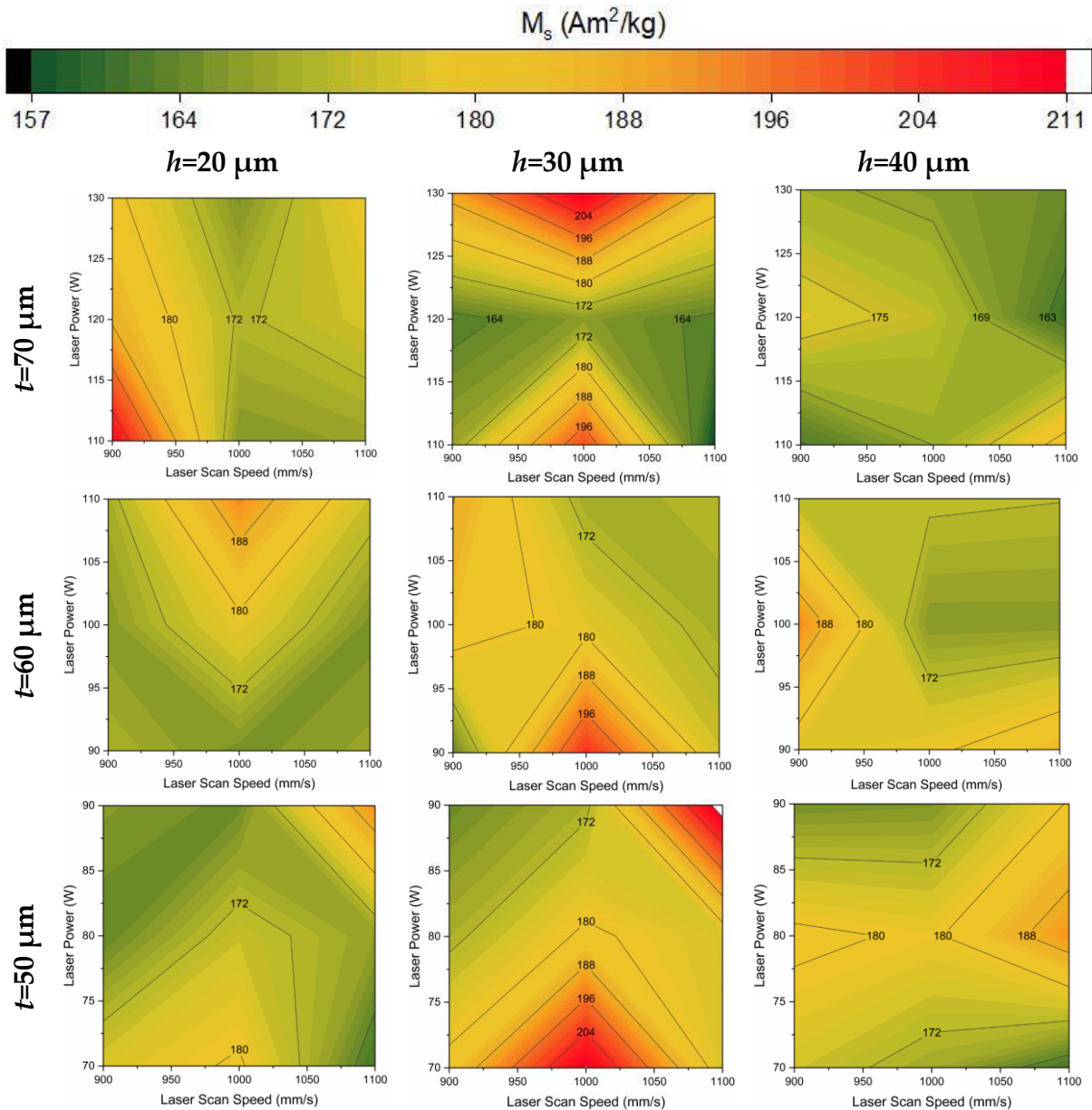


Figure 5.9: Colour-mapped graphs showing saturation magnetization (M_s) variations as a function of laser power and laser scan speed at three different layer thickness (t) and hatch spacing (h) with the scale bar on top of the graphs.

In this study, coercivity (H_c) depends on the defects (pores and cracks), amorphous content and crystallite size. As mentioned before, H_c is reduced by increasing the amount of amorphous phase and increasing the crystallite size, while decreasing the magneto-crystalline anisotropy. At $h = 20 \mu\text{m}$ and $40 \mu\text{m}$ (Figure 5.10), H_c was mainly affected by the porosity content, which means coercivity is higher where bulk density values are lower. However, in order to comprehend better why coercivity changes with different process parameters, detailed microstructural analysis should be conducted for each sample and will be examined in another study in which coercivity will be tried to be reduced by lowering P and v without compromising saturation

magnetization. This is because despite high bulk density and M_s achieved in this study, the coercivity is too high (1.35 - 2.72 kA/m) for soft-magnetic materials applications.

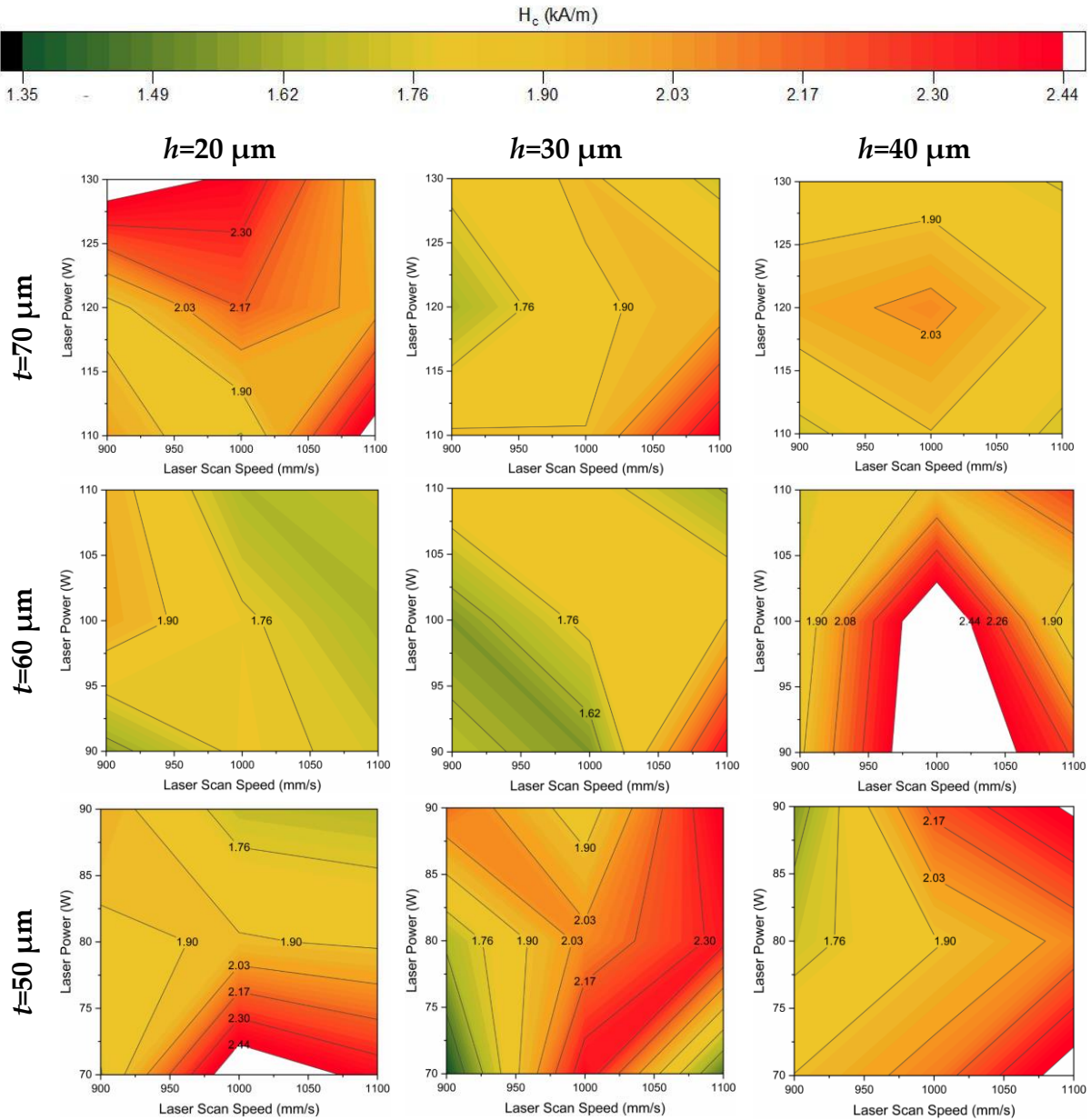


Figure 5.10: Colour-mapped graphs showing coercivity (H_c) variations as a function of laser power and laser scan speed at three different layer thickness (t) and hatch spacing (h) with the scale bar on top of the graphs.

5.4 Conclusion

FeSiBCrC BMGs were LPBF-processed with the help of different laser process parameters in the aim of obtaining high bulk density and excellent soft-magnetic properties. The results can be summarised as follows:

1. The thermal gradients evolved during laser scanning influences the microstructure (the amorphous content and α -Fe(Si)), having significant effect on the soft-magnetic properties. M_s increases with lowering the amorphous content and the increased number of crystallites in the microstructure.
2. Because of the brittle nature of the BMGs, high thermal internal stresses tend to develop in the microstructures, leading to cracks. To prevent cracks formation, rapid cooling rate (high v) and high energy input (high P) should be avoided. Therefore, low P and v ought to be used along with low h and t to decrease cracks and porosity.
3. The controlling parameters for saturation magnetization are v and h , influencing the size and distribution of nanocrystallites in the microstructure. h of 30 μm and v of 1000 mm/s gives the highest M_s ($\geq 200 \text{ Am}^2/\text{kg}$) at low laser power in this study. Those process parameters provided higher undercooling (nucleation rate is dominant) such that α -Fe(Si) phases decreased in size and were distributed at a smaller distance, facilitating exchange interaction among them.

Acknowledgments

I would like to express my very great appreciation to Dr Richard Rowan-Robinson for kindly giving permission for the usage of the graph (Figure 5.1) that he created and to the Republic of Turkey Ministry of National Education for funding this project.

References

- [1] V. Sufiiarov, D. Erutin, A. Kantyukov, E. Borisov, A. Popovic and D. Nazarov, "Structure, Mechanical and Magnetic Properties of Selective Laser Melted Fe-Si-B Alloy," *Materials*, vol. 15, no. <https://doi.org/10.3390/ma15124121>, p. 4121, 2022.
- [2] V. Chaudhary, S. Mantri, R. Ramanujan and R. Banerjee, "Additive manufacturing of magnetic materials," *Progress in Material Science*, vol. 114, no. <https://doi.org/10.106/j.pmatsci.2020.100688>, p. 100688, 2020.
- [3] Y. Nam, B. Koo, M. Chang, S. Yang, J. Yu, Y. Park and J. Jeong, "Selective laser melting vitrification of amorphous soft magnetic alloys with help of double-scanning-induced compositional homogeneity," *Materials Letters*, vol. 261, p. 127068, 2020.
- [4] L. Thorsson, M. Unosson, M. Perez-Prado, X. Jin, P. Tiberto, G. Barrera, B. Adam, N. Neuber, A. Ghavimi, M. Frey, R. Busch and I. Gallino, "Selective laser melting

- of a Fe-Si-Cr-B-C based complex-shaped amorphous soft-magnetic electric motor rotor with record dimensions," *Materials and Design*, vol. 215, p. 110483, 2022.
- [5] T. Debroy, H. Wei, J. Zuback and T. Mukherjee, "Additive manufacturing of metallic components – Process, structure and properties," *Progress in Materials Science*, vol. 92, no. 5, pp. 112-224, 2018.
- [6] H. Fayazfar, M. Salarian, A. Rogalsky, D. Sarker , P. Russo, V. Paserin and E. Toyserkani, "A critical review of powder-based additive manufacturing of ferrous alloys: Process parameters, microstructure and mechanical properties," *Materials and Design*, vol. 144, no. <https://doi.org/10.1016/j.matdes.2018.02.018>, pp. 98-128, 2018.
- [7] C. Zhang, D. Ouyang, S. Pauly and L. Liu, "3D printing of bulk metallic glasses," *Materials Science and Engineering: R: Reports*, vol. 145, no. <https://doi.org/10.1016/j.mser.2021.100625>, p. 100625, 2021.
- [8] H. Jung, S. Choi, K. Prashanth, M. Stoica, S. Scudino, S. Yi, U. Kuhn, D. Kim, K. Kim and J. Eckert, "Fabrication of Fe-based bulk metallic glass by selective laser melting: A parameter study," *Materials and Design*, vol. 86, pp. 703-708, 2015.
- [9] S. Alleg, R. Drablia and N. Fenineche, "Effect of the Laser Scan Rate on the Microstructure, Magnetic Properties, and Microhardness of Selective Laser-Melted FeSiB," *Journal of Superconductivity and Novel Magnetism*, vol. 31, pp. 3565-3577, 2018.
- [10] L. Zrodowski, B. Wysocki and R. Wroblewski, "New approach to amorphization of alloys with low glass forming ability via selective laser melting," *J. Alloys Compd.*, vol. 771, pp. 769-776, 2019.
- [11] S. Gao, X. Yan, C. Chang, E. Aubry, P. He, M. Liu, H. Liao and N. Fenineche, "Microstructure and magnetic properties of FeSiBCrC soft magnetic alloy manufactured by selective laser melting," *Materials Letters*, vol. 290, p. 129469, 2021.
- [12] M. Narwam, K. Al-Rubaie and M. Elbestawi, "Process-Structure-Property Relationships of AISI H13 Tool Steel Processed with Selective Laser Melting," *Materials*, vol. 12, no. <https://doi.org/10.3390/ma12142284>, p. 2284, 2012.
- [13] Q. Jiang, P. Zhang, J. Tan, Z. Yu, Y. Tian, S. Ma and D. Wu, "Influence of the microstructure on mechanical properties of SLM additive manufacturing Fe-

- based bulk metallic glasses,” *Journal of Alloys and Compounds*, vol. 894, no. <https://doi.org/10.1016/j.jallcom.2021.162525>, p. 162525, 2022.
- [14] M. Ozden and N. Morley, “Optimizing Laser Additive Manufacturing Process for Fe-based Nanocrystalline Soft-Magnetic Materials,” *Journal of Alloys and Compounds*, vol. 960, p. 170644, 2023.
- [15] A. Yazdani, G. Hohne, S. Misture and O. Graeve, “A method to quantify crystallinity in amorphous metal alloys: A differential scanning calorimetry study,” *PLoS ONE*, vol. 15, p. e0234774, 2020.
- [16] Y. Zhang, B. Song, L. Zhang, Z. Wang and Y. Shi, “Microstructure and Crack Distribution of Fe-based Amorphous Alloys Manufactured by Selective Laser Melting,” in *Solid Freeform Fabrication 2017: Proceedings of the 28th Annual International Solid Freeform Fabrication Symposium – An Additive Manufacturing Conference*, Austin Texas, 2017.
- [17] X. Li, C. Kang, H. Huang, L. Zhang and T. Sercombe, “Selective laser melting of an Al₈₆Ni₆Y_{4.5}Co₂La_{1.5} metallic glass: Processing, microstructure evolution and mechanical properties,” *Materials Science & Engineering A*, vol. 606, pp. 370-379, 2014.
- [18] W. Xing, D. Ouyang, N. Li and L. Liu, “Insight into micro-cracking in 3D-printed Fe-based BMGs by selective laser melting,” *Intermetallics*, vol. 103, pp. 101-106, 2018.
- [19] A. Hariharan, L. Lu, J. Risse, A. Kostka, B. Gault, E. Jagle and D. Raabe, “Misorientation-dependent solute enrichment at interfaces and its contribution to defect formation mechanisms during laser additive manufacturing of superalloys,” *Phys. Rev. Materials*, vol. 3, p. 123602, 2019.
- [20] H. Kang, K. Song, L. Li, X. Liu, Y. Jia, G. Wang, Y. Wang, S. Lan, X. Lin, L. Zhang and C. Cao, “Simultaneously healing cracks and strengthening additively manufactured Co₃₄Cr₃₂Ni₂₇Al₄Ti₃ high-entropy alloy by utilizing Fe-based metallic glasses as a glue,” *Journal of Materials Science & Technology*, vol. <https://doi.org/10.1016/j.jmst.2023.08.048>, pp. In Press, Journal Pre-proof, 2023.
- [21] M. Wilard and M. Daniil, “Nanocrystalline Soft Magnetic Alloys Two Decades of Progress,” *Handbook of Magnetic Materials*, vol. 21, no. <https://doi.org/10.1016/B978-0-444-59593-5.00004-0>, pp. 173-342, 2013.

- [22] M. McHenry and D. Laughlin, "Magnetic Properties of Metals and Alloys," *Physical Metallurgy (Fifth Edition)*, vol. 19, no. <https://doi.org/10.1016/B978-0-444-53770-6.00019-8>, pp. 1881-2008, 2014.
- [23] T. Bitoh, A. Makino and A. Inoue, "Origin of low coercivity of Fe-(Al, Ga)-(P, C, B, Si, Ge) bulk glassy alloys," *Materials Transactions*, vol. 44 (10), no. DOI: 10.2320/matertrans.44.2020, pp. 2020-2024, 2003.
- [24] K. Suzuki, R. Parsons, B. Zang, K. Onodera, H. Kishimoto, T. Shoji and A. Kato, "Nanocrystalline soft magnetic materials from binary alloy presursors with high saturation magnetization," *AIP Advances*, vol. 9, no. <https://doi.org/10.1062/1.5079778>, p. 035311, 2019.
- [25] Y. Yoshizama, S. Oguma and K. Yamauchi, "New Fe-Based Soft Magnetic Alloys Composed of Ultrafine Grain Structure," *J. App. Phys.*, vol. 64(10), no. <https://doi.org/10.1063/1.342149>, pp. 6044-6046, 1988.
- [26] T. Kulik, J. Ferenc and M. Kowalczyk, "Temperature of Nanocrystallisation of Magnetically Soft Alloys for High-Temperature Applications," *J. Mater. Process. Technol.*, Vols. 162-163, no. <https://doi.org/10.1016/j.jmatprotec.2005.02.086>, pp. 215-219, 2005.
- [27] J. Rasek, J. Lelatko, P. Kwapulinski, G. Badura, L. Pajak, Z. Stoklasa and G. Haneczok, "Crystallization and Optimization of Soft Magnetic Properties Effect in FeSiB, FeNbSiB, FeCuNbSiB, FeCuZrCoSiB Amorphous Alloys," *Solid State Phenom.*, vol. 163, no. <https://doi.org/10.4028/www.scientific.net/SSP.163.225>, pp. 225-228, 2010.
- [28] O. Czyz, J. Kusinski, A. Radziszewska, Z. Liao, E. Zschech, M. Kac and R. Ostrowski, "Study of Structure and Properties of Fe-Based Amorphous Ribbons after Pulsed Laser Interference Heating," *Journal of Materials Engineering and Performance*, vol. 29, no. <https://doi.org/10.1007/s11665-020-05109-w>, pp. 6277-6285, 2020.
- [29] V. Tsepelev and Y. Starodubtsev, "Nanocrystalline Soft Magnetic Iron-Based Materials from Liquid State to Ready Product," *Nanomaterials*, vol. 11, no. <https://doi.org/10.3390/nano11010108>, p. 108, 2021.
- [30] G. Herzer, "Grain size dependence of coercivity and permeability in nanocrystalline ferromagnets," *IEEE Trans. Magn.*, vol. 26, pp. 1397-1402, 1990.

- [31] G. Herzer, "Chapter 3 Nanocrystalline soft magnetic alloys," *Handbook of Magnetic Materials*, vol. 10, no. [https://doi.org/10.1016/S1567-2719\(97\)10007-5](https://doi.org/10.1016/S1567-2719(97)10007-5), pp. 415-462, 1997.
- [32] M. Celikbilek, A. Ersundu and S. Aydin, "Crystallization Kinetics of Amorphous Magnetic Materials," in *Advances in Crystallization Processes*, Istanbul, Turkey, Intech, 2012, pp. 127-162.
- [33] N. Prasad and K. Varma, "Crystallization Kinetics of the LiBO₂-Nb₂O₅ Glass Using Differential Thermal Analysis," *Journal of the American Ceramic Society*, vol. 88(2), no. <https://doi.org/10.1111/j.1551-2916.2005.00055.x>, pp. 357-361, 2005.
- [34] R. Li, J. Liu, Y. Shi, L. Wang and W. Jiang, "Balling behavior of stainless steel and nickel powder during selective laser melting process," *The International Journal of Advanced Manufacturing Technology*, vol. 59, pp. 1025-1035, 2012.

Chapter 5 – Research Paper II

APPENDIX D: The 3D-printed samples coded according to their laser process parameters.

Table j: The LPBF-processed samples by using layer thickness of 50 μm , coded according to the process parameters (laser power (P), laser scan speed (v), hatch spacing (h)).

h (μm)	20			30			40		
P (W)/ v (mm/s)	70	80	90	70	80	90	70	80	90
900	Sample 1	Sample 4	Sample 7	Sample 10	Sample 13	Sample 16	Sample 19	Sample 22	Sample 25
1000	Sample 2	Sample 5	Sample 8	Sample 11	Sample 14	Sample 17	Sample 20	Sample 23	Sample 26
1100	Sample 3	Sample 6	Sample 9	Sample 12	Sample 15	Sample 18	Sample 21	Sample 24	Sample 27

Table k: The LPBF-processed samples by using layer thickness of 60 μm , coded according to the process parameters (laser power (P), laser scan speed (v), hatch spacing (h)).

h (μm)	20			30			40		
P (W)/ v (mm/s)	90	100	110	90	100	110	90	100	110
900	Sample 28	Sample 31	Sample 34	Sample 37	Sample 40	Sample 43	Sample 46	Sample 49	Sample 52
1000	Sample 29	Sample 32	Sample 35	Sample 38	Sample 41	Sample 44	Sample 47	Sample 50	Sample 53
1100	Sample 30	Sample 33	Sample 36	Sample 39	Sample 42	Sample 45	Sample 48	Sample 51	Sample 54

Table l: The LPBF-processed samples by using layer thickness of 70 μm , coded according to the process parameters (laser power (P), laser scan speed (v), hatch spacing (h)).

h (μm)	20			30			40		
P (W)/ v (mm/s)	110	120	130	110	120	130	110	120	130
900	Sample 55	Sample 58	Sample 61	Sample 64	Sample 67	Sample 70	Sample 73	Sample 76	Sample 79
1000	Sample 56	Sample 59	Sample 62	Sample 65	Sample 68	Sample 71	Sample 74	Sample 77	Sample 80
1100	Sample 57	Sample 60	Sample 63	Sample 66	Sample 69	Sample 72	Sample 75	Sample 78	Sample 81

Chapter 6: Research Paper 3

The preceding two works failed to provide substantial information regarding the change in coercivity under various process parameters, and they did not contribute to its applicability in soft-magnetic applications, where the coercivity should be less than 1 kA/m. To enhance our comprehension of how different process parameters influence coercivity, a comprehensive microstructural analysis of each sample was necessary. The study in this chapter undertook such an analysis, aiming to reduce coercivity while maintaining the high saturation magnetization and high bulk density. This was achieved by lowering the laser power and scan speed, along with reducing the hatch spacing. Furthermore, a novel scanning technique was introduced in this study. Following the initial scan with higher energy density, a second scan was applied with lower energy density to each powder layer before spreading the subsequent layer. This was done to increase amorphous content, reduce the size of α -Fe(Si) crystallites, and consequently decrease coercivity.

Enhancing soft-magnetic properties of Fe-based nanocrystalline materials with a novel double-scanning technique

Merve G. Ozden^{1,*} and Nicola A. Morley¹

¹ Department of Material Science and Engineering, University of Sheffield, Sheffield, S1 3JD, UK, mgozden1@sheffield.ac.uk

* Correspondence: mgozden1@sheffield.ac.uk

Citation: Ozden, M.G., Morley, N.A. Enhancing soft-magnetic properties of Fe-based nanocrystalline materials with a novel double-scanning technique. *Advanced Engineering Materials* 2023, 2300700. <https://doi.org/10.1002/adem.202300700>.

Copyright: © 2023 by the Authors. *Advanced Engineering Materials* published by Wiley-VCH GmbH. This is an open access article under the terms of the Creative Commons Attribution-Non-Commercial-No Derivatives License, which permits use and distribution in any medium, provided the original work is properly cited, the use is non-commercial and no modifications or adaptations are made.

Abstract

This paper presents a novel scanning technique for the laser powder bed fusion (LPBF) of Fe-based soft-magnetic alloys, which have low glass forming ability, and

microstructural change happened during LPBF process. This technique involves double scanning where: (i) the first scan applied uses high energy density ($E=P/vht$, where P is laser power, v is laser scan speed, h is hatch spacing and t is layer thickness) with different process parameters (P : 30, 40 and 50 W, v : 500, 600 and 700 mm/s, h : 20 and 30 μm and t : 50 μm) to achieve high density and (ii) the second scan employed before the spreading subsequent powder layer, uses low E ($= 20 \text{ J/mm}^3$, $P= 20 \text{ W}$, $v= 1000 \text{ mm/s}$, $h= 20 \text{ }\mu\text{m}$ and $t= 50 \text{ }\mu\text{m}$) to refine the microstructure and thus reduce coercivity. To comprehend microstructural change, amorphous phase content and particle size distribution of the $\alpha\text{-Fe(Si)}$ phase (main phase in the microstructure) were measured. The double scanning strategy refined the microstructure to finer crystallites with a narrow particle size distribution within a higher percentage amorphous matrix. This increased the saturation magnetization (M_s) to a maximum value of 226.81 Am^2/kg and reduced the coercivity (H_c) to a lowest value recorded (130 A/m). Likewise, the bulk density (94.59% - 99.25%) was enhanced significantly with double scanning, especially the samples produced using high P (50 W) resulting from the relieving of the mechanical and thermal stress evolving during the process.

Keywords: Laser powder bed fusion, Fe-based nanocrystalline alloys, soft-magnetic behaviour, bulk metallic glasses, laser additive manufacturing and energy density

6.1 Introduction

Soft-magnetic alloys have been playing a critical role in power generation, transformation, and energy conversion, making them a significant engineering material for both industry and academia [1-6]. The excellent efficiency and low core loss demonstrated by Fe-based soft magnetic bulk metallic glasses (BMGs) have generated immense interest in their use as core materials in power electronics and industrial transformers [1, 7]. Soft magnetic BMGs lack crystal structures or long-range orders, resulting in no magneto-crystalline anisotropy energy [8]. In contrast, nano-crystalline soft magnetic alloys have reduced effective magneto-crystalline anisotropy energy and thus low hysteresis loss [9-11]. They are typically produced using planar flow casting techniques, with a thickness range of 15-30 μm and composed of fully or partially amorphous phases. These alloys are also referred to as Metal Amorphous Nanocomposites (MANCs) [12]. Fe-based amorphous ribbons have higher electrical resistivity of 1.0-1.3 $\mu\Omega\text{m}$ compared to silicon steels due to their lack of long-range orders, contributing to lower eddy current loss [5]. Nevertheless, their saturation polarization (J_s) is relatively inferior in comparison to that of silicon steel. Developing Fe-based BMGs with high J_s and low core loss is crucial for enhancing the power density and efficiency of advanced electronic devices [2]. Various approaches

have been taken to increase the J_s of Fe-based BMGs, such as the modifying compositions [13, 14] and nanocrystallization [15]. However, the composition modulation by increasing Fe content and adjusting metalloid elements has limitations due to the trade-off between J_s and glass forming ability [16]. Co substitution has been found to be effective in improving J_s without reducing the glass forming ability [17, 18], but it can bring about increased magnetic anisotropy and Curie temperature (T_c), along with worsening magnetic softness [19]. Nanocrystallization encounters difficulties in the producibility as generally Fe-based nano-crystalline alloys having high J_s cannot be manufactured into application-level sized parts resulting from the low glass forming ability [17, 20].

Fe-based soft magnetic nano-crystalline alloys, containing nanoscale phases embedded in the amorphous matrix, offer various benefits: (i) the presence of the α -Fe phase provides high saturation magnetization (M_s) [16, 21] (ii) superior magnetic softness contributes to low core loss (1/10-1/4 of the commercial silicon steels) [1, 22-25] and (iii) the dual-phase coupling results in low magnetostriction and super-high permeability (Figure 6.1) [6, 9, 26-28]. Furthermore, as the structural correlation length of nano-crystalline alloys is less than the exchange correlation length of the magnetic spins, the magneto-crystalline anisotropy (K_1) is averaged out over the randomly oriented grains, leading to a low coercivity (H_c) [29-32]. Fe-based nano-crystalline alloys are typically produced upon crystallization from an amorphous matrix through various methods, such as single roller spinning followed by annealing [3], or consolidation (hot pressing) of mechanically alloyed powder [33].

The current techniques for producing Fe-based soft-magnetic alloys are limited by the material's glass forming ability, dimensional limitations, and the geometric complexity. Laser powder bed fusion (LPBF) technology, which uses a laser to consolidate powders in a layer-by-layer manner, can overcome these limitations. Achieving high cooling rates (up to 10^{6-8} K/s) during this process makes it a good option for fabricating Fe-based amorphous/nano-crystalline alloys with complex shapes [34-36]. However, controlling microstructure is challenging due to the complex thermal nature of the process. Researchers are using various methods to improve the quality of the LPBF-processed samples, such as optimizing process parameters and using multi-scanning strategies. The degree of amorphization of the resulting material is an important factor for Fe-based amorphous/nano-crystalline materials. To increase the amorphous content and keep crystallite size of the α -Fe phase minimal (< 20 nm), crystallization must be suppressed during both the cooling of the molten metal and the absorption of the melt's heat by the previously solidified part [37]. For this

purpose, researchers have utilized different scanning strategies to build 3D parts with reduced crystallinity. The initial approach involved performing two laser scans to each layer before spreading the subsequent layer, which allowed the scientists to process Fe-based amorphous/nanocrystalline alloy with M_s of 1.22 T and high density of 96% [38]. This method also increased the amorphization degree to 47% and decreased the coercivity. Another approach involved a two-stage laser scanning process: pre-laser melting followed by short-pulse laser treatment to induce amorphization [39]. This strategy fabricated a sample with a maximum relative density of 94.1% and an amorphous phase content of 89.6%. Although these works succeeded in increasing the amorphous phase content, bulk density (> 99%) and soft-magnetic properties (high M_s (< 1.5 T) and low H_c (< 1 kA/m)), it still needs improvement. With this aim, a novel scanning strategy was introduced to LPBF-process Fe-based nano-crystalline soft-magnetic alloys to control the microstructure during the process.

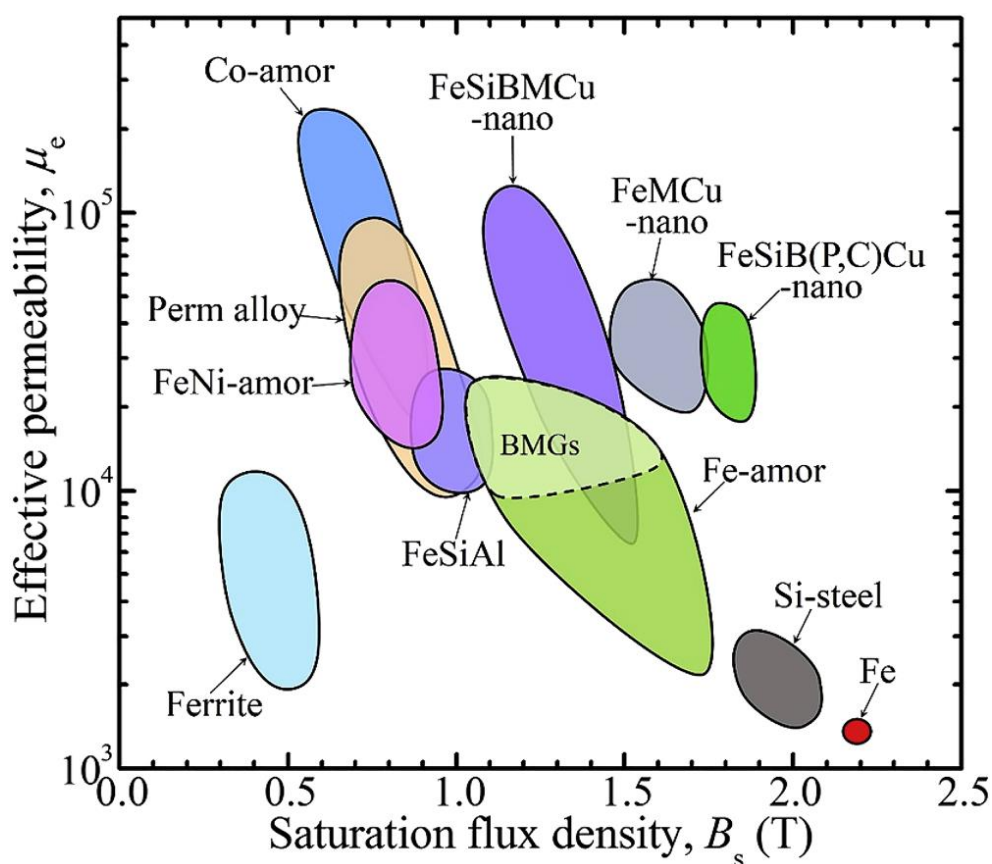


Figure 6.1: The graph showing the relations between effective permeability at 1kHz and saturation flux density of soft-magnetic materials [40].

6.2 Experimental Procedure

6.2.1 Materials

For this study, the commercial FeSiBCrC amorphous powder, provided by Epson Atmix Corporation, Japan, was used with the elemental compositions of 87.38 (Fe), 6.85 (Si), 2.54 (B), 2.46 (Cr) and 0.77 (C) in mass %. The Fe-Si-B-Cr-C system is more readily available and sustainable compared to other competitive materials, which contain Co or rare earth materials such as Nd and Dy. The only high-priced element is boron, which is present in a smaller quantity (2.54%) compared to other Fe-based amorphous/nano-crystalline alloys. The powder characterization was presented in our previous work [41], which indicated that the powder was fully amorphous, spherical in shape and has a narrow particle size distribution with D10, D50, and D90 of 9.49, 23.4, and 47.5 μm , respectively. Additionally, it exhibits soft-magnetic behavior, with M_s of 102 Am^2/kg and H_c of 2.27 kA/m.

6.2.2 Methods

To begin with, the powder was sifted through a sieve with a mesh size of 53 μm to narrow the size distribution of the particles, which will aid in their spreadability and flowability over the powder bed. A cylindrical sample with a diameter of 6 mm and a height of 5 mm was then printed using an Aconity Mini machine. From the main laser process parameters, low laser powers ($P= 30, 40$ and 50 W) were utilized to increase cooling rate and inhibit crystallization. On the other hand, it was indicated in our previous works [41, 42] that energy density ($E= P/vht$, where v is laser scan speed, h is hatch spacing and t is layer thickness) must be higher than 45 J/mm^3 to obtain high bulk density ($> 97\%$). In order to increase energy density, relatively low laser scan speeds ($v= 500, 600$ and 700 mm/s) and hatch spacing ($h= 20$ and 30 μm) were exploited with the layer thickness being kept constant at $t = 50$ μm . For the first scan, a combination of the different laser process parameters was used to achieve energy density values within the range: 42.86-100 J/mm^3 , to build 3D parts with high density, these are presented in Table 6.1. The second scan with a low energy density ($E= 20$ J/mm^3 , $P= 20$ W, $v= 1000$ mm/s, $h= 20$ μm and $t= 50$ μm) was applied to each powder layer before spreading the subsequent layer. The reasons for this were: (1) to provide thermal stress relaxation, eliminating residual stress in the microstructure, (2) to decrease the crack density in the microstructure (due to the brittle nature of the BMGs, the formation of cracks during laser additive manufacturing is inevitable [43-45]) and (3) to refine the microstructure by increasing amorphization degree and introducing small-sized (<20 nm) α -Fe crystallites into amorphous matrix, which should eventually increase the saturation magnetization (M_s) and lower the coercivity (H_c). It

was shown that low energy density promotes amorphization during the LPBF process [46, 47]. In addition, the specimens were produced using the meander scanning strategy as illustrated in Figure 6.2, with a starting angle of 22.5° and a rotation of 67° after each layer. The second laser scan followed the same path of the first scan. To avoid oxidation, the residual oxygen content in the chamber was kept below 0.01%.

Table 6.1: The process parameters used in this study.

E (J/mm ³)	$h = 20 \mu\text{m}$			$h = 30 \mu\text{m}$
	$P = 30 \text{ W}$	$P = 40 \text{ W}$	$P = 50 \text{ W}$	$P = 50 \text{ W}$
$v = 500 \text{ mm/s}$	60	80	100	66.67
$v = 600 \text{ mm/s}$	50	66.67	83.33	55.56
$v = 700 \text{ mm/s}$	42.86	57.14	71.43	47.62

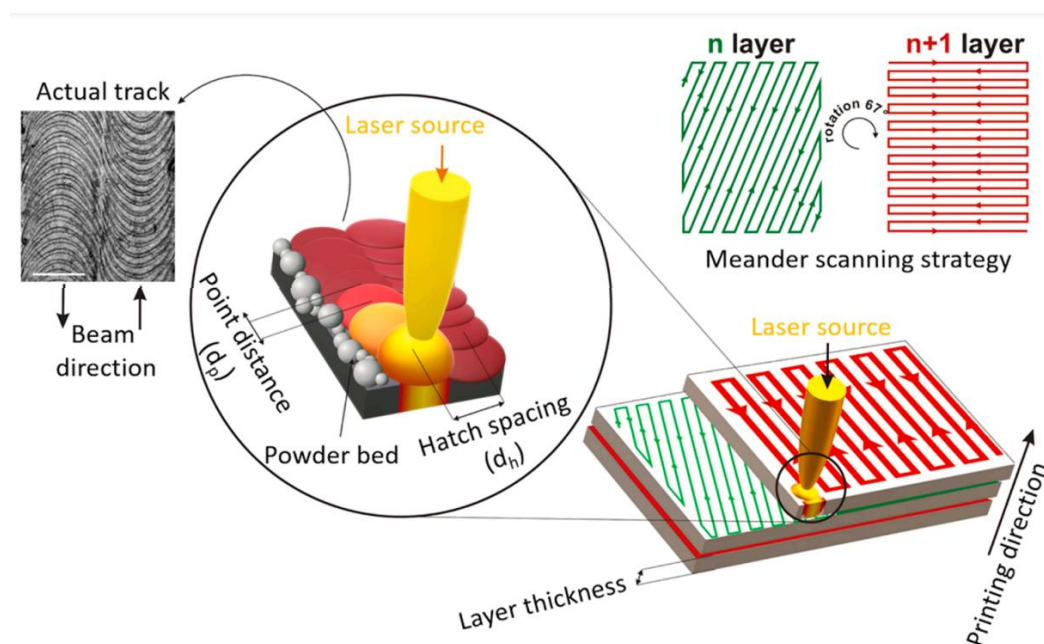


Figure 6.2: Micrograph depicting the laser-melted track (top left) and the meandering scanning technique (right) [48].

For characterization, the Archimedes technique was employed to measure the densities of the printed samples thrice using distilled water. To determine the bulk density percentage, the mean density and theoretical density (7.294 gr/cm^3) were used for each sample. For the microstructural imaging, each sample was subjected to grinding, polishing, and etching for 3 minutes using a 2% nital solution (98 ml HNO_3 and 2 ml ethanol). The micrographs were captured using INSPECT F50 HR-SEM (High Resolution-Scanning Electron Microscope). The crystallite sizes of $\alpha\text{-Fe}$ phases were measured using the ImageJ program from the SEM-microstructures. Differential scanning calorimetry (DSC) was utilized to quantify the crystallization enthalpies of LPBF-processed samples by heating the samples at a rate of $20 \text{ }^\circ\text{C/min}$ to $1400 \text{ }^\circ\text{C}$.

Then, the amorphous phase content was calculated using a technique outlined in these articles [39, 46, 49]. Finally, the soft-magnetic properties (M_s and H_c) were determined from the magnetization hysteresis ($M-H$) loops obtained via a SQUID magnetometer MPMS3 from Quantum Design, with fields up to 160 kA/m at 300 K.

6.3 Results and Discussion

The development of the microstructure in Fe-based amorphous/nano-crystalline alloys during the LPBF procedure is a complicated process due to the heterogeneous nature of the thermal evolution. The microstructure can be divided into two regions: molten pools (MP) and heat affected zone (HAZ), both of which experience different cooling rates resulting in distinct microstructures (as shown in Figure 6.3(b)). The cooling rate decreases from the MP region to the HAZ because of the formation of high thermal gradients during laser scanning. It is well known that the growth of the ordered Fe_3Si phase is dendritic, whereas the disordered $\alpha\text{-Fe}(\text{Si})$ phase appears as equiaxial grains in the microstructure [39]. In addition, phase identification (XRD and TEM analysis) was presented in our previous article [41]. In the MP region, $\alpha\text{-Fe}(\text{Si})$ nano-grains with varying sizes were observed (Figure 6.3(c) and (d)), while the HAZ mainly contains Fe_3Si nano-crystalline clusters with the average size of 30 nm in an amorphous matrix (Figure 6.3(d)). The MP region provides more supercooling, enabling the nucleation and growth of the disordered $\alpha\text{-Fe}(\text{Si})$ phase. The grains in the MP region were found to be coarser than those in the HAZ region (Figure 6.4(d)) due to decreased nucleation rates and increased growth velocity resulting from a high driving force for atomic diffusion [50]. This ultimately leads to grain coarsening.

In general, even though the cooling rate of the Fe-based BMGs in LPBF process is a lot higher than their critical cooling rate, some regions in the microstructure will experience low temperatures ($< T_g$ (glass transition temperature)) or very short exposure time to heat input, leading to mechanical stress, contamination, prolonged thermal exposure and thermal cycling, which are the major reasons that promote nucleation [51, 52]. For this reason, in this study the crystallization was high as the amorphous phase content was less than 16%, implying that amorphous phase was retained from parent powder. As it can be seen in the microstructures (Figure 6.3), the samples possess pores and cracks, acting as nucleation sites and facilitating nucleation. Large metallurgical pores in Figure 6.3(a) can result from the combination of low laser power (50 W) and high hatch spacing (30 μm), creating a gap between melt-pools. The formation of perfectly shaped spherical small pore (Figure 6.3(b)), on the other hand, is due to the trapped gas bubbles at the lower end of the melt-pool. The intergranular pores (Figure 6.3(c)) are caused by the shrinkage of the grains

during solidification. Cracks are inevitable in the BMGs. In LPBF samples, the cracks generally originated from either the excessive heats between layers, so form in the HAZ, then grow through the build axes (z axes, $-z$ direction) or existing pores. All these defects can be improved to an extent by post-processing such as stress-relief annealing. In this study, double scanning was applied to eliminate those defects during the printing without the need of any secondary processing. It improved the bulk density significantly (Figure 6.4), especially at the relatively high laser power ($P=50$ W) since high P creates more mechanical and thermal stress in the microstructure. Furthermore, increasing P influences the bulk density more than laser scan speed (v) and hatch spacing (h), which did not change the porosity level enormously. This is because the laser power is a critical parameter for complete melting and consolidation of powder particles. Also, the energy density of the first scan may have an effect on the consolidation behaviour as the bulk density improves the most (from 98.22% to 99.43%) at higher energy density (100 J/mm³) (Figure 6.5).

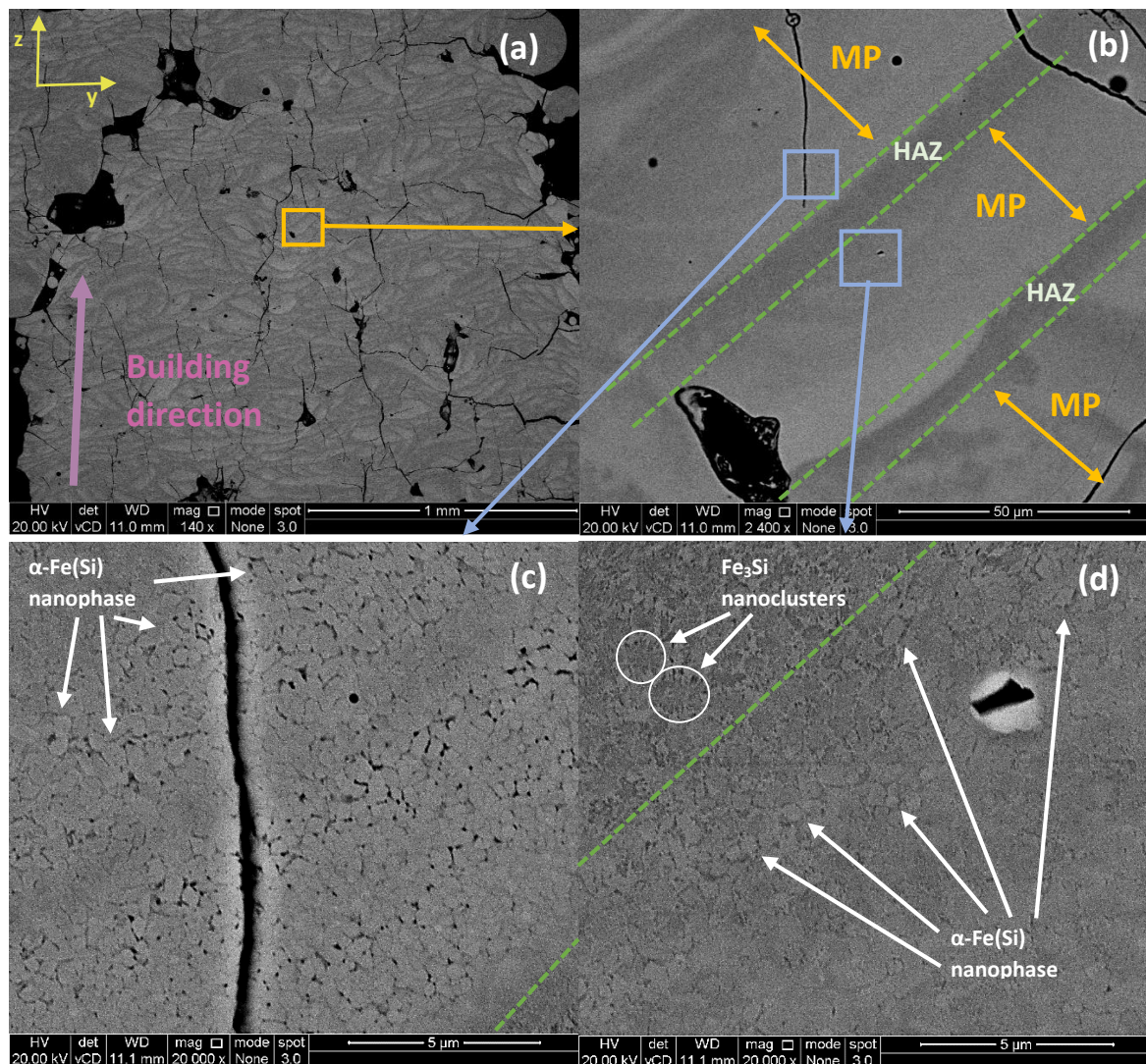


Figure 6.3: The SEM micrographs of the sample produced with P of 50 W, v of 700 mm/s, h of 30 μm and t of 50 μm , taken in the building direction (cross-sectional view): **(a)** at low magnification and at high magnifications showing **(b)** melt-pool (MP) region (lighter areas) and heat affected zone (HAZ) (darker areas), **(c)** $\alpha\text{-Fe(Si)}$ phase with different size in MP region and **(d)** Fe_3Si nanoclusters in HAZ and $\alpha\text{-Fe(Si)}$ nano-phase in MP region.

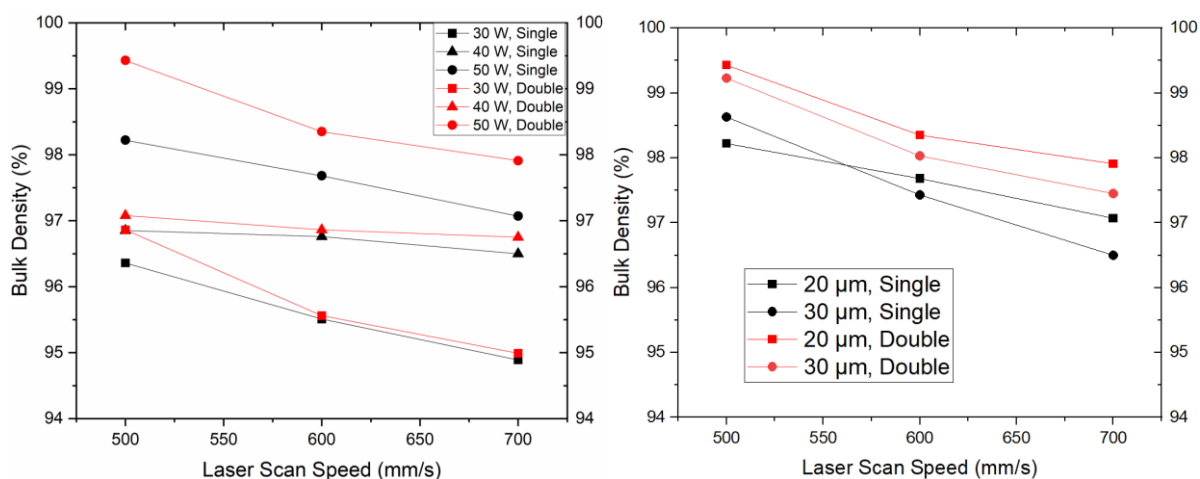


Figure 6.4: Bulk density values as a function of laser scan speed. Left Image shows the effect of laser power (30, 40 and 50 W) and double scan (hatch spacing is constant and 20 μm) whereas the right image indicates the influence of hatch spacing (20 and 30 μm) and double scan (laser power is constant and 50 W).

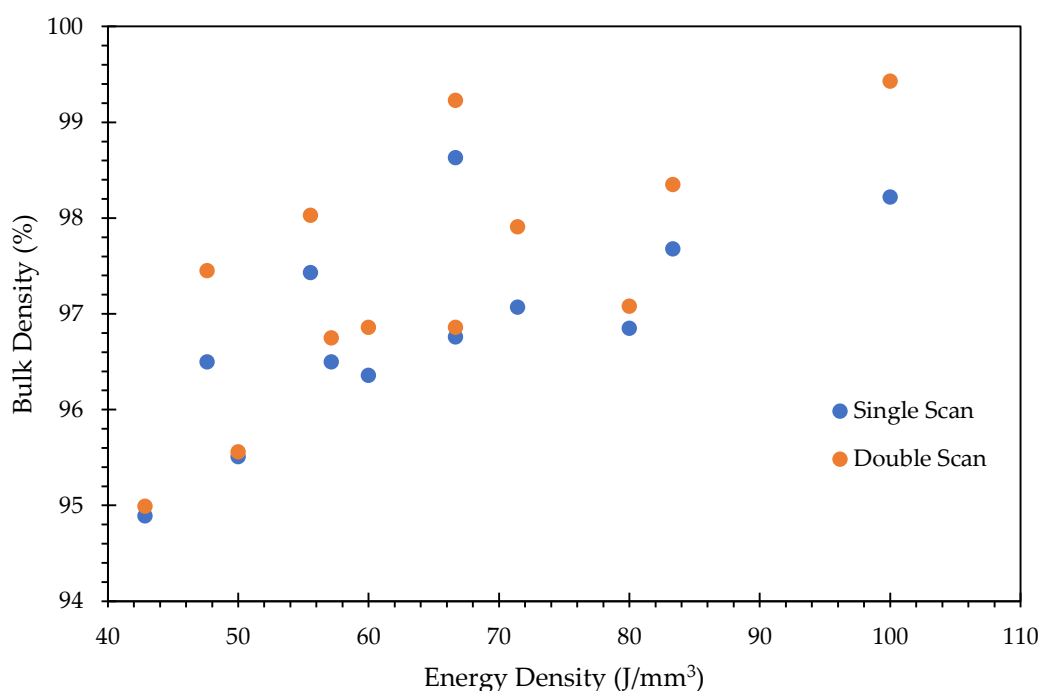


Figure 6.5: The graph showing the relationship between energy density and bulk density of both single-scanned and double-scanned samples.

The saturation magnetization (M_s) values of the printed samples, ranging from 160 to 230 Am^2/kg (Figure 6.6), are substantially higher than the parent powder (102 Am^2/kg) and the other LPBF-processed Fe-based nano-crystalline materials (max. 199 Am^2/kg) [39, 46, 53-55]. This can be attributed to the presence of the nanocrystalline phases in the microstructure. M_s of soft-magnetic nanocrystalline alloys depends strongly on the fraction of crystalline and amorphous phases, the crystalline phase amount and

distribution, and the alloy composition with the amount of magnetic transition metals (Fe, Co, and Ni) being the most influential factor [56]. In all 3D-printed samples, the alloy composition is identical, and thus, the M_s values differ based on the size and distribution of the α -Fe(Si) phase throughout the samples.

Typically, Fe-based nanocrystalline alloys show superior soft-magnetic behaviour when they contain fine α -Fe nano-crystallites (10-15 nm) embedded into an amorphous matrix, separated by 1-2 nm for exchange interaction, with H_c ranging from 0.4 to 8 A/m, and M_s values reaching up to 1.3 T (~1000 kA/m) [57]. In this study, the saturation induction (B_s) can go up to 2 T (~1500 kA/m), probably owing to the larger size of the α -Fe(Si) phases (< 1000 nm) and the high exchange interaction among grains in the microstructure. Amorphous phase content (Figure 6.6) and particle size distribution of α -Fe phase (Figure 6.7 and 6.8) were quantified for each sample in order to understand how M_s (Figure 6.9) and H_c (Figure 6.10) changes with different process parameters.

It is obvious that the double scanning increases the amorphous phase content to 10% - 16% (Figure 6.6), suggesting that the second scan with low E provides higher supercooling, promoting amorphous phase formation. Moreover, generally low P and high v increase the amorphization degree, which is influenced by low laser power (low heat input providing temperature just above T_g) and exposure time to heat input (not too short for high bulk density and not too long to avoid crystallization). These parameters can depend on the material's compositions, powder particle size and other laser process parameters. The exposure time is determined from the combinations of laser scan speed and hatch spacing. Increasing v and decreasing h reduces exposure time, which in turn increases cooling rate.

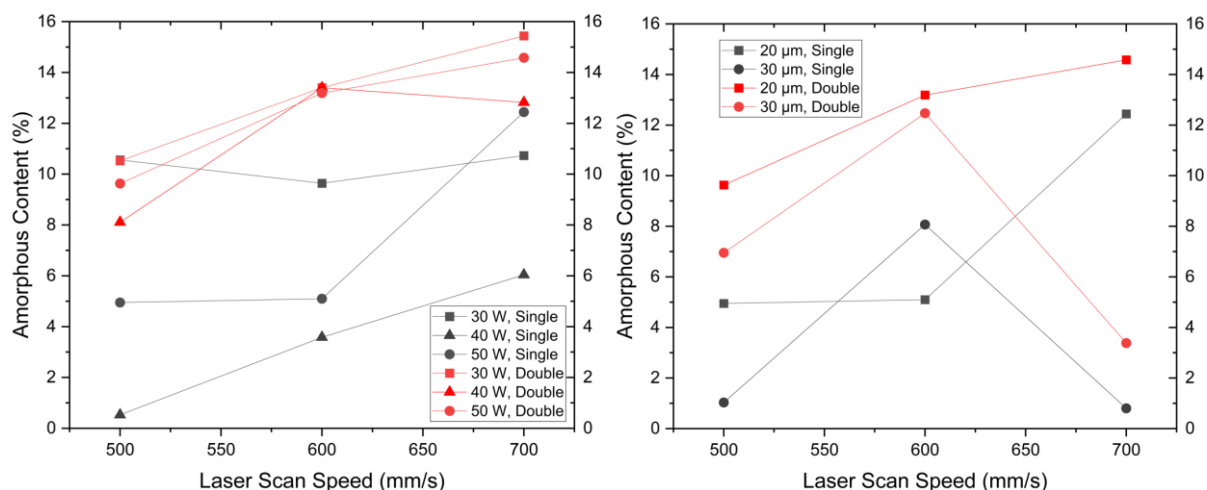


Figure 6.6: The graphs of amorphous content and laser scan speed. Left Image shows the effect of laser power (30, 40 and 50 W) and double scan (hatch spacing is constant and 20 μm) whereas the right image indicates the influence of hatch spacing (20 and 30 μm) and double scan (laser power is constant and 50 W).

Despite the improvement in the bulk density amorphous content, double scanning does not affect M_s notably, except at $P=40\text{ W}$, $v=500$ and 600 mm/s , at $P=30\text{ W}$, $v=700\text{ mm/s}$ and at $P=50\text{ W}$ and $h=30\text{ }\mu\text{m}$ (Figure 6.9). Despite the high M_s (225.64 Am^2/kg) of the sample processed with $P=30\text{ W}$ and $v=700\text{ mm/s}$ with double scanning, its porosity level is too high (%6) (Figure 6.5) to be characterized as bulk part. This is also why the coercivity is also quite high (5.14 kA/m for single scan and 3.16 kA/m for double scan) (Figure 6.10). The saturation magnetization depends on the $\alpha\text{-Fe(Si)}$ particle size and distribution in this study as the amorphous phase content (<16%) is so low that it does not affect the M_s substantially. It was found that a narrow particle size distribution with the majority of particles in the range of 200-400 nm brought about the high M_s (>200 Am^2/kg) whereas a wider particle size distribution led to low M_s (<160 Am^2/kg). From theory, the soft-magnetic properties of small grains (35 nm – 100 μm) depend upon the interplay between the ferromagnetic exchange interaction and the local magnetocrystalline anisotropy energy [30]. The coercivity is nearly the same for all the samples studied, within the range of 1.5-2.5 kA/m (Figure 6.10), which suggests that the exchange interaction dominates the magnetization process rather than magnetic anisotropy energy. The exchange interaction causes the magnetic moments to align parallel with each other, hindering the magnetization that follows the easy axis of each individual crystallite [30]. However, its dependence on the grain size is still unclear in the crystallite size range of 35 nm – 100 μm . In this work, it is observed that a narrow size distribution with the mean size of around 300 nm improves the M_s , which means a high deviation from the mean grain size reduces the exchange interaction. The reason for low M_s at high v ($=700\text{ mm/s}$) may be due to the

higher amorphous phase content and wider particle size distribution. Mostly, the double scanning reduced the mean crystallite size and most importantly the standard deviation from the mean. This implies that it refines the microstructure to a finer grain size.

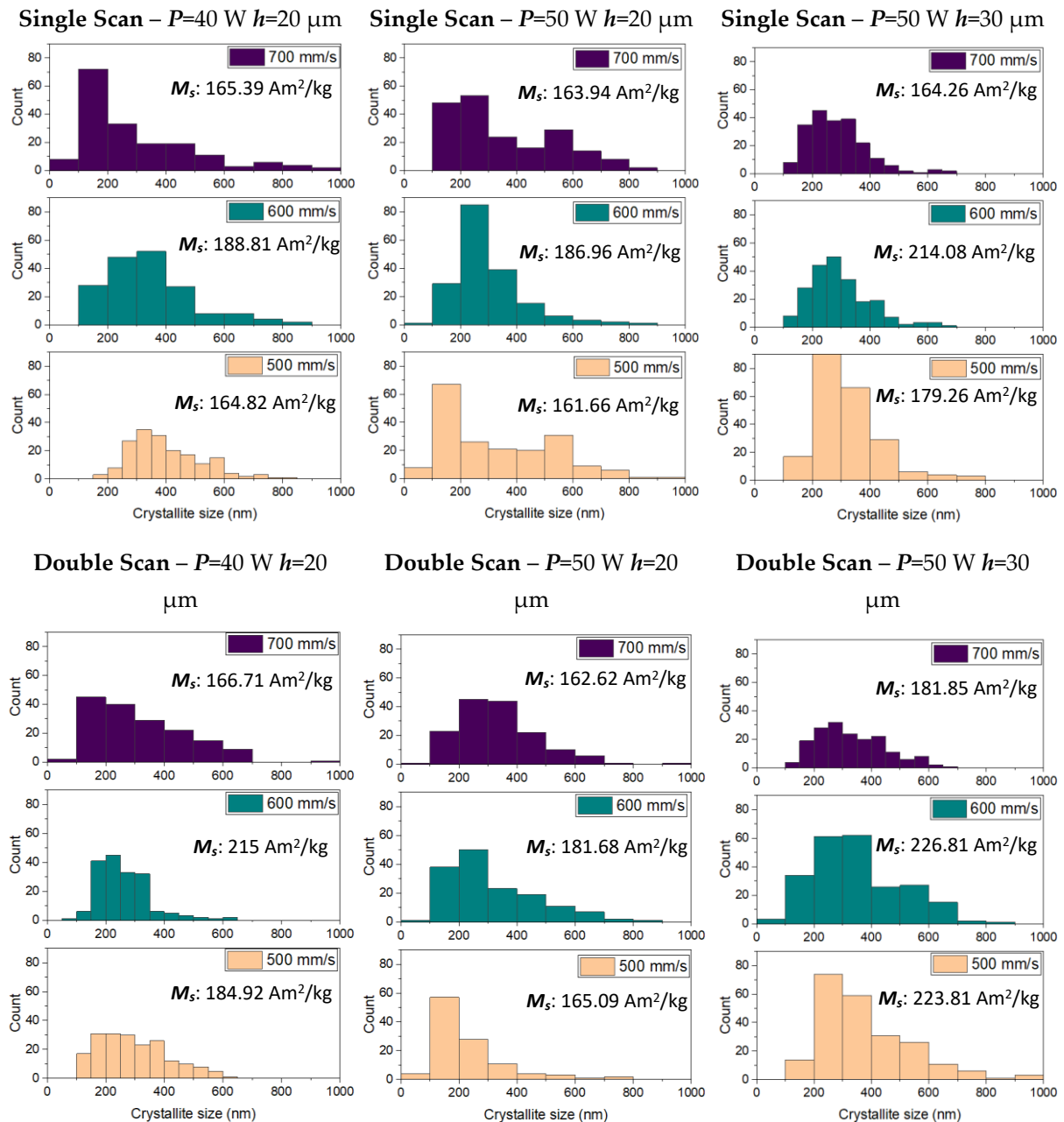


Figure 6.7: The histograms showing particle size distribution of α -Fe(Si) phase in the MP region with different processing conditions; laser scan speeds = 500, 600 and 700 mm/s (P : laser power and h : hatch spacing).

This work has successfully produced a LPBF-processed sample with the lowest coercivity recorded (130 A/m) using a low laser power (30 W) and double scanning (Figure 6.10). The reason for this is that the sample has a higher amorphous phase

content, finer grain size with a narrow particle size distribution (191.01 ± 72.15 nm) compared with that of the single scan sample (348.55 ± 176.44 nm). In addition, due to the small grain size, M_s increased (173.18 Am²/kg).

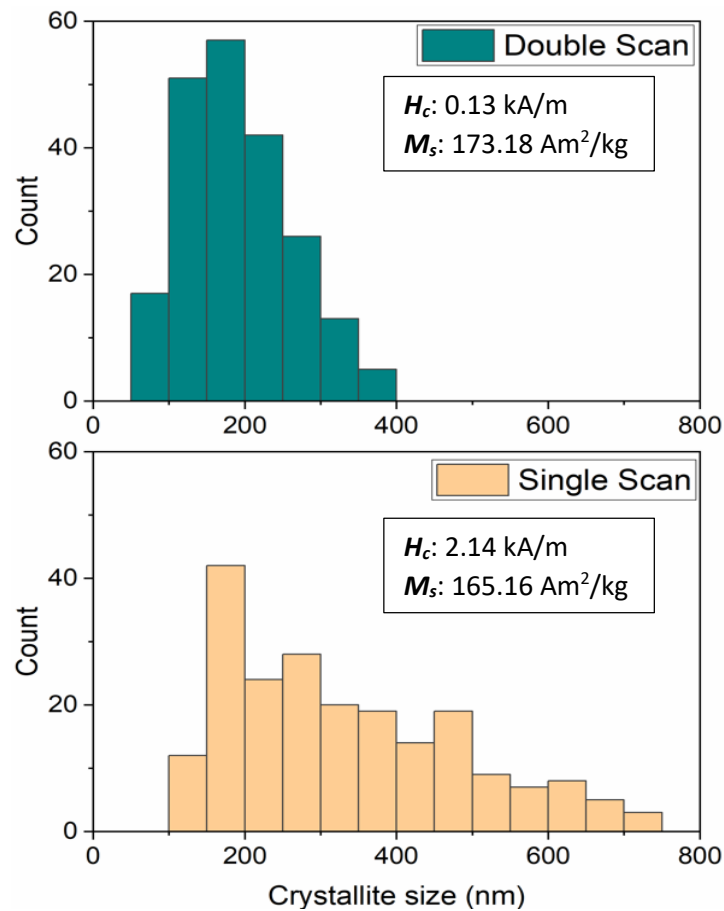


Figure 6.8: The histograms showing particle size distribution of α -Fe(Si) phase in the MP region with different processing conditions (single scan and double scan). The sample was processed with laser power of 30 W, hatch spacing of 20 μ m and laser scan speed of 500 mm/s.

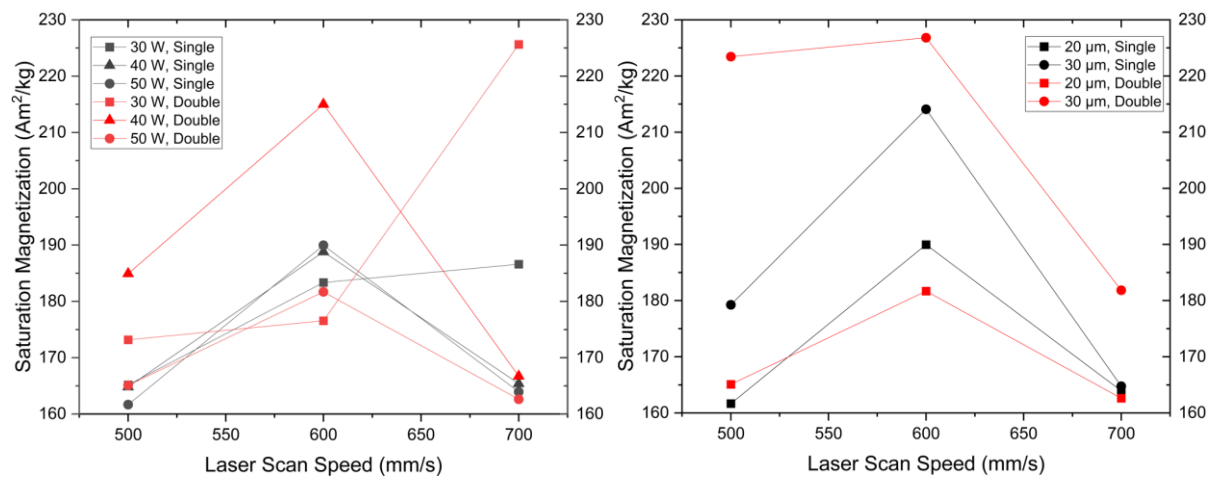


Figure 6.9: The graphs of saturation magnetization versus laser scan speed. Left Image shows the effect of laser power (30, 40 and 50 W) and double scan (hatch spacing is constant and 20 µm) whereas the right image indicates the influence of hatch spacing (20 and 30 µm) and double scan (laser power is constant and 50 W).

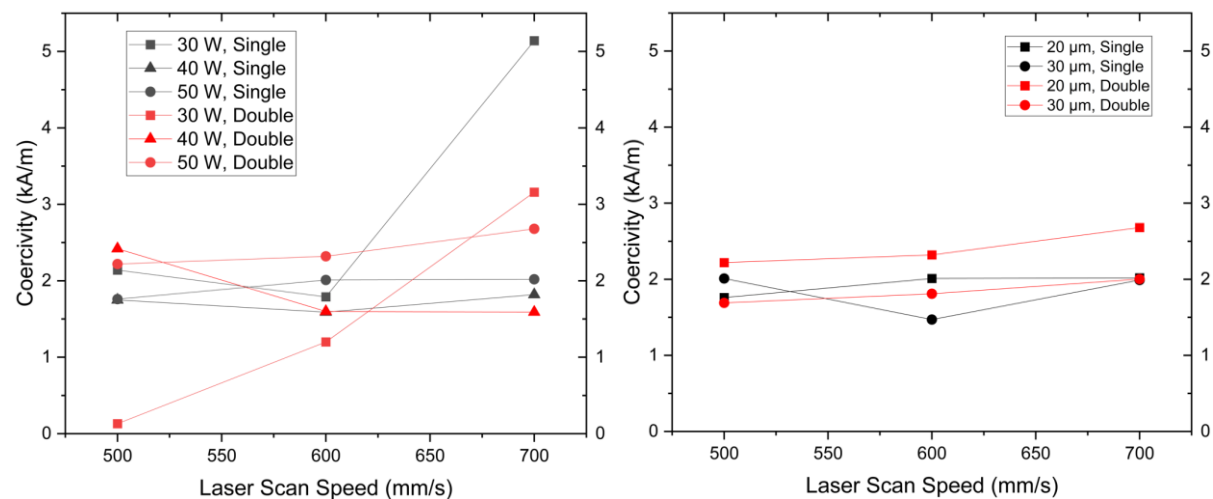


Figure 6.10: Coercivity values as a function of laser scan speed. Left Image shows the effect of laser power (30, 40 and 50 W) and double scan (hatch spacing is constant and 20 µm) whereas the right image indicates the influence of hatch spacing (20 and 30 µm) and double scan (laser power is constant and 50 W).

6.4 Conclusion

This study introduced a newly developed scanning technique to improve the soft-magnetic properties of LPBF-processed Fe-based amorphous/nanocrystalline alloys with varying laser process parameters. This technique involved the first scan with high E (the combination of different laser process parameters) to obtain the 3D parts with high bulk density, followed by a second scan with low E before the spreading of the subsequent powder layer. This was done to decrease the coercivity by increasing the amorphous content and controlling the microstructure. With this new technique, the lowest coercivity (130 A/m) was successfully achieved using the LPBF process. The

double-scan technique also improved the bulk density (<99.5%), the amorphous phase content (< 16%) and the saturation magnetization (<230 Am²/kg). The particle size distribution of the α -Fe(Si) phase (main phase in the microstructure) was also quantified to understand the magnetization mechanism that the 3D printed samples undergo. It was found that double scanning with low E helped to refine the microstructure to have finer crystallite size with a narrow particle size distribution. This enhanced the soft-magnetic properties, including increasing M_s (226.81 Am²/kg) at high P (50 W) and h (30 μ m) and reducing the coercivity to the lowest recorded value (130 A/m) at low P (30 W). Although the new technique has led to a higher M_s , bulk density and the lowest H_c value (for the LPBF process), the amorphous content is still relatively low. To further reduce coercivity, an increase in the amorphization degree is likely to benefit, as for excellent soft-magnetic behaviour, H_c is expected to be lower than 100 A/m. Moreover, at low H_c , the M_s (173.18 Am²/kg) and bulk density (97%) is relatively low. Employing three scans using low E (≤ 20 J/mm³) after the first scan using high E (≥ 60 J/mm³) and low P (≤ 30 W) could refine the microstructure further (increase amorphous content, lowering particle size), which may achieve the fabrication of high bulk density parts with the superior soft-magnetic properties via the LPBF process. To reduce the particle size and increase the amorphous content, the heat input to the powder layer (energy density) needs to be low, whereas achieving high bulk density and M_s needs a higher energy density. This study indicated that to resolve that conflict, a multiple scanning mechanism is necessary to be applied such as described above.

Acknowledgments

I would like to express my very great appreciation to the Republic of Turkey Ministry of National Education for funding this project.

CRedit author statement

Merve G. Ozden – Conceptualization, methodology, validation, formal analysis, investigation, resources, data curation, writing – original draft, writing – review & editing, visualization, project administration and funding acquisition.

Nicola A. Morley – Conceptualization, methodology, resources, writing – review & editing, supervision and project administration.

References

- [1] T. Liu, F. Li, A. Wang, L. Xie, Q. He, J. Luan, A. He, X. Wang, C. Liu and Y. Yang, “High performance Fe-based nanocrystalline alloys with excellent thermal stability,” *Journal of Alloys and Compounds*, vol. 776, pp. 606-613, 2019.
- [2] O. Gutfleisch, M. Willard, E. Bruck, C. Chen, S. Sankar and J. Liu, “Magnetic materials and devices for the 21st century: stronger, lighter, and more energy efficient,” *Adv Mater.*, vol. 15;23, no. 7, pp. 821-842, 2011.
- [3] T. Liu, H. Zhang, F. Kong, A. Wang, Y. Dong, A. He, X. Wang, H. Ni and Y. Yang, “Grain refinement mechanism of soft-magnetic alloys with nanocrystals embedded in amorphous matrix,” *Journal of Materials Research and Technology*, vol. 9, no. 3, pp. 3558-3565, 2020.
- [4] J. Silveyra, E. Ferrara, D. Huber and T. Monson, “Soft magnetic materials for a sustainable and electrified world,” *Science*, vol. 362, no. 6413, p. eaao0195, 2018.
- [5] D. Azuma, N. Ito and M. Ohta, “Recent progress in Fe-based amorphous and nanocrystalline soft magnetic materials,” *Journal of Magnetism and Magnetic Materials*, vol. 501, p. 166373, 2020.
- [6] H. Li, A. Wang, T. Liu, P. Chen, A. He, Q. Li, J. Luan and C. Liu, “Design of Fe-based nanocrystalline alloys with superior magnetization and manufacturability,” *Materials Today*, vol. 42, pp. 49-56, 2021.
- [7] M. Cai, J. Wang, Q. Wang, Z. Guo, Q. Luo, J. Zhou, T. Liang, X. Li, Q. Zeng and B. Shen, “Improvement of soft-magnetic properties for Fe-based amorphous alloys with high saturation polarization by stress annealing,” *Materials Research Letters*, vol. 11, no. 7, pp. 595-603, 2023.
- [8] R. Alben and J. Becker, “Random anisotropy in amorphous ferromagnets,” *Journal of Applied Physics*, vol. 49, pp. 1653-1658, 1978.
- [9] G. Herzer, “Modern soft magnets: Amorphous and nanocrystalline materials,” *Acta Materialia*, vol. 61, pp. 718-734, 2013.
- [10] G. Herzer, “Soft Magnetic Nanocrystalline Materials,” *Scripta Metallurgica et Materialia*, vol. 33, no. 10/11, pp. 1741-1756, 1995.

- [11] G. Herzer, "Chapter 3 Nanocrystalline soft magnetic alloys," *Handbook of Magnetic Materials*, vol. 10, pp. 415-462, 1997.
- [12] A. Leary, V. Keylin, A. Devaraj, V. DeGeorge, P. Ohodnicki and M. McHenry, "Stress induced anisotropy in Co-rich magnetic nanocomposites for inductive applications," *Journal of Materials Research*, vol. 31, pp. 3089-3107, 2016.
- [13] Y. Ogawa, M. Naoe, Y. Yoshizama and R. Hasegawa, "Magnetic properties of high Bs Fe-based amorphous material," *Journal of Magnetism and Magnetic Materials*, vol. 304, no. 2, pp. 675-677, 2006.
- [14] J. Zhang, C. Chang, A. Wang and B. Shen, "Development of quaternary Fe-based bulk metallic glasses with high saturation magnetization above 1.6 T," *Journal of Non-Crystalline Solids*, vol. 358, no. 12-13, pp. 1443-1446, 2012.
- [15] N. Yodoshi, S. Ookawa, R. Yamada, N. Nomura, K. Kikuchi and A. Kawasaki, "Effects of nanocrystallisation on saturation magnetisation of amorphous Fe₇₆Si₉B₁₀P₅," *Materials Research Letters*, vol. 6, no. 1, pp. 100-105, 2018.
- [16] L. Shi and K. Yao, "Composition design for Fe-based soft magnetic amorphous and nanocrystalline alloys with high Fe content," *Materials and Design*, vol. 189, p. 108511, 2020.
- [17] A. Setyawan, K. Takenaka, P. Sharma, M. Nishijima, N. Nishiyama and A. Makino, "Magnetic properties of 120-mm wide ribbons of high Bs and low core-loss NANOMET alloy," *Journal of Applied Physics*, vol. 117, p. 17B715, 2015.
- [18] L. Hou, X. Fan, Q. Wang, W. Yang and B. Shen, "Microstructure and soft-magnetic properties of FeCoPCCu nanocrystalline alloys," *Journal of Materials Science and Technology*, vol. 35, no. 8, pp. 1655-1661, 2019.
- [19] Q. Luo, D. Li, M. Cai, S. Di, Z. Zhang, Q. Zeng, Q. Wang and B. Shen, "Excellent magnetic softness-magnetization synergy and suppressed defect activation in soft magnetic amorphous alloys by magnetic field annealing," *Journal of Materials Science and Engineering*, vol. 116, pp. 72-82, 2022.
- [20] T. Liu, A. He, F. Kong, A. Wang, Y. Dong, H. Zhang, X. Wang, H. Ni and Y. Yang, "Heterostructured crystallization mechanism and its effect on enlarging the processing window of Fe-based nanocrystalline alloys," *Journal of Materials Science and Technology*, vol. 68, pp. 53-60, 2021.

- [21] B. Sharma , X. Zhang, Y. Zhang and A. Makino, "Competition driven nanocrystallization on high Bs and low core loss Fe-Si-B-P-Cu soft magnetic alloys," *Scr. Mater*, vol. 95, pp. 3-6, 2015.
- [22] M. Ohta and Y. Yoshizawa, "Effect of heating rate on soft magnetic properties in nanocrystalline Fe_{80.5}Cu_{1.5}Si₄B₁₄ and Fe₈₂Cu₁Nb₁Si₄B₁₂ alloys," *Appl. Phys. Express*, vol. 2, p. 023005, 2009.
- [23] A. Makino, "Nanocrystalline soft magnetic Fe-Si-B-P-Cu alloys with high B of 1.8-1.9T contributable to energy saving," *IEEE Trans. Magn.*, vol. 48, pp. 1331-1335, 2012.
- [24] K. Suzuki, R. Parsons, B. Zhang, K. Onodera, H. Kishimoto and A. Kato, "Copper-free nanocrystalline soft magnetic materials with high saturation magnetization comparable to that of Si steel," *Appl. Phys. Lett.* , vol. 110, p. 012407, 2017.
- [25] X. Tong, Y. Zhang, Y. Wang, X. Liang, K. Zhang, F. Zhang, Y. Cai, H. Ke, G. Wang, J. Shen, A. Makino and W. Wang, "Structural origin of magnetic softening in a Fe-based amorphous alloy upon annealing," *Journal of Materials Science and Technology*, vol. 96, pp. 233-240, 2022.
- [26] M. McHenry, M. Willard and D. Laughlin, "Amorphous and nanocrystalline materials for applications as soft magnets," *Progress in Materials Science*, vol. 44, pp. 291-433, 1999.
- [27] T. Liu, A. He, A. Wang, X. Wang, H. Zhang and H. Ni, "Stabilizing Fe-based nanocrystalline alloys via a high-entropy strategy," *Journal of Alloys and Compounds*, vol. 896, p. 163138, 2022.
- [28] X. Li, Y. Dong, X. Liu, S. Wu, R. Zhao, H. Wu, W. Gao, A. He, J. Li and X. Wang, "Structure evolution of Fe-based nanocrystalline soft magnetic powder cores with excellent properties," *Materials Science and Engineering B*, vol. 285, p. 115965, 2022.
- [29] G. Herzer, "Grain structure and magnetism of nanocrystalline ferromagnets," *IEEE Trans. Magn.*, vol. 25, pp. 3327-3329, 1989.
- [30] G. Herzer, "Grain size dependence of coercivity and permeability in nanocrystalline ferromagnets," *IEEE Trans. Magn.*, vol. 26, pp. 1397-1402, 1990.

- [31] K. Suzuki and J. Cadogan, "Random magnetocrystalline anisotropy in two-phase nanocrystalline systems," *Phys. Rev. B*, vol. 58, pp. 2730-2739, 1998.
- [32] A. Hernando, P. Marin, M. Lopez, T. Kulik, K. Varga and G. Hadjipanayis, "Size dependence of coercivity in nanostructured soft alloys," *Phys. Rev. B*, vol. 69, p. 052501, 2004.
- [33] N. Kone and T. Hua, "Preparation and Study of the Crystallization Behavior of the Fe₈₇Zr₇B_{5-x} Nanocrystalline Soft-Magnetic Alloys," *Journal of Energy and Power Engineering*, vol. 14, pp. 100-110, 2020.
- [34] G. Barrionuevo, J. Ramos-Grez, M. Walczak, X. Sanchez-Sanchez, C. Guerra, A. Debut and E. Haro, "Microstructure simulation and experimental evaluation of the anisotropy of 316 L stainless steel manufactured by laser powder bed fusion," *Rapid Prototyp. J.*, vol. 29, no. 3, pp. 425-436, 2022.
- [35] J. Ravalji and S. Raval, "Review of quality issues and mitigation strategies for metal powder bed fusion," *Rapid Prototyp. J.*, vol. 29, no. 4, pp. 792-817, 2022.
- [36] M. Khorasani, A. Ghasemi, M. Leary, E. Sharabian, L. Cordova, I. Gibson, D. Downing, S. Bateman, M. Brandt and B. Rolfe, "The effect of absorption ratio on melt-pool features in laser-based powder bed fusion of IN718," *Opt. Laser Technol.*, vol. 153, p. 108263, 2022.
- [37] V. Sufiiarov, D. Erutin, A. Kantyukov, E. Borisov, A. Popovich and D. Nazarov, "Structure, Mechanical and Magnetic Properties of Selective Laser Melted Fe-Si-B Alloy," *Materials*, vol. 15, p. 4121, 2022.
- [38] Y. Nam, B. Koo, M. Chang, S. Yang, J. Yu, Y. Park and J. Jeong, "Selective laser melting vitrification of amorphous soft magnetic alloys with help of double-scanning-induced compositional homogeneity," *Mater. Lett.*, vol. 261, pp. 1-4, 2020.
- [39] L. Zrodowski, B. Wysocki and R. Wroblewski, "New approach to amorphization of alloys with low glass forming ability via selective laser melting," *J. Alloys Compd.*, vol. 771, pp. 769-776, 2019.
- [40] J. Zhou, J. You and K. Qiu, "Advances in Fe-based amorphous/nanocrystalline alloys," *Journal of Applied Physics*, vol. 132, p. 040702, 2022.

- [41] M. Ozden and N. Morley, "Optimizing Laser Additive Manufacturing Process for Fe-based Amorphous Magnetic Materials," *Journal of Alloy and Compounds*, vol. 960, p. 170644, 2023.
- [42] M. Ozden, F. S. Freeman and N. Morley, "Soft-Magnetic Behavior of Fe-Based Nanocrystalline Alloys Produced Using Laser Powder Bed Fusion," *Advanced Engineering Materials*, vol. 25, no. 19, p. 2300597, 2023.
- [43] S. Pauly, L. Lober, R. Petters, M. Stoica, S. Scudino, U. Kuhn and J. Eckert, "Processing metallic glasses by selective laser melting," *Materials Today*, vol. 16, pp. 37-41, 2013.
- [44] H. Hung, S. Choi, K. Prashanth, M. Stoica, S. Scudino, S. Yi, U. Kuhn, D. Kim, K. Kim and J. Eckert, "Fabrication of Fe-based bulk metallic glass by selective laser melting: A parameter study," *Materials and Design*, vol. 86, pp. 703-708, 2015.
- [45] F. Xie, Q. Chen, J. Gao and Y. Li, "Laser 3D printing of Fe-based bulk metallic glass: microstructure evolution and crack propagation," *JMEPEG*, vol. 28, pp. 3478-3486, 2019.
- [46] Y. Nam, B. Koo, M. Chang, S. Yang, J. Yu, Y. Park and J. Jeong, "Selective laser melting vitrification of amorphous soft magnetic alloys with the help of double-scanning-induced compositional homogeneity," *Materials Letters*, vol. 261, p. 127068, 2020.
- [47] D. Ouyang, W. Xing, N. Li, Y. Li and L. Liu, "Structural evolutions in 3D-printed Fe-based metallic glass fabricated by selective laser melting," *Additive Manufacturing*, vol. 23, pp. 246-252, 2018.
- [48] K. Fryzowicz, R. Dziurka, R. Bardo and M. Marciszko-Wiackowska, "Point-by-point laser exposure for crack susceptibility reduction in Powder Bed Fusion processing of H11 tool steel," *Journal of Materials Processing Technology*, vol. 316, p. 117946, 2023.
- [49] A. Yazdani, G. Hohne, S. Misture and O. Graeve, "A method to quantify crystallinity in amorphous metal alloys: A differential scanning calorimetry study," *PLoS ONE*, vol. 15, p. e0234774, 2020.

- [50] C. Yang , G. Yang, Y. Lu, Y. Chen and Y. Zhou, "Phase selection in highly undercooled Fe-B eutectic alloy melts," *Trans. Nonferrous Met. SOC. China*, vol. 16, pp. 39-43, 2006.
- [51] P. Zhang, J. Tan, Y. Tian, H. Yan and Z. Yu, "Research progress on selective laser melting (SLM) of bulk metallic glasses (BMGs): a review," *The International Journal of Advanced Manufacturing Technology*, vol. 118, pp. 2017-2057, 2022.
- [52] J. Lee, Y. Kim, J. Ahn, H. Kim, S. Lee and B. Lee, "Deformation-induced nanocrystallization and its influence on work hardening in a bulk amorphous matrix composite," *Acta Mater*, vol. 52, pp. 1525-1533, 2004.
- [53] S. Alleg, R. Drablia and N. Fenineche, "Effect of the laser scan rate on the microstructure, magnetic properties, and microhardness of selective laser-melted FeSiB," *Journal of Superconductivity of Novel Magnetism*, vol. 31, pp. 3565-3577, 2018.
- [54] S. Gao, X. Yan, C. Chang, E. Aubry, P. He, M. Liu, H. Liao and N. Fenineche, "Microstructure and magnetic properties of FeSiBCrC soft magnetic alloy manufactured by selective laser melting," *Materials Letters*, vol. 290, p. 129469, 2021.
- [55] L. Thorsson, M. Unosson, M. Perez-Prado, X. Jin, P. Tiberto, G. Barrera, B. Adam, N. Neuber, A. Ghavimi, M. Frey, R. Busch and I. Gallino, "Selective laser melting of a Fe-Si-Cr-B-C based complex-shaped amorphous soft-magnetic electric motor rotor with record dimensions," *Materials and Design*, vol. 215, p. 110483, 2022.
- [56] M. Willard and M. Daniil, "Nanocrystalline soft magnetic alloys two decades of progress," *Handbook of Magnetic Materials*, vol. 21, pp. 173-342, 2013.
- [57] S. Sgobba, "Physics and measurements of magnetic materials," *CERN*, vol. 4, pp. 39-63, 2010.

7 Conclusions and Future Work

7.1 Conclusions

The primary aim of this thesis has been to advance the use of laser additive manufacturing (LAM) for Fe-based amorphous/nanocrystalline soft-magnetic composites due to its dimensional flexibility, allowing to build 3D parts with a high degree of complexity in one go. This eliminated the need of post-processing, decreasing energy, production time and cost. For this purpose, this thesis presented an extensive experimental study on the laser powder bed fusion (LPBF) process optimization to attain Fe-based amorphous/nanocrystalline 3D bulk parts with superior soft-magnetic properties (high saturation magnetization (M_s) and low coercivity (H_c)) as well as high bulk density.

Initially, the volumetric energy input (E) with the range of 37-90 J/mm³ was utilized because it contains all the major laser process parameters; laser power (P), laser scan speed (v), hatch spacing (h) and layer thickness (t) (Chapter 4). In order to have a general idea about their effects on the properties of the sample, their different combinations were employed, P (= 90, 100, 120 and 150 W), v (= 700, 1000 and 1300 mm/s), t (= 30, 50, 70 μ m) and h (= 20, 30, 40, 50 and 60 μ m). As a result of the laser scanning process, nanocrystalline alloys were created which consisted of a disordered α -Fe(Si) and metastable Fe₂B nanophases, along with Fe₃Si nanocrystalline clusters, accompanied by a small amorphous phase constituting less than 10%. Although technically bulk density enhanced as P and t increases, v and h decreases (meaning high E), the highest density (99.45%) was attained with relatively low E (= 61.22 J/mm³, P =150 W, v =700 mm/s, h =50 μ m and t =70 μ m). This showed that the aforementioned parameters are interdependent to achieve minimal porosity and cracks. In that case, when dealing with a larger layer thickness of 70 μ m, it is advisable to utilize a high laser power (150 W) in conjunction with wider hatch spacing (50 μ m) and lower scan speed (700 mm/s), to obtain a greater level of density. In general, the use of high laser power (forming the large cracks), high laser scan speed (resulting in the balling effect) and high hatch spacing (leading to the insufficient overlapping between melt-pools) caused the failure or fracture of the parts.

The bulk density of the printed parts tended to increase as the energy density was increased, up to around 55 J/mm³. Beyond this point, the bulk density remained between 97% and 99%. When the energy density is below 55 J/mm³, there are numerous pores present in the microstructures due to insufficient energy being inputted into the powder bed. At the same energy densities, different bulk densities

were observed, indicating that energy density alone is not a reliable parameter to regulate the porosity level in the printed parts. Additionally, When E , v , and t were kept constant (at 60 J/mm³, 1000 mm/s, and 50 μm , respectively), the M_s of the samples differed depending on the values of P and h . The sample with P : 90 W and h : 30 μm had a saturation magnetization of 206 Am²/kg, whereas the sample with P : 150 W and h : 50 μm had a saturation magnetization of 150 Am²/kg. Consequently, it is necessary to individually investigate the effects of the primary process parameters on the final properties, which was the main purpose of the study in Chapter 5.

Another reason to conduct the research in Chapter 5 was the strong microstructural dependence of soft-magnetic behaviour. In Chapter 4, It was determined that the H_c (1.16-2.76 kA/m) is primarily affected by the size of the crystallites, rather than the presence of pores and cracks in the sample. In addition, M_s changes between 130-206 Am²/kg, influenced by crystallite size and distribution in the microstructure.

The findings in Chapter 4 helped to define the process parameters used in Chapter 5. To achieve high bulk density and M_s , layer thicknesses greater than 50 μm (50, 60 and 70 μm) and low hatch spacing values (20, 30 and 40 μm) were applied along with a moderate scan speed (900, 1000, 1100 mm/s). Also, as discussed in Chapter 4, to achieve bulk dense parts with increasing t , it was imperative to increase the P . Thus, for $t = 50 \mu\text{m}$, P values of 70, 80, and 90 W were used, for $t = 60 \mu\text{m}$, P values of 90, 100, and 110 W were employed, and for $t = 70 \mu\text{m}$, P values of 110, 120, and 130 W were used. This study indicated that to minimize porosity ($\leq 1\%$) and preventing cracks formation, it was necessary to use the combination of low P , v , h and t , which decrease energy input to the powder. Furthermore, the microstructure, which includes the amorphous and $\alpha\text{-Fe(Si)}$ and Fe_3Si phases, is affected by the thermal gradients that arise during laser scanning. These thermal gradients have a significant impact on the soft-magnetic properties. A decrease in the amorphous content and an increase in the amount of $\alpha\text{-Fe(Si)}$ crystallites in the microstructure result in an increase in M_s . It was found that using a hatch spacing of 30 μm and a scanning speed of 1000 mm/s at low laser power played an important role in obtaining high saturation magnetization ($\geq 200 \text{ Am}^2/\text{kg}$). The given process parameters resulted in increased undercooling which primarily affected the nucleation rate. As a result, the $\alpha\text{-Fe(Si)}$ phases decreased in size and were more closely distributed, promoting exchange interaction between them. On the other hand, this work did neither give much valuable information about the change in coercivity with different process parameters, nor reduce it (1.35-2.72 kA/m) to be used in soft-magnetic applications, where H_c is needed to be lower than 1 kA/m.

The only thing can be said that the use of low P (70 W), low v (900 mm/s) with the layer thickness of 50 μm lowered the coercivity significantly to 1.35 kA/m.

In order to gain a better understanding of how different process parameters affect coercivity, it was necessary to conduct a thorough microstructural analysis of each sample. This analysis was performed in the following study (Chapter 6) where efforts were made to decrease coercivity without compromising saturation magnetization and bulk density, by reducing P (30, 40 and 50 W) and v (500, 600 and 700 mm/s) along with low h (20, 30 μm) and t (50 μm). In addition to this, a newly designed scanning technique was introduced in this study. After the first scan applied using the process parameters mentioned above, the second scan was subjected with low E ($= 20 \text{ J/mm}^3$, $P= 20 \text{ W}$, $v= 1000 \text{ mm/s}$, $h= 20 \mu\text{m}$ and $t= 50 \mu\text{m}$) to every powder layer before spreading subsequent powder layer in order to increase amorphous content, decrease $\alpha\text{-Fe(Si)}$ crystallite size, and so reduce H_c .

This double scanning technique resulted in an improvement in several key properties of the printed parts, including bulk density (maximum of 99.5%), amorphous phase content (less than 16%), and saturation magnetization (less than 230 Am^2/kg). The particle size distribution of the main phase in the microstructure, $\alpha\text{-Fe(Si)}$, was also analysed to gain insight into the magnetization mechanism of the printed samples. By utilizing this strategy, the microstructure was refined to have a finer crystallite size and narrower particle size distribution. This led to an enhancement in the soft-magnetic properties, such as an increase in saturation magnetization (226.81 Am^2/kg) at high P (50 W) and h (30 μm) to the highest value recorded and a reduction in coercivity at low P (30 W) to the lowest value ever recorded (130 A/m).

7.2 Future Work

While the new technique has yielded positive results, such as higher M_s , bulk density, and the lowest H_c value for the LPBF process, the amorphous content is still relatively low. To further reduce coercivity and achieve excellent soft-magnetic behaviour, H_c should be lower than 100 A/m. However, at low H_c , M_s (173.18 Am^2/kg) and bulk density (97%) are relatively low. To refine the microstructure further, three scans using low E ($\leq 20 \text{ J/mm}^3$) after the first scan using high E ($\geq 60 \text{ J/mm}^3$) and low P ($\leq 30 \text{ W}$) could be employed to increase the amorphous content and lower particle size, potentially resulting in the fabrication of high bulk density parts with superior soft-magnetic properties via the LPBF process. To reduce particle size and increase amorphous content, the energy density needs to be low, while achieving high bulk density and M_s requires a higher energy density. To address this conflict, a multiple scanning mechanism, such as described above, is necessary.

Chapter 7 – Conclusions and Future Work

In this work, the process parameters were optimized to achieve high bulk density along with good soft-magnetic behaviour. Hence, another approach can be to study the powder spreadability with various particle size distribution and/or to play with alloy compositions in aim to increase glass forming ability. In the latter case, the increasing B content or introducing a small radius element like P to the alloy system as in the HBNA would increase atomic size difference, causing an increase in glass forming ability. The properties of the HBNA and the other types of Fe-based nanocrystalline alloys were discussed in the introduction part of the thesis (Chapter 1).

It was found that improving powder spreadability can be achieved by decreasing the recoating velocity and increasing the layer thickness [1]. However, a lower recoating velocity would result in longer manufacturing time, and higher layer thicknesses are limited by the bonding between the layers. The quality of the powder bed is also affected by the particle characteristics, such as the size distribution. A narrower size distribution that lacks smaller particles can result in better powder spreadability [2, 3]. Despite multiple research efforts in this field, a universally accepted metric for measuring spreadability in all powder-bed-based additive manufacturing processes with varying process parameters is yet to be established. Hence, future research can focus on defining a spreadability criterion that can accurately predict powder spreadability without the need for experimental testing, especially for the Fe-based soft-magnetic materials. Generally, the researchers that studied the powder spreadability has concentrated on achieving high bulk density and mechanical properties. There must be a work solely focused on the effect of powder spreadability and flowability on the magnetic properties as well as the bulk density of Fe-based nanocrystalline alloys.

References

- [1] M. Sehhat and A. Mahdianikhotbesara, "Powder spreading in laser-powder bed fusion process," *Granular Matter*, vol. 23, p. 89, 2021.
- [2] B. Liu, R. Wildman, C. Tuck, I. Ashcroft and R. Hague, "Investigation the Effect of Particle Size Distribution on Processing Parameters Optimisation in Selective Laser Melting Process," *International Solid Freeform Fabrication Symposium*, p. <http://dx.doi.org/10.26153/tsw/15290>, 2011.
- [3] J. Kruth, X. Wang, T. Laoui and L. Froyen, "Lasers and materials in selective laser sintering," *Assembly Automation*, vol. 23, no. 4, pp. 357-371, 2003.